

The Pennsylvania State University

The Graduate School

Department of Graduate Program

**THERMALLY STABLE COAL-BASED JET FUEL:
CHEMICAL COMPOSITION, THERMAL STABILITY,
PHYSICAL PROPERTIES AND THEIR RELATIONSHIPS**

A Thesis in

Fuel Science

by

Suchada Butnark

© 2003 Suchada Butnark

Submitted in Partial Fulfillment
of the Requirements
for the Degree of

Doctor of Philosophy

December 2003

The thesis of Suchada Butnark has been reviewed and approved* by the following:

Harold H. Schobert
Professor of Fuel Science
Thesis Advisor
Chair of Committee

Chunshan Song
Professor of Fuel Science

Semih Eser
Associate Professor of Energy and Geo-
Environmental Engineering

M. Mercedes Maroto-Valer
Assistant Professor of Energy and Geo-
Environmental Engineering

M. Albert Vannice
W.H. Joyce Chair in Chemical Engineering

Ljubisa R. Radovic
Professor of Energy and Geo-Environmental
Engineering
Graduate Program Chair, Fuel Science Option

* Signatures are on file in the Graduate School

Abstract

The pilot-scale production of the thermally stable coal-based jet fuel, so-called JP-900, has recently been performed using coal-derived liquids and a blend of coal-derived liquids with petroleum refinery streams. The hydrotreatment and dearomatization of light cycle oil (LCO) and refined chemical oil (RCO) were selected processes for the production of thermally stable compounds. Up to now, three generations of coal-based jet fuels have been produced in pilot plants and their thermal stability properties have been tested under static and dynamic conditions in autoxidative and pyrolytic regimes. In the present work, chemical compositions and structures, physical properties, combustion characteristics, and decomposition in a static system in the pyrolytic regime were studied for the candidate fuels.

Chemical compositions and structures of coal-based jet fuel were determined by GC/MS, ^{13}C NMR and ^1H NMR analyses. Quantitative analysis by GC/MS was used to classify chemical composition into nine groups of compounds, while ^1H NMR analysis was used to identify and quantify hydrogen structures in seven regions, based on their chemical shifts. The results from GC/MS and ^1H NMR characterization have been compared and show a significant agreement in terms of major composition in jet fuels.

The static tests in batch reactors were conducted in the pyrolytic regime at very high temperatures in the absence of oxygen. The pyrolytic stability in static conditions was determined by heating 5 mL of sample in a 25 mL-microautoclave at 480°C under 100 psig of UHP N_2 for different periods of time. Preliminary results have shown that the

hydrotreated LCO/RCO 1:3 having boiling range 180-270°C had the highest stability. Rates of solid deposition were also obtained for the jet fuels that have been produced from feedstock containing high RCO (the coal tar distillate component) concentration. In addition, it was found that the specific jet fuel distillation end point is one of the most important parameters controlling the jet fuel's chemical composition.

However, to produce a thermally stable jet fuel that can be utilized in the actual jet engines, the fuel quality has to meet ASTM specification requirements. The properties study has shown that all coal-based jet fuels meet ASTM specifications with high flash points and low cloud points. But, the problem associated with high aromatic contents in hydrotreated jet fuels is low smoke point, resulting in high sooting tendencies and emissions. Net heat of combustion of high-aromatic jet fuels is also relatively low, even though the energy density of the fuels is found to be high.

To study the relationships among chemical composition, solid deposition rate and other physical properties, mathematical models were established using multiple linear regression (MLR) and artificial neural network (ANN) approaches. ANN is more effective than MLR, as it can establish non-linear relationships of complex systems and can also accurately predict unseen data sets. For visualization purposes, the ternary diagrams have been used to display relationships among three main components with properties. An optimum chemical composition was developed to meet requirements of slow solid deposition rate, net heat of combustion at 18,400 Btu/lb and smoke point at 19 mm. Based on the existing data, the 1:1 blend of saturated LCO and saturated RCO, composing 0.76% aromatics, 68.47% cycloalkanes (46.98% decalin and 21.49% other cycloalkanes) and 30.77% alkanes and the others, is the only sample having chemical

composition that can meet all requirements. However, coal-based jet fuels which are composed of large amounts of aromatics, tetralins or decalins can still be desirable JP-900 if the limitations on aromatics, net heat of combustion and smoke points are flexible.

Finally, the correlations between hydrogen structures of coal-based jet fuels and solid deposition rate have been created using MLR and ANN. These correlations are statistically, physically and chemically satisfied. It was found that the structures of hydrogen donors in decalin, tetralin and indane are the main contribution to suppression of solid deposition. Based on this structure-thermal stability relationship, reaction mechanisms of pyrolytic degradation of coal-based jet fuels have been proposed.

Table of Contents

Lists of Figures	xi
Lists of Tables.....	xvii
Acknowledgements.....	xx
Chapter 1 Introduction	1
1.1 Introduction	1
1.2 Objectives	3
1.3 Hypotheses	4
1.4 Statement on Units	4
Chapter 2 Literature Review	5
2.1 Conventional Jet Fuels	5
2.2 The Development of JP-900	7
2.3 Thermal Stability	7
2.3.1 Autoxidative Stability	8
Role of Antioxidant.....	9
2.3.2 Pyrolytic Stability.....	10
2.3.2.1 Pyrolysis of Alkanes	11
2.3.2.2 Pyrolysis of Cycloalkanes.....	13
2.3.2.3 Pyrolysis of Alkylbenzenes.....	14
2.3.3 Effects of Autoxidation on Pyrolysis	15
2.3.4 Heat of Formation of Hydrocarbon Radicals	15
2.3.5 Hydrogen Donors for Thermally Stable Jet Fuel	18
2.3.5.1 Tetrahydronaphthalene (Tetralin)	18
2.3.5.2 Decahydronaphthalene (Decalin).....	19
2.3.5.3 Indane.....	21
2.3.6 Activation Energy of Hydrogen-Abstraction Reactions	21
2.3.7 Quantitative Structure-Property Relationship	25
2.4 Specification of Jet Fuel for U.S. Aircraft and Properties Testing.....	26
2.4.1 Chemical Composition of Jet Fuel and Its Relationships with Properties	27
2.4.2 Jet Fuel Thermal Oxidation Test (JFTOT).....	28
2.4.3 Combustion Properties	30
2.4.3.1 Hydrogen-to-Carbon Ratio (H/C)	31
2.4.3.2 Heat of Combustion and Energy Density	31
2.4.3.3 Smoke Point	32

2.4.4 Volatility.....	34
Flash Point.....	34
2.4.5 Fluidity	36
2.4.5.1 Viscosity.....	36
2.4.5.2 Cloud Point and Freezing Point	37
2.5 Graphical and Numerical Analyses	38
2.5.1 Ternary Diagrams.....	38
2.5.2 Multiple Linear Regression (MLR).....	39
2.5.2.1 Coefficient of Multiple Determination (R^2)	39
2.5.2.2 Coefficient of Multiple Determination Adjusted (R_a^2)	40
2.5.2.3 Mean Square Error (MSE).....	41
2.5.2.4 t-Test	41
2.5.2.5 F-Test	41
2.5.3 Artificial Neural Network (ANN)	42
2.5.3.1 Neural Network Structure	43
2.5.3.2 Multiple Layers of Neural Network.....	47
2.5.3.3 Neural Network Training	49
Chapter 3 Experimental Methods	50
3.1 Samples.....	50
3.1.1 Conventional Jet Fuels	50
3.1.2 Coal-Based Jet Fuels	50
3.2 Characterization of Jet Fuel Samples	56
3.2.1 GC/MS Quantitation	56
3.2.2 ^{13}C and ^1H NMR Analyses.....	59
3.3 Thermal Stability Tests.....	61
3.3.1 Thermal Stability Tests in Batch Conditions (Static Test).....	61
3.3.2 Quartz Crystal Microbalance Test.....	63
3.3.3 Thermal Stability Tests in Flow Conditions (Dynamic Test)	64
3.3.4 Thermal Stressing of Jet Fuels on Inconel 718	66
3.4 Physical Properties Testing	66
3.4.1 Hydrogen-to-Carbon Ratio.....	66
3.4.2 Net Heat of Combustion.....	67
3.4.3 Smoke Point	68
3.4.4 Flash Point.....	69
3.4.5 Viscosity.....	70
3.4.6 Cloud Point.....	71
3.5 Combustion Test.....	71
3.6 Graphical and Numerical Analyses	73
3.6.1 Ternary Diagrams.....	73
3.6.2 Multiple Linear Regression (MLR).....	73
3.6.3 Artificial Neural Network (ANN)	74
3.6.3.1 Constructing Training Sets.....	74
3.6.3.2 Training Methodology	75

Chapter 4 Characterization of Coal-Based Jet Fuels	76
4.1 Characterization of Conventional and Coal-Based Jet Fuel.....	76
4.1.1 GC/MS Quantitative Analysis.....	76
4.1.2 ¹³ C and ¹ H NMR Analyses.....	84
Chapter 5 Thermal Stability Tests	94
5.1 Thermal Stability Test of the First Generation Jet Fuel Candidates in Static Condition.....	94
5.1.1 Solid Deposition Rate.....	95
5.1.2 Chemical Distribution and Material Balance of Chemical Composition	101
5.1.3 Changes of Hydrogen Types during Stressing.....	105
5.1.4 Conversion of Decalin and Tetralin to Naphthalene.....	109
5.1.5 Addition of Decalin and Tetralin to Hydrotreated LCO/RCO and Saturated LCO/RCO	112
5.2 Thermal Stability Test of the First Generation Jet Fuel Candidates in Dynamic Condition	114
5.2.1 Carbon Deposit on Stainless Steel Surface	114
5.2.2 Carbon Deposit on Inconel 718 Surface	115
5.3 Comparison between Thermal Stability in Static and Dynamic Condition.....	115
5.4 Thermal Stability Test of the Second Generation Jet Fuel Candidates using Quartz Crystal Microbalance (QCM).....	116
5.5 Thermal Stability Test of the Third Generation Jet Fuel Candidates in Static Conditions	120
Chapter 6 Properties Testing.....	122
6.1 Results and Discussion of H/C Ratio	122
6.2 Results and Discussion of Heat of Combustion Test and Energy Density	123
6.3 Results and Discussion of Smoke Point Test	128
6.4 Results and Discussion of Flash Point Test.....	128
6.5 Results and Discussion of Viscosity Test.....	131
6.6 Results and Discussion of Cloud Point Test.....	134
6.7 Results and Discussion of Combustion Tests.....	135
6.8 Summary of Thermal Stability, Properties and Combustion Test.....	136
Chapter 7 Relationship of Chemical Composition and Properties: Graphical and Numerical Analyses	137
7.1 Relationship of Chemical Composition and Solid Deposition Rate (Static Condition)	138

7.1.1 Multiple Linear Regression (MLR) of Chemical Composition- Thermal Stability Relationship	145
7.1.2 Artificial Neural Network (ANN) Approach of Chemical Composition -Thermal Stability Relationship	149
7.2 Relationship of Chemical Composition and Combustion Properties	155
7.2.1 Relationship of Chemical Composition and Net Heat of Combustion (Q_n)	155
7.2.2 Relationship of Chemical Composition and Net Energy Density	161
7.2.3 Relationship of Chemical Composition and Smoke Point (S)	162
7.3 Relationship of Chemical Composition and Flash Point (T_f)	167
7.4 Relationship of Chemical Composition and Viscosity	172
7.5 Summary and Application of Graphic, MLR and ANN Models	174
7.5.1 Optimization of Chemical Composition	176
7.5.2 Proposed Route for Production of Prototype JP-900	179
Chapter 8 Relationship of Pyrolytic Stability and Hydrogen Types from ^1H NMR Spectroscopy: Quantitative Analyses	180
8.1 Relationship of Hydrogen Types and Solid Deposition Rate	181
8.2 Mechanisms for Coal-Based Jet Fuel Stressing in Pyrolytic Regime in Static Condition	195
Chapter 9 Conclusions and Suggestions for Future Work	202
9.1 Conclusions	202
9.1.1 General Conclusions	202
9.1.2 Conclusions from Ternary Diagram	205
9.2 Suggestions for Future Work	206
Bibliography	207
Appendix A Nomenclature	219
Appendix B GC/MS Analysis of Chemical Composition of Jet Fuels	222
B.1 Response Factor of Compound Classes and Determination of Eight Compound Classes' Concentration	222
B.2 MATLAB Source Code for Peak Identification	224
B.3 Chromatogram of Petroleum and Coal-Based Jet Fuels from GC/MS Analysis	226
Appendix C Thermal Stability and Properties Test Results	230
C.1 Weight of Gases in Static Thermal Stability Test	230
C.1.1 Calculation of N_2 Weight before Stressing	230

C.1.2 Calculation of Gas Weight after Stressing	231
C.2 Chemical Distribution of Stressed Jet Fuels with the Increasing Time ..	234
C.3 Summary of Thermal Stability and Properties Testing Results.....	240
Appendix D Numerical Analyses	254
D.1 MATLAB Source Code for Ternary Diagram Plots	254
D.2 Multiple Linear Regression Analysis	257
D.3 Artificial Neural Network Analysis.....	260

Lists of Figures

Figure 2-1: Fuel deposition regimes diagram [12].	8
Figure 2-2: Schematic of overall process of solid formation from alkanes [32].	13
Figure 2-3: Radical stabilization via hydrogen transfer from tetralin and decalin [59].	20
Figure 2-4: Schematic diagram of the JFTOT [77].	29
Figure 2-5: Schematic diagram of the typical architecture of ANN [96].	43
Figure 2-6: Structure of neuron [96].	44
Figure 2-7: Transfer function: (a) logistic, (b) linear and (c) tanh [96].	45
Figure 2-8: Multiple layers in neural network: (a) abbreviated notation [97] and (b) example of the first layer in a matrix form.	48
Figure 2-9: Neural network training [97].	49
Figure 3-1: The 25-mL microautoclave used for stressing jet fuel [58].	63
Figure 3-2: Flow reactor [113].	65
Figure 3-3: Smoke point lamp.	69
Figure 3-4: Schematic of model gas turbine combustor [122].	73
Figure 4-1: The distribution of chemical composition of petroleum-based and coal-based (first generation) jet fuels.	80
Figure 4-2: The distribution of chemical composition of coal-based (third generation) jet fuels of different boiling ranges.	83
Figure 4-3: NMR spectra of JP-8: (a) ^{13}C and (b) ^1H	85
Figure 4-4: ^{13}C spectra of (a) EI-001 (hydrotreated LCO), (b) EI-002 (hydrotreated (LCO/RCO)) and (c) EI-003 (hydrotreated RCO).	86
Figure 4-5: ^{13}C spectra of (a) EI-004 (saturated LCO), (b) EI-005 (saturated (LCO/ RCO)) and (c) EI-006 (saturated RCO).	87

Figure 4-6: ^1H spectra of (a) EI-001 (hydrotreated LCO), (b) EI-002 (hydrotreated LCO/RCO) and (c) EI-003 (hydrotreated RCO).	88
Figure 4-7: ^1H spectra of (a) EI-004 (saturated LCO), (b) EI-005 (saturated LCO/RCO) (c) EI-006 and (saturated RCO).	89
Figure 4-8: Percentages of different hydrogen types of JP-8 and coal-based jet fuels.....	91
Figure 5-1: Yields of stressed (a) JP-8 and (b) JP-8+100 after thermal stressing reaction in 25-mL microautoclave at 480°C from 0-360 minutes.	97
Figure 5-2: Yields of stressed (a) EI-001, (b) EI-002 and (c) EI-003 after thermal stressing reaction in 25-mL microautoclave at 480°C from 0-360 minutes.	98
Figure 5-3: Yields of stressed (a) EI-004, (b) EI-005 and (c) EI-006 after thermal stressing reaction in 25-mL microautoclave at 480°C from 0-360 minutes.	99
Figure 5-4: Comparison of the solid deposit with time between petroleum-based jet fuel and (a) hydrotreated fuels, and (b) saturated fuels.	100
Figure 5-5: Chemical distribution of stressed (a) EI-001, (b) EI-002 and (c) EI-003 with increasing stressing time.....	102
Figure 5-6: Chemical distribution of stressed (a) EI-004, (b) EI-005 and (c) EI-006 with the increasing time.....	104
Figure 5-7: Changes in the hydrogen type of the ^1H NMR spectrum of the EI-002 (hydrotreated LCO/RCO).	106
Figure 5-8: Changes in the hydrogen type of the ^1H NMR spectrum of the EI-005 (saturated LCO/RCO).	107
Figure 5-9: Percentages of different hydrogen types upon stressing (a) EI-002 or hydrotreated LCO/RCO and (b) EI-005 or saturated LCO/RCO.	108
Figure 5-10: Comparison of tetralin/naphthalene, decalin/naphthalene and (tetralin+ decalin)/naphthalene of stressed (a) EI-001, (b) EI-002 and (c) EI-003.	110
Figure 5-11: Comparison of tetralin/naphthalene, decalin/naphthalene and (tetralin+ decalin)/naphthalene of stressed (a) EI-004, (b) EI-005 and (c) EI-006.	111
Figure 5-12: Comparison of the solid deposit as the increase of time of (a) EI-002 and its blends and (b) EI-005 and its blends.....	113

Figure 5-13: Plots of QCM headspace oxygen and mass accumulation at 140°C for (a) JP-8 and (b) JP-8+100.	118
Figure 5-14: Plots of QCM headspace oxygen and mass accumulation at 140°C for three coal-derived jet fuels: (a) EI-025, (b) EI-029 and (c) EI-007 [7].	119
Figure 5-15: Comparison of the solid deposit with time between (a) petroleum-based jet fuel and (b) third generation of coal-based jet fuels.	121
Figure 6-1: H/C ratios of petroleum-based and first generation coal-based jet fuels.	123
Figure 6-2: Net heats of combustion of (a) petroleum-based and first generation coal-based jet fuels and (b) third generation coal-based jet fuels.	124
Figure 6-3: Net energy densities of (a) petroleum-based and first generation coal-based jet fuels and (b) third generation coal-based jet fuels.	127
Figure 6-4: Smoke points of (a) petroleum-based and first-generation coal-based jet fuels and (b) third-generation coal-based jet fuels.	129
Figure 6-5: Flash points of (a) petroleum-based and first-generation coal-based jet fuels and (b) third-generation coal-based jet fuels.	130
Figure 6-6: Viscosities of (a) petroleum-based and first generation coal-based jet fuels and (b) third generation coal-based jet fuels.	133
Figure 6-7: Cloud points of petroleum-based and first-generation coal-based jet fuels.	135
Figure 7-1: Ternary diagram plot between chemical composition (wt%) and solid deposition rate of jet fuel ($R_s \times 10^4$ wt%/min): (a) contour plot and (b) 3-D plot.	140
Figure 7-2: Ternary diagram plot between chemical composition (wt%) and solid deposition rate of jet fuel ($R_s \times 10^4$ wt%/min): (a) contour plot and (b) 3-D plot.	141
Figure 7-3: Ternary diagram between chemical composition (wt%) versus contour lines of ($R_s \times 10^4$ wt%/min) of jet fuels: (a) X_1 = tetralin and (b) X_2 = decalin.	144
Figure 7-4: Scatter plots between solid deposition rates of twenty-seven jet fuel samples and their compositions: (a) alkanes, (b) cycloalkanes, (c) decalins, (d) tetralins and (e) aromatics.	146

Figure 7-5: Scatter plots between solid deposition rates of sixty-eight jet fuel samples and their compositions: (a) alkanes, (b) cycloalkanes, (c) decalins, (d) tetralins and (e) aromatics.	147
Figure 7-6: Actual vs. fitted solid deposition rate on twenty-seven jet fuel samples.	149
Figure 7-7: Actual vs. network solid deposition rate on forty-one jet fuel samples. ...	151
Figure 7-8: Actual vs. network solid deposition rate on sixty-eight jet fuel samples.	153
Figure 7-9: Ternary diagram plot between chemical composition (wt%) and jet fuels' net heat of combustion: A contour plot.	155
Figure 7-10: Scatter plots between net heat of combustion of fifty-four jet fuel samples and their compositions: (a) total aromatics, (b) total cycloalkanes, (c) alkanes, alkenes and cycloalkenes, (d) alkanes, alkenes, cycloalkanes and cycloalkenes.	157
Figure 7-11: Actual vs. predicted net heats of combustion on fifty-four jet fuel samples: (a) MLR, (b) ANN and two variables, and (c) ANN and three variables.	160
Figure 7-12: Ternary diagram plot between chemical composition (wt%) and jet fuels' net energy density: A contour plot.	161
Figure 7-13: Ternary diagram plot between chemical composition (wt%) and jet fuels' flash points (°F): (a) contour plot and (b) 3-D plot.	163
Figure 7-14: Scatter plots between smoke points of seventeen jet fuel samples and their compositions: (a) cycloalkanes and (b) total aromatics.	164
Figure 7-15: Actual vs. predicted smoke point on seventeen jet fuel samples: (a) MLR and (b) ANN.	166
Figure 7-16: Ternary diagram between chemical composition (wt%) versus contour lines of flash point (°F) of jet fuels.	167
Figure 7-17: Scatter plots between flash points of thirty jet fuel samples and their compositions: (a) total aromatics (excluding tetralins), (b) total cycloalkanes (including decalins), (c) decalins, (d) tetralins and (e) alkanes.	169
Figure 7-18: Actual vs. predicted flash point on thirty jet fuel samples: (a) MLR and (b) ANN.	171

Figure 7-19: Scatter plots between viscosity of twelve jet fuel samples and their compositions: (a) total aromatics (including tetralins), (b) total cycloalkanes (including decalins), (c) tetralins, (d) decalins and (e) alkanes.	173
Figure 7-20: Ternary diagram plot between chemical composition and solid deposition rate ($R_s \times 10^4$ wt%/min). Area in the yellow lines indicates slow solid deposition rate ($0-250 \times 10^{-4}$ wt%/min). Green lines point out area of net heat of combustion under ASTM limit. Blue line indicates smoke point limitation. Pink area displays the optimum area.....	177
Figure 8-1: ^1H NMR spectra of (a) decalin and (b) tetralin.....	183
Figure 8-2: ^1H NMR spectra of (a) naphthalene and (b) indane.....	184
Figure 8-3: Chemical shifts of ^1H NMR spectra in seven regions.....	185
Figure 8-4: Scatter plots between solid deposition rates of forty-four jet fuel samples and their hydrogen structures in percentages: (a) region A, (b) region B, (c) region C, (d) region D, (e) region (E), (f) region E1, (g) region F and (h) region G.....	187
Figure 8-5: Actual vs. predicted solid deposition rate on forty-four jet fuel samples: (a) MLR and (b) ANN.	190
Figure 8-6: Correlation between solid deposition rate ($R_s \times 10^4$) (wt%/min) and $(H_C + H_D + H_{E1}) / (H_A + H_B)$ ratio.	192
Figure 8-7: Scatter plots showing the correspondence between hydrogen structures (%) from ^1H NMR analysis and chemical composition (wt%) from GC/MS analysis.	193
Figure 8-8: Major reactions of decalin in coal-based jet fuels: (a) dehydrogenation of decalin [58], (b) dehydrogenation of decalin followed with cracking [55], and (c) formation of biradical [55, 138].	197
Figure 8-9: Major reactions of tetralin in coal-based jet fuels: (a) dehydrogenation [32, 53, 138], (b) isomerization [51, 53, 138], and (c) cracking [53, 138].	199
Figure 8-10: Condensation of aromatics to (a) biphenyl and (b) binaphthyl [23] and (c) solid formation from polyaromatics [32].	200
Figure B-1: Chromatogram of JP-8 from GC/MS analysis.	226
Figure B-2: Chromatogram of JP-8 +100 from GC/MS analysis.	226
Figure B-3: Chromatogram of EI-001 (hydrotreated LCO) from GC/MS analysis. ...	227

Figure B-4: Chromatogram of EI-002 (hydrotreated LCO/RCO) from GC/MS analysis.	227
Figure B-5: Chromatogram of EI-003 (hydrotreated RCO) from GC/MS analysis. ...	228
Figure B-6: Chromatogram of EI-004 (saturated LCO) from GC/MS analysis.	228
Figure B-7: Chromatogram of EI-005 (saturated LCO/RCO) from GC/MS analysis.	229
Figure B-8: Chromatogram of EI-006 (saturated RCO) from GC/MS analysis.	229
Figure C-1: GC trace of gas formation from stressing of hydrotreated LCO/RCO at 480°C (100 psig N ₂) for 2 hours.	232
Figure C-2: Pressure record of hydrocarbon gases produced from stressing (a) petroleum-based jet fuels, (b) hydrotreated fuels and (c) saturated fuels at 480°C under N ₂ 100 psig.	233
Figure C-3: Chemical distribution of stressed EI-001 (hydrotreated LCO) with the increasing time: (a) class 1-5 and (b) class 5-9.....	234
Figure C-4: Chemical distribution of stressed EI-002 (hydrotreated LCO/RCO) with the increasing time: (a) class 1-5 and (b) class 5-9.....	235
Figure C-5: Chemical distribution of stressed EI-003 (hydrotreated RCO) with the increasing time: (a) class 1-5 and (b) class 5-9.....	236
Figure C-6: Chemical distribution of stressed EI-004 (saturated LCO) with the increasing time: (a) class 1-5 and (b) class 5-9.....	237
Figure C-7: Chemical distribution of stressed EI-005 (saturated LCO/RCO) with the increasing time: (a) class 1-5 and (b) class 5-9.....	238
Figure C-8: Chemical distribution of stressed EI-006 (saturated RCO) with the increasing time: (a) class 1-5 and (b) class 5-9.....	239
Figure C-9: Comparison of (a) NO _x emissions and (b) CO emissions corrected to 15% oxygen. (Chamber pressure = 0.56 MPa (5atm): T _{up} = 700°K (800°F)).....	252
Figure C-10: JP-8 vs. coal based jet fuel (a) soot sweep comparison and (b) pressure drop across peanut injector. (Chamber pressure = 0.56 MPa (5atm): T _{up} = 660°K (530°F))	253

Lists of Tables

Table 2-1: Heats of formation for hydrocarbon radicals [46, 48].	17
Table 2-2: Experimental E_a values for H-abstraction reactions [49, 62].	24
Table 2-3: U.S. Military specifications for aviation gas turbine fuel, JP-8 (adapted from CRC Handbook [69] and ASTM D 1655).	27
Table 2-4: Parameters of JFTOT [1].	29
Table 3-1: Lists of coal-based jet fuel candidates.	53
Table 3-2: Lists of coal-based jet fuel blends.	56
Table 3-3: Typical chemical shifts in ^{13}C -NMR spectra [106].	59
Table 3-4: Typical chemical shifts in ^1H -NMR spectra [107].	60
Table 4-1: Summary of eight basic compound classes present in fuel candidates.	77
Table 4-2: Fuel mixtures of conventional and PARC's first generation jet fuels in eight compound classes.	79
Table 4-3: Fuel mixtures of PARC's second generation jet fuels in eight compound classes.	81
Table 4-4: Fuel mixtures of PARC's third generation jet fuels in eight compound classes.	82
Table 4-5: Different types of carbon and hydrogen composition based on chemical shifts.	84
Table 4-6: ^1H NMR chemical shifts in seven regions (%) of conventional and PARC's first generation jet fuels in eight compound classes.	92
Table 6-1: Heat of combustion of pure compounds from API Technical Data Book [131] and Perry's Chemical Engineers' Handbook [120].	125
Table 6-2: Viscosities and freezing points of some compounds from API Technical Data Book [131].	132

Table 7-1: ANN results for five compound classes vs. solid deposition rate ($R_s \times 10^4$ wt%/min) of forty-one jet fuel samples.....	151
Table 7-2: ANN results for five compound classes vs. solid deposition rate ($R_s \times 10^4$ wt%/min) of sixty-eight jet fuel samples.....	153
Table 7-3: ANN results for two compound classes vs. net heat of combustion of fifty-four jet fuel samples.	158
Table 7-4: ANN results for three compound classes vs. net heat of combustion of fifty-four jet fuel samples.	159
Table 7-5: ANN results for three compound classes vs. smoke point of seventeen jet fuel samples.	165
Table 7-6: ANN results for three compound classes vs. flash point of thirty jet fuel samples.	170
Table 7-7: Coordinates (X_1, X_2, X_3) correspond with the optimized areas shaded in pink color.	178
Table 8-1: ^1H NMR chemical shifts in seven regions (%) of pure compounds.....	185
Table 8-2: ANN results for six hydrogen types vs. ($R_s \times 10^4$) (wt%/min) of forty-hour jet fuel samples.....	189
Table B-1: Response factor (RF) of hydrocarbon compounds to THF internal standard.....	223
Table C-1: Solid deposition rate of model compounds, petroleum-based and coal-based jet fuels (static condition).	240
Table C-2: Chemical composition versus solid deposit in flow condition (stainless steel surface) [129].	242
Table C-3: Chemical composition versus solid deposit in flow condition (Inconel 718 surface) [116]	243
Table C-4: QCM deposition results for the petroleum-based jet fuels and the second generation of coal-based jet fuels.	244
Table C-5: H/C ratios of petroleum-based and coal-based jet fuels.	245
Table C-6: Heat of combustion and energy density of model compounds, petroleum-based and coal-based jet fuels.	247

Table C-7: Smoke points of model compounds, petroleum-based and coal-based jet fuels.....	249
Table C-8: Flash points of petroleum-based and coal-based jet fuels.	250
Table C-9: Viscosity of petroleum-based and coal-based jet fuels.....	251
Table C-10: Cloud points of petroleum-based and coal-based jet fuels.	251

Acknowledgements

I would like to express my sincere gratitude to my advisor, Dr. Harold Schobert, for his guidance, encouragement and opportunities to present parts of this research through many conferences. His invaluable advice regarding my study and research are deeply appreciated. I would also like to respectfully acknowledge the contributions of my committee members, Dr. Chunshan Song, Dr. Semih Eser, Dr. M. Mercedes Maroto-Valer and Dr. M. Albert Vannice for their insightful discussions during the exams. I wish to thank Dr. Mark Badger, Dr. Xiaoliang Ma and Dr. Caroline Burgess for their helpful comments, guidance and support. Thanks are also due to Dr. William Roush for numerous advice through the use of neural network, Dr. Les Rudnick for interesting discussions of JP-900 candidates, Dr. David Clifford for the help and discussion on GC/MS and NMR analyses, Mr. Ron Copenhaver for the generous assistance with fabrication of the tubing bombs and Mr. Ronald Wasco for providing effective analyses instruments.

I extend my appreciation to alumni and graduate students in the Fuel Science Program and staffs of the Energy Institute for their friendly support, especially Dr. Melissa (Roan) Hess, James Strohm, Yi Yang, Maria Escallon, Scott Berkous, Ragini Acharya and Dr. Silvano Saretto, who provided me a great deal of discussions and input to my thesis. Special thanks are due to Dr. Surapong Lertrattanapanich for the help on MATLAB programming and neural network modeling and Dr. Pramote Hochareon for the assistance with document editing.

I would like to dedicate this thesis to my beloved parents, Mr. Chid Butnark and Mrs. Supa Butnark, who always understand and believe in me. My deepest gratitude goes directly to them for their continuous love, encouragement and patience for all years long.

The financial support has been supported by the U.S. Department of Defense and Air Force Office of Scientific Research. Koppers Industries and United Refining Company are gratefully appreciated for their contributions of coal tar distillates and light cycle oil feedstock respectively. The production of JP-900 candidates by PARC Technical Services, Inc. is also acknowledged.

Chapter 1

Introduction

1.1 Introduction

When the aviation gas turbine engines (jet engines) patent was issued to Sir Frank Whittle in the 1930s, it was understood that the engines could run on most liquid fuels [1]. However, it was found later that the engine performance would be much better if fuel properties were limited to a narrow range of specifications [2]. As a result, the current requirements for petroleum-based jet fuels have been established for aviation gas turbine engines. Those specifications are aromaticity, smoke point, viscosity, heat of combustion, freezing point, flash point, distillation range, vapor pressure and thermal oxidative stability.

Current jet fuels, JP-8 for the military aircraft and Jet A/Jet A-1 for commercial aviation, are produced from petroleum through refinery processes. The fuels' properties are tested by standard methods (ASTM Volume 05.01) to meet the specifications. With an expected increase in thermal stability requirement for operating temperatures as high as 900°F for advanced aircraft, coal-derived naphthenic jet fuels have shown an advantage over petroleum-derived paraffinic jet fuels [3]. In order to achieve acceptance of the new thermally stable coal-based jet fuel (or the so-called JP-900 [3]) for real gas turbine engines, the prototype jet fuel's specifications have to be established, along with the fuel system and engine tests.

In the present study, the pilot-scale production of prototype JP-900 is being performed using coal-derived liquids and a blend of coal-derived liquids with petroleum refinery streams. The hydrotreatment and dearomatization of light cycle oil (LCO) from BP Corporation [4] and the United Refining Company and refined chemical oil (RCO) from Koppers Industries [5] have shown a capability to produce chemical components resulting in thermal stability improvement over the conventional JP-8. For this particular work, the hydrotreated and dearomatized (saturated) fuel candidates and their blends were characterized and their compositions were classified. Analyses of their properties such as thermal stability, aromatic and olefinic components, heats of combustion (calorific value), flash points, viscosities and smoke points were also performed.

The pyrolytic stability of the coal-based jet fuels was extensively studied by stressing the fuels in static conditions. This type of stressing is important in that it will be encountered both during high-Mach flight of advanced jet aircraft and after landing, where some fuel is confined in very hot fuel lines for a certain period of time [6]. The composition changes throughout the stressing were also observed and were a part of the analysis of the design of JP-900's final formula.

One of the major challenges for coal-based thermally stable jet fuels is to make the samples resistant to thermal oxidative degradation [7]. For this purpose, some jet fuel candidates were thermally oxidized in a quartz crystal microbalance (QCM) system. In addition, the information and analyses about autoxidative stability as well as pyrolytic stability of coal-based jet fuels in dynamic condition will be discussed.

To develop future aircraft fuels, there is a growing need for reliable computational tools for thermal stability and physical properties prediction [2]. As the chemistry of

oxidative reactions and thermal degradation of a real fuel is very complicated, the numerical prediction of overall stability is considered a starting point for a model construction. In this work, two well-known computational tools, multiple linear regression (MLR) and artificial neural network (ANN), are introduced in order to correlate prototype JP-900's major chemical components with its thermal stability and properties. These models can explain the composition effects on properties. They can also be used to predict properties of the fuels if their compositions are identified. In addition, composition-properties relationships will also be graphically presented by ternary diagrams. Then all models will be optimized to help determine the most desirable chemical composition.

1.2 Objectives

The specific objectives of this work as part of JP-900 development are summarized below:

- (i) to design and produce a prototype coal-based jet fuel that is stable under operating temperature as high as 480°C (900°F) for extended periods of time, while still meeting the specification standard of current jet fuels.
- (ii) to optimize the chemical compositions of thermally stable JP-900 and find a relationship of major components (alkanes, cycloalkanes, aromatics, decalins and tetralins) to thermal stability from experimental results using numerical methods.

- (iii) to find the structure-thermal stability relationship. The hydrogen structures that show highest ability of hydrogen abstracting are expected to affect thermal stability significantly.
- (iv) to find the major compositions to properties relationships of this JP-900.

1.3 Hypotheses

(i) The relationships between major chemical components (alkanes, cycloalkanes, aromatics, decalins and tetralins) and properties (thermal stability and physical properties) can be established using different numerical approaches. And, the most desirable chemical composition for coal-based jet fuels can be optimized from the numerical studies.

(ii) Addition of decalin and tetralin can help improve thermal stability of the jet fuels. Optimum composition between these two components and other major components can be made to meet high thermal stability and specifications of physical properties.

(iii) Structure-thermal stability relationships can also be created. The easiest abstractable hydrogen structure that affects solid deposition significantly can be obtained from the models.

1.4 Statement on Units

In this thesis, when specifications or measurements are in English units in the original literature, they will be reported in English units to avoid some errors.

Chapter 2

Literature Review

Current jet fuel is a petroleum-based fuel that is used in large quantities (about 1.67 million barrels/day [8] or 26 billion gallons annually [9]) in the U.S. transportation sector. Most of it is used by airlines. For military purposes, the Air Force uses about 5 billion gallons [10] of jet fuel annually.

The composition of jet fuel is very complex and can vary from sample to sample as a result of variation in crude sources and refining processes [1]. To provide acceptable performance in gas turbine engines, the fuel properties have to be limited by physical and chemical properties specifications. Those specifications are aromaticity, smoke point, viscosity, heat of combustion, freezing point, flash point, distillation range, vapor pressure and thermal stability.

2.1 Conventional Jet Fuels

Jet fuel is primarily composed of alkanes, cycloalkanes, aromatics (~25% by volume), olefins (~5% by volume) and small amounts of heteroatomic compounds, such as sulfur compounds of which the U.S. now allows at maximum 4000 ppm [11].

Current jet fuels for commercial aviation and military purposes are produced from petroleum through refinery processes. Jet fuel comes in a variety of grade designators; here are the common civilian and military grades in use today [12, 13]:

Jet-A is a narrow-cut kerosene product. This is the standard commercial and general aviation grade available in the United States. It usually contains no additives but may be treated with anti-icing chemicals [13].

Jet-A1 is identical to Jet-A but is used outside the United States. It is the fuel of choice for long-haul flights where the fuel temperature may fall to near the freezing point. It often contains a static dissipater additive [13].

Jet-B is a wide-cut kerosene with lighter gasoline-type naphtha components, contains static dissipater and has a very low flash point [13].

JP-4 is a military designation for a fuel like Jet-B but contains a full additive package including corrosion inhibitor, anti-icing and static dissipater [12].

JP-5 is another military fuel. It has a higher flash point (140°F min.) than JP-4 and was designed for use by the US Navy on board aircraft carriers. It contains anti-icing and corrosion inhibitors [12].

JP-7 is a highly refined kerosene, mainly alkanes and cycloalkanes, used for high-altitude high-Mach flights [12].

JP-TS is a JP-7 base stock with thermal oxidative stability package and lower freezing point. Maximum allowable temperature is higher than 900°F [14].

Two grades of the kerosene type of aviation turbine fuel used in this work are:

JP-8 is a kerosene-type turbine fuel that contains a static dissipator additive, corrosion inhibitor/lubricity improver, and fuel system icing inhibitor, and may contain an antioxidant and metal deactivator [15].

JP-8+100 is a JP-8 type kerosene turbine fuel which contains a qualified thermal stability improver additive. The additives are described as SPEC AID 8Q462, from BetzDearborn, The Woodlands, TX [15].

2.2 The Development of JP-900

Penn State's jet fuel project has three major components: production, stabilization and combustion. For the ongoing production (in this study), Penn State and PARC Technical Services have been developing an advanced coal-based thermally stable jet fuel that can be used as the source of propulsion energy for the aircraft and an on-board heat sink. The goal of this project is to design and make a coal-based jet fuel that is capable of withstanding temperatures up to 480°C (900°F) for extended periods of time, while still meeting quality standards for current jet fuels [16]. In addition to the fuel's quality, a secondary objective of this JP-900 has been the displacement of imported petroleum by coal [16].

2.3 Thermal Stability

The stability of a jet fuel, or the fuel's tendency to degrade or change its initial characteristics prior to combustion due to oxidative and/or thermal conditions in the fuel's environment, is a major consideration in the design of aircraft fuel systems [2]. Hazlett [17] classified the jet fuel degradation into three regimes, explained by the mechanism of deposit formation: liquid-phase autoxidation at low temperatures (150-

260°C) and gas phase or supercritical pyrolysis at high temperatures ($\geq 400^\circ\text{C}$), and a combination of these two in the transition region (260-400°C). The temperature profile versus solid deposit is shown in Figure 2-1 [12].

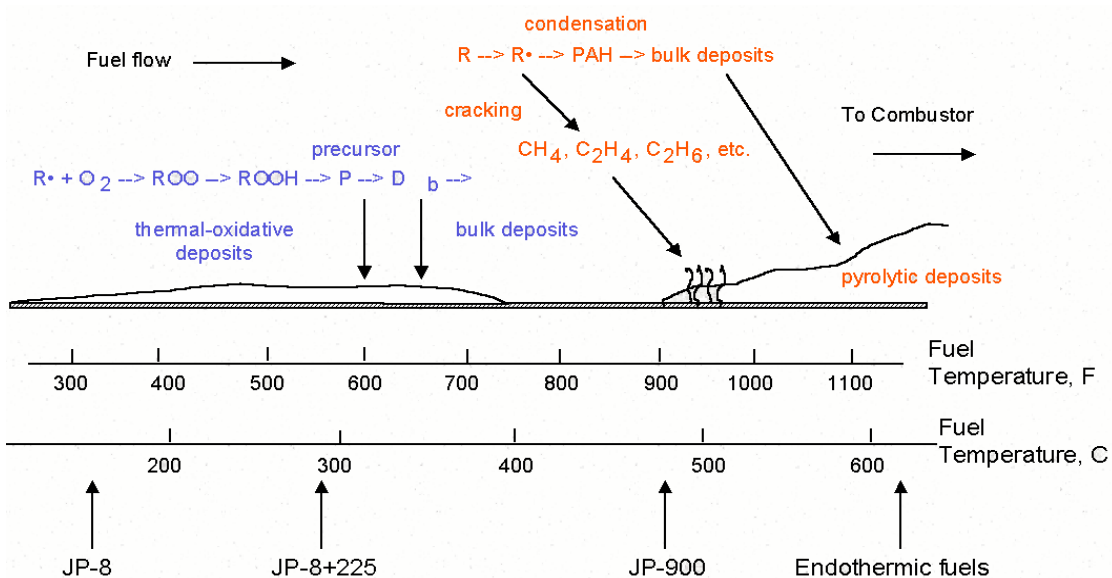


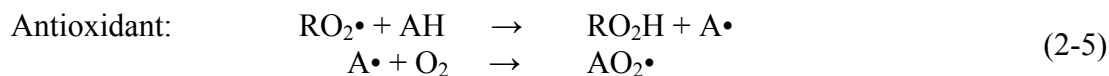
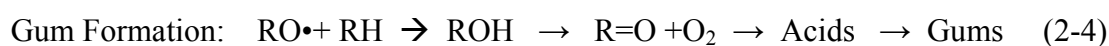
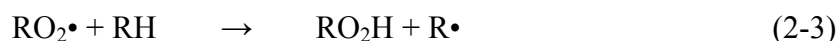
Figure 2-1: Fuel deposition regimes diagram [12].

2.3.1 Autoxidative Stability

Temperatures ranging between 150 and 260°C define the autoxidative regime. Oxidation of fuel components by dissolved oxygen is a process in the formation of deposits in thermally stressed jet fuels. Peroxide species are the key intermediates in the autoxidation scheme that produces insolubles.

As a fuel is heated, the dissolved oxygen in the fuel (~70 ppm in fuel exposed to air) begins to react with the fuel, forming hydroperoxides, deposits and other products [1]. As the fuel is further heated, the deposition then soon decreases due to the

consumption of the dissolved oxygen in the fuel. The mechanism of autoxidation reactions can be shown as follows [18].



Reaction (2-1) is a simple initiation process that forms the alkyl radical. Reactions (2-2) to (2-4) are oxidation of a hydrocarbon fuel where the alkyl peroxide is a key in the propagation of autoxidation reaction to form gum and deposits. Finally, reaction (2-5) is the antioxidant chemistry that is associated with the antioxidant [19].

Role of Antioxidant

Antioxidants are generally molecules with an easily abstracted hydrogen atom. The antioxidant reaction must compete with the autoxidation reaction and has to be faster than the autoxidation so that the radical formed (when a hydrogen atom is abstracted) does not propagate the free radical reaction to form autoxidative deposits. Thus, an easily abstractable hydrogen atom is necessary for a molecule to be a good antioxidant that does not contribute to deposit formation as it is oxidized [19].

Some storage antioxidants are hindered phenols but they tend to promote pyrolytic instabilities. For typical additives, metal deactivators (MDA) have shown to decrease solid deposit by preventing the initial hydrogen abstraction from paraffins which initiates the autoxidation process [20]. Recently, a new antioxidant that has been expected to prevent both autoxidative and pyrolytic deposits is dihexylphenylphosphine [21].

2.3.2 Pyrolytic Stability

The term “thermal stability” in this study relates to the type of instability of fuel that occurs in the pyrolytic regime when the fuel is used as the main coolant for electronic and mechanical parts of aircraft systems [22]. Unlike autoxidative stability, which is limited by the amount of dissolved oxygen in the fuel, pyrolytic deposition is controlled by the temperature and time history of the fuel [14].

Pyrolytic reactions take place when the fuel is exposed to temperatures greater than 400°C. The reaction proceeds via free-radical processes: initiation, propagation and termination.

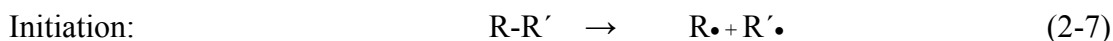
The critical point in building a chemical reaction mechanism is the knowledge of rate coefficients and thermodynamic data [2]. There have been extensive studies on the kinetic modeling of decomposition of hydrocarbons such as long straight-chain alkanes [23-26], aromatics [23, 27], and polycyclic aromatic hydrocarbons (PAH) [23, 28]. The first approach is to treat a jet fuel as a single chemical compound and to propose a free-radical mechanism for the thermal cracking of short alkanes that may be used to predict the product distribution [29]. This work has been found to agree with semi-quantitative experiments for decomposition of longer alkanes performed by Voge [30].

For the formation of pyrolytic carbon, Frenklach et al. [31] suggested that cycloalkanes and aromatics should be included in modeling the chemical reactions. The gas-phase reactions mechanisms have also been proposed on the radical addition to unsaturated hydrocarbons and the growth of PAH from cycloalkanes and aromatics [32].

2.3.2.1 Pyrolysis of Alkanes

The proposed mechanism by Kossiakoff and Rice [29] suggested that radical initiation takes place by the thermolysis of carbon-carbon bonds, resulting in alkyl radicals. The alkyl radicals can then react with another fuel molecule, abstracting hydrogen and resulting in a stable species and a new alkyl radical. This is followed by the decomposition of the new radical into one or more radicals as well as an ethyl or methyl radical or a hydrogen atom.

Initiation occurs by the homolysis of carbon-carbon single bonds.

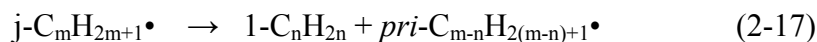
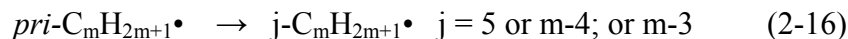
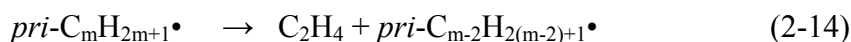
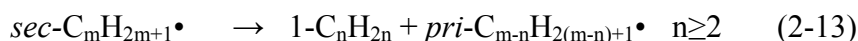
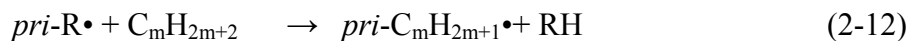
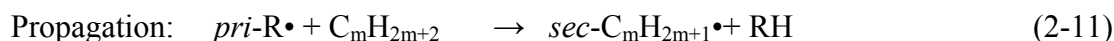
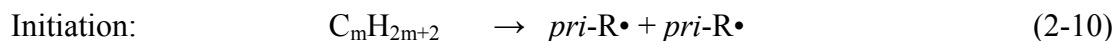


The chain is propagated by β -scission and hydrogen abstraction.



New radicals are formed by β -scission of a larger radical and hydrogen abstraction. The rearrangement of radicals from one type to another stable type also occurs.

Song *et al.* [6] proposed general reaction mechanisms for thermal cracking of *n*-tetradecane, which is a representative component of unbranched long-chain alkanes in jet fuels, under elevated pressure at 400-450°C. The pyrolysis of *n*-tetradecane proceeds by radical reaction pathways. As in every radical chain mechanism, the elementary reactions include initiation, propagation and termination. The propagation reactions can be divided into hydrogen abstraction (Equations (2-11), (2-12) and (2-15)), radical decomposition (Equations (2-13), (2-14) and (2-17)), radical addition (which is the opposite of radical decomposition), and radical isomerization (Equation (2-16)).



The work on the pyrolysis of jet fuels under the JP-900 program has established overall compositional changes in liquid fuel via the following sequence (Figure 2-2) [32]:

Long-chain alkanes → alkenes → cycloalkenes/cycloalkanes → alkylbenzenes → polyaromatics → solids

Dienes + cycloalkene → Multi-ring cycloalkenes → polyaromatic → solids

R· + aromatics → R-aromatics → Polyaromatics → solids

R· + solid → R-solids → Deposit-thickening/Larger particles

Figure 2-2: Schematic of overall process of solid formation from alkanes [32].

The sequences are considered to be dependent on fuel composition. The first step is generally the formation of an alkene, followed by the cyclization to form alkyl cycloalkenes or cycloalkanes which can undergo dehydrogenation to form alkylbenzenes. The polyaromatic hydrocarbons (PAH) can be generated from cyclic structures (as seen in first, second and third step) to finally form solid. The fourth reaction describes the thickening of the deposit layer.

2.3.2.2 Pyrolysis of Cycloalkanes

Fabuss *et al.* [33] studied the pyrolysis of twenty-eight saturated cyclic hydrocarbons, including C₁ to C₄ cyclohexanes, at 427°C and high pressures and developed a general correlation between decomposition rate and molecular structure. Lai and Song [34] also pyrolyzed cyclohexane and seven *n*-alkylcyclohexanes in or near the supercritical phase in a batch reactor at 450°C and continuously increasing pressure for 6-480 min. They found that the thermal stability of alkylcyclohexanes decreased with increasing side-chain length and that the major reaction pathways of alkylcyclohexanes were strongly dependent on the side-chain length. Yu and Eser [35] conducted studies at

425-475°C with pressures around 340-1100 psi and found that there was an additional reaction pathway of isomerization, in addition to dehydrogenation and ring opening, at low conversions. The isomerization products became minor compared to the formation of the ring-opening products of toluene and benzene when the conversion is increased.

2.3.2.3 Pyrolysis of Alkylbenzenes

A large amount of alkylbenzenes is also present in jet fuel. Thermal pyrolysis of *n*-alkylbenzenes has been studied by many investigators. The early works focused on the compounds with short alkyl chains, including toluene, ethylbenzene, *n*-propylbenzene and *n*-butylbenzene [36, 37] as well as long-chain alkylbenzenes in relation to the processing of heavy crude oils and coal [38, 39]. Savage and Klein [39] proved that the thermolysis mechanism of a long-chain alkylbenzene was entirely free-radical and was a sequence of elementary steps including radical initiation, hydrogen abstraction, β -scission and termination. And, the major product found in the thermolysis of long-chain *n*-alkylbenzenes at relatively higher pressure and lower temperature conditions was toluene. Yu and Eser [40] explained the reaction of *n*-butylbenzene by free-radical mechanisms, dominated by side-chain cracking, and found that the major liquid products from *n*-butylbenzene were styrene (low-pressure subcritical region) and toluene (supercritical region).

In the study of thermal reactivity of various model compounds, Peng *et al.* [41] observed that *n*-butylbenzene exhibited the highest reactivity among long-chain alkanes, *n*-butylcyclohexanes, decalin and tetralin. They also incorporated a semiempirical

quantum chemical method, PM3, with the pyrolysis experiment of *n*-pentylbenzene to help in proposing a mechanism. The pyrolysis occurred dominantly by the hydrogen abstraction from the α -position, followed by an intramolecular hydrogen transfer to form a γ -position radical and then, β -scission of the γ -position radical. In addition, Peng (1995) has demonstrated that the global kinetic parameters have shown a gradual increase in rate constants with increasing chain length at same temperature; and the activation energy (E_a) decreased slowly with increasing chain length [42].

2.3.3 Effects of Autoxidation on Pyrolysis

There is little work that examines both the autoxidative and pyrolytic regimes. Edwards and Libero [43] briefly examined the effects of autoxidation on pyrolysis and suggested that the oxygenated compounds formed in the autoxidative phase of the reactions were able to react with the radicals produced in the pyrolytic regime and force termination. However, Yoon (1996) [44] has shown that the classic antioxidants, e.g. hindered phenols, secondary aromatic amines, organosulfur compounds, organotin stabilizers and aryl derivatives of tin, had a significant effect on the rate of degradation of Jet A-1 fuel and some of them even promoted carbonaceous solids. Some conventional hydrogen donor solvents (e.g. tetralin and tetrahydroquinoline) used in coal liquefaction were then evaluated. Tetralin, tetrahydroquinoline and benzyl alcohol were found to be high temperature (>400°C) stabilizers for jet fuel [45].

2.3.4 Heat of Formation of Hydrocarbon Radicals

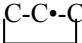


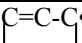


Pyrolysis reactions of jet fuel are primarily involved with hydrocarbon free radicals. See Equation (2-19). These free radicals are recognized as important short-lived,

highly reactive intermediates in a variety of organic reactions [46] in the gas phase and frequently in the liquid phase as well [47]. To understand the fundamental thermal chemistry and mechanism of free radical processes, the standard-state heats of formation (or enthalpies of formation, ΔH_f°) of the radicals are found to provide very essential information [48]. However, the experimentally determined ΔH_f° values of hydrocarbon radicals in the literature are limited. Thus, many approaches have been developed to estimate ΔH_f° of radicals on the basis of empirical, semiempirical, or theoretical studies [48, 49].



The ΔH_f° of different radicals from experiments have been summarized in Table 2-1. Unfortunately, ΔH_f° values of chemical compositions ($\text{C}_{10}\text{-C}_{15}$) in jet fuels are not available. But, one can use the information of heats of formation of these radicals to derive group values and thus provide predictive capabilities for entire classes of molecules [47]. For example, tertiary alkyl radicals are more likely to occur than primary and secondary alkyl radicals because of their low heats of formation to form free radicals. Cycloalkanes tend to be the most stable components, as their heats of formation of free radicals are very high when compared to other long-chain alkanes of the same carbon numbers. This is an explanation why naphthenic compounds (cycloalkanes and decalins) are desirable components for thermally stable jet fuels. From Table 2-1, alkenyl, cycloalkenyl, aryl, alkynyl and vinyl compounds are also stable components by themselves but they are precursors to polyaromatics which lead to solid deposition [11].

Table 2-1: Heats of formation for hydrocarbon radicals [46, 48].

No.	Radical	Structure	ΔH_f° (kcal/mol)
	<i>Primary alkyl radicals</i>		
1	<i>n</i> -propyl	C-C-C•	23.9
2	<i>n</i> -pentyl	C-C-C-C-C•	13
3	<i>n</i> -hexyl	C-(C) ₄ -C•	8
	<i>Secondary alkyl radicals</i>		
4	<i>i</i> -propyl	C-C•-C	21.9
5	<i>n</i> -pent-2-yl	C-C•-C-C-C	12
6	<i>n</i> -pent-3-yl	C-C-C•-C-C	11.2
7	<i>n</i> -hex-2-yl	C-C•-C-C-C-C	7
	<i>Tertiary alkyl radicals</i>		
8	<i>tert</i> -butyl	(C) ₃ C•	11.5
9	<i>tert</i> -pentyl	C-C-C•(C) ₂	6.7
10	3-methyl-3-pentyl	C-C-C•(C)-C-C	3.4
	<i>Cyclo alkyl radicals</i>		
11	cyclopropyl		66.9
12	cyclopentyl		24
13	cyclohexyl		18
	<i>Alken-α-yl radicals</i>		
14	allyl	C=C-C•	39.5
15	1-penten-3-yl	C=C-C•-C-C	25
	<i>Arylalk-α-yl radicals</i>		
16	benzyl	Ph-C•	48.4
	<i>Cycloalken-α-yl radicals</i>		
17	cyclopropenyl		105
18	cyclopenten-3-yl		38.4
19	cyclohexen-3-yl		30
	<i>Alkyn-α-yl radicals</i>		
20	propargyl	C≡C-C•	81.0
21	2-pentyn-4-yl	C-C≡C-C•-C	65.2
22	4-methyl-2-pentyn-4-yl	C-C≡C-C•-(C) ₂	53.0
	<i>Vinyl radicals</i>		
23	propen-2-yl	C=C•-C	55.3
24	phenyl	Ph•	81.0

2.3.5 Hydrogen Donors for Thermally Stable Jet Fuel

In previous studies, naphthenic model compounds have shown superior thermal stability in this regime [44]. And, hydrogen donors such as tetrahydronaphthalene (tetralin) are considered high-temperature thermal stabilizers for jet fuels [44, 45]. From a recent study, mixtures of tetralins, methyltetralins and decalins present in coal-based jet fuels could help improve thermal stability [50]. However, the high aromatic content that is present in such fuel has been found to promote formation of solid deposits [11]. As a result, the compromise between such hydrogen donors and aromatic contents is a significant key to jet fuel's thermal stability, which can be measured by the solid deposition rate.

2.3.5.1 Tetrahydronaphthalene (Tetralin)

Tetralin is the simplest model of hydroaromatic hydrocarbons that constitute the basis of the solvent in coal-liquefaction processes. It has been used as a hydrogen donor solvent for studying coal liquefaction, semicoking, and coking conditions where the temperature is being varied in the range of 350-1000°C [51-56]. However, it can also degrade at this high temperature. Bredael and Vinh [53] suggested three routes of tetralin degradation:

- (i) By rupture of the saturated ring and elimination of gaseous fragments.

This leads to ethylbenzene, ethylene, benzene and toluene.

- (ii) Degradation of tetralin by opening the saturated ring and intramolecular recombination, with dehydrogenation to form 2-methylindene. This compound decomposes at the same temperature as tetralin, into indene and methane.
- (iii) Degradation of tetralin into naphthalene by direct dehydrogenation.

2.3.5.2 Decahydronaphthalene (Decalin)

Unlike tetralin, decalin undergoes thermal cracking and yields large amounts of monoaromatics (BTX-type compounds) and gases (such as methane and ethylene) at temperatures of 700-950°C [55, 57]. The thermal cracking of decalin begins with the cleavage of one ring into alkylalicyclic compounds. These are subjected to dealkylation, dehydrogenation and secondary rupture to form fragments with 4 and 5 C atoms, which are precursors to aromatic compounds [57].

However, decalin may also serve as an H-donor at high temperatures. The excellent thermal stability of decalin at high temperatures is desirable for use as fuel for future high-Mach aircraft [58]. It was reported that decalin, especially *trans*-decalin [59], may be one of the potential endothermic jet fuels that also serve as the primary heat sink to cool hot surfaces and system components of aircraft [60].

The final product of H-transfer reactions for both tetralin and decalin is naphthalene (Figure 2-3). Naphthalene is one of the major products from thermal stressing of samples containing either tetralin or decalin. H-donation from tetralin and

decalin contributes mainly to inhibiting the radical reactions and suppressing solid formation, but the effectiveness of H-transfer is substantially higher with tetralin than with decalin. This is probably because the benzylic radical from tetralin is more stable than the tertiary radical formed by H-abstraction from decalin [59]. Considering the first-order rate constants for the decomposition, decalin also shows a higher relative value than tetralin [35]. It appears that tetralin is the most stable compound among jet fuel model compounds [35, 40, 61].

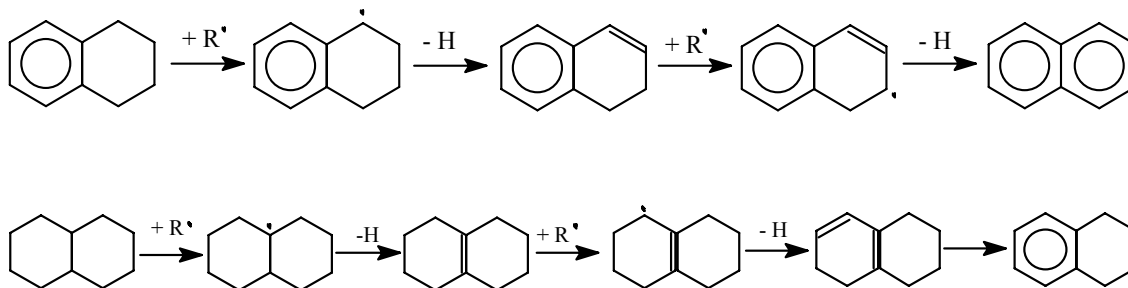


Figure 2-3: Radical stabilization via hydrogen transfer from tetralin and decalin [59].

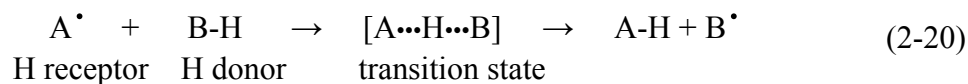
Usually, tetralin did not disproportionate to naphthalene and decalin, although this has been suggested in the literature as a mechanism for the formation of naphthalene observed [52].

2.3.5.3 Indane

Indane can act as a hydrogen donor by generating H atoms for initiation and also quenching the radical intermediates by the transfer of naphthenic H atom from the naphthenic ring [56]. This indicates that for the thermal cracking or pyrolysis of hydrocarbons, the hydrogen required to satisfy the stoichiometry of the cracking reactions can also be provided by dehydrogenation of indane to indene.

2.3.6 Activation Energy of Hydrogen-Abstraction Reactions

As previously discussed, thermal degradation of jet fuels involves free radicals. And, one of the most important reactions in free-radical processes is hydrogen abstraction or hydrogen transfer to stabilize free radicals. The activation energy of hydrogen abstraction reactions is essential for understanding of the hydrogen-transfer mechanism and for kinetic modeling of the processes [49]. Equation (2-20) shows the transfer of hydrogen atom from a hydrogen donor (B-H) to a radical (A•) [62].



The experimental determination of E_a for hydrogen abstraction is very complicated and difficult due to the instability of most radicals. As a consequence, many methods have been developed to estimate the E_a value of H abstraction reactions on the basis of empirical, semiempirical or theoretical studies. An early empirical method, the Bell-Evans-Polanyi relationship [63-65], is used routinely to correlate and predict rates of

hydrogen abstraction by hydrocarbon radicals due to its simple linear function of the reaction enthalpy (ΔH). It can be expressed as:

$$E_a = E_0 + \alpha \Delta H_r \quad (2-21)$$

The reaction enthalpy would be given by:

$$\Delta H_r = BDE(\text{B-H}) - BDE(\text{A-H}) \quad (2-22)$$

where $BDE(\text{B-H})$ = bond dissociation energy of hydrogen donor or
broken bond energy

and $BDE(\text{A-H})$ = formed bond energy.

The E_a is directly proportional to the BDE (B-H) of the hydrogen donor and α and β are assumed to be constants for homogenous series, thus Equation (2-23) can be expressed as:

$$E_a = \alpha BDE(\text{B-H}) + \beta \quad (2-23)$$

From the use of Bell-Evans-Polanyi relationship, Willems and Froment [66] reported the structural contribution method as:

$$E_a = E_{ref} + \sum \Delta E_c \quad (2-24)$$

The E_{ref} is the reference activation energy and the ΔE_c is a correction term, depending on the structural contributions from the radical and the hydrogen donor.

Ma and Schobert (2003) [62] estimated the activation energy (E_a) using ground-state thermochemical properties: reaction enthalpy (ΔH), broken bond energy ($BDE(\text{B-H})$) and formed bond energy ($BDE(\text{A-H})$). They also found a significant effect

of the π conjugate transition state structures on the correlation, which is discussed in terms of quantum chemical understanding.

Camaioni *et al.* (1996) described the use of semiempirical molecular orbital theoretical methods to calculate barriers for a series of hydrogen atom transfer identity reactions involving alkyl, alkenyl, arylalkyl and hydroaryl systems. They found that the barrier for hydrogen abstraction reactions decreases with the degree of alkyl substitution at the radical site, and increases with the degree of conjugation.

Some available experimental E_a values of different hydrogen receptors and hydrogen donors have been summarized in Table 2-2. It can be seen that one of the best hydrogen donor abilities is allylic hydrogen. The activation energy values (E_a) for abstracting allylic hydrogen at a C_α position (C-C-C=C) to stabilize $C\cdot$ and C-C \cdot hydrogen acceptors are 7.3 and 8.3 kcal/mol respectively. These E_a are the lowest compared to the other hydrogen donors in Table 2-2; however, this allylic hydrogen is not an abundant structure in coal-based jet fuels.

Table 2-2: Experimental E_a values for H-abstraction reactions [49, 62].

No.	Reactants		E_a (kcal/mol)
	Radical A \cdot	H donor B-H	
Without π -conjugate TSS			
1	C \cdot	C	14.6
2	C \cdot	C-C	11.6
3	C \cdot	C-C-C	11.5
4	C \cdot	C-C-C-C	11.4
5	C \cdot	C-C-C-C-C	10.9
6	C \cdot	C-C-C	10.0
7	C \cdot	C-C-C-C	10.0
8	C \cdot	C₃C (t-Bu)	8.3
9	C-C \cdot	C	15.4
10	C-C \cdot	C-C	13.4
11	C-C \cdot	C-C-C	12.3
12	C-C \cdot	C-C-C-C	12.3
13	C-C \cdot	C-C-C	11.4
14	C-C \cdot	C-C-C-C	10.4
15	C-C \cdot	C₃C (t-Bu)	10.0
With π -conjugate TSS			
16	C \cdot	C=C-C	8.8
17	C \cdot	C=C-C-C	7.3
18	C \cdot	C=C-C(C)-C	7.3
19	C \cdot	Ph-C	9.5
20	C \cdot	Ph-C (C)₂	7.8
21	C-C \cdot	C=C-C	9.8
22	C-C \cdot	C=C-C-C	8.3
23	C-C \cdot	Ph-C	10.0
24	C-C-C \cdot	C=C-C	9.8
25	C-C-C \cdot	C=C-C-C	8.3
26	C-C-C \cdot	C=C-C	9.7
27	Ph-C \cdot	C	25.9
28	Ph-C \cdot	C-C	22.6
29	Ph-C \cdot	C=C-C	15.5
30	Ph-C \cdot	Ph-C	15.8
31	Ph-C \cdot	Ph-C-C	14.5
32	Ph-C \cdot	Tetralin	13.2
33	Ph-C \cdot	9,10 Dihydrophenanthrene	11.9
34	Ph-C \cdot	9,10 Dihydroanthracene	9.6
35	Tetralin radical	Ph-C	20.0

2.3.7 Quantitative Structure-Property Relationship

The solid deposit formation mechanisms and the interaction of intermediates is important information; however, there has been no clear evidence of quantitative modeling of such complex hydrocarbon mixtures as jet fuel. Recently, very interesting work on PAH published by Mukherjee et al. [67] has shown a topological attempt to explain the importance of molecular weight growth channels involving direct polymerization of aromatics, and it pointed out that their results can be explained by steric and statistical factors. Kazakova [2] also suggested the structure-oriented lumping and Probability Density Functions (PDF) methods that allow avoidance of extreme complexity in detailed modeling by using statistical sampling from a large set of compounds (Quantitative Structure Property Relationship (QSPR) technique). The thermal stability or decomposition rate constant can be described as a linear function of descriptors derived from the compound structures.

To study the complex mixtures of chemical structures, molecular modeling techniques [2] and characterization methods have been used. Andrésen *et al.* [23] used solution-state and solid-state ^{13}C NMR techniques to correlate chemical structures with the formation of aromatic compounds and solid deposition during thermal degradation of jet fuels in the pyrolytic regime. The work shows that NMR and HPLC are powerful tools for characterization of important structures in jet fuel.

2.4 Specification of Jet Fuel for U.S. Aircraft and Properties Testing

To develop a new formula of JP-900, it is very important that the quality of the fuel meets specifications. Generally, aviation fuel specifications contain three main sections, covering [68]:

- (1) suitability (included as a safeguard against the possible failure in service of a fuel)
- (2) composition (stipulates that the fuel must consist entirely of hydrocarbons except for approved additives such as oxidation inhibitors)
- (3) chemical and physical requirements (define the allowable limits for many chemical and physical properties and standard test methods to be employed)

Some of the properties addressed in this study are shown in Table 2-3.

Table 2-3: U.S. Military specifications for aviation gas turbine fuel, JP-8 (adapted from CRC Handbook [69] and ASTM D 1655).

Specification			JP-8 (Kerosene)	Standard Test Method (ASTM)
Composition:	Aromatics, vol%	MAX.	25.0	D 1319
	Olefins, vol%	MAX.	5.0	D 1319
	Sulfur, w%	MAX.	0.3	D 1266/ D 2887/ D 2622
Stability:	JFTOT ΔP , mm Hg	MAX.	25	D 3241 (Test at 260°C)
Combustion:	Net heat of combustion, Btu/lb	MIN.	18,400	D 2382/ D 3338/D 240
	Smoke point, mm	MIN.	19.0	D 1322
	Naphthalene, vol%	MIN.	3.0	D 1840
Volatility:	Distillation			D 2887
	Temp. 10% recov., °C	MAX.	186	
	Temp. Final BP, °C	MAX.	330	
	Flash point, °F (°C)	MIN.	100(38)	D 93
	Density, kg/m ³ (15°C)	MAX.	775-840	D 1298
Fluidity:	Freezing Point, °F (°C)	MAX.	-58 (-50)	D 2386
	Viscosity @ -20°C (cSt)	MAX.	8.0	D 445

2.4.1 Chemical Composition of Jet Fuel and Its Relationships with Properties

Jet fuel composition is dominated by alkanes and cycloalkanes. ASTM specification allows up to five vol% olefins [1]. Aromatic hydrocarbon concentrations are limited to 20 vol% for commercial jet fuels (Jet A and Jet A1) and 25 vol% for military purposes (JP-8). The specification also has a minimum limit of 3 vol% of naphthalenes, but this level is rarely approached because the distillation end point (about 330°C) of jet fuels [1] allows an abundance of naphthalene (boiling point 218°C).

Many investigators have found direct relationships between chemical composition in jet fuels and their properties. Cookson and coworkers [70-73] predicted the linear property-composition relationship of jet fuel in terms of alkanes, branched plus cyclic saturates, and aromatics using ^{13}C NMR spectroscopy. The smoke point, aromatic content, freezing point, net heat of combustion and specific gravity were predicted by multiple linear regressions. Work by Garrigues *et al.* [74] suggested the multivariate correlation of Fourier transform infrared spectrometry for prediction of kerosene properties, but the numbers of samples they used were small and did not produce accurate results. A few studies have also used NMR [29-32] to characterize chemical structures and to construct structure-property relationships of diesel fuel or jet fuel.

2.4.2 Jet Fuel Thermal Oxidation Test (JFTOT)

The JFTOT was introduced into U.S. military specifications in 1972 and into ASTM and British specifications in 1973 [75]. Figure 2-4 shows the schematic diagram of the JFTOT. In its operation for quality control (specification) purposes, the maximum temperature on the tube in the heater tube test section is maintained at 260°C throughout the test. In order to pass a test, a fuel must not produce a lacquer that is darker than a specified limit and the pressure drop developed across the test filter must not exceed 25 mm Hg [76].

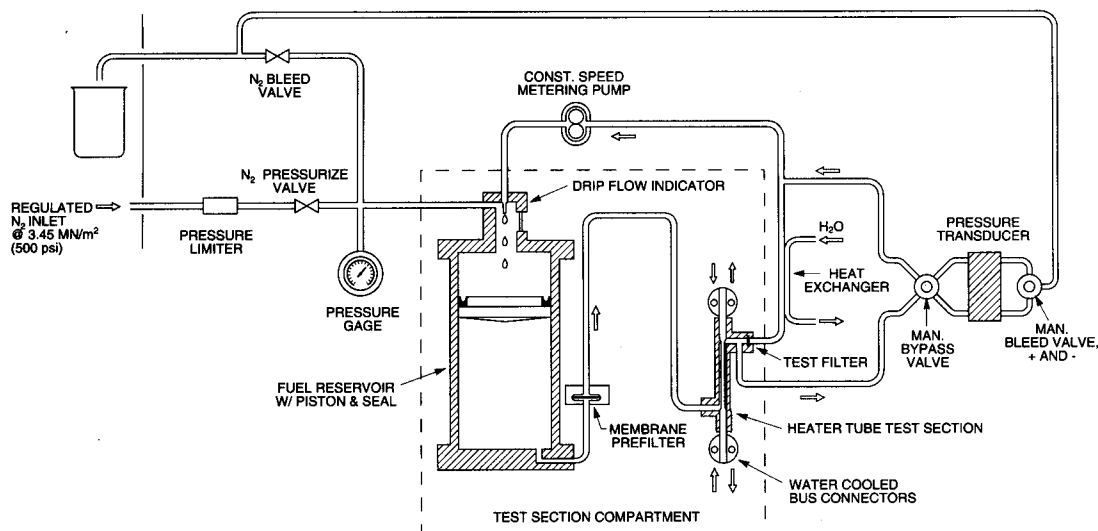


Figure 2-4: Schematic diagram of the JFTOT [77].

Table 2-4: Parameters of JFTOT [1].

Parameter	
Fuel volume	0.6 L (0.16 gal)
Fuel flow rate	3 mL/min
Test time	2.5 h
Temperature control and operating temperature	Heater tube, 260°C
System pressure	3.45 MPa (500 psig)
Length of heater tube	60 mm
Fuel residence time in heater tube	13 s
Filter	17 μ m stainless steel
Flow regime	Laminar
Rating criteria	1. Filter pressure drop 2. Tube deposits

ASTM D1655 defines the specification of aviation turbine fuel to have a maximum filter pressure drop at 25 mm Hg and color code below code three, which means no abnormal color deposits. The JFTOT is used as a pass/fail rating instrument for specification purposes. Consequently, no generally accepted method for determining precision is available [1].

The use of JFTOT in all refineries producing Jet A/A-1 fuel together with its straightforward operation and rapid test time give it a universal appeal. However, there are difficulties with this technique to assess JFTOT deposit levels [76]. Considering the thermal stability test in this research, the JFTOT technique is not suitable for this work due to two weaknesses:

- (1) It requires 0.16 gallons of fuel (Table 2-4) and we have never had such quantities of prototype fuels through most of the history of Penn State's JP-900 program.
- (2) The operating temperature limit is only 260°C, which is below the temperature in the pyrolytic regime.

2.4.3 Combustion Properties

Combustion quality, indicated by heat of combustion and smoke point, is largely a function of the hydrocarbon composition or hydrogen-to-carbon ratio (H/C) of the fuel. The jet fuels with compositional differences can vary widely in burning quality as measured by smoke formation, carbon deposition and flame radiation.

Alkanes have excellent heat of combustion in contrast to those of aromatics (particularly the heavy polynuclear types) while cycloalkanes have intermediate

combustion characteristics. Naphthalenes are major aromatic components in jet fuel; their content is sometimes regulated to be less than 25 vol%.

2.4.3.1 Hydrogen-to-Carbon Ratio (H/C)

The hydrogen content relates directly to heat of combustion but indirectly to combustion temperature. The increase in hydrogen content or H/C ratio tends to improve the heat of combustion and smoke point of the jet fuel. Goodger and Vere (1985) [78] indicated that, in some U.S. specifications for military fuels, minimum hydrogen content is set at 13.5% (for JP-5 and JP-8) as an alternative to a minimum smoke point specification of 19 mm.

2.4.3.2 Heat of Combustion and Energy Density

In aviation practice, the heat of combustion is described as ‘specific energy’, the energy released per unit mass of fuel in MJ/kg (or Btu/lb) [78]. The gross heat of combustion (Q_g) at constant volume of a fuel containing carbon, hydrogen, oxygen, nitrogen and sulfur is the quantity of heat liberated when a unit mass of the fuel is burned in oxygen in an enclosure of constant volume and constant temperature at 25°C. The products are carbon dioxide, nitrogen dioxide, sulfur dioxide and water (ASTM D 2382). So, the Q_g is the heat produced when the sample burns, plus the heat given off from condensing and cooling of water vapor to the temperature of the bomb [79]. However, this heat of condensation from water vapor is not available for useful work and product

gases are invariably hot at the exit from the combustion chamber [78]. Thus, the net heat of combustion is obtained by subtracting the latent heat from the gross value.

The net heat of combustion (Q_n) can be defined as the quantity of heat liberated when a unit mass of the fuel is burned in oxygen at a constant pressure of 1 atm (ASTM D 2382). The net heat of combustion (Btu/lb) can be calculated as Equation (2-25):

$$Q_n \text{ (Btu/lb)} = Q_g \text{ (Btu/lb)} - 91.23 H \quad (2-25)$$

where H is weight percent of hydrogen in the sample.

Goodger and Vere [78] proposed that, in some applications, it is important to convert heat of combustion into a fuel volume basis, or ‘energy density’ in MJ/L. The conversion of units can be made from Equation (2-26):

$$\text{Energy Density (MJ/L)} = \text{Heat of Combustion (MJ/kg)} \times \text{density (kg/L)} \quad (2-26)$$

Intrinsically, subsonic aircraft favor low-density fuel because their performances tend to be limited by mass. With the supersonic aircraft, on the other hand, the thin aerofoil wing sections restrict the space for fuel storage, and this volume limitation calls for heavier fuels of high energy density.

2.4.3.3 Smoke Point

Smoke point, determined by ASTM D 1322, gives an indication of the tendencies to soot formation and smoke generation in the combustion chamber. Extensive experimental data on smoke point for complex hydrocarbon mixtures and fuels blended from pure hydrocarbons studied by Gülder *et al.* [33] were used to show the quantitative

relationship between sooting tendency and fuel molecular structures. Correlation of carbon types of 93 fuels with smoke points is shown as Equation (2-27).

$$S = a_0 + a_1x_1 + a_2x_2 + a_3x_3 + a_4x_4 + a_5x_5 + a_6\psi^3 \quad (2-27)$$

where $x_1 = C_2/C_a^2$, $x_2 = C_3/C_a^2$, $x_3 = \ln(C_\alpha + 2)$, $x_4 = (C_\alpha + 2)/(C_2 + C_3)$, $x_5 = C_2/C_3$ and ψ = hydrogen-to-carbon ratio. Carbon types were classified from hydrogen attached to carbon from ^1H NMR as follows: C_a (carbons on mono and condensed aromatic rings); C_α (carbons at α position to aromatic rings); C_2 (R-CH₂, CH carbons including β -CH₂, CH₃, and γ , δ -CH₂ to aromatic rings); and C_3 (R-CH₃ carbons including terminal and branched and γ , δ to aromatic rings). Coefficients from multiple regression analysis were $a_0 = 11.1$, $a_1 = -7.76$, $a_2 = 28.86$, $a_3 = -8.59$, $a_4 = 21.9$, $a_5 = 0.429$, $a_6 = 3.63$. A correlation coefficient was 0.95.

Gülde *et al.* [33] have also correlated measured flame radiation (F_1 , KW/m²), obtained in a T-63 gas turbine engine by Naegeli and Moses (1980) [80], to a function, in terms of smoke point and hydrogen-to-carbon ratio, in the following Equation:

$$F_1 = aS^b \exp[\phi S/\psi^2] \quad (2-28)$$

A similar relationship was also obtained by Olson *et al.* [81] who measured maximum soot volume fractions of a large number of hydrocarbons at half the total smoke point flame heights using a laminar diffusion wick flame. The soot volume fraction (F_2), in terms of smoke point and hydrogen-to-carbon ratio is shown below:

$$F_2 = aS^b \exp[\phi(\psi/S)^2] \quad (2-29)$$

Note that for both Equations (2-28) and (2-29), S is the smoke point, ψ the hydrogen-to-carbon ratio and a , b , and ϕ are constants.

For a relationship between jet fuel smoke points and chemical composition, Cookson *et al.* [73] have found a linear model for kerosene-type jet fuel as follows:

$$S = 44 N + 19 BC \quad (2-30)$$

where S is smoke point, N is n -alkane, and BC is branched plus cyclic saturates. The smoke points of kerosenes that are dominated by alkanes are higher than 25 mm in this work; thus, the significant effects are due to n -alkanes. However, they also found that the smoke point is a very sensitive to naphthalene content.

2.4.4 Volatility

Flash Point

Flash point is an indirect measurement of volatility of jet fuel. It is the lowest temperature, corrected to a barometric pressure of 101.3 kPa (760 mmHg), at which a substance will ignite in air with an initiator (spark or flame). Flash point is one of the most widely used, important characteristics of the flammability properties of liquids and low-melting substances (ASTM 1298, [82]).

Katritzky and coworkers [82] have investigated the correlation of flash point with some physical descriptors such as boiling point and molecular characteristics. From their work, the significant QSAR equations from the extraction of molecular descriptors have been successfully developed for the prediction of flash point of unavailable or unknown

compounds. A method for flash point prediction was based on multi-parameter regression methodology of the CODESSA computer program [83]. They obtained the best model (Equation (2-31)) from a three-parameter correlation with $R^2 = 0.9529$. The parameters were experimental boiling point temperature (T_b), relative negative surface charge ($RNSC$) and H-donors charged surface area ($HDCA$). $RNSC$ characterized the dispersion of partial charges in the molecule while $HDCA$ accounts for hydrogen bonding donor ability. Both descriptors were obtained from molecular modeling by MOPAC computer program.

$$T_f = (0.72 \pm 0.014)T_b + (76.99 \pm 11.97) RNSC + (2.05 \pm 0.33) HDCA - (8.40 \pm 7.63) \quad (2-31)$$

The best published equation for estimation of flash point with boiling point as a parameter appear in an exponential function [82]. Satnayaranaya and Rao [84] relate the flash point to the boiling point for 1200 organic compounds and 21 petroleum fractions as Equation (2-32) with an average absolute error of less than 1%. T_f denotes flash point temperature (K) where as T_b represents the normal boiling temperature (K). And, a , b , c are constants.

$$T_f = a + b(c/T_b)e^{-c/T_b}/(1-e^{-c/T_b})^2 \quad (2-32)$$

2.4.5 Fluidity

2.4.5.1 Viscosity

Kinematic viscosity is a measure of the resistive flow of a fluid under gravity, the pressure head being proportional to the density of the fluid (ASTM 445). The viscosity of fuels at low temperature is limited to ensure that adequate fuel flow and pressure are maintained under all operating conditions [68]. This is why the specification limits the viscosity of aviation fuel to be a maximum 8 cSt (cm²/s) at -20°C.

Riazi [85] derived a correlation of kinematic viscosities in terms of boiling point and molecular weight from data on viscosities of light and heavy fractions. In his work, one-parameter correlations (T_b) can be developed for viscosities at 100 and 210°F. A five-order polynomial has been chosen, and Equation (2-33) was proposed for light fractions:

$$v = a + bT_0 + cT_0^2 + dT_0^3 + eT_0^5 \quad (2-33)$$

where v = viscosity for alkanes, cycloalkanes and aromatics

$$T_0 = T_b/1000,$$

$$T_b = \text{normal boiling point, } ^\circ\text{F}$$

$$v_{100}: a = 0.581, b = -3.68, c = 20.37, d = -22.953 \text{ and } e = 43.917 \text{ (light } n\text{-alkanes)}$$

$$v_{210}: a = -0.0652, b = 2.718, c = -6.195, d = 10.356 \text{ and } e = 0 \text{ (light } n\text{-alkanes)}$$

$$v_{100}, v_{210} = \text{kinematic viscosities at 100 and 210}^\circ\text{F}$$

For heavy petroleum fractions, viscosity correlation depends on boiling point and molecular weight. Equation (2-34) can be used for alkane, cycloalkane and aromatic compounds.

$$\ln v = a + b \ln M + c T_b \quad (2-34)$$

where v = viscosity for alkanes, cycloalkanes and aromatics,

M = molecular weight

T_b = boiling point

a, b, c = correlation constants.

2.4.5.2 Cloud Point and Freezing Point

Cloud point defines the temperature at which a cloud of wax crystals first appears in a liquid when it is cooled under specified test conditions. Method ASTM D 2500 and ASTM D 3117 can be used to determine the cloud point. However, there is no specification for the cloud point of the conventional jet fuels.

Hu and Burns [86] related component cloud point T_j and volume fractions v_j of the blending components as the following equation:

$$T_c^{1/x} = \sum v_j T_j^{1/x} \quad (2-35)$$

where x is an adjustable parameter, T_c is the blended cloud point.

Saiban and Travor (1997) [87] developed a semi-empirical model for predicting the cloud points following the blending of diesel fuel components. A linear relationship is

found between cloud point and characteristic enthalpy of different components and blends. Thus, the optimized equation of cloud points is:

$$T_c = \frac{\sum_{j=1}^i e^{\alpha T_j} e^{\beta v_j} v_j T_j}{\sum_{j=1}^i e^{\alpha T_j} e^{\beta v_j} v_j} \quad (2-36)$$

where T_j is the component cloud point (K), v_j is the component volume fraction, and T_c is the blended cloud point. α and β are associated with the concentration of nucleating sites in the components.

Freezing point, the temperature at which crystals of hydrocarbons formed on cooling disappear when the fuel temperature is allowed to rise (ASTM D 2386), is more meaningful to the low-temperature properties and fluidity of jet fuel. JP-8 has a freezing point specification of maximum -58°F (-50°C). The freezing point of aviation fuels can be obtained from ASTM D 2386.

2.5 Graphical and Numerical Analyses

2.5.1 Ternary Diagrams

Ternary diagrams are used to represent the relative percentage of three components. These components can be three major chemical compositions. The only requirement is that the three components have to sum to 100% and any point represents the relative percentage of three components. Cookson *et al.* [88] have shown the composition-property relations for jet and diesel fuels in ternary diagrams for visualization proposes. Three main components are paraffins, naphthenes and aromatics.

2.5.2 Multiple Linear Regression (MLR)

Multiple regression analysis is one of the most widely used of all statistical tools [89]. It is used to predict the variance in a dependent variable, based on linear combinations of independent variables. Multiple regression can establish that a set of independent variables explains some proportion of the variance in a dependent variable at a significant level (significance test of R^2), and can establish the relative predictive importance of the independent variables (comparing coefficients or beta weights) [90].

The multiple linear regression equation is in the form $Y = b_0 + b_1X_1 + b_2X_2 + \dots + b_nX_n + e$ where Y is the true dependent, the b 's are the regression coefficients for the corresponding X (independent) terms, b_0 is the constant or intercept, and e is the error term. This equation has no interaction effects between each independent variable and it is called “main effects models” [90].

The estimation of the unknown parameters in the regression model is called fitting the model to the data. Then, the next phase of a regression analysis is to check model adequacy. The outcome may indicate either that the model is reasonable or that the original fit must be modified [91].

2.5.2.1 Coefficient of Multiple Determination (R^2)

R^2 is the percent of the variance in the dependent variable explained uniquely or jointly by the independent variables. R^2 can also be interpreted as the proportionate reduction in error in estimating the dependent variable when knowing the independent variables [90]. Mathematically, R^2 is from:

$$R^2 = \frac{SSR}{SST} = 1 - \frac{SSE}{SST} = 1 - \frac{\sum (Y_i - \hat{Y}_i)^2}{\sum (Y_i - \bar{Y}_i)^2} \quad (2-37)$$

where SSR = sum of squares due to regression,
 SSE = sum of squares due to the fitted model,
 SST = total sum of squares,
 Y_i = the actual value of Y (output) for the i^{th} case,
 \hat{Y}_i = regression prediction for the i^{th} case,
and \bar{Y}_i = average of total Y_i .

2.5.2.2 Coefficient of Multiple Determination Adjusted (R_a^2)

This is the coefficient of determination adjusted for the number of independent variables in the regression model. Unlike the coefficient of determination, R^2 -adjusted may decrease if variables entered in the model do not add significant effects to the model fit [92].

$$R_a^2 = 1 - \frac{\sum (Y_i - \hat{Y}_i)^2}{\sum (Y_i - \bar{Y}_i)^2} \frac{(n-1)}{(n-k-1)} \quad (2-38)$$

where n is sample size and k is the number of terms in the model not counting the constant (i.e., the number of independent variables) [90].

2.5.2.3 Mean Square Error (*MSE*)

MSE in MLR is calculated as the difference between the target output and the network output divided by degree of freedom ($n-k-1$). The average of the sum of these errors is expected to be minimized [89, 90].

$$MSE = \frac{SSE}{(n-k-1)} = \frac{\sum (\hat{Y}_i - Y_i)^2}{(n-k-1)} \quad (2-39)$$

2.5.2.4 t-Test

T-tests are used to assess the significance of individual b coefficients, specifically testing the null hypothesis that the regression coefficient is zero. The t-test is a test only of the unique variance that an independent variable accounts for [89, 90].

2.5.2.5 F-Test

The F test is used to test the significance of R^2 , which is the same as testing the significance of the regression model as a whole [90]. The F-test can be interpreted as a ratio of the variance explained by the model and the variance not explained by the model (i.e., that due to the model error or experimental error) [2]. If $P(F) < .05$, then the model is considered significantly better than would be expected by chance. F is a function of R^2 , the number of independent variables, and the number of cases. F is computed with k and

$(n - k - 1)$ degrees of freedom, where k = number of terms in the equation not counting the constant [90].

$$F = \frac{\left[\frac{R^2}{k} \right]}{\left[\frac{(1 - R^2)}{(n - k - 1)} \right]} \quad (2-40)$$

The F -test measures the significance of the entire model while the t -test reflects significance of the parameter within the model [2].

2.5.3 Artificial Neural Network (ANN)

Artificial Neural Networks (ANN) is an alternative to multiple linear regression (MLR). ANN is a biologically inspired tool for information processing, but is different from conventional computing or statistical systems [93] such as MLR. The information is stored in the topology of the network itself and in the connections of the matrix [93], or “a black box” [94]. This network consists of artificial neurons (which are designed to mimic the function of the neural cells of a living organism [94, 95]), layers (which the neurons are organized into) and interconnections between neurons of each layer. The network “learns” by a process involving the modification of the connection weights between neurons and layers [93]. See Figure 2-5. In summary, the network processes a number of inputs from the outside world to produce an output, the network's classifications or predictions.

The uses of neural networks to construct a quantitative relationship of structure, performance, and fuel properties (e.g. gasoline's octane number and diesel's cetane number) were investigated [31, 42-45] at the beginning of the last decade. New

theoretical models have been developed to predict fuel properties (outputs) from structure identification (inputs), which can be characterized by techniques such as NMR, LC and GC/MS [29-32, 44].

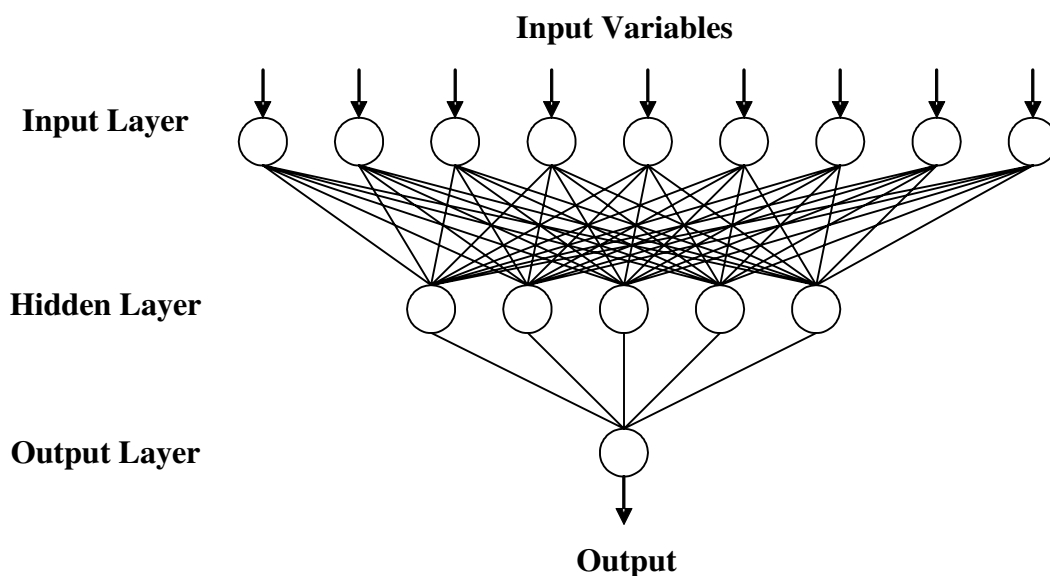


Figure 2-5: Schematic diagram of the typical architecture of ANN [96].

2.5.3.1 Neural Network Structure

Layer

The ANN consists of three layers: input layer, hidden layer and output layer. The *input layer* receives the input data outside the network while the *output layer* produces the network output. All other layers are called *hidden layers*, which contain interconnected neurons and the relevant information interpretation from adjusting the weights on the connections [97]. Each connection has a ‘weight’ associated with it. Input variables fed to the input layer are weighted and passed on to the hidden layer. Each

neuron in the hidden layer produces output by applying a transfer function to the sum of the weighted input values. These outputs are then weighted by the connections between the hidden and output layers [96].

Neuron

A neuron is a basic building block of simulated neural networks which processes a number of input values to produce an output value. Usually a neuron sums the input values and then applies a nonlinear function to the sum to arrive at the output value [96]. (Figure 2-6).

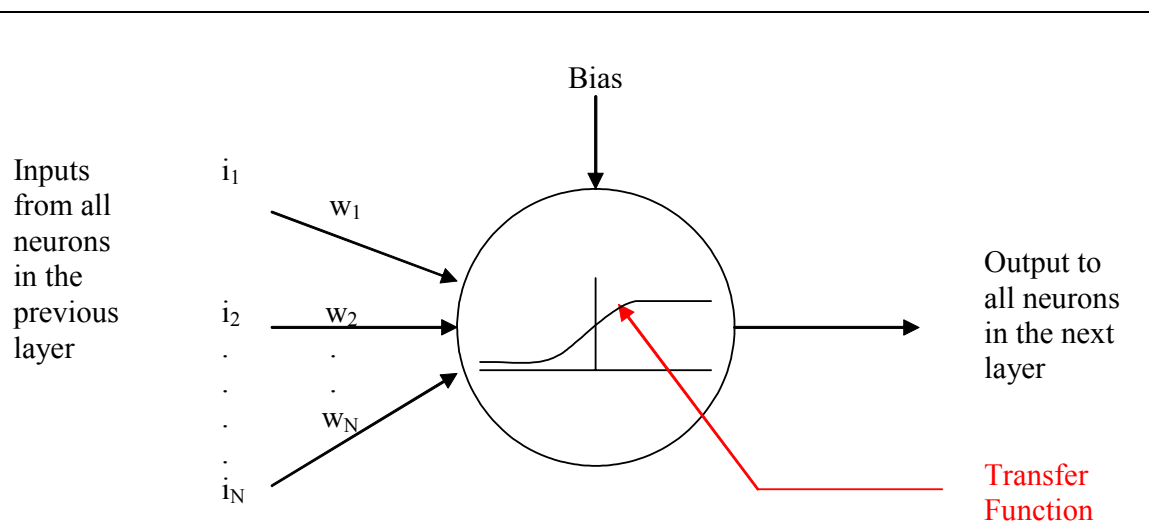


Figure 2-6: Structure of neuron [96].

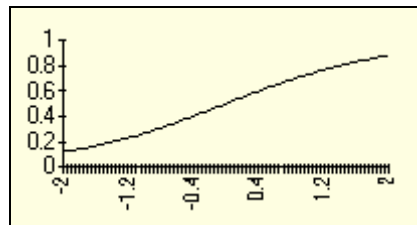
Transfer Functions in Neuron

A nonlinear function is known as transfer function (f) [94, 95, 97] or activation function [96]. Typically transfer functions can be a step function and a sigmoid curve. Figure 2-7 shows three main types of commonly used transfer functions.

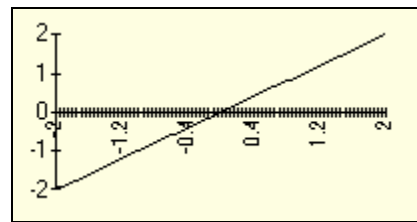
1. Logistic or Log-Sigmoid Transfer Function

This function is useful for most neural network applications. It maps values into the (0, 1) range [96]. This transfer function is always used when the outputs are categories and it is commonly used in backpropagation networks. In NeuroShell 2 software, the default transfer function is the logistic function. The equation for this function is as follows:

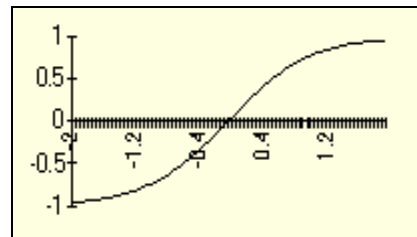
$$f(x) = \frac{1}{(1 + e^{-x})} \quad (2-41)$$



(a)



(b)



(c)

Figure 2-7: Transfer function: (a) logistic, (b) linear and (c) tanh [96].

2. *Linear Transfer Function*

Use of this function should generally be limited to the output layer [96]. If the last layer of a multilayer network has sigmoid neurons, then the outputs of the network are limited to a small range. If linear output neurons are used the network outputs can take on any value [97]. Equation (2-42) shows the linear transfer function.

$$f(x) = x \quad (2-42)$$

3. *Tanh (Tan-Sigmoid Transfer Function)*

This transfer function generates outputs between -1 and 1. The equation can be shown as:

$$f(x) = \tanh(x) \quad (2-43)$$

Weighting Factors

Weights are adaptive coefficients within the network that determine the intensity of the input signal. It is written as weight matrix.

Learning Functions

The network learns by a process involving the modification of the connection weights between neurons and layers. When weight adjustments are made in preceding layers of feedforward networks by “backing up” from outputs, it is called “Back Propagation”.

2.5.3.2 Multiple Layers of Neural Network

A network can have several layers. Each layer has a weight matrix \mathbf{W} , a bias vector \mathbf{b} , and an output vector \mathbf{a} [97]. An example of three layers of a neural network is shown in Figure 2-8. The network has R inputs, S_1 neurons in the first layer, S_2 neurons in the second layer and S_3 or 1 neuron in the third (output) layer. A constant input 1 is fed to the biases for each neuron. The outputs of each intermediate layer are the inputs to the following layer.

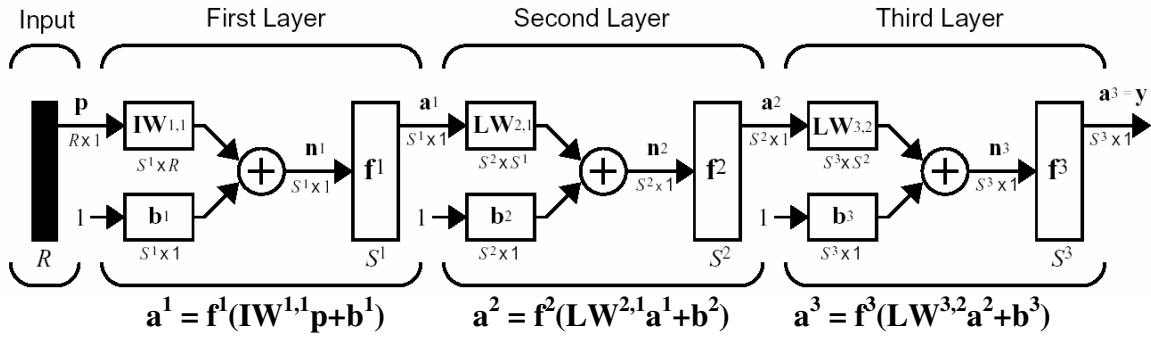
The first layer can be analyzed as one layer network with R inputs, S_1 neurons, and an $S_1 \times R$ weight matrix $\mathbf{IW}^{1,1}$. (Note that \mathbf{IW} stands for input weight matrices and \mathbf{LW} abbreviates layer weight matrices [97].) The input vector elements (\mathbf{p}) enter the network through the weight matrix $\mathbf{IW}^{1,1}$ and pass through the transfer function (\mathbf{f}^1). The output of this layer is vector \mathbf{a}^1 and the associated bias is vector \mathbf{b}^1 .

Corresponding with Figure 2-8 (a), Figure 2-8 (b) shows an explanation of the above mathematical notation in a simple picture. To understand the network better, the author expanded the equation $\mathbf{a}^1 = \mathbf{f}^1(\mathbf{IW}^{1,1}\mathbf{p} + \mathbf{b}^1)$ into matrices.

Now that all the vectors and matrices of the first layer have been identified, it can be treated as a single layer network on its own. This approach can be taken with any layer of the network [97]. Thus, one can write the final equation of the three layers neural network as follows:

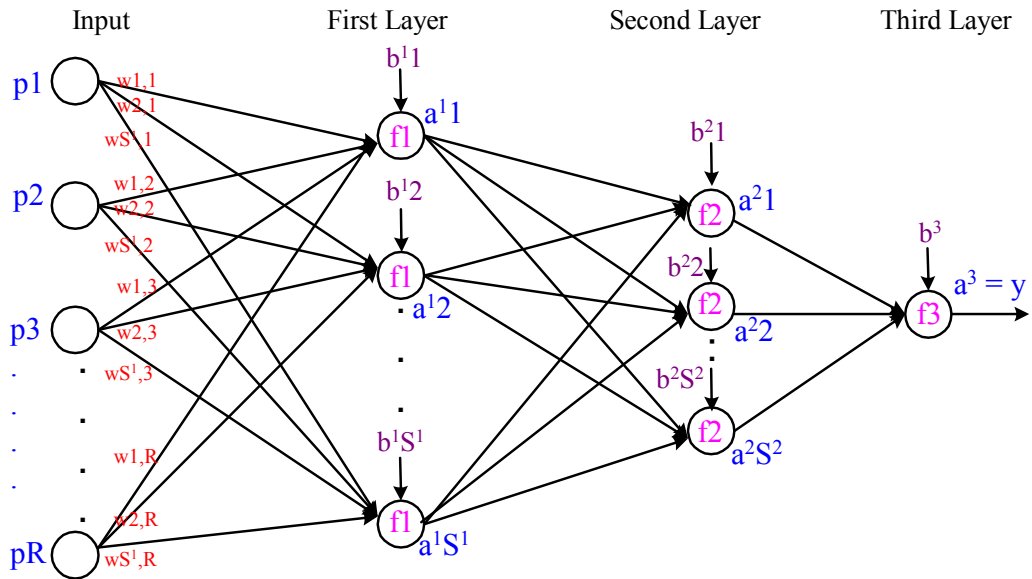
$$\mathbf{a}^3 = \mathbf{f}^3 (\mathbf{LW}^{3,2} \mathbf{f}^2 (\mathbf{LW}^{2,1} \mathbf{f}^1 (\mathbf{IW}^{1,1} \mathbf{p} + \mathbf{b}^1) + \mathbf{b}^2) + \mathbf{b}^3) = \mathbf{y} = \hat{\mathbf{Y}} \quad (2-44)$$

where \mathbf{y} or $\hat{\mathbf{Y}}$ is the final output.



$$\mathbf{a}^3 = \mathbf{f}^3(\mathbf{LW}^{3,2}\mathbf{f}^2(\mathbf{LW}^{2,1}\mathbf{f}^1(\mathbf{IW}^{1,1}\mathbf{p} + \mathbf{b}^1) + \mathbf{b}^2) + \mathbf{b}^3) = \mathbf{y} = \hat{\mathbf{y}}$$

(a)



$$\left\langle \mathbf{a}^1 = \mathbf{f}^1(\mathbf{IW}^{1,1}\mathbf{p} + \mathbf{b}^1) \right\rangle$$

$$\mathbf{a}^1 = \mathbf{f}^1 \left(\begin{bmatrix} w_{1,1} & w_{1,2} & \dots & w_{1,R} \\ w_{2,1} & w_{2,2} & \dots & w_{2,R} \\ \vdots & \vdots & \ddots & \vdots \\ w_{S^1,1} & w_{S^1,2} & \dots & w_{S^1,R} \end{bmatrix} \begin{bmatrix} p_1 \\ p_2 \\ \vdots \\ p_R \end{bmatrix} + \begin{bmatrix} b^1_1 \\ b^1_2 \\ \vdots \\ b^1_{S^1} \end{bmatrix} \right)$$

(b)

Figure 2-8: Multiple layers in neural network: (a) abbreviated notation [97] and (b) example of the first layer in a matrix form.

2.5.3.3 Neural Network Training

From Figure 2-9, neural networks are commonly adjusted, or trained, so that particular inputs lead to a desired output (target) [97]. The network is then trained, based on a comparison of the network output and the target, until the network output matches the target. During training the weights and biases of the network are iteratively adjusted to minimize mean square error (*MSE*) between the target and the network output reaches the preset value [97]. Note that the *MSE* is calculated by:

$$MSE = \frac{1}{N} \sum_{i=1}^N (\hat{Y}_i - Y_i)^2 \quad (2-45)$$

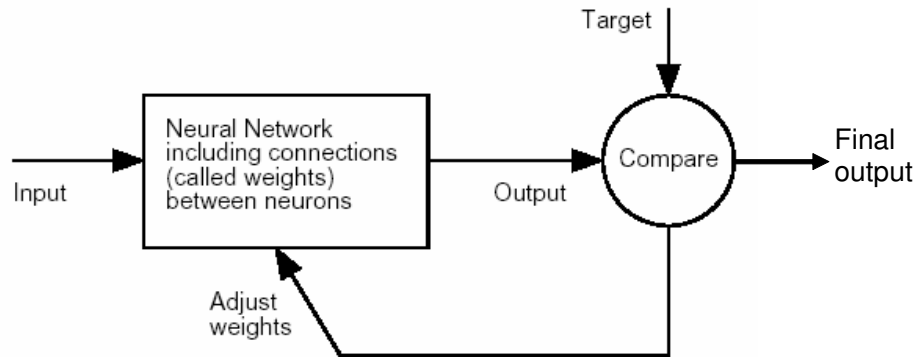


Figure 2-9: Neural network training [97].

Chapter 3

Experimental Methods

This Chapter will introduce the advanced thermally stable coal-based jet fuel candidates produced by PARC Technical Services. The fuel candidates' quality has been evaluated by numerous experimental methods focused on thermal stability and some physical properties tests. The results will be compared with the conventional jet fuels (JP-8 and JP-8+100). And, the final selection of the JP-900's new formula will be made based on the ASTM specification and numerical analyses of the entire data sets.

3.1 Samples

3.1.1 Conventional Jet Fuels

Two grades of kerosene type jet fuel, JP-8 and JP-8+100 from the US Air Force, were selected to represent the current petroleum-based jet fuels' specification (Table 2-3). In general, the components in these fuels are mainly alkanes and cycloalkanes with aromatics less than 25 vol%.

3.1.2 Coal-Based Jet Fuels

The operating conditions used to produce all JP-900 candidates and some of their properties are summarized in Table 3-1. Blends of these fuels chosen for this work are displayed in Table 3-2 [98].

The First Generation of PARC Fuels

The scope of the first project (early 2000) at PARC Technical Services, Inc. was to produce six hydrotreated and deeply saturated product fuels from the following feeds [5]: light cycle oil (LCO) provided by BP Corporation [99], refined chemical oil (RCO) provided by Koppers Industries, Inc., and their 1:1 blends [5]. The hydrotreatment and aromatic saturation processes were performed in PARC's adiabatic hydrotreatment pilot unit. The severe hydrotreatment was performed in order to achieve an extremely low heteroatom content, thus avoiding the poisoning of the noble metal catalyst used in the subsequent aromatic saturation step. Aromatic saturation was then performed on each of the hydrotreated samples.

The first generation of jet fuel candidates is presented as:

- Hydrotreated fuels: EI-001, EI-002 and EI-003 (Table 3-1). The hydrotreating process using Crosfield NiMo (850 1/20, Trilobe) catalyst was operated at 710 psi and 685-725°F [5, 100].
- Saturated fuels: EI-004, EI-005 and EI-006 (Table 3-1). The aromatic saturation of hydrotreated samples was performed at 2100 psi and 400-500°C using Pt-Pd (Engelhard DESAT) catalyst [5, 100].
- The blends of EI-001, EI-003, EI-004 and EI-006. Eighteen blends of four PARC candidates have been created by the author from the six pairs at the blending ratios 3:1, 1:1 and 1:3 (Table 3-2).
- Four blends of EI-002 with 10% decalin, 20% decalin, 10% tetralin and 20% tetralin (Table 3-2).

- Four blends of EI-005 with 10% decalin, 20% decalin, 10% tetralin and 20% tetralin (Table 3-2).
- Two blends of EI-002 with Norpar-13 and EI-005 with Norpar-13 at blending ratio 1:1 (Table 3-2).

The Second Generation of PARC Fuels

Twenty-four hydrotreated samples have been produced using LCO/RCO 1:1 and 1:3 blends. For this work, the LCO was provided by United Refining Co. and was slightly higher in sulfur and nitrogen contents than that of the BP sample. Two kinds of catalyst, Crosfield CoMo (465 1/20, Trilobe) and Crosfield NiMo (850 1/20, Trilobe), were used in the hydrotreatment process for a comparison [101]. These fuel candidates are EI-007 through EI-030 in Table 3-1.

The Third Generation of PARC Fuels

The feeds used in this study were also light cycle oil (LCO) provided by United Refining and refined chemical oil (RCO) provided by Koppers. Two blends were made at 1:1 and 1:3 weight ratios of LCO:RCO for feed to an adiabatic hydrotreatment pilot unit using CoMo catalyst (CRITERION SYNCAT-3). These fuels are EI-031 through EI-038 in Table 3-1. To study the boiling point effects on thermal stability, the products from the hydrotreatment of the 1:1 and 1:3 blends of LCO and RCO were distilled to produce fuels with boiling ranges of 180-270°C, 180-300°C and 180-320°C [102-104]. These fractions were then subjected to pyrolytic stability tests.

Table 3-1: Lists of coal-based jet fuel candidates.

PSU Sample Number	PARC Designation	Dates Produced at PARC	PSU Designation	Catalyst	P (psig)	T (°F)	LHSV	H ₂ (SCFB)	HDS (%)	HDN (%)	Boiling Range (°C)
GENERATION I											
EI-001	P67 37	12/99-4/00	HDT LCO	NiMo	710	685	1	2400	99.9	98.9	152-373
EI-002	P67 43	12/99-4/00	HDT (RCO/LCO 1:1)	NiMo	710	680, 700	1, 0.5	3100	100.0	99.5	163-376
EI-003	P67 44	12/99-4/00	HDT RCO	NiMo	710	685, 725	0.5, 1	~3000	99.9	94.5	165-377
EI-004	P67 42	12/99-4/00	SAT LCO	NiMo, Pt-Pd	710, 2100	685, 400-600	1	~1400	-	-	138-341
EI-005	P67 45	12/99-4/00	SAT (RCO/LCO 1:1)	NiMo, Pt-Pd	710, 2100	(680,700), 450	0.5-1	~1800	-	-	116-358
EI-006	P67 46	12/99-4/00	SAT RCO	NiMo, Pt-Pd	710, 2100	(685,725), 500	0.5-1	~1600	-	-	119-369
GENERATION II											
EI-007	110-126-3	5/01-6/01	N/A	CoMo	600	715	0.4	1364	98.3	90.3	N/A
EI-008	110-126-6	5/01-6/01	N/A	CoMo	600	685	0.4	N/A	95.5	82.3	N/A
EI-009	110-126-7	5/01-6/01	N/A	CoMo	600	710	0.4	N/A	95	87.1	N/A
EI-010	111-126-3	5/01-6/01	N/A	NiMo	600	715	0.4	1768	96.3	95.8	N/A
EI-011	111-126-6	5/01-6/01	N/A	NiMo	600	690	0.4	1621	88.1	93	N/A
EI-012	111-126-7	5/01-6/01	N/A	NiMo	600	715	0.4	1645	87.2	90.6	N/A
EI-013	112-126-3	5/01-6/01	N/A	NiMo	600	710	0.3	N/A	N/A	N/A	N/A
EI-014	112-126-6	5/01-6/01	N/A	NiMo	600	680	0.3	N/A	82.6	96.4	N/A

Table 3-1 (continued)

PSU Sample Number	PARC Designation	Dates Produced at PARC	PSU Designation	Catalyst	P (psig)	T (°F)	LHSV	H ₂ (SCFB)	HDS (%)	HDN (%)	Boiling Range (°C)
EI-015	112-126-7	5/01-6/01	N/A	NiMo	600	705	0.3	2627	85.3	97.1	N/A
EI-016	113-126-3	5/01-6/01	N/A	NiMo	850	715	0.55	2134	97.3	99.2	N/A
EI-017	113-126-6	5/01-6/01	N/A	NiMo	850	680	0.55	N/A	89.9	98.3	N/A
EI-018	113-126-7	5/01-6/01	N/A	NiMo	850	710	0.55	2663	85.3	97.1	N/A
EI-019	110-126-1	5/01-6/01	N/A	CoMo	600	685	0.75	1690	93.1	89.6	N/A
EI-020	110-126-2	5/01-6/01	N/A	CoMo	600	710	0.85	1294	96	87.2	N/A
EI-021	110-126-4	5/01-6/01	N/A	CoMo	600	710	1	1259	96.3	80.8	N/A
EI-022	111-126-1	5/01-6/01	N/A	NiMo	600	685	0.75	1844	93.3	98.1	N/A
EI-023	111-126-2	5/01-6/01	N/A	NiMo	600	710	0.85	1676	97.2	94.2	N/A
EI-024	111-126-4	5/01-6/01	N/A	NiMo	600	710	1	1410	95.3	87.7	N/A
EI-025	112-126-1	5/01-6/01	N/A	NiMo	600	685	0.5	1454	93.5	99.3	N/A
EI-026	112-126-2	5/01-6/01	N/A	NiMo	600	710	0.7	1553	98.5	97.5	N/A
EI-027	112-126-4	5/01-6/01	N/A	NiMo	600	710	0.7	1417	75.2	92.9	N/A
EI-028	113-126-1	5/01-6/01	N/A	NiMo	850	685	1	2064	96.2	99	N/A
EI-029	113-126-2	5/01-6/01	N/A	NiMo	850	710	1.1	1823	98.3	98.3	N/A
EI-030	113-126-4	5/01-6/01	N/A	NiMo	850	710	1.25	1538	97.2	95.6	N/A

Table 3-1 (continued)

PSU Sample Number	PARC Designation	Dates Produced at PARC	PSU Designation	Catalyst	P (psig)	T (°F)	LHSV	H ₂ (SCFB)	HDS (%)	HDN (%)	Boiling Range (°C)
GENERATION III											
EI-031	x571 cut 2	2/02-3/02	HDT (RCO/LCO 1:1) cut 180-270°C	CoMo	600-800	710	0.8	~1100	97.7	81.4	180-270
EI-032	x571 cut 2-3	2/02-3/02	HDT (RCO/LCO 1:1) cut 180-300°C	CoMo	600-800	710	0.8	~1100	97.7	81.4	180-300
EI-033	x571 cut 2-4	2/02-3/02	HDT (RCO/LCO 1:1) cut 180-320°C	CoM	600-800	710	0.8	~1100	97.7	81.4	180-320
EI-034	x572 cut 2	2/02-3/02	HDT (RCO/LCO 3:1) cut 180-270°C	CoMo	600	715	0.4	~1600	98	69.7	180-270
EI-035	x572 cut 2-3	2/02-3/02	HDT (RCO/LCO 3:1) cut 180-300°C	CoMo	600	715	0.4	~1600	98	69.7	180-300
EI-036	x572 cut 2-4	2/02-3/02	HDT (RCO/LCO 3:1) cut 180-320°C	CoMo	600	715	0.4	~1600	98	69.7	180-320
EI-037	x610* cut 2	5/02	HDT (RCO/LCO 1:1) cut 180-270°C	CoMo	600-800	710	0.8	~1100	97.7	81.4	180-270
EI-038	x620** cut 2	5/02	HDT (RCO/LCO 3:1) cut 180-270°C	CoMo	600	715	0.4	~1600	98	69.7	180-270

Note: * x610 cut 2 is similar to x571 cut 2.

** x620 cut 2 is similar to x572 cut 2.

Table 3-2: Lists of coal-based jet fuel blends.

PSU Sample Number	PSU Designation	PSU Sample Number	PSU Designation
BLEND			
B-001	HDT LCO: HDT RCO 3:1	B-015	HDT RCO: SAT LCO 1:3
B-002	HDT LCO: HDT RCO 1:1	B-016	HDT RCO: SAT RCO 3:1
B-003	HDT LCO: HDT RCO 1:3	B-017	HDT RCO: SAT RCO 1:1
B-004	SAT LCO: SAT RCO 3:1	B-018	HDT RCO: SAT RCO 1:3
B-005	SAT LCO: SAT RCO 1:1	B-019	HDT (LCO/RCO) + 10% Decalin
B-006	SAT LCO: SAT RCO 1:3	B-020	HDT (LCO/RCO) + 10% Tetralin
B-007	HDT LCO: SAT LCO 3:1	B-021	HDT (LCO/RCO) + 20% Decalin
B-008	HDT LCO: SAT LCO 1:1	B-022	HDT (LCO/RCO) + 20% Tetralin
B-009	HDT LCO: SAT LCO 1:3	B-023	SAT (LCO/RCO) + 10% Decalin
B-010	HDT LCO: SAT RCO 3:1	B-024	SAT (LCO/RCO) + 10% Tetralin
B-011	HDT LCO: SAT RCO 1:1	B-025	SAT (LCO/RCO) + 20% Decalin
B-012	HDT LCO: SAT RCO 1:3	B-026	SAT (LCO/RCO) + 20% Tetralin
B-013	HDT RCO: SAT LCO 3:1	B-027	HDT (LCO/RCO): Norpar-13 1:1
B-014	HDT RCO: SAT LCO 1:1	B-028	SAT (LCO/RCO): Norpar-13 1:1

3.2 Characterization of Jet Fuel Samples

The jet fuel samples were characterized using a Shimadzu GC-17 coupled with a Shimadzu QP-5000 MS detector fitted with a Restek XTi-5 column with dimensions of 30 m and 0.25 mmID. The column coated with 5% phenyl had 0.25 μm film thickness. All instrument control was performed by the "Class-5000" application software running on a PC. The column temperature was programmed from 40°C to 290°C at a rate of 10°C/min with a final isothermal period of 10 min.

3.2.1 GC/MS Quantitation

For a quantitative GC/MS analysis, tetrahydrofuran was used as an internal standard to quantify the weight percentage from GC intensity for eight major classes of compounds. The internal standard method is a very reliable approach because it can be

used to account for variations such as inexact injection volumes and lost samples [105].

The GC quantitative methods can be described as follows:

1. Prepare a known tetrahydrofuran (THF) standard at a constant concentration (0.5 mg/ 1 mL CS₂) for all standards and samples.
2. Select major compounds to be standards. In this case, the following standards can represent major chemical structures in the coal-based jet fuels.
 - Alkane: octane, decane, undecane, dodecane, tridecane, tetradecane and eicosane
 - Alkene: 1-decene
 - Cycloalkane: methylcyclohexane, bicyclohexyl and decalin
 - Hydroaromatic: indane, indene, tetralin, methyltetralin and 9,10-dihydroanthracene
 - Aromatic: benzene, toluene, ethylbenzene, trimethylbenzene, butylbenzene, cyclohexylbenzene, benzaldehyde, naphthalene, 1-methylnaphthalene, 2-methylnaphthalene, biphenyl, dibenzofuran, acenaphthene, acenaphthylene, anthracene, phenanthrene, flouranthrene, pyrene and binaphthalene.
3. Prepare three known concentrations of each standard at 0.5, 1 and 2 mg/mL CS₂.
4. Run the series of standards and obtain all peak areas from GC/MS. It is assumed that the variations in the internal standard area are representative of the whole analysis.
5. Plot the calibration curve based on the corrected peak areas. Calculate the value of response factor (R.F.) of each standard from the slope of the curve. C_{known} and

A_{known} in Equation (3-1) are the known concentration and peak area of the standard.

$$RF = \frac{\left(\frac{C_{\text{known}}}{C_{\text{istd}}} \right)}{\left(\frac{A_{\text{known}}}{A_{\text{istd}}} \right)} \quad (3-1)$$

6. The RFs of the standards are listed in Table B.1.
7. Prepare the samples at concentration around 10-30 mg/mL CS₂. Obtain the peak area of each target compound. C_{unknown} is to be determined from:

$$C_{\text{unknown}} = \frac{RF \times A_{\text{known}} \times C_{\text{istd}}}{A_{\text{istd}}} \quad (3-2)$$

where

C_{unknown}	=	Unknown concentration of the target
C_{istd}	=	Concentration of internal standard
A_{known}	=	Known peak area of the target
A_{istd}	=	Peak area of the internal standard

8. After concentrations or weights of major target compounds are determined, all compounds will be grouped into eight compound classes. To convert the integrated peak areas into percent weight and divided into eight groups, these steps have been performed using the Microsoft Excel and MATLAB source code shown as example in Appendix B.1.

3.2.2 ^{13}C and ^1H NMR Analyses

Multinuclear liquid-state NMR spectroscopy (^{13}C NMR and ^1H NMR) was performed with a Bruker AMX360 using a field of 9.4 Tesla. A sample was diluted in CDCl_3 (with 1% tetramethylsilane (TMS)) approximately to 1:1 ratio and charged into a 5 mm tube. A recycle delay of 45 seconds was used along with a 70° tip angle to ensure complete relaxation.

Table 3-3 and Table 3-4 represent the chemical shifts of ^{13}C -NMR and ^1H -NMR as follows:

Table 3-3: Typical chemical shifts in ^{13}C -NMR spectra [106].

Structure	Chemical shift (ppm)
Carbonyl (ketone)	205-220
Carbonyl (aldehyde)	190-200
Carbonyl (ester, acid)	170-185
Aromatic	125-150
Alkenes	115-140
Alkynes	67-85
$\text{R}\underline{\text{C}}\text{H}_2\text{OH}$	50-65
$\text{R}\underline{\text{C}}\text{H}_2\text{Cl}$	40-45
$\text{R}\underline{\text{C}}\text{H}_2\text{NH}_2$	37-45
$\text{R}_3\underline{\text{C}}\text{H}$	25-35
$\underline{\text{C}}\text{H}_3\text{CO-}$	20-30
$\text{R}_2\underline{\text{C}}\text{H}_2$	16-25
$\text{R}\underline{\text{C}}\text{H}_3$	10-15

 Table 3-4: Typical chemical shifts in ^1H -NMR spectra [107].

Structure	Chemical shift (ppm)
RCH_3	0.8 - 1.2
R_2CH_2	1.1 - 1.5
R_3CH	~1.5
ArCH_3	2.2 - 2.5
R_2NCH_3	2.2 - 2.6
R_2CHOH	3.2 - 4.3
R_2CHCl	3.5 - 3.7
RC(=O)CHR_2	2.0 - 2.7
$\text{RCH}_2\text{CR}=\text{CR}_2$	~1.7
$\text{RC}=\text{CH}$	4.9 - 5.9
ArH	6.0 - 8.0
RC(=O)H	9.4 - 10.4
$\text{RC}\equiv\text{CH}$	2.3 - 2.9
R_2NH	2.0 - 4.0
ROH	1.0 - 6.0
ArOH	6.0 - 8.0
RCO_2H	10.0 - 12.0

The present study classified the aliphatic and aromatic hydrogens of coal-based jet fuels from ^1H NMR spectra into seven groups based on the literature [73, 108-110]:

- A: chemical shift at 0.7–1.1 ppm, expecting to represent saturated primary (RCH_3),
- B: chemical shift at 1.1–1.4 ppm, expecting to represent saturated secondary (RCH_2),
- C: chemical shift at 1.4-1.6 ppm, expecting to represent saturated tertiary (R_3CH),
- D: chemical shift at 1.7-2.0 ppm, expecting to represent allylic ($\text{RCH}_2\text{CR}=\text{CR}_2$),
- E: chemical shift at 2.0-5.0 ppm, expecting to represent aromatic methyl (ArCH_3), alkynyl ($\text{RC}\equiv\text{CH}$), methyl ketone (RCOCH_3) and alcohol (ROH),

Song and Nomura [110] divided this region into:

- chemical shift at 2-2.35 ppm, CH_3 α to an aromatic ring
- chemical shift at 2.35-3.4 ppm, CH_2 α to an aromatic ring
- chemical shift at 3.4-5.0 ppm, CH_2 α to two aromatic rings

F: chemical shift at 6.5-7.05 ppm, expecting to represent one-ring aromatics (ArH), and

G: chemical shift at 7.05-9.0 ppm, expecting to represent two or multi-ring aromatics (ArH).

The chemical shift at 5.0-6.5 ppm is expected to represent vinylic ($\text{RC}=\text{CH}$) but it was not considered a main structure for the study in Chapter 8.

3.3 Thermal Stability Tests

3.3.1 Thermal Stability Tests in Batch Conditions (Static Test)

The thermal stability tests of JP-900 fuel candidates have been performed in various flow systems in autoxidative and pyrolytic regimes [6, 7]. In this work, the static tests in batch reactors have been performed in the pyrolytic regime at very high temperatures in the absence of oxygen. Pyrolytic stability was determined by heating 5 mL of sample in a 25 mL microautoclave (Figure 2-1) at 480°C under 100-150 psig of ultra-high purity (UHP) N_2 after being degassed six times with 1000 psig UHP N_2 (99.999 %) to remove some dissolved oxygen from the fuel samples. The reaction times were 5, 15, 30, 45, 60, 120, 180, 240 and 360 minutes. After completion of each pyrolysis run, the microautoclave was cooled down and the weight percent of the solids, liquids and gases produced was determined. The tube and stem of the microautoclave

were washed in hexane until the hexane remained clear and then dried. The amount of solid deposition can be determined from the weight gain on the tube wall and reactor lid [58, 111], and the error in the measurements is about ± 0.1 wt% [10]. The stressed liquid products were also analyzed by GC/MS using the method described earlier. And, some of the gas products were also analyzed using headspace GC (Perkin Elmer Autosystem). The detection of hydrocarbon gas products has been performed by FID (Flame Ionization Detector) and packed column – Chemipack C18.

Accuracy in the measurement of gas weights before and after reaction could be checked by calculated results from ideal gas equation ($PV = nRT$). Examples are shown in Appendix C.

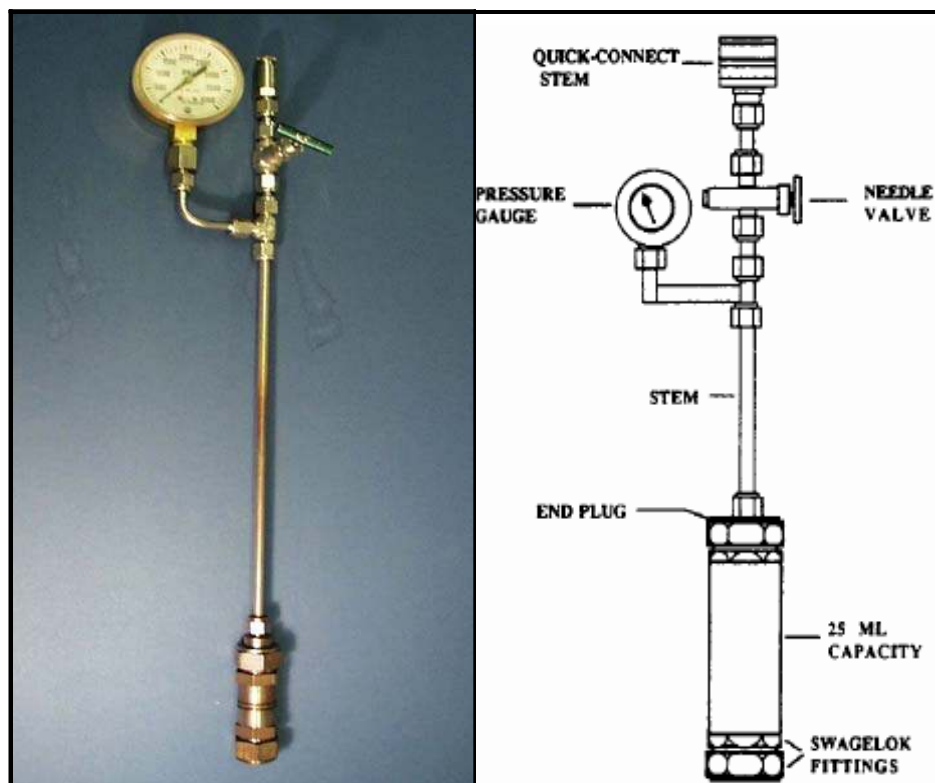


Figure 3-1: The 25-mL microautoclave used for stressing jet fuel [58].

3.3.2 Quartz Crystal Microbalance Test

One of the major challenges for coal-based thermally stable jet fuels is to make the samples resistant to thermal oxidative degradation [7]. The second generation of JP-900 candidates (samples EI-007 to EI-030) was thermally oxidized in a quartz crystal microbalance (QCM) system at the University of Dayton Research Institute, Dayton, OH by Steven Zabarnick. A 60 mL sample of jet fuel was heated to 140°C for 15 hours in a 100 mL stainless steel Parr bomb reactor with *in-situ* monitoring of oxidation and surface deposition [7, 112].

3.3.3 Thermal Stability Tests in Flow Conditions (Dynamic Test)

Fuels were either run as received or sparged for two hours with UHP nitrogen and runs were performed for seven hours in a flow reactor [113], Figure 3-2. The furnace temperature was set at 700°C, resulting in a fuel bulk outlet temperature of 480-520°C. The experiments were performed by Melissa (Roan) Hess [114] and James Strohm [115]. The results were compared to the results from static tests.

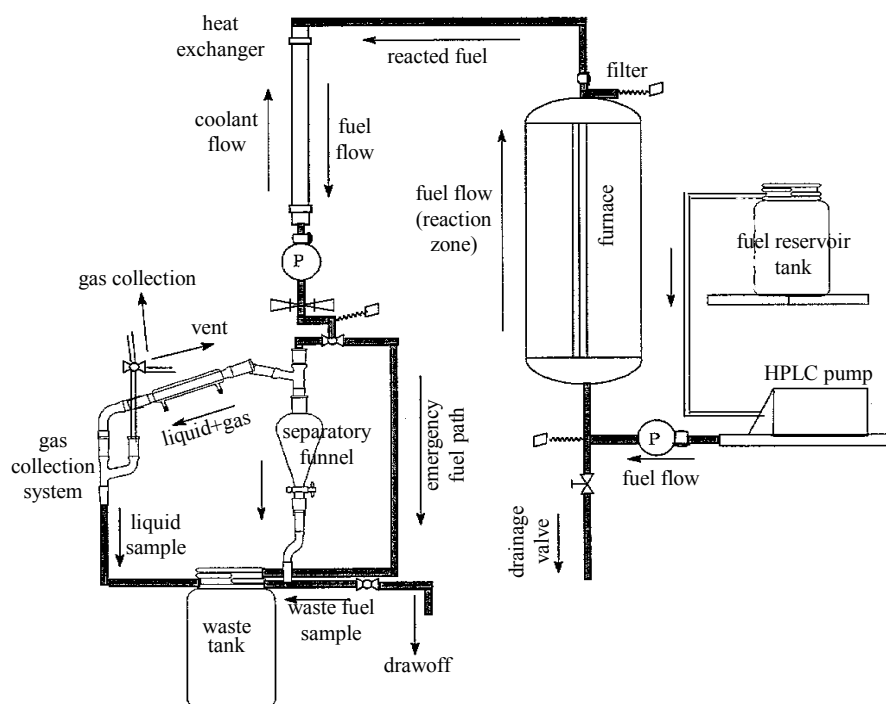


Figure 3-2: Flow reactor [113].

3.3.4 Thermal Stressing of Jet Fuels on Inconel 718

Altin *et al.* [116] performed the tests in flow reactor in the presence of an Inconel 718 foil coupon. The nominal composition of Inconel 718 alloy is Ni: 52.5, Fe: 18.5, Cr: 19, Mo: 3.05, Al: 0.5, Ti: 0.9, Nb+Ta: 5.13, Cu: 0.15, Mn: 0.18, Si: 0.18, C: 0.04 and S: 0.0008 (wt%). Thermal stressing of fuels was carried out at 470°C fuel temperature (525°C wall temperature) and 35 atm. The deposits formed on Inconel 718 surface was characterized by temperature-programmed oxidation.

3.4 Physical Properties Testing

3.4.1 Hydrogen-to-Carbon Ratio

Elemental analysis for the H/C ratio was obtained from a LECO CHN-600 analyzer. The determination is made by burning a weighed quantity of sample in pure oxygen at ~950°C; carbon dioxide, water vapor, oxides of nitrogen, elemental nitrogen, and oxides of sulfur are possible products of combustion [117]. This method gave the total percentages of carbon, hydrogen, and nitrogen in the oil sample as analyzed. The calibration was performed using a standard sample, residual fuel oil from LECO Corporation, which is composed of $88.8 \pm 0.26\%$ carbon and $9.2 \pm 0.12\%$ hydrogen [117].

3.4.2 Net Heat of Combustion

The net heat of combustion was measured using a Parr Calorimeter (Model 1563) following ASTM D 2382. Heat of combustion may give an indication of combustion performance, as it is an important consideration in the design of the combustion system.

The sample was placed inside the bomb setup. A wire fuse was set and the bomb was closed and pressurized with 25.5 atm oxygen. The bomb was placed in a bucket of water and thermocouple leads were connected. After the ignition by electrical current, heat release were measured by the temperature difference of the water [79]. The error associated with the measured value is ± 60 Btu/lb.

Once the reaction inside has stopped, the bomb was removed and gases inside were released. The bomb was disassembled and the unburned piece of wire was measured to determine the heat release given off by the combustion of the fuse wire. The inside of the bomb was washed with diluted methyl orange indicator and titrated with 0.0709 N Na_2CO_3 to determine the heat produced during the formation of nitric and sulfuric acids. The heat released by the hydrocarbon combustion was then subtracted by heat produced by the combustion of the fuse wire and the formation of nitric and sulfuric acids.

The final value of heat of combustion obtained in a bomb calorimeter test represents the gross heat of combustion [79] which is defined as enthalpy change for the following reaction when balanced: $\text{Fuel} + \text{O}_2 (\text{g}) \rightarrow \text{CO}_2 (\text{g}) + \text{H}_2\text{O}(\text{l})$. The net heat of combustion does not include the latent heat of vaporization as discussed in Chapter 2. Thus, the values were calculated from Equation 2-25 (Q_n (Btu/lb) = Q_g (Btu/lb) – 91.23 H) where the H in weight% was obtained from CHN-analyzer.

3.4.3 Smoke Point

The minimum flame height at which soot comes from a laminar diffusion flame tip generated by a standard wick burner was measured under ASTM D 1322. It can predict the soot formation tendency of aviation gas turbine fuels. The apparatus consists of smoke point lamp and wick made from woven solid circular cotton of yarn. The lamp was placed in a vertical position in a room. A piece of extracted and dried wick was soaked in the sample and placed in the wick tube of the candle containing 20 mL of the fuel sample. The wick was cut horizontally so that 6 mm projects from the end of the candle. After that, the candle was inserted into the lamp, lightened and adjusted until the flame height was 10 mm. After burning for 5 minutes, the candle was raised until a smoke tail appeared and then it was lowered until the pointed tip of the flame just disappeared, leaving a slightly blunted flame (ASTM D 1322). Thus, the smoke point was marked and the test was repeated to meet the repeatability of the test, which is 2 mm.

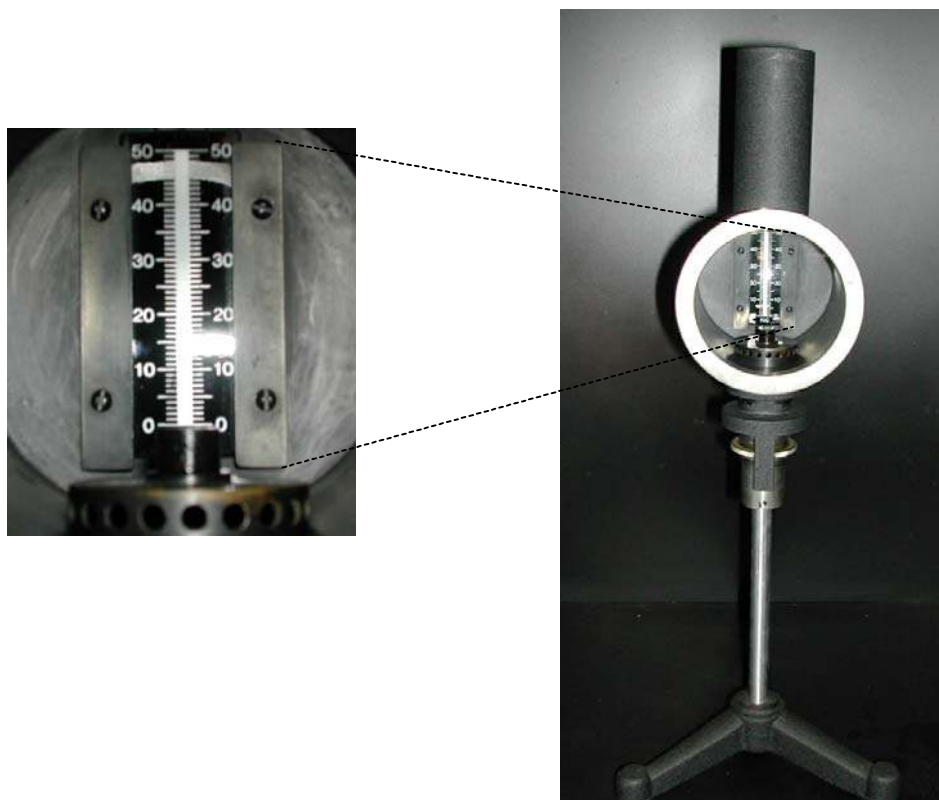


Figure 3-3: Smoke point lamp.

3.4.4 Flash Point

Flash point in this study was measured by the continuously closed cup flash point tester (MINIFLASH-FLP from Grabner Instruments), which used 1-mL sample with no open flame and 30 seconds manipulation time [118]. This method follows ASTM D 6450: CCCFP Method which refers to Standard Test Method for Flash-Point by Continuously Closed Cup (CCCFP) [118].

The sample to be tested was poured into the sample cup, which is placed into the sample cup lift in the front opening of the tester. The sample cup was then automatically lifted onto the oven plate, forming a closed measuring chamber. The vapor was then

ignited following the programmed steps and the pressure increase was monitored. When this increased pressure was above a programmed threshold, the measurement stopped, and the temperature was recorded as the flash point temperature of the sample. The repeatability of the test was $\pm 2^\circ\text{F}$.

3.4.5 Viscosity

The measurement of Saybolt universal viscosity was performed at 100°F in Saybolt universal seconds (SUS) using a Saybolt universal viscometer manufactured by Precision Scientific Petroleum Instruments Company. The method followed ASTM D 88 (1956).

Fuels were placed in the wells and heated by electric heater to 100°F in about 10-15 minutes. After the sufficient time, a cork at the bottom of the well is pulled. The time (efflux time) for sixty milliliters of fuel to drain was measured in seconds and multiplied by orifice correction factor as Equation (3-3) (ASTM D 88, 1956) [119]. In this case, the orifice correction factor is 1.011. The error associated with Saybolt universal viscosity is ± 0.1 seconds (ASTM 88). After that, the conversion of Saybolt universal viscosity to kinematic viscosity in centistokes (cSt) using the table of conversion in ASTM D 2161 or Equation (3-4) [120].

$$F = \frac{V}{t} \quad (3-3)$$

where F = orifice correction factor,

V = Saybolt universal viscosity (corrected time in second),

and t = efflux time in seconds at 100°F .

$$\nu = 0.00226t - \frac{1.95}{t} \quad (3-4)$$

where ν = kinematic viscosity (cSt)

and $32 < t < 100$.

3.4.6 Cloud Point

The cloud point test is chosen to describe the low-temperature and fluidity properties of the coal-based jet fuel samples. The advantage of the cloud point test over the freezing point test is that the coal-based jet fuels tended to have very low fluidity, resulting in very low cloud points that could not be reached by the available equipment in the laboratory.

For the experimental method, Berkhou *et al.* [121] prepared an acetone and dry ice bath inside a 600 mL beaker insulated with Styrofoam. Bath temperature was then monitored by a low-temperature thermometer and adjusted by the addition of crushed ice. After an initial test of each fuel, a fresh 10-mL sample was placed in a culture tube and immersed in the cold bath. Crushed dry ice was added to the cold bath until the fuel sample turned cloudy. This temperature was then recorded for the cloud point of jet fuel.

3.5 Combustion Test

A schematic diagram of the model gas turbine combustor at the Propulsion Engineering Research Center, The Pennsylvania State University is shown below [122].

The incoming compressed air is preheated by cooling the outer section of the combustor and the exhaust stream. This pre-warmed air was then heated to 800°K before entering the combustor. It flowed past the injector and entrained the fuel spray. The fuel air mixture was then introduced into the 45-mm diameter, 350-mm long modular combustion chamber. The liquid fuel line consisted of an inner tube through which the liquid fuel flowed. For the present study, a Delavan pressure atomizer, commonly referred to as a peanut injector, was used as the fuel injector [122].

Upon achieving a stable liquid fuel flame, both the liquid fuel flow rate and the air flow rate were increased until the desired combustion chamber pressure of 0.5 MPa is achieved. Temperatures and pressure at various locations along the rig were monitored.

Soot volume fractions were determined by measuring the laser extinction of a 514.5 nm laser beam which was focused through two nitrogen purged quartz windows located 248 mm downstream from the dump plane [122]. The combustion tests of JP-8, EI-037 and EI-038 were performed by Silvano Saretto of the Department of Mechanical Engineering, The Pennsylvania State University.

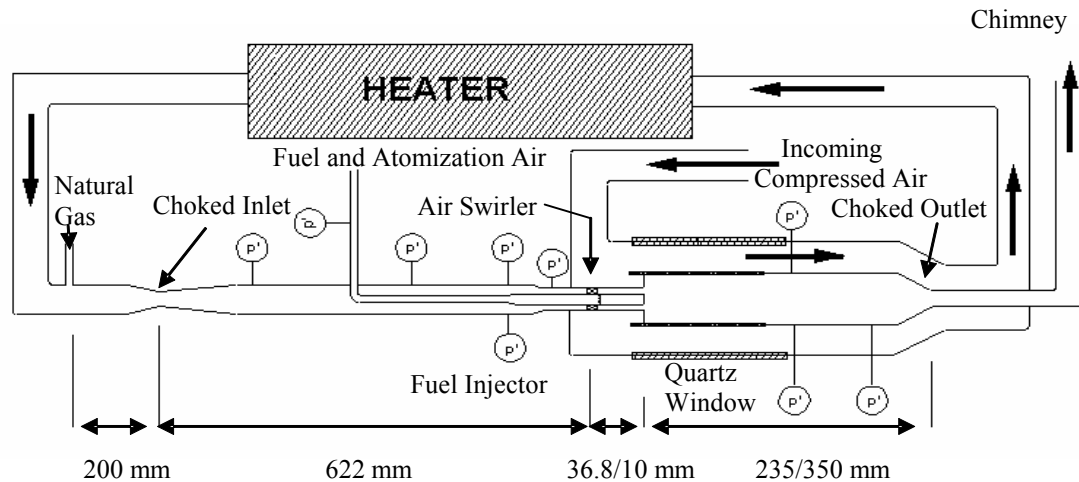


Figure 3-4: Schematic of model gas turbine combustor [122].

3.6 Graphical and Numerical Analyses

3.6.1 Ternary Diagrams

MATLAB source code was written for plotting ternary diagrams. The MATLAB program from MathWorks, Inc. used in this work is version 6.5. The program is available at the computer laboratory of Center of Academic Computing, The Pennsylvania State University. Optimization of jet fuel composition can be made through the visual ternary diagrams. The constraints for optimization are based on ASTM requirements.

3.6.2 Multiple Linear Regression (MLR)

Multiple linear regression (MLR) analysis has been performed on data sets of independent input (chemical compositions and hydrogen structures) and dependent output (thermal stability and physical properties). MLR function in Minitab Release 13.3

statistical program was used for the analysis. The program is also available at the computer laboratory of Center of Academic Computing, The Pennsylvania State University.

3.6.3 Artificial Neural Network (ANN)

The artificial neural network (ANN) approach was selected for non-linear modeling of the composition-properties of candidate fuels. The neural network software called “NeuroShell 2” was obtained from Ward Systems Group, Inc., MD. Input variables (chemical compositions in Table 3-1 and Table 3-2) versus each output variable (thermal stability and properties from Table C-1, C-5, C-6 and C-7) were trained for the composition-properties relationships.

3.6.3.1 Constructing Training Sets

The NeuroShell 2 module offers two different methods for selecting a training set from available data sets. The options are:

1. Use all available data for the training set.
2. Choose a production set of data as a subset of available data. The production set is used to test the network’s results with data that the network has never seen before. In the current study, 10 percent of available data set were extracted as a production set and the rest (90 percent) were used as a training set.

3.6.3.2 Training Methodology

Architectures used in training of the network are back propagation (BP) methods. The architectures (number of layers and neurons) and transfer functions were randomly selected from the default in the NeuroShell 2 software to train each model. The architectures and transfer functions were chosen as final ANN models based on the training that gave the lowest *MSE* and highest R^2 results.

Chapter 4

Characterization of Coal-Based Jet Fuels

This major aspect of this chapter is to discuss the chemical compositions and structures of coal-based jet fuel or JP-900. PARC's jet fuel candidates have been characterized by GC/MS and ^1H NMR quantitative analyses.

4.1 Characterization of Conventional and Coal-Based Jet Fuel

4.1.1 GC/MS Quantitative Analysis

Jet fuel candidates were characterized using a Shimadzu GC-17 coupled with Shimadzu QP-5000 MS detector fitted with a Restek XTi-5 column. The GC quantitation method has also been performed using tetrahydrofuran (THF) as an internal standard. The basic compound classes in jet fuel candidates have been determined as (Table 2-1 and Figure 4-1):

Table 4-1: Summary of eight basic compound classes present in fuel candidates.

Class 1	<i>n</i> -alkane, <i>i</i> -alkane, alkene, alkyne, and cycloalkene
Class 2	cycloalkane
Class 3	indane, indene
Class 4	alkylbenzene
Class 5	naphthalene and methylnaphthalene
Class 6	other aromatics (biphenyl and 3-, 4-ring aromatics)
Class 7	decalin and methyldecalin
Class 8	tetralin and methyltetralin

GC/MS analysis was conducted on the fresh petroleum-derived jet fuels (JP-8 and JP-8+100) and coal-based jet fuel (or the so-called JP-900) candidates. The fuel mixtures of all jet fuels were reported as eight basic compound classes in Table 4-2 to Table 4-3. The sample number EI-0XX was assigned [98] for the samples that exist at The Energy Institute whereas the sample numbers B-0XXs were for jet fuel samples that have been blended for this work.

From Table 4-2 to Table 4-3, the GC/MS results indicate that the distinction between petroleum-derived and PARC's coal-based jet fuels is mainly the amount of alkanes, cycloalkanes and aromatics. The conventional JP-8 and JP-8+100 are composed of alkanes as a major component while cyclic structures are abundant in six JP-900 candidates.

The first generation jet fuels consist of six candidates from six different feedstock and blends. The distribution of compound classes taken from the conventional jet fuels and six prototype JP-900 fuel candidates from the first generation is shown in Table 4-2 and Figure 4-1. Hydrotreated LCO (EI-001) and saturated LCO (EI-004) (see Table 3-1) are the only products that come from the petroleum stream, light cycle oil. The

hydrotreated LCO (EI-001) shows a greater distribution of components in different classes. Upon saturation of EI-001, the products shifted to cycloalkanes. The long-chain components are not favored for thermally stable jet fuel, while cycloalkanes and hydroaromatics are preferred because of their thermal stability at elevated temperature [50, 58, 123]. Conversely, hydrotreated RCO (EI-003) has a higher hydroaromatic content than EI-001 and is dominated by tetrahydronaphthalene (tetralin). As with EI-003, the hydrotreated LCO/RCO, EI-002, is also dominated by tetralin, but has a higher alkane content due to the inclusion of LCO. Upon saturation, the majority of components for saturated RCO (EI-006) and saturated LCO/RCO (EI-005) are converted to cycloalkanes, mainly decahydronaphthalene (decalin). From previous work, cycloalkanes like decalin and hydroaromatics like tetralin are preferred components for highly thermally stable jet fuel [50, 123].

From Table 4-2, the B-001 to B-018 were blended from six mixtures of four fuel candidates (EI-001, EI-003, EI-004 and EI-006). With three different blending ratios, sixteen blends were made with varied distributions of compound classes. To study the effects of decalin and tetralin contents on the fuels' properties, EI-002 and EI-005 were blended with 10% and 20% of decalin and tetralin, respectively. The blends were called B-019 to B-026 (Table 4-2).

Table 4-2: Fuel mixtures of conventional and PARC's first generation jet fuels in eight compound classes.

Sample No.	Jet fuel candidates	Class 1	Class 2	Class 3	Class 4	Class 5	Class 6	Class 7	Class 8
Petroleum-derived jet fuels									
N/A	JP-8	78.01	9.83	0.32	7.95	2.27	1.16	0.00	0.46
N/A	JP-8+100	78.23	5.50	0.30	11.80	3.43	0.00	0.73	0.00
First generation of coal-based jet fuels									
EI-001	HDT LCO	24.84	3.03	2.66	29.30	10.13	0.44	7.31	22.29
EI-002	HDT (LCO/RCO)	7.86	2.77	4.00	11.95	13.13	13.21	7.70	39.38
EI-003	HDT RCO	0.55	2.52	4.02	4.13	18.56	19.38	8.79	42.05
EI-004	SAT LCO	41.27	23.08	0.00	0.67	2.25	0.00	24.93	7.80
EI-005	SAT (LCO/RCO)	18.00	28.84	0.00	0.20	0.00	0.00	49.57	3.39
EI-006	SAT RCO	8.71	27.71	0.00	0.05	0.00	0.00	63.54	0.00
B-001	HDT LCO: HDT RCO 3:1	25.43	1.21	1.41	17.44	11.68	4.78	7.77	30.27
B-002	HDT LCO: HDT RCO 1:1	14.91	0.85	2.78	11.73	12.08	17.41	6.75	33.50
B-003	HDT LCO: HDT RCO 1:3	4.89	2.45	4.17	9.36	17.78	15.03	8.92	37.41
B-004	SAT LCO: SAT RCO 3:1	38.21	22.96	0.00	1.50	0.83	0.00	36.51	0.00
B-005	SAT LCO: SAT RCO 1:1	30.77	21.49	0.76	0.00	0.00	0.00	46.98	0.00
B-006	SAT LCO: SAT RCO 1:3	18.38	23.01	0.00	0.00	0.00	0.00	58.61	0.00
B-007	HDT LCO: SAT LCO 3:1	33.97	7.57	1.22	16.48	9.41	1.11	8.63	21.61
B-008	HDT LCO: SAT LCO 1:1	35.79	8.24	0.00	13.46	10.05	0.30	12.11	20.05
B-009	HDT LCO: SAT LCO 1:3	33.05	12.80	0.00	12.63	7.55	0.00	16.43	17.55
B-010	HDT LCO: SAT RCO 3:1	15.24	12.28	0.20	21.22	2.93	0.32	30.48	17.34
B-011	HDT LCO: SAT RCO 1:1	15.52	19.16	0.00	11.73	4.14	1.19	38.03	10.24
B-012	HDT LCO: SAT RCO 1:3	11.24	18.71	0.00	8.05	1.62	0.00	52.48	7.90
B-013	HDT RCO: SAT LCO 3:1	6.80	5.79	4.10	4.95	14.11	12.94	13.88	37.43
B-014	HDT RCO: SAT LCO 1:1	19.03	6.23	2.48	4.45	11.15	9.83	16.61	30.22
B-015	HDT RCO: SAT LCO 1:3	29.36	13.36	1.50	1.77	12.10	8.90	16.26	16.75
B-016	HDT RCO: SAT RCO 3:1	2.02	7.35	3.33	4.07	15.82	12.42	23.31	31.68
B-017	HDT RCO: SAT RCO 1:1	3.05	12.45	2.29	3.05	11.62	7.51	37.02	23.02
B-018	HDT RCO: SAT RCO 1:3	3.58	20.29	1.27	2.28	8.12	1.30	48.60	14.55
B-019	HDT (LCO/RCO) + 10%D	10.94	2.27	3.18	11.37	12.85	17.52	15.58	26.29
B-020	HDT (LCO/RCO) + 10%T	8.42	1.78	3.66	7.92	13.17	11.61	7.74	45.70
B-021	HDT (LCO/RCO) + 20%D	6.72	1.68	2.91	6.81	11.36	10.63	30.48	29.41
B-022	HDT (LCO/RCO) + 20%T	7.53	1.92	3.28	8.55	11.28	10.95	7.18	49.32
B-023	SAT (LCO/RCO) + 10%D	20.94	21.32	0.00	0.00	0.00	0.00	55.73	2.01
B-024	SAT (LCO/RCO) + 10%T	21.20	20.72	0.00	0.00	0.00	0.00	43.15	14.93
B-025	SAT (LCO/RCO) + 20%D	14.52	18.12	0.00	0.00	0.00	0.00	64.65	2.71
B-026	SAT (LCO/RCO) + 20%T	19.49	17.90	0.00	0.00	0.00	0.00	37.32	25.29
B-027	HDT (LCO/RCO) + norpar-13	71.32	0.47	0.83	5.34	1.88	2.52	2.83	14.81
B-028	SAT (LCO/RCO) + norpar-13	76.58	6.63	0.00	0.00	0.00	0.00	16.79	0.00

Note: D: Decalin
T: Tetralin

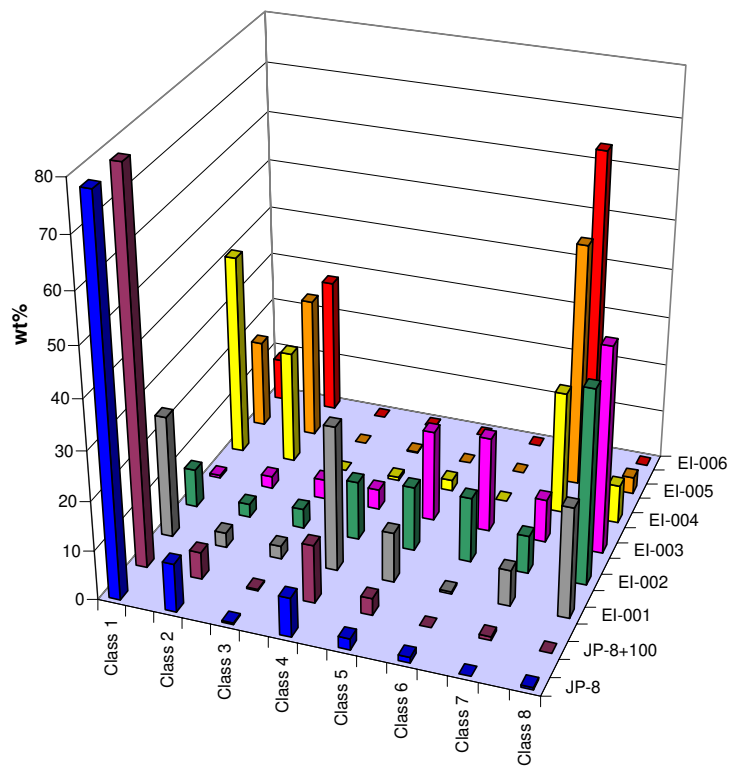


Figure 4-1: The distribution of chemical composition of petroleum-based and coal-based (first generation) jet fuels.

Table 4-3: Fuel mixtures of PARC's second generation jet fuels in eight compound classes.

Sample No.	Jet fuel candidates	Class 1	Class 2	Class 3	Class 4	Class 5	Class 6	Class 7	Class 8
Second generation of coal-based jet fuels									
EI-007	110-126-3	2.51	1.86	2.29	5.75	14.68	37.10	3.42	32.39
EI-008	110-126-6	2.40	1.84	2.61	4.32	10.94	30.97	2.64	44.28
EI-009	110-126-7	2.77	3.10	2.78	5.92	12.38	31.63	3.41	38.01
EI-010	111-126-3	1.17	2.18	3.64	3.77	17.97	25.21	7.45	38.61
EI-011	111-126-6	1.57	2.53	3.71	3.89	12.74	30.47	5.59	39.49
EI-012	111-126-7	1.49	1.49	3.32	4.03	15.37	34.26	4.58	35.46
EI-013	112-126-3	1.22	1.67	2.61	2.71	28.87	29.93	7.68	25.33
EI-014	112-126-6	1.17	1.80	3.16	3.29	11.58	29.58	7.96	41.47
EI-015	112-126-7	1.74	2.92	3.26	4.93	12.26	26.97	8.90	39.02
EI-016	113-126-3	2.33	3.40	2.83	4.87	10.03	24.75	17.02	34.77
EI-017	113-126-6	2.27	2.84	3.25	4.22	6.90	27.82	9.13	43.59
EI-018	113-126-7	3.06	4.91	4.08	5.58	7.09	24.10	12.26	38.91
EI-019	110-126-1	5.21	2.35	1.81	9.18	13.63	36.61	2.23	28.98
EI-020	110-126-2	1.98	0.92	1.89	7.59	19.16	37.34	0.84	30.28
EI-021	110-126-4	1.87	0.57	2.13	6.00	16.18	41.72	1.55	30.00
EI-022	111-126-1	6.90	3.84	2.25	10.47	11.78	26.74	5.00	33.01
EI-023	111-126-2	3.06	1.26	2.46	6.32	16.71	27.95	4.35	37.90
EI-024	111-126-4	3.49	2.05	2.85	7.95	17.34	34.45	2.20	29.68
EI-025	112-126-1	10.83	3.48	1.67	10.47	9.03	24.25	7.53	32.74
EI-026	112-126-2	2.93	2.22	2.01	7.46	15.51	30.14	6.23	33.50
EI-027	112-126-4	1.97	1.97	2.29	5.85	17.01	32.12	4.22	34.56
EI-028	113-126-1	6.04	3.35	0.24	7.84	6.29	26.22	9.66	40.35
EI-029	113-126-2	2.21	1.76	1.73	6.73	11.96	34.94	7.92	32.76
EI-030	113-126-4	3.05	2.55	1.95	7.38	11.94	35.79	5.02	32.33

The second generation jet fuel candidates (Table 4-3) are all hydrotreated products from the blends of LCO:RCO 1:1 and 1:3 so the contents of all compound classes are similar to hydrotreated LCO/RCO (EI-002) of the first generation. All tetralin-rich fuels consist of 0.2-9 wt% alkane, 25-45% tetralin, and more than 40% total aromatics. The main purpose for the production of this generation focused on making

hydrotreated products that can be evaluated in small-scale thermal stability tests such as the QCM test and the batch reactor thermal stability test.

Table 4-4: Fuel mixtures of PARC's third generation jet fuels in eight compound classes.

Sample No.	Jet fuel candidates	Class 1	Class 2	Class 3	Class 4	Class 5	Class 6	Class 7	Class 8
Third generation of coal-based jet fuels									
EI-031	HDT (LCO/ RCO 1:1) cut 180-270°C	1.05	1.27	4.21	6.62	38.92	4.62	1.25	42.06
EI-032	HDT (LCO/ RCO 1:1) cut 180-300°C	2.52	0.94	3.04	6.17	38.48	19.72	0.89	28.24
EI-033	HDT (LCO/ RCO 1:1) cut 180-320°C	1.49	0.91	3.37	4.32	38.74	17.79	1.05	32.33
EI-034	HDT (LCO/ RCO 1:3) cut 180-270°C	0.78	1.38	4.97	4.60	17.67	14.72	0.84	55.03
EI-035	HDT (LCO/ RCO 1:3) cut 180-300°C	1.22	1.22	3.86	5.89	19.62	21.71	0.71	45.76
EI-036	HDT (LCO/ RCO 1:3) cut 180-320°C	1.48	1.10	3.59	5.95	18.90	24.91	0.66	43.41
EI-037	HDT (LCO/ RCO 1:1) cut 180-270°C	1.07	1.29	3.41	7.34	35.92	11.08	1.16	38.73
EI-038	HDT (LCO/ RCO 1:3) cut 180-270°C	0.42	0.62	5.26	2.92	23.91	11.31	1.42	54.15

Similar to the second generation, the third generation of jet fuel candidates was produced from the hydrotreatment of the 1:1 and 1:3 blends of LCO: RCO. The main objective for the production was to determine the effect of distillation cut point for three different jet fuel ranges, 180-270°C, 180-300°C and 180-320°C [104]. Table 4-4 and Figure 4-2 show that the boiling range 180-270°C for both EI-031 and EI-034 were very rich in tetralin and naphthalene components because the boiling point of tetralin (207°C) and naphthalene (218°C) in this range. The 180-270°C range also contained higher amounts of cycloalkanes and other hydroaromatics such as indane and indene, while the 180-300°C and 180-320°C ranges were distinguished by the increasing amount of multi-ring aromatics.

All chromatograms of EI-001 through EI-006 are displayed in Appendix B.

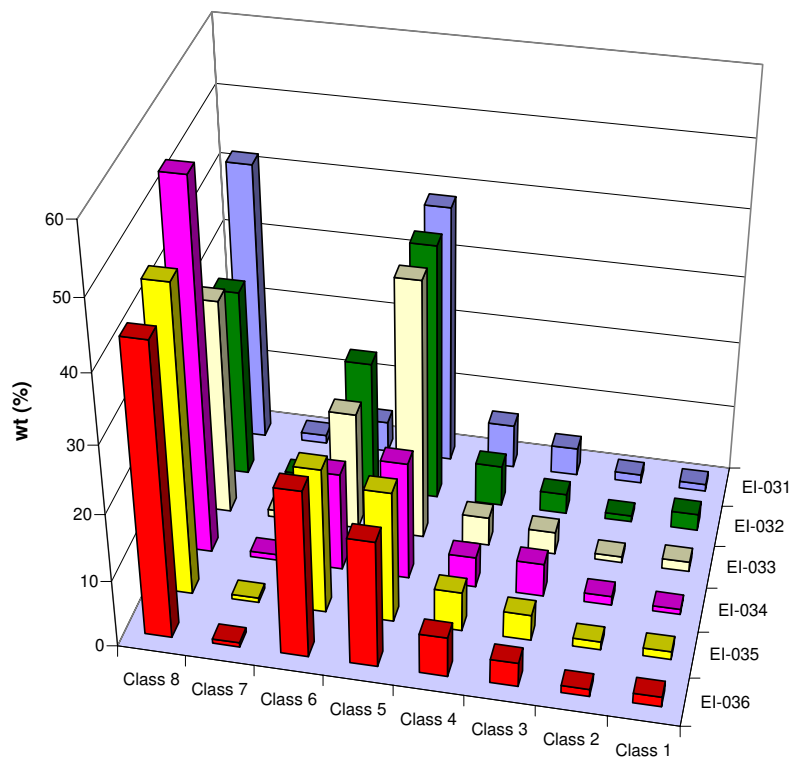


Figure 4-2: The distribution of chemical composition of coal-based (third generation) jet fuels of different boiling ranges.

4.1.2 ^{13}C and ^1H NMR Analyses

JP-8 and the first generation coal-based jet fuels were also examined by ^{13}C and ^1H NMR analyses. Figure 4-3 shows the ^{13}C and ^1H NMR spectra of JP-8, while the ^{13}C NMR spectra of hydrotreated and saturated coal-based jet fuels are presented in Figure 4-4 and Figure 4-5 respectively. ^1H NMR spectra of the jet fuels are also displayed in Figure 4-6 and Figure 4-7.

For this particular work, two main regions (aliphatics and aromatics) were defined to do the integration. For ^{13}C -NMR, percentages of aliphatic carbons were obtained from chemical shift between 10-60 ppm, while alkene and aromatic carbons compositions were integrated in the chemical shift region 110-160 ppm. In case of ^1H -NMR, the integration of chemical shift from 0.2-4.0 ppm gave the percentages of aliphatic hydrogens and chemical shift from 6.5-9 ppm yielded the percentage of aromatic hydrogens. The results of aliphatic and aromatic percentages after integration of the spectrum are reported in Table 4-5.

Table 4-5: Different types of carbon and hydrogen composition based on chemical shifts.

Sample number	Sample name	^{13}C NMR		^1H NMR	
		Aliphatic carbon	Alkene + aromatic carbon	Aliphatic hydrogen	Aromatic hydrogen
N/A	JP-8	90.3	9.7	96.4	3.6
EI-001	HDT LCO	72.2	27.8	89.1	10.9
EI-002	HDT (LCO/RCO)	58.6	41.4	80.3	19.7
EI-003	HDT RCO	41.5	58.5	66.4	33.6
EI-004	SAT LCO	100	0	100	0
EI-005	SAT (LCO/RCO)	100	0	100	0
EI-006	SAT RCO	100	0	100	0

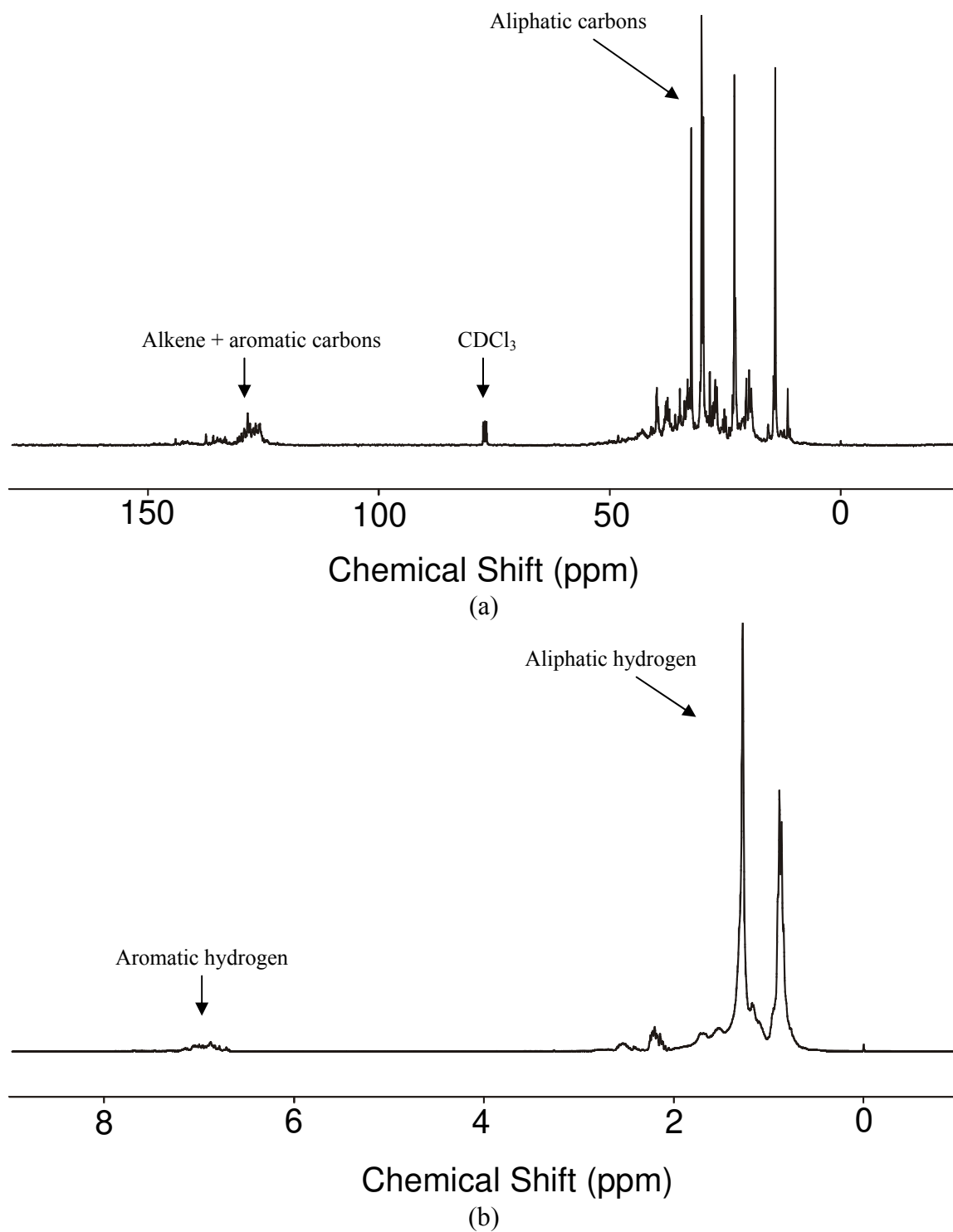


Figure 4-3: NMR spectra of JP-8: (a) ^{13}C and (b) ^1H .

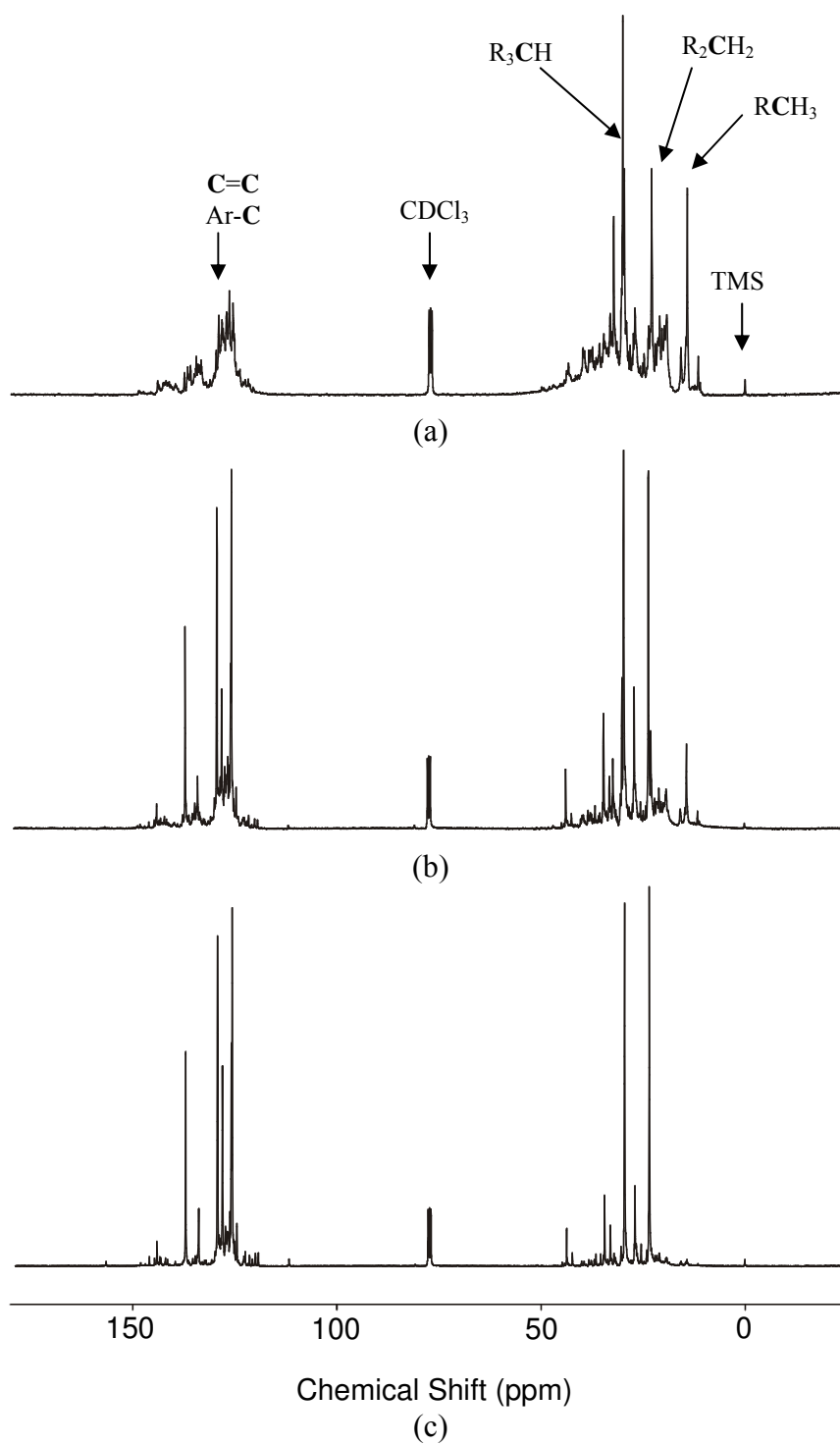


Figure 4-4: ^{13}C spectra of (a) EI-001 (hydrotreated LCO), (b) EI-002 (hydrotreated LCO/RCO) and (c) EI-003 (hydrotreated RCO).

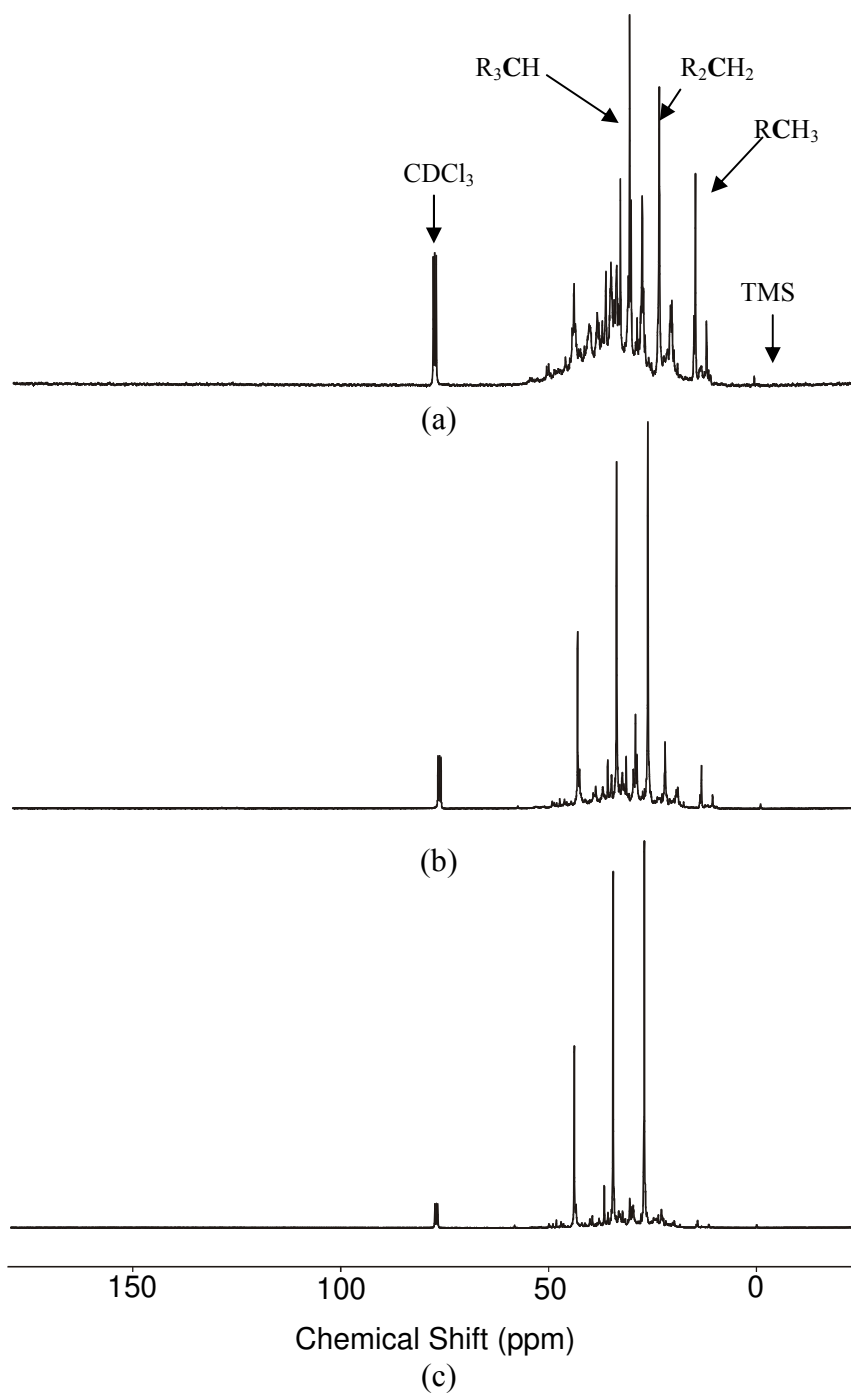


Figure 4-5: ^{13}C spectra of (a) EI-004 (saturated LCO), (b) EI-005 (saturated (LCO/RCO)) and (c) EI-006 (saturated RCO).

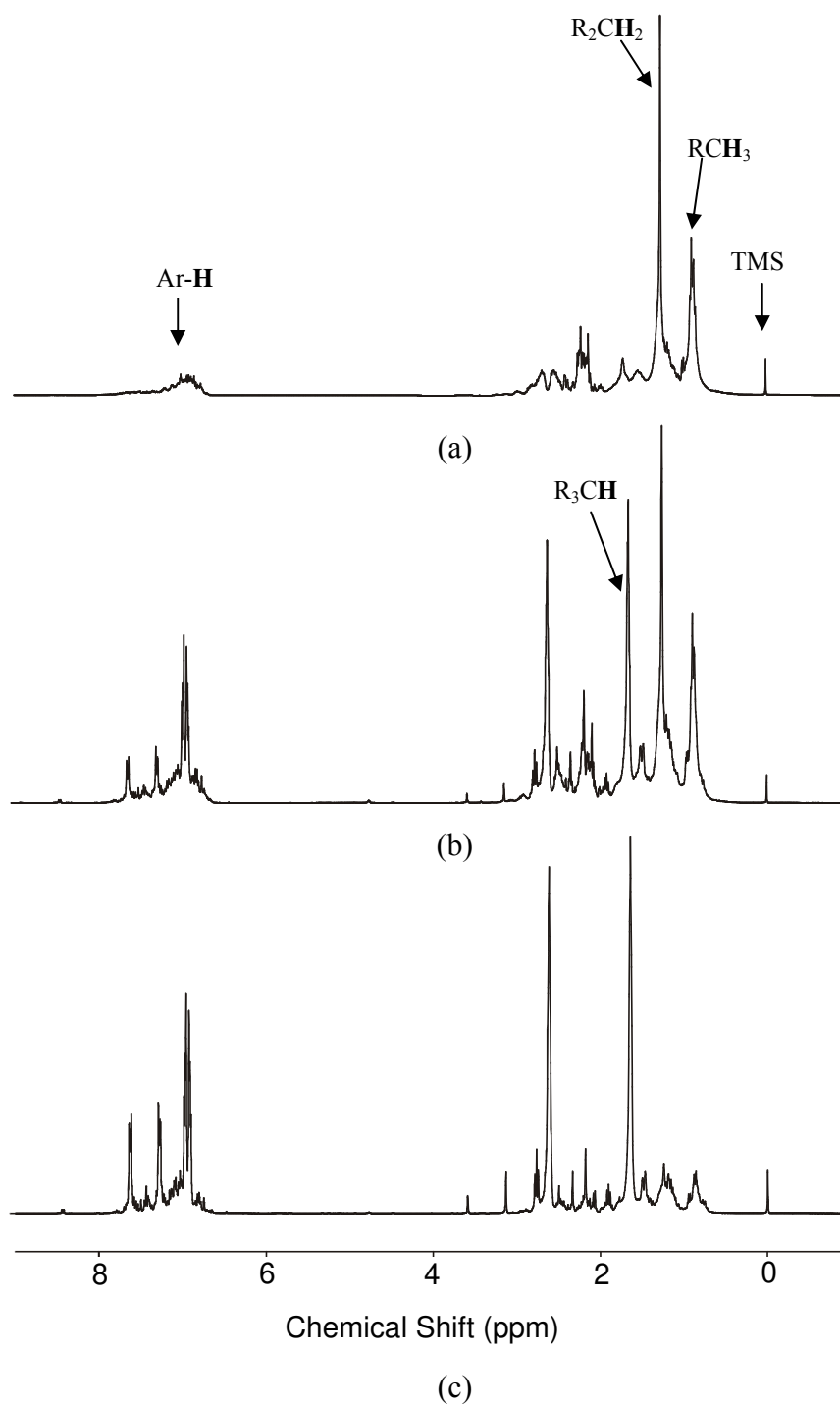


Figure 4-6: ^1H spectra of (a) EI-001 (hydrotreated LCO), (b) EI-002 (hydrotreated LCO/RCO) and (c) EI-003 (hydrotreated RCO).

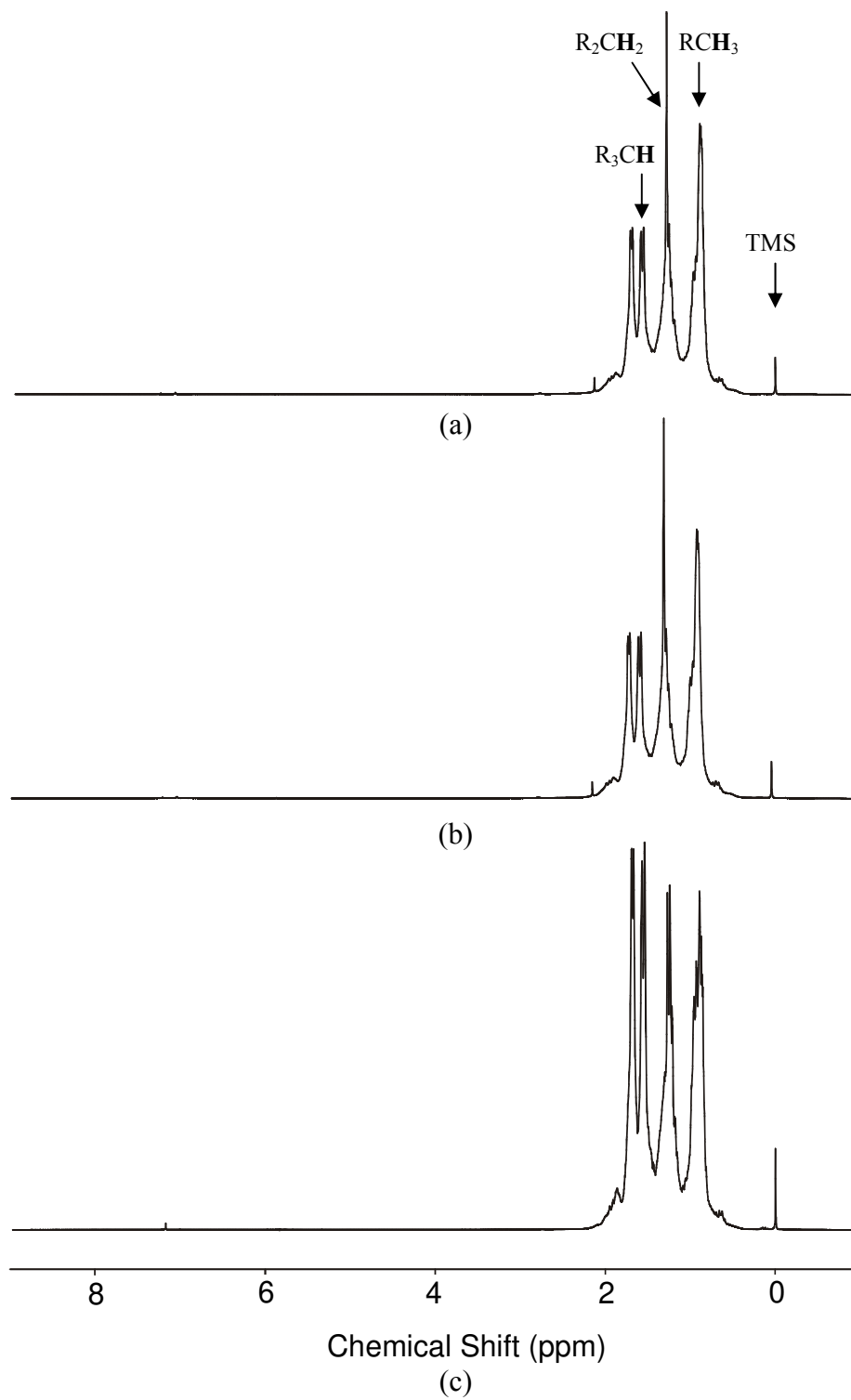


Figure 4-7: ^1H spectra of (a) EI-004 (saturated LCO), (b) EI-005 (saturated LCO/RCO) (c) EI-006 and (saturated RCO).

The results from Table 4-5 and the four figures agreed with the results from GC/MS, in that both aliphatic and aromatic components are abundant in hydrotreated fuels. From ^{13}C and ^1H spectra, the proportion of aromatic contents increased from EI-001 to EI-003 (when RCO components were increasingly added to the feed). EI-004, EI-005 and EI-006 (or saturated fuels) have shown no traces of aromatics though GC/MS has detected very small amounts of naphthalenes, benzenes and tetralins.

Chemical shifts from 10-60 ppm of ^{13}C NMR spectra correspond to the aliphatic region, which can be further integrated to obtain RCH_3 , R_2CH_2 and R_3CH separately. Unlike the aliphatic region, it is difficult to distinguish the chemical shifts of alkenes ($\text{C}=\text{C}$) and aromatics ($\text{Ar}-\text{C}$). Their chemical shifts (115-140 ppm for alkenes and 125-150 ppm for aromatics) overlap with each other. However, chemical shifts from ^1H NMR can be integrated into seven regions separately. Figure 4-8 displays quantitative classification of hydrogen types into: A: chemical shift at 0.7–1.1 ppm; B: chemical shift at 1.1–1.4 ppm; C: chemical shift at 1.4-1.6 ppm; D: chemical shift at 1.7-2.0 ppm; E: chemical shift at 2.0-5.0 ppm; F: chemical shift at 6.5-7.05 ppm; and G: chemical shift at 7.05-9.0 ppm.

JP-8 was dominated by saturated secondary and primary hydrogens. Saturated fuels (EI-004 to EI-006) are also highly aliphatic but presented more saturated primary hydrogen. For hydrotreated fuels (EI-001 to EI-003), the aromatics can be observed to be significant and they increased with the RCO amount added to the feedstock. But, the methyl substitution in aromatics seemed to decrease with increasing RCO amount. This result is explained by the decrease in the ratio of aromatic carbon and aromatic hydrogen ($\text{C}_{\text{ar}}/\text{H}_{\text{ar}}$) from EI-001 to EI-003.

^1H NMR chemical shifts of forty-four samples (petroleum-based, coal-based jet fuels and their blends) are presented in Table 4-6. The information will be used for further discussion in Chapter 8.

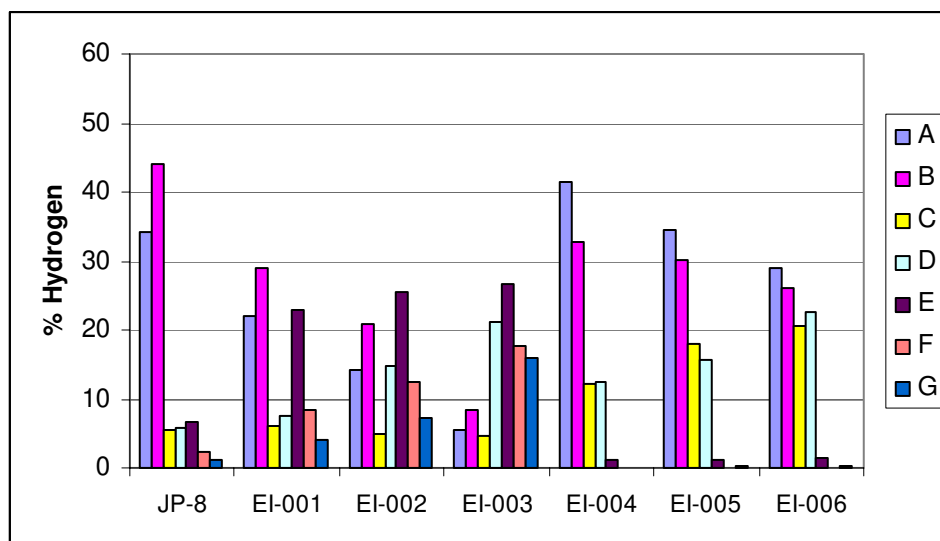


Figure 4-8: Percentages of different hydrogen types of JP-8 and coal-based jet fuels.

Table 4-6: ¹H NMR chemical shifts in seven regions (%) of conventional and PARC's first generation jet fuels in eight compound classes.

Sample No.	Jet fuel candidates	Region A	Region B	Region C	Region D	Region E	Region F	Region G
Petroleum-derived jet fuels								
N/A	JP-8	34.26	44.07	5.51	5.76	6.78	2.40	1.22
N/A	Norpar-13	21.87	76.45	1.62	0.05	0.00	0.00	0.00
First generation of coal-based jet fuels								
EI-001	HDT LCO	22.05	28.86	6.08	7.60	22.91	8.52	3.98
EI-002	HDT (LCO/RCO)	14.08	20.95	4.80	14.88	25.62	12.41	7.27
EI-003	HDT RCO	5.64	8.39	4.56	21.08	26.74	17.66	15.92
EI-004	SAT LCO	41.46	32.77	12.15	12.37	1.16	0.03	0.05
EI-005	SAT (LCO/RCO)	34.61	30.11	17.97	15.68	1.20	0.12	0.30
EI-006	SAT RCO	29.05	25.97	20.64	22.57	1.37	0.11	0.29
B-001	HDT LCO: HDT RCO 3:1	19.33	24.55	7.20	11.20	22.35	8.02	7.35
B-002	HDT LCO: HDT RCO 1:1	16.65	22.03	4.49	13.82	22.89	10.46	9.66
B-003	HDT LCO: HDT RCO 1:3	12.61	16.62	6.06	14.63	24.01	13.10	12.97
B-004	SAT LCO: SAT RCO 3:1	39.46	32.00	13.50	13.90	0.74	0.14	0.26
B-005	SAT LCO: SAT RCO 1:1	36.21	31.21	16.36	14.90	1.03	0.08	0.22
B-006	SAT LCO: SAT RCO 1:3	33.17	28.37	19.68	17.70	0.90	0.07	0.13
B-007	HDT LCO: SAT LCO 3:1	28.57	30.02	8.70	8.11	16.34	4.66	3.60
B-008	HDT LCO: SAT LCO 1:1	32.30	32.23	10.13	8.91	10.77	3.01	2.66
B-009	HDT LCO: SAT LCO 1:3	40.17	33.68	11.41	6.93	4.05	1.73	2.02
B-010	HDT LCO: SAT RCO 3:1	21.17	25.06	9.17	9.49	13.79	18.69	2.63
B-011	HDT LCO: SAT RCO 1:1	25.94	29.33	13.04	15.13	11.32	2.86	2.38
B-012	HDT LCO: SAT RCO 1:3	28.03	28.57	15.81	18.18	6.41	1.65	1.36
B-013	HDT RCO: SAT LCO 3:1	19.91	17.82	7.27	16.62	16.52	9.88	11.99
B-014	HDT RCO: SAT LCO 1:1	28.81	23.27	9.17	14.40	10.77	6.21	7.38
B-015	HDT RCO: SAT LCO 1:3	35.49	32.62	10.10	11.13	5.03	1.99	3.64
B-016	HDT RCO: SAT RCO 3:1	15.96	16.05	10.55	23.24	18.56	3.42	12.23
B-017	HDT RCO: SAT RCO 1:1	20.77	19.52	15.32	19.93	10.88	6.50	7.07
B-018	HDT RCO: SAT RCO 1:3	25.93	24.02	19.08	19.81	6.55	0.27	4.34
B-019	HDT (LCO/RCO) + 10%D	14.61	22.27	8.36	14.55	22.06	9.92	8.22
B-020	HDT (LCO/RCO) + 10%T	12.93	18.83	4.14	15.97	25.62	12.56	9.95
B-021	HDT (LCO/RCO) + 20%D	14.67	23.31	13.22	13.95	19.07	8.82	6.96
B-022	HDT (LCO/RCO) + 20%T	11.68	16.65	5.13	16.89	26.39	14.23	9.03
B-023	SAT (LCO/RCO) + 10%D	33.55	30.20	16.80	18.40	0.78	0.06	0.21
B-024	SAT (LCO/RCO) + 10%T	33.13	27.63	15.52	18.54	2.84	1.93	0.41
B-025	SAT (LCO/RCO) + 20%D	31.91	30.02	20.66	16.67	0.61	0.08	0.05
B-026	SAT (LCO/RCO) + 20%T	30.86	24.72	15.67	18.50	5.39	4.46	0.40
B-027	HDT (LCO/RCO) + Norpar-13	18.95	54.38	2.76	5.28	10.19	4.29	4.15
B-028	SAT (LCO/RCO) + Norpar-13	27.88	55.88	8.09	7.48	0.46	0.14	0.07

Table 4-6 (continued)

Sample No.	Jet fuel candidates	Region A	Region B	Region C	Region D	Region E	Region F	Region G
Third generation of coal-based jet fuels								
EI-031	HDT (LCO/ RCO 1:1) cut 180-270°C	6.82	10.04	2.85	14.77	29.89	14.71	20.93
EI-032	HDT (LCO/ RCO 1:1) cut 180-300°C	6.86	10.63	2.82	12.45	30.83	12.88	23.52
EI-033	HDT (LCO/ RCO 1:1) cut 180-320°C	7.25	11.45	2.95	11.41	31.06	12.00	23.88
EI-034	HDT (LCO/ RCO 1:3) cut 180-270°C	4.36	5.73	3.07	21.07	29.96	19.98	15.83
EI-035	HDT (LCO/ RCO 1:3) cut 180-300°C	5.52	7.93	3.49	19.15	32.09	18.75	13.07
EI-036	HDT (LCO/ RCO 1:3) cut 180-320°C	6.06	8.24	2.57	19.17	31.95	17.53	14.48
EI-037	HDT (LCO/ RCO 1:1) cut 180-270°C	6.82	10.04	2.85	14.77	29.89	14.71	20.93
EI-038	HDT (LCO/ RCO 1:3) cut 180-270°C	4.36	5.73	3.07	21.07	29.96	19.98	15.83

Chapter 5

Thermal Stability Tests

The thermal stability test results of petroleum-based and coal-based fuels in a batch reactor, a quartz crystal microbalance and a flow reactor were also an important part of the final selection of jet fuel's chemical composition.

5.1 Thermal Stability Test of the First Generation Jet Fuel Candidates in Static Condition

The static tests in batch reactors have been performed in the pyrolytic regime at very high temperatures, i.e., 480°C (or 900°F) in the absence of oxygen. In this work, the pyrolytic stability was determined by heating 5 mL of sample in a 25 mL microautoclave at 480°C under 100 psig of UHP N₂ for 5, 15, 30, 45, 60, 120, 180, 240 and 360 minutes. After completion of stressing at different resident times, the solid deposits and gas formed were collected while the remaining liquid was obtained from the difference between the reactant weight and solid and gas yields. Solid, gas and remaining liquid yields are presented from Figure 5-1 to Figure 5-4.

The solid and gas yields from petroleum-based jet fuel, JP-8 and JP-8+100, are shown in Figure 5-1 whereas those of the hydrotreated and saturated coal-based jet fuels

are presented in Figure 5-2 and Figure 5-3, respectively. It is clear that most of the coal-based fuels produced lower solid and gas yields with increasing time than the JP-8 and JP-8+100 did. However, the stressed JP-8 and JP-8+100 did not show a major difference in the yields between each other. As the compound distributions of JP-8 and JP-8+100 are similar, this confirms that the chemical composition is the major factor of jet fuel pyrolysis under this particular condition. The comparison between petroleum-based and coal-based jet fuels also strongly supported the statement.

With increasing concentration of RCO feed (or coal tar distillate component) to produce the hydrotreated fuel candidates, lower solid deposition and gas formation were observed. This may be due to the increase of thermally stable components, such as decalin and tetralin, and the reduction of unstable alkanes. Similarly, in the saturated fuels, the higher the RCO in the feed mixture, the more thermally stable compounds in the candidate fuel. However, under pyrolytic conditions, light fractions (such as materials derived from LCO) tended to decompose, resulting in high gas formation and increase of solid deposition. The influence of the high concentration of light compounds, such as alkanes and alkenes, in EI-004 and EI-005 may also give rise to the increase level of gas formation.

5.1.1 Solid Deposition Rate

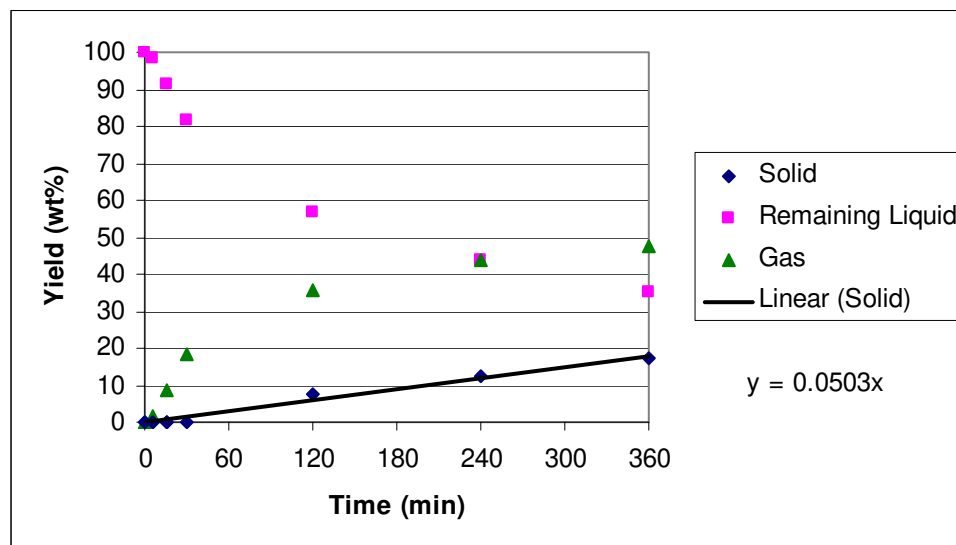
To study the jet fuel reaction in a batch system, simple kinetic models of hydrocarbon mixtures have been previously discussed [124, 125]. However, it is still impractical to model the chemical changes of all components of a real mixture like jet fuel that is comprised of hundreds of chemical species [126]. To simplify the

measurement of thermal stability in a batch reactor and describe the time dependence of the liquid degradation to solid deposit on the wall, the rate of solid deposit with increasing time was plotted in the following graphs (Figure 5-1 to Figure 5-3). The stressing at 480°C in the batch system at long residence time represents the most severe thermal stressing that the fuels can experience. The comparison of solid deposit rates as a function of time of all fuels is shown in Figure 5-4.

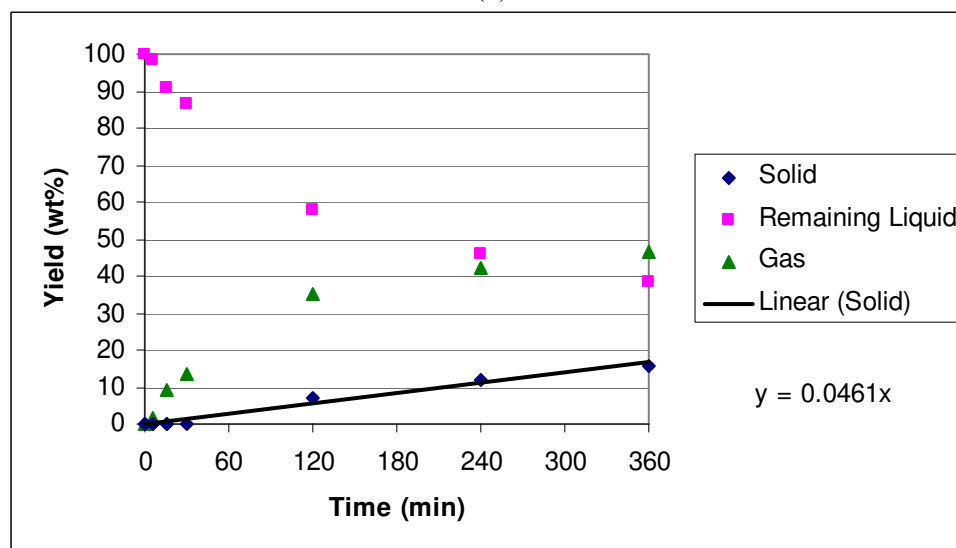
The solid deposit rates of JP-8 and JP-8+100 obtained from the normal plots in Figure 5-1 were 0.0503 and 0.0461 wt%/min respectively. Comparing to hydrotreated fuel candidates, the deposit rates of EI-001, EI-002 and EI-003 were 0.0523, 0.0201 and 0.0014 wt%/min (Figure 5-2). EI-001 (hydrotreated LCO) tended to yield high deposit weight after 240 minutes reaction time, so the overall rate is higher than those of JP-8 and JP-8+100.

The deposit rates of saturated fuels were slightly higher than the hydrotreated ones. In Figure 5-3, EI-004, EI-005 and EI-006 yielded solid at the rate of 0.0341, 0.0171 and 0.0100 wt%/min.

In Figure 5-4, the solid deposits with the increasing time of JP-8, JP-8+100 and coal-based jet fuels have been compared. For most fuels, the solid started to form after 10-15 minutes. Only hydrotreated RCO formed no solid until a reaction time of 30 minutes was reached.

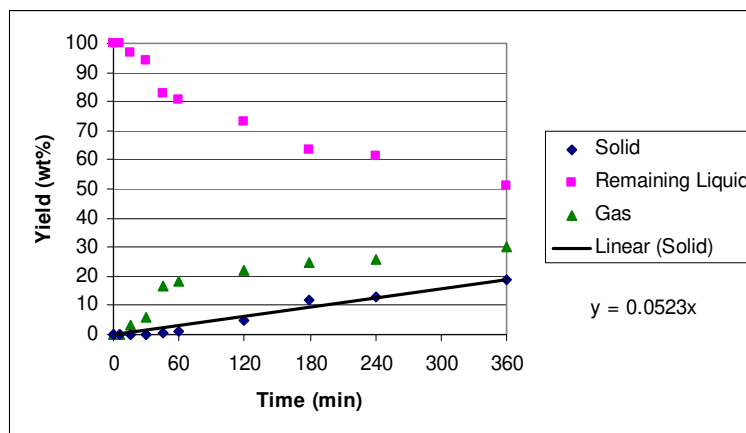


(a)

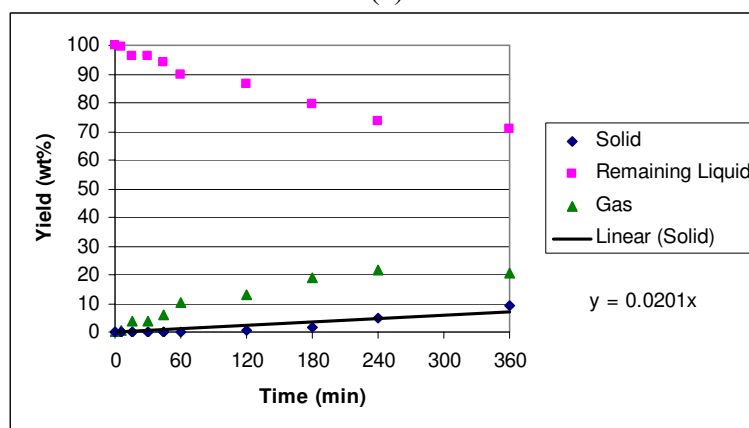


(b)

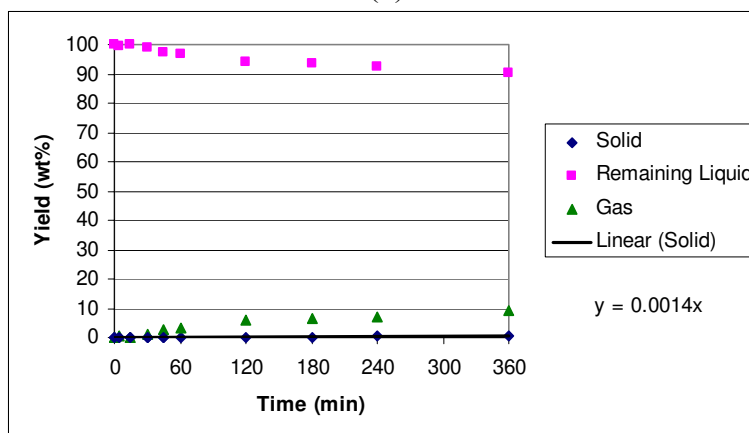
Figure 5-1: Yields of stressed (a) JP-8 and (b) JP-8+100 after thermal stressing reaction in 25-mL microautoclave at 480°C from 0-360 minutes.



(a)

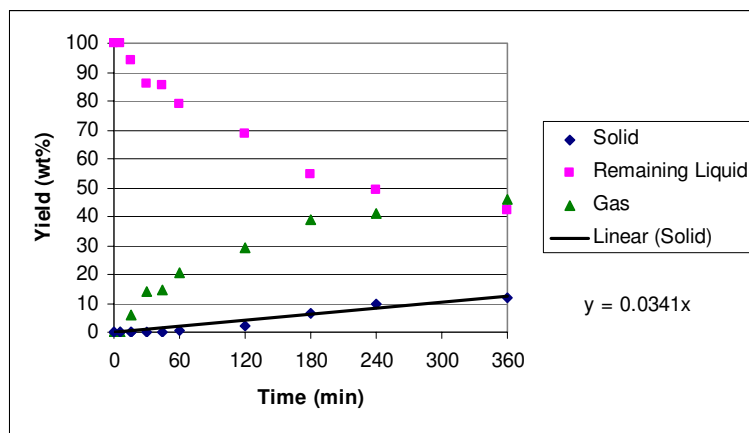


(b)

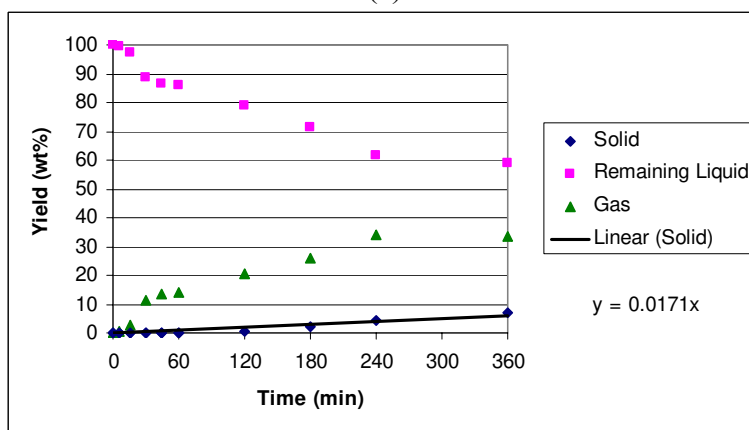


(c)

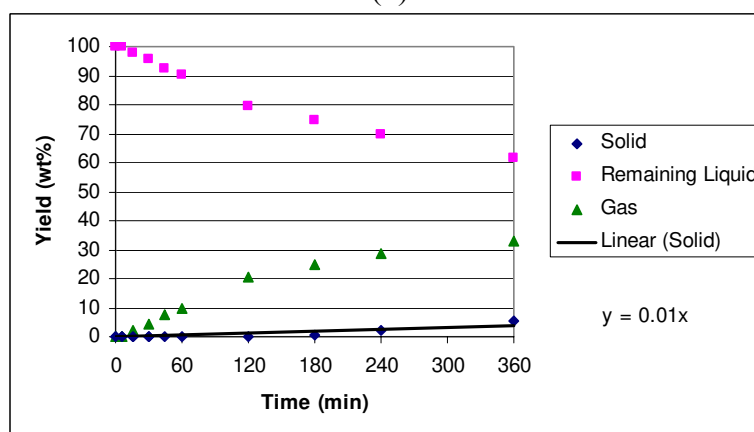
Figure 5-2: Yields of stressed (a) EI-001, (b) EI-002 and (c) EI-003 after thermal stressing reaction in 25-mL microautoclave at 480°C from 0-360 minutes.



(a)

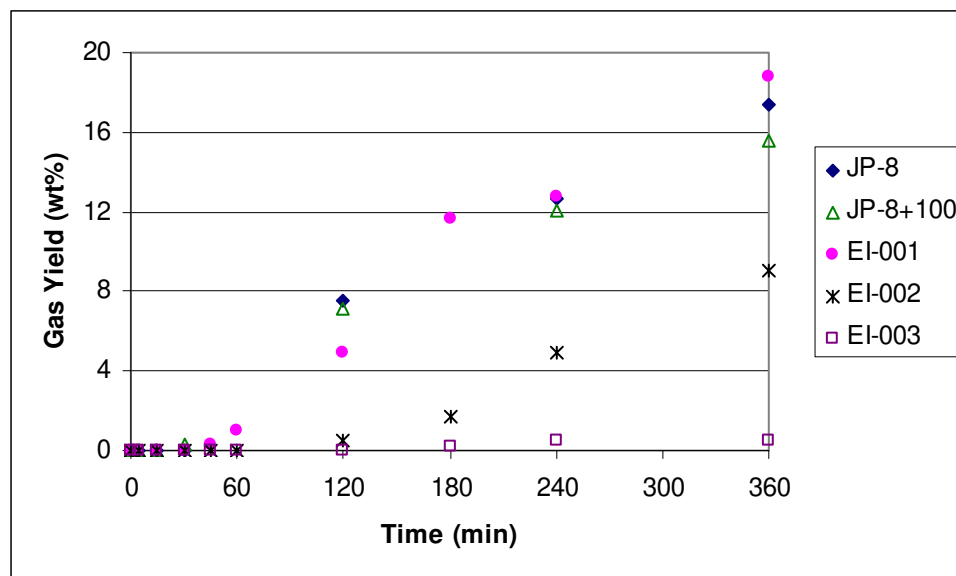


(b)

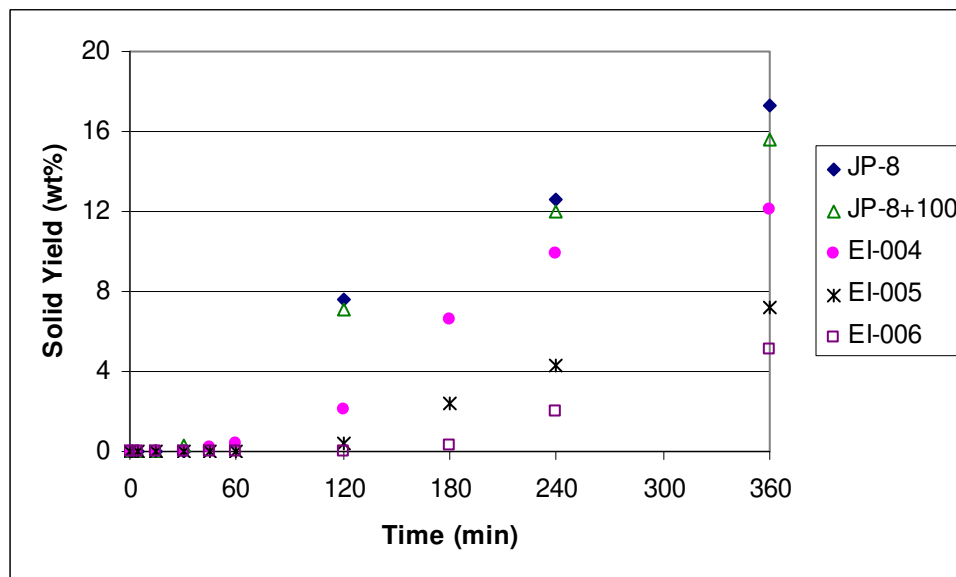


(c)

Figure 5-3: Yields of stressed (a) EI-004, (b) EI-005 and (c) EI-006 after thermal stressing reaction in 25-mL microautoclave at 480°C from 0-360 minutes.



(a)



(b)

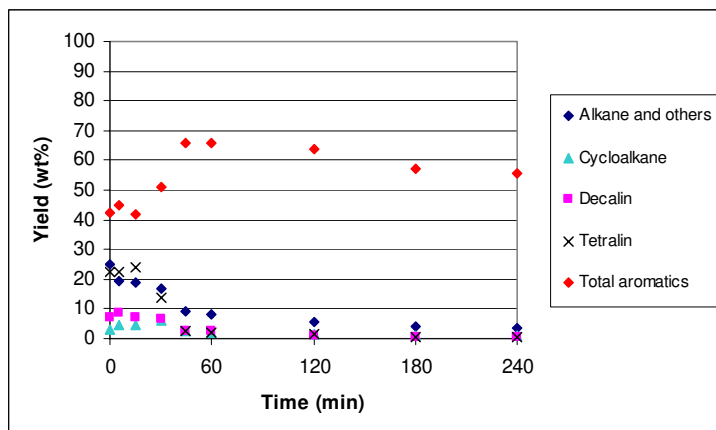
Figure 5-4: Comparison of the solid deposit with time between petroleum-based jet fuel and (a) hydrotreated fuels, and (b) saturated fuels.

5.1.2 Chemical Distribution and Material Balance of Chemical Composition

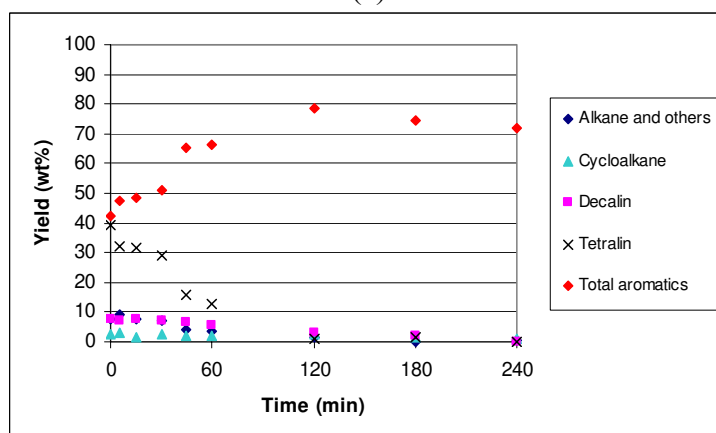
Product distributions of hydrotreated and saturated fuels were determined from GC/MS. Figure 5-5 and Figure 5-6 display the overall chemical changes during stressing hydrotreated and saturated fuels respectively. The major chemical composition of all fuel candidates is summarized in terms of alkanes (including small amounts of alkenes, alkynes and cycloalkenes), cycloalkanes, decalin, tetralin and aromatics (alkylbenzenes, naphthalene, and other aromatics) whereas other minor products such as indanes have been reported in Appendix C.2. All chemical compositions are reported as the weight percentages of remaining liquid.

Fresh EI-001, EI-002 and EI-003 are similar in the amount of total aromatics before the reaction occurred. In Figure 5-5 (a), the aromatics in EI-001 started to rise after a 30-minute stressing time and declined after 60 minutes to produce solid deposit corresponding to the result in Figure 5-4 (a). Most of the total aromatics are mainly naphthalene, followed by alkylbenzenes and multi-ring aromatics (Figure C-3 to Figure C-8 shown in Appendix C.2).

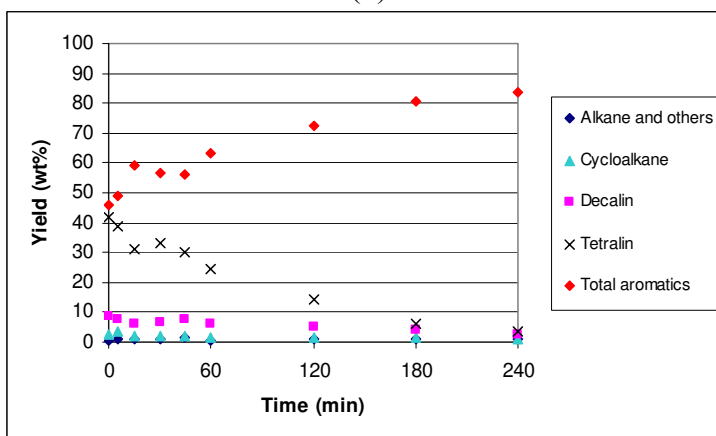
For stressed EI-002 (Figure 5-5 (b)), the increase in total aromatics in the time period of 15 to 120 minutes was significant. In contrast to total aromatic contents, tetralin substantially decreased as soon as the reaction started. After a 45-minute time period, the small amounts of alkanes, cycloalkanes and decalin were all converted to aromatics. Soon after 120 minutes, the trend of converting aromatics in the stressed hydrotreated LCO/RCO blend (EI-002) to final solids become similar to that of hydrotreated LCO (EI-001), but the deposition of solid was much slower. This might be the result of the higher amount of the hydrogen donor (tetralin) that helps stabilize the growth of polyaromatics.



(a)



(b)

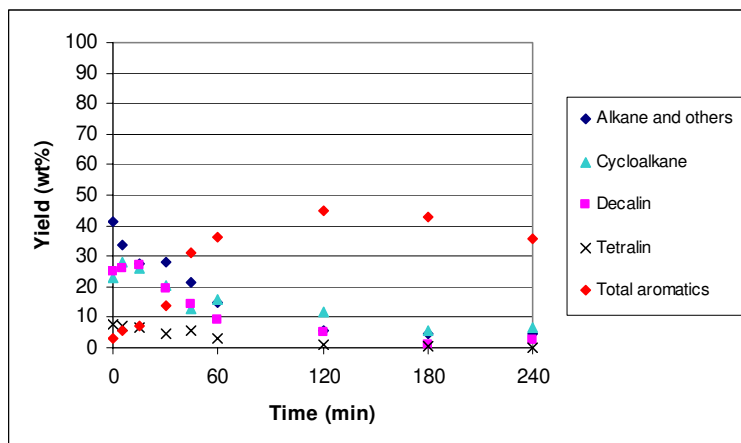


(c)

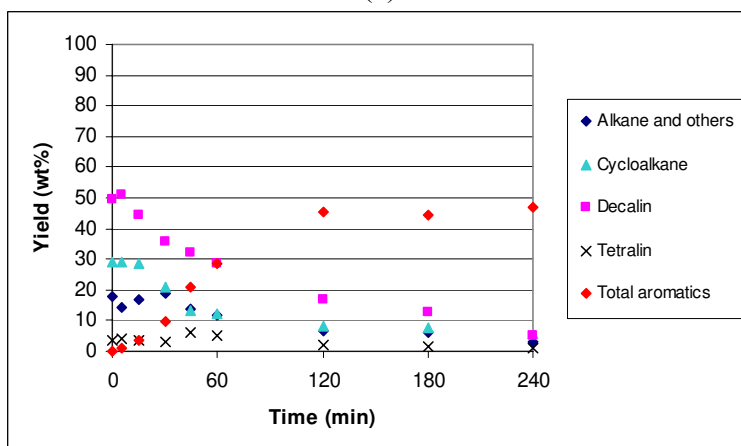
Figure 5-5: Chemical distribution of stressed (a) EI-001, (b) EI-002 and (c) EI-003 with increasing stressing time.

Tetralin in hydrotreated RCO (Figure 5-5 (c)) was also consumed, but at a slower rate than for the hydrotreated LCO/RCO blend (EI-002). But, the total aromatics continue to increase during a 240-minute reaction time. Most of the aromatics in the stressed products are mainly naphthalene, resulting in the precipitation of solid naphthalene after the completion of reaction.

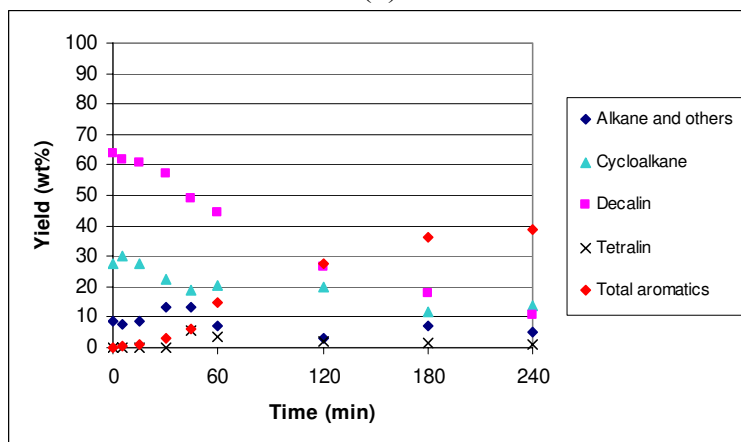
Similar to hydrotreated LCO and hydrotreated LCO/RCO blends, the total aromatic content in stressed saturated LCO (EI-004) in Figure 5-6 (a) also rose and then declined at the same time as solid precipitated out. In Figure 5-6 (b), the saturated LCO/RCO blend and saturated RCO, which are mostly comprised of thermally stable compounds such as decalin and cycloalkanes, continuously converted to aromatics along with solid deposits beginning 15 minutes after stressing. Tetralin in saturated LCO/RCO and RCO rose slightly around 45 minutes after stressing, probably as a result of decalin dehydrogenation. It also dehydrogenated further to naphthalene after 60 minutes. The major aromatic contents as a function of stressing time are naphthalene and alkylbenzenes. The increase in toluene and alkylbenzenes is shown as a sign of dehydrogenation of the major cyclohexane components.



(a)



(b)



(c)

Figure 5-6: Chemical distribution of stressed (a) EI-004, (b) EI-005 and (c) EI-006 with the increasing time.

5.1.3 Changes of Hydrogen Types during Stressing

A study of the distribution of hydrogen types by ^1H NMR spectroscopy has shown some agreement with the results from GC/MS. Figure 5-7 and Figure 5-8 give examples of the changes of hydrogen types determined from ^1H NMR spectra of EI-002 (hydrotreated LCO/RCO) and EI-005 (saturated LCO/RCO) stressed from 30 to 240 minutes. Aromatic hydrogen is dominant in EI-002, while EI-005 is highly aliphatic. Upon stressing, the aliphatic hydrogen of both samples has been converted to aromatic hydrogen with increasing residence time, but the increase in the production of aromatic hydrogen is faster for the EI-002 than the EI-005.

Figure 5-9 shows the regions of different chemical shifts, representing different hydrogen types. For hydrotreated LCO/RCO (EI-002), the significant increases in two-ring and/or multi-ring aromatics (region G) are very significant compared to other functional groups (Figure 5-9 (a)). The disappearance of all aliphatic and monoaromatic hydrogens also agreed with GC/MS results. However, there is no significant change for the E region, which represents aromatic methyl, alkynyl, methyl ketone and alcohol.

In Figure 5-9 (b), the conversion of aliphatic to aromatic hydrogens is significant in saturated LCO/RCO (EI-005). But the percentage of two-ring and/or multi-ring hydrogens remaining after 240-minute stressing is not as high as that in EI-002, which is highly dominated by naphthalenes.

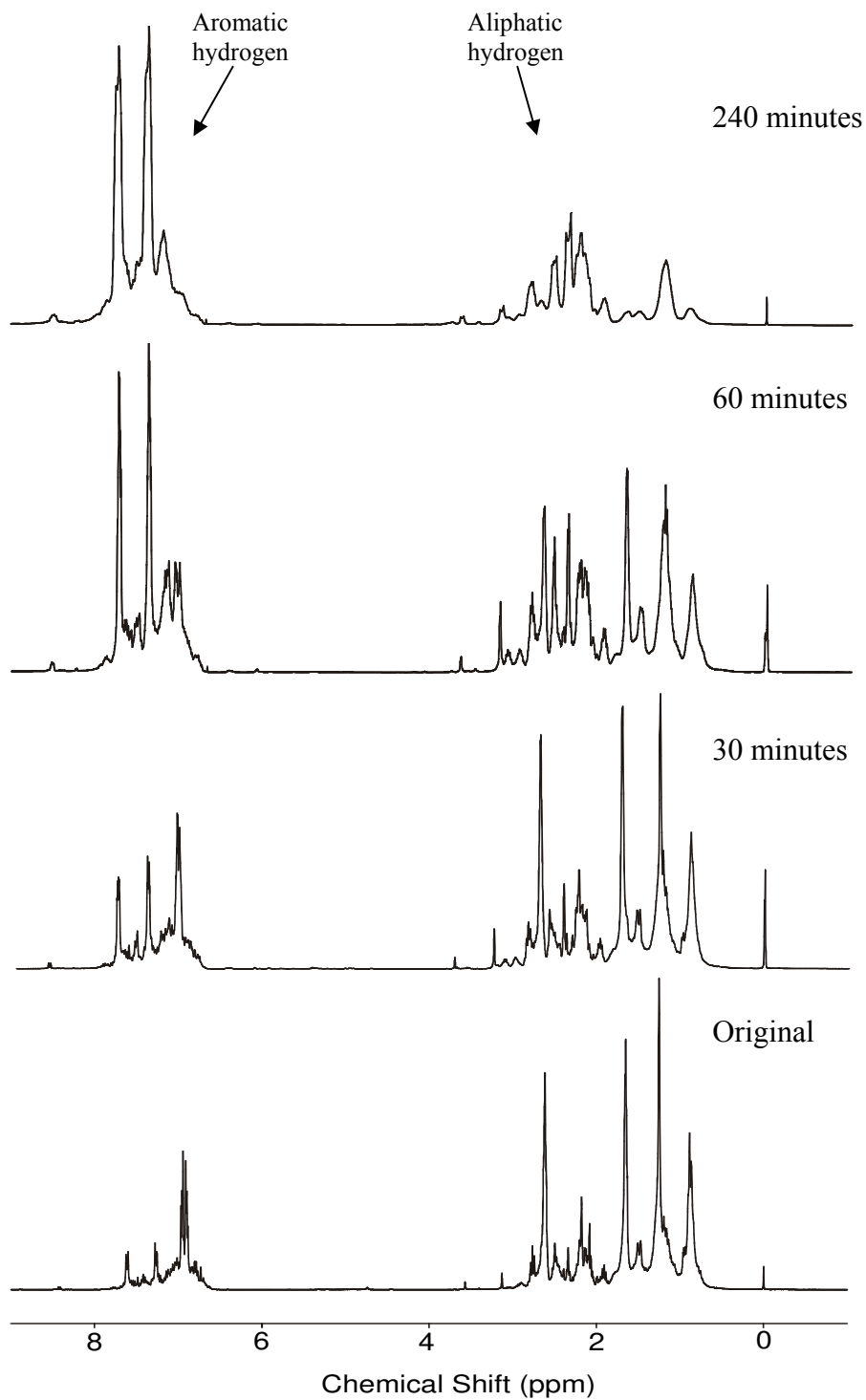


Figure 5-7: Changes in the hydrogen type of the ^1H NMR spectrum of the EI-002 (hydrotreated LCO/RCO).

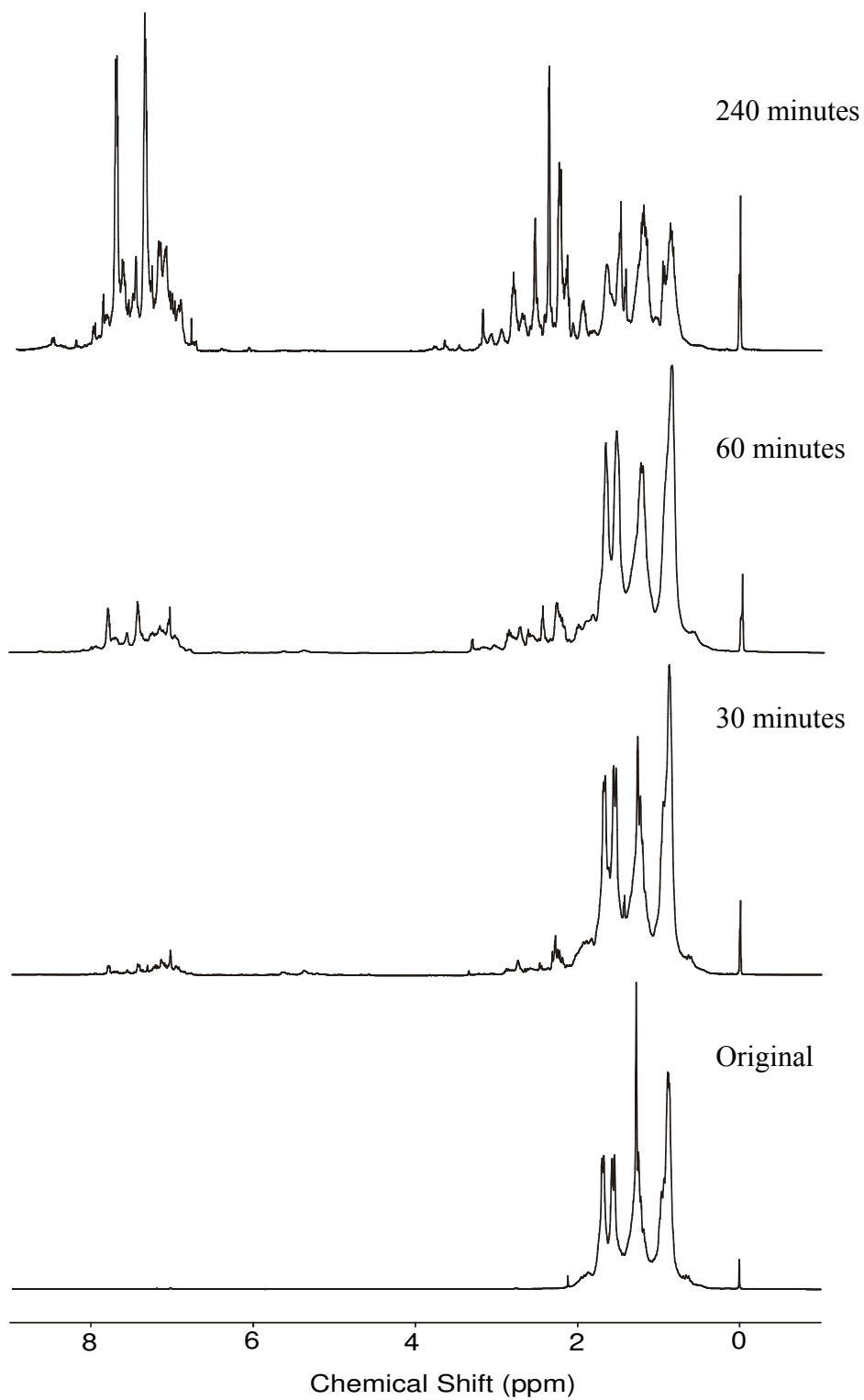
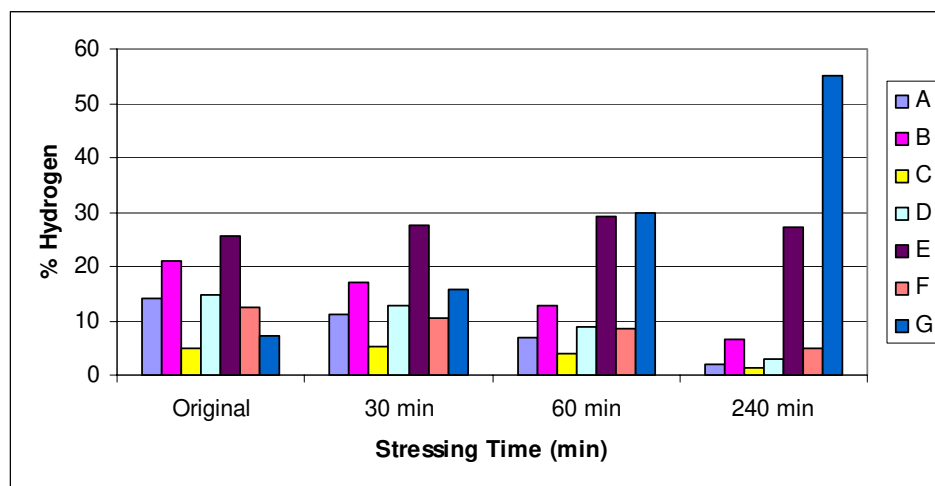
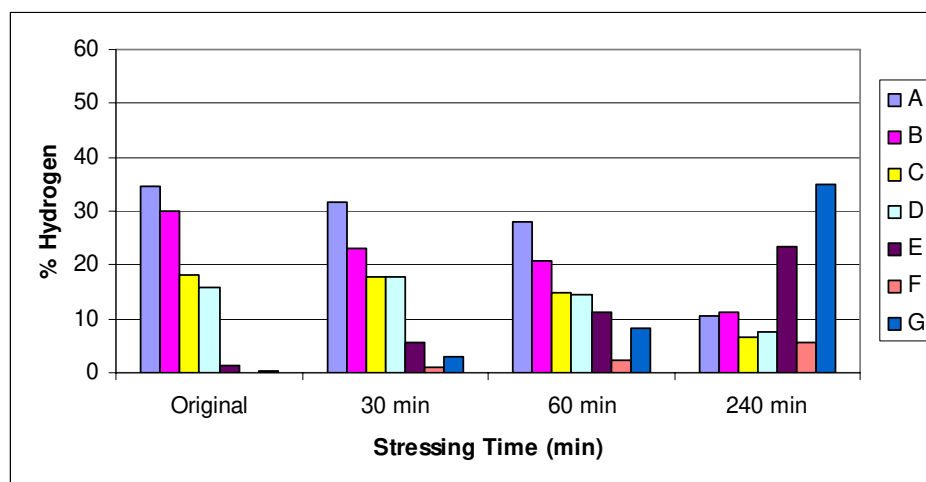


Figure 5-8: Changes in the hydrogen type of the ^1H NMR spectrum of the EI-005 (saturated LCO/RCO).



(a)



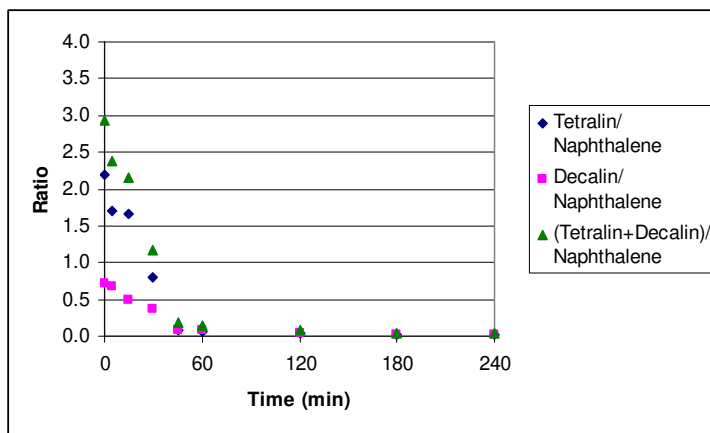
(b)

Figure 5-9: Percentages of different hydrogen types upon stressing (a) EI-002 or hydrotreated LCO/RCO and (b) EI-005 or saturated LCO/RCO.

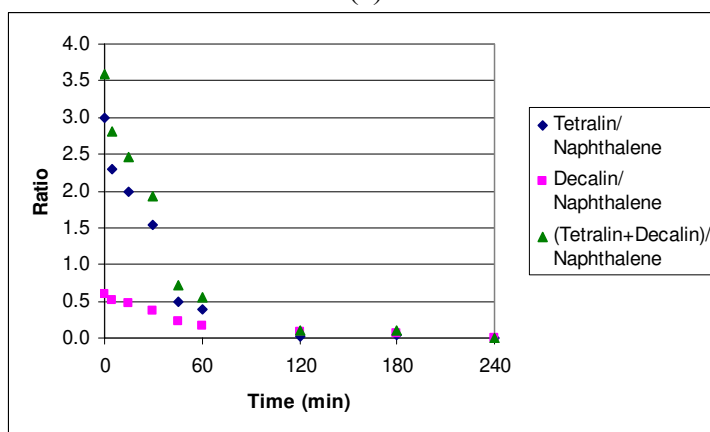
5.1.4 Conversion of Decalin and Tetralin to Naphthalene

Decalin, tetralin and naphthalene are predominant components in the study of pyrolytic stability of the coal-based jet fuels. Two supporting reasons are: (1) naphthalene is a main component in the feedstock (light cycle oil and refined chemical oil) and (2) decalin, tetralin and naphthalene can be interconverted at different pressure and temperature conditions [35, 51-55, 127, 128].

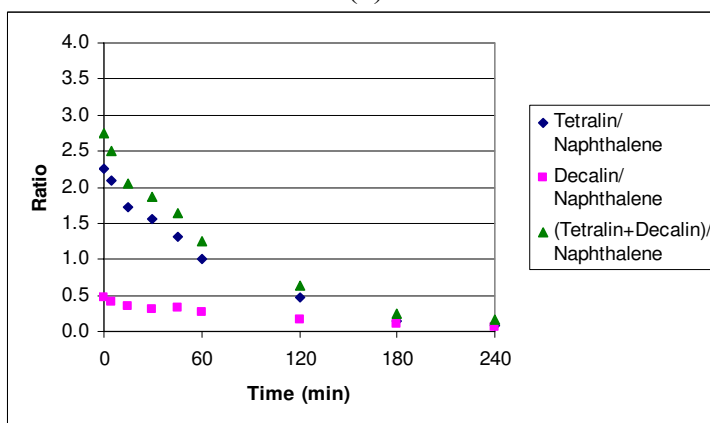
Figure 5-10 and Figure 5-11 display the ratios of tetralin/naphthalene, decalin/naphthalene and (tetralin+decalin)/naphthalene of stressed hydrotreated and saturated fuels, respectively. Tetralin played an important role in stabilizing radicals during pyrolytic stressing of hydrotreated fuels while decalin helped in improving stability of saturated fuels. From Figure 5-10, the tetralin/naphthalene and decalin/naphthalene ratios decreased rapidly and converged to zero after 45-minute and 120-minute stressings of EI-001 (hydrotreated LCO) and EI-002 (hydrotreated LCO/RCO), respectively. In the case of EI-003 (hydrotreated RCO), the ratios declined gradually to zero after stressing for about 240 minutes. The tetralin in EI-003 mostly dehydrogenated to naphthalene and resulted in an increase of naphthalene from 20% to about 30-40%. This result agrees with the discussion of solid formation in the previous section. The major stressed yield was naphthalene, not solid deposit. And, the dehydrogenation of tetralin to naphthalene yielded H \cdot , which capped radicals and slowed or even stopped the solid formation process. However, one problem that does exist with this fuel at high conversions of tetralin to naphthalene is that the naphthalene formation is too great and undesirable solid naphthalene begins to precipitate out of the fuel at room temperature [115].



(a)

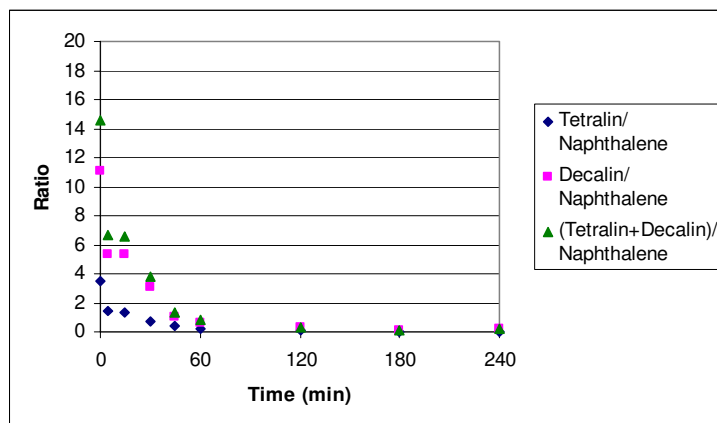


(b)

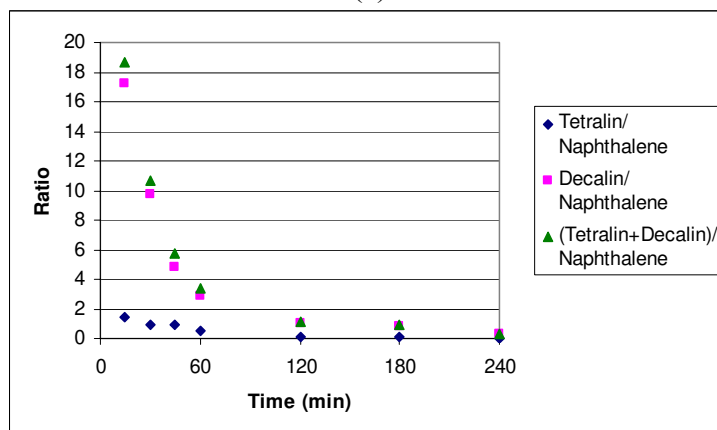


(c)

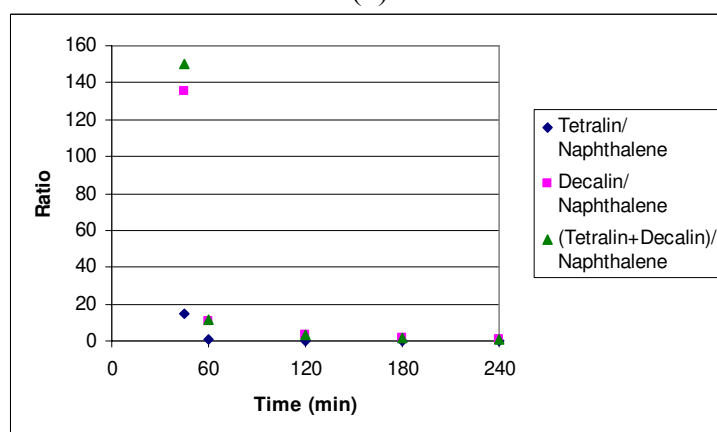
Figure 5-10: Comparison of tetralin/naphthalene, decalin/naphthalene and (tetralin+decalin)/naphthalene of stressed (a) EI-001, (b) EI-002 and (c) EI-003.



(a)



(b)



(c)

Figure 5-11: Comparison of tetralin/naphthalene, decalin/naphthalene and (tetralin+ decalin)/naphthalene of stressed (a) EI-004, (b) EI-005 and (c) EI-006.

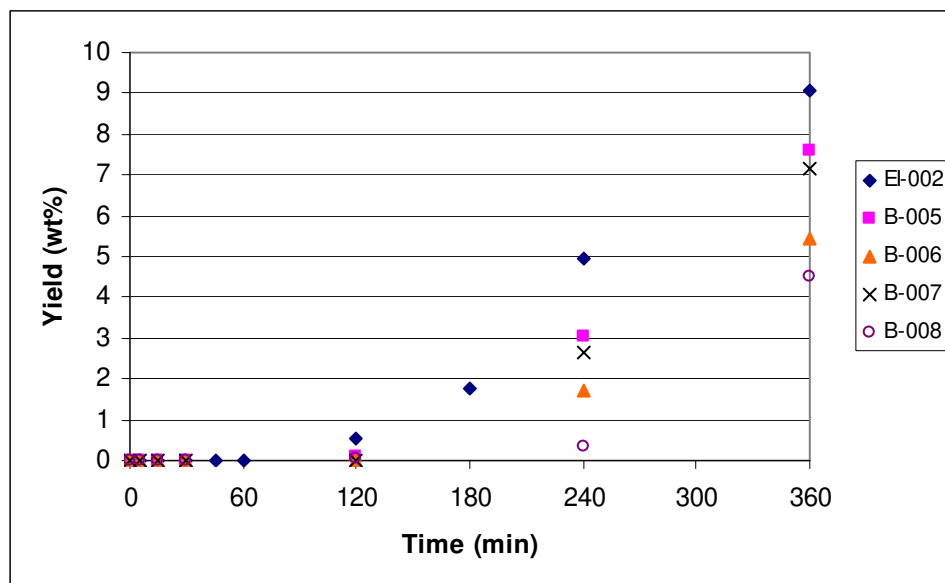
Fresh saturated fuels showed high ratios of decalin/naphthalene, and these ratios decreased as the fuels were stressed for a period of time. After a 30-minute stressing time, the decalin/naphthalene ratios of saturated LCO (EI-004) and saturated LCO/RCO (EI-005) have decreased and converged to zero, indicating a rapid rise of naphthalene concentration.

In stressed saturated RCO, during the first 0-30 minutes there was very little naphthalene and aromatics (Figure 5-6 (c) and Figure 5-11 (c)). For that period of time, the high decalin content also showed a superior ability of controlling naphthalene and total aromatic contents. However, the naphthalene started to be present after 30 minutes and then continued to increase as a result of decalin dehydrogenation.

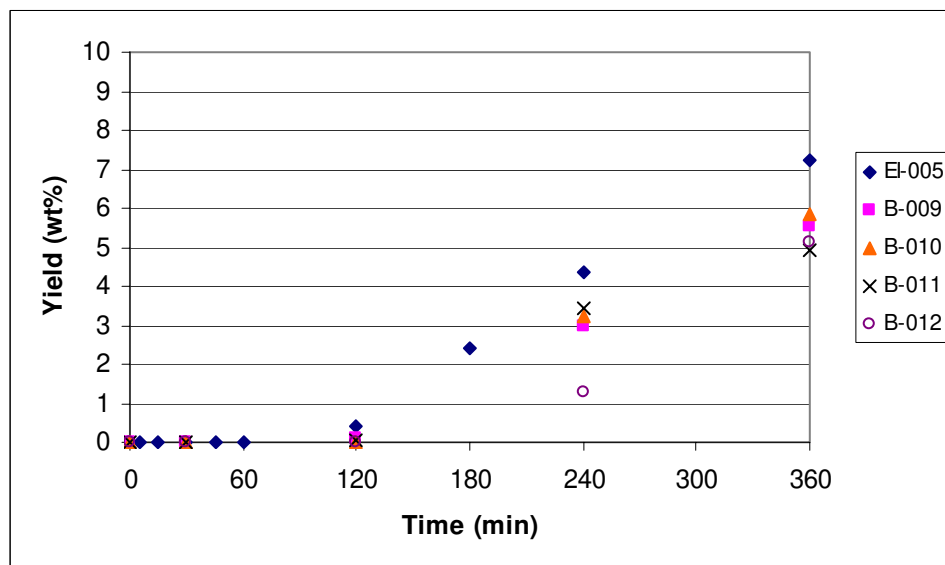
5.1.5 Addition of Decalin and Tetralin to Hydrotreated LCO/RCO and Saturated LCO/RCO

For improvement of pyrolytic stability, decalin and tetralin were added to existing coal-based jet fuel candidates to study their effects. About 10 and 20 wt% of decalin and tetralin were mixed with hydrotreated and saturated LCO/RCO blends (EI-002 and EI-005) and stressed in a 25-mL microautoclave at 480°C. The results are shown in Figure 5-12.

The solid started to form after stressing for 120 minutes for both hydrotreated and saturated blends, but saturated LCO/RCO showed a slower rate of deposition than the hydrotreated blend. After blending decalin and tetralin to the tetralin-rich hydrotreated LCO/RCO, the solid formation dramatically decreased, especially in the 20% tetralin blend.



(a)



(b)

Figure 5-12: Comparison of the solid deposit as the increase of time of (a) EI-002 and its blends and (b) EI-005 and its blends.

For the decalin-rich saturated LCO/RCO (EI-005), the extra decalin added also helped in inhibiting solid formation. The addition of tetralin to this fuel also improved the thermal stability, but not as well as the addition of decalin.

5.2 Thermal Stability Test of the First Generation Jet Fuel Candidates in Dynamic Condition

5.2.1 Carbon Deposit on Stainless Steel Surface

Roan *et al.* performed thermal stability tests in a flow reactor at 700°C and 700 psig for 7 hours [113, 114], as described in Chapter 3. The results of petroleum-based jet fuels and the first generation coal-based fuels are shown in Table C-2 [129]. The conclusions have been made as the following:

- JP-8 and JP-8+100 were quite stable in the thermal oxidative regime (150-250°C) but not in the pyrolytic regime.
- The pyrolytic stability (indicated by solid formation) of hydrotreated fuels is shown to have been improved by hydrogen donation from tetralin (the major component in hydrotreated fuels). But, a previous study has shown that the influence of dissolved oxygen was detrimental to the thermal stability of tetralin [45]. This is clearly seen by the rise in solid formation of hydrotreated RCO (EI-003), hydrotreated LCO/RCO blend (EI-002), and hydrotreated LCO (EI-001) during the oxidative regime temperatures of 150-250°C. For hydrotreated RCO, which contains more than 40% of tetralin, solid deposit formation was higher than 600 $\mu\text{g}/\text{cm}^2$.

- Saturated fuels (EI-004 to EI-006) displayed superior thermal stability throughout the temperature profile along the axial distance. Compared to saturated LCO/RCO (EI-005), saturated LCO (EI-004) showed better stability in the oxidative regime but tended to give poor pyrolytic stability. As shown in Table C-2, saturated RCO (EI-006) gave a significantly lower solid deposition rate throughout the temperature profile.

5.2.2 Carbon Deposit on Inconel 718 Surface

The results from thermal stressing on Inconel 718 alloy [116] are shown in Table C-3. Carbon deposit from stressing EI-003 (HDT RCO) is the highest among the jet fuel candidates while that of EI-001 (HDT LCO) is the lowest. It is possible to summarize that the components from petroleum stream (LCO) tend to inhibit solid deposition on Inconel 718 alloy surface while components from coal tar distillates (RCO) promote the deposition.

5.3 Comparison between Thermal Stability in Static and Dynamic Condition

In general, the thermal stability tests in batch and flow conditions cannot be compared. The system in a batch reactor had a long residence time and constant temperature over the entire test, but the flow system provided short residence time for fuel samples to flow across an increasing temperature. The circulation of fresh fuel results in better heat transfer, representing a system closer to a real heat exchanger.

As shown in Table C-2, all solid deposits of six fuel candidates, in both batch and flow systems, displayed higher pyrolytic stability than JP-8 and JP-8+100. Unlike the pyrolytic stability, the six fuel candidates' thermal oxidative stability (which can be quantified only in the flow test) has shown some variation. The hydrotreated fuels have significant amounts of solid at temperatures around 150-250°C, whereas the saturated fuels produced a very low amount of solid. The oxidative regime cannot be studied in the batch reactor tests as they were conducted in this study, because the batch reactor tests were run only at 480°C.

5.4 Thermal Stability Test of the Second Generation Jet Fuel Candidates using Quartz Crystal Microbalance (QCM)

From the study in a previous section, most of the coal-based jet fuels, both hydrotreated and saturated fuels, have shown excellent pyrolytic stability relative to conventional fuels such as JP-8. However, the hydrotreated LCO/RCO blend is likely to be developed for the future of JP-900 as a result of its economic feasibility and available hydrotreater facilities at the United Refining Company [130].

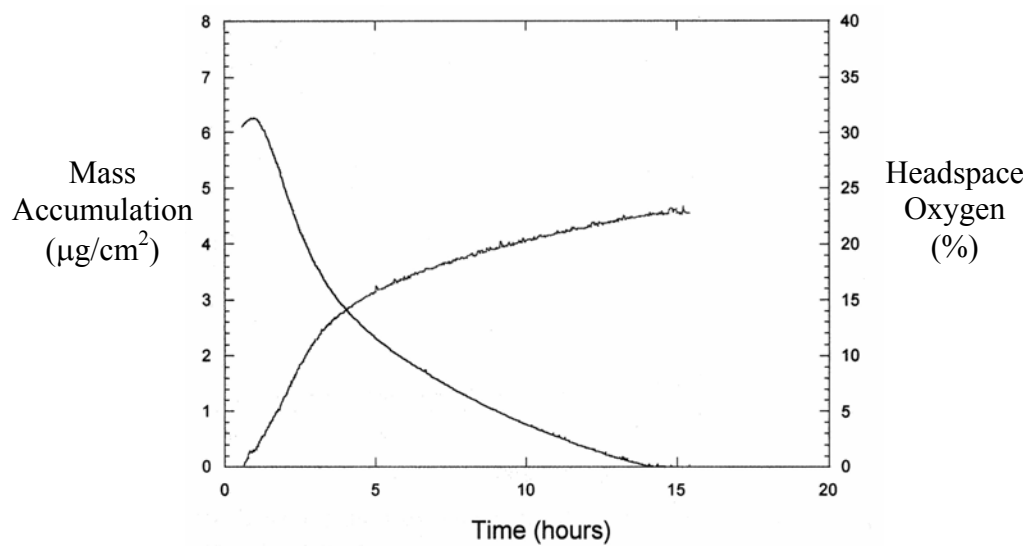
One of the major challenges for the hydrotreated jet fuels, the composition of which is dominantly tetralin, is to make them resistant to thermal oxidative degradation. Thus, a study of thermal oxidative stability of second-generation hydrotreated jet fuels was performed using a quartz crystal microbalance (QCM) technique. All twenty-four jet fuel samples were tested by the University of Dayton Research Institute [7], and the results have been summarized in Table C-4.

Under the conditions in the QCM system, the fuels that produced surface deposits $< 3 \mu\text{g}/\text{cm}^2$ are considered light depositors. Fuels producing 3 to $8 \mu\text{g}/\text{cm}^2$ are medium depositors, and those producing $> 8 \mu\text{g}/\text{cm}^2$ are heavy depositors [7]. Fast oxidizing fuels consume oxygen in 5 hours, medium oxidizers in 5 to 12 hours, and slow oxidizers in >12 hours [7].

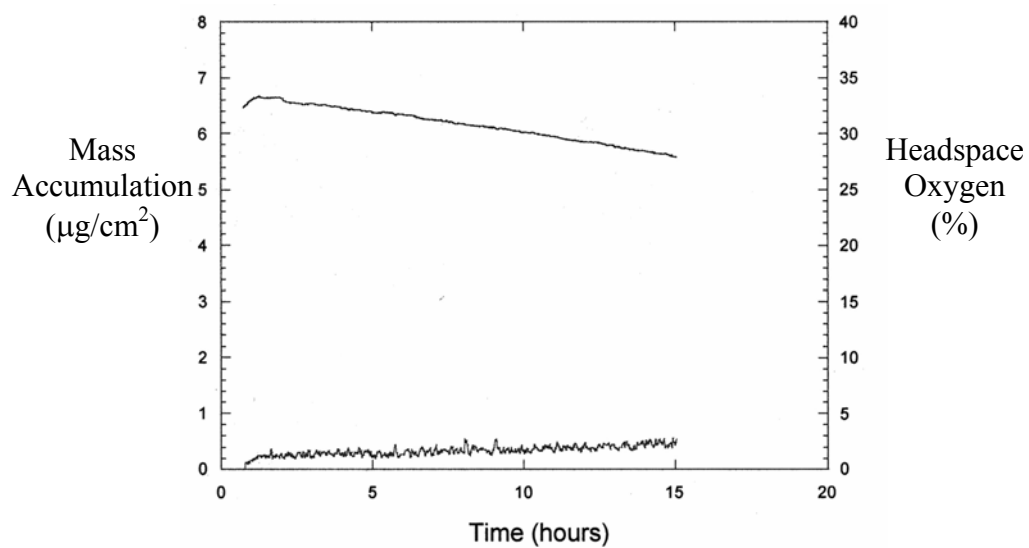
In Figure 5-13, JP-8 has given moderate to high deposition and slow to moderate oxidation. JP-8+100 has shown a better result of slow oxidation due to the antioxidant in it, and very low deposition due to the dispersant.

Figure 5-14 displays the QCM results of three coal-based jet fuels: EI-025, EI-029 and EI-007. As shown in previous work by Coleman *et al.* [45], tetralin was stable in the pyrolytic regime, but decomposed to form insoluble black deposits at temperatures around 250°C . The results from this work agreed with previous work. All fuel samples that contain high concentrations of tetralin consumed oxygen very rapidly, and this rapid oxidation might affect the long-term storage stability of these fuels.

For the oxidative deposition, the three fuel samples showed variation in surface deposits, even though the tetralin concentrations in those samples are similar. As a result, no direct correlation between the oxidative stability (Table C-4) and tetralin concentration (Table 4-3) can be established. The involvement of other components in these complex mixtures, even those present in a small amount, could play a big role in stability. However, one conclusion that can be drawn from this result is that some hydrotreated coal-based jet fuels containing high tetralin concentrations can yield acceptable oxidative solid deposition. As seen from Table C-4, twelve out of twenty fuel samples were light depositors.



(a)



(b)

Figure 5-13: Plots of QCM headspace oxygen and mass accumulation at 140°C for (a) JP-8 and (b) JP-8+100.

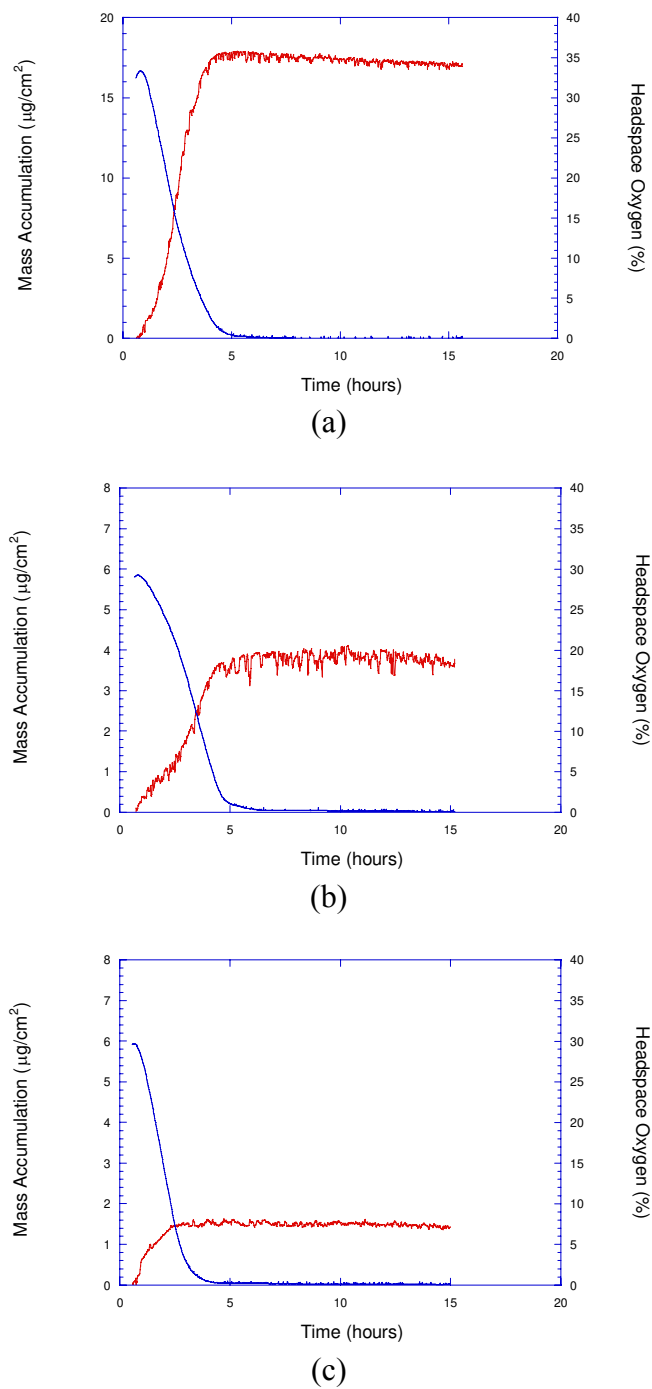
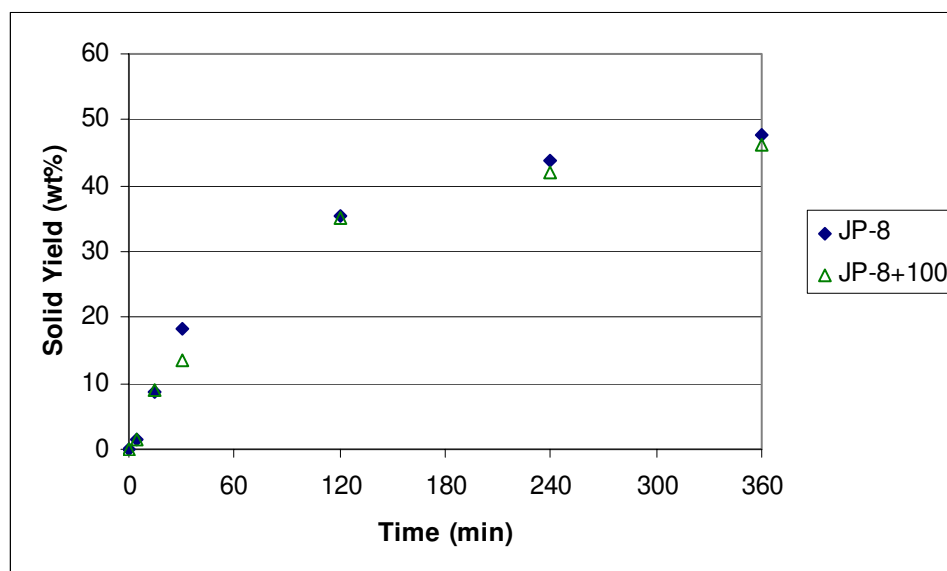


Figure 5-14: Plots of QCM headspace oxygen and mass accumulation at 140°C for three coal-derived jet fuels: (a) EI-025, (b) EI-029 and (c) EI-007 [7].

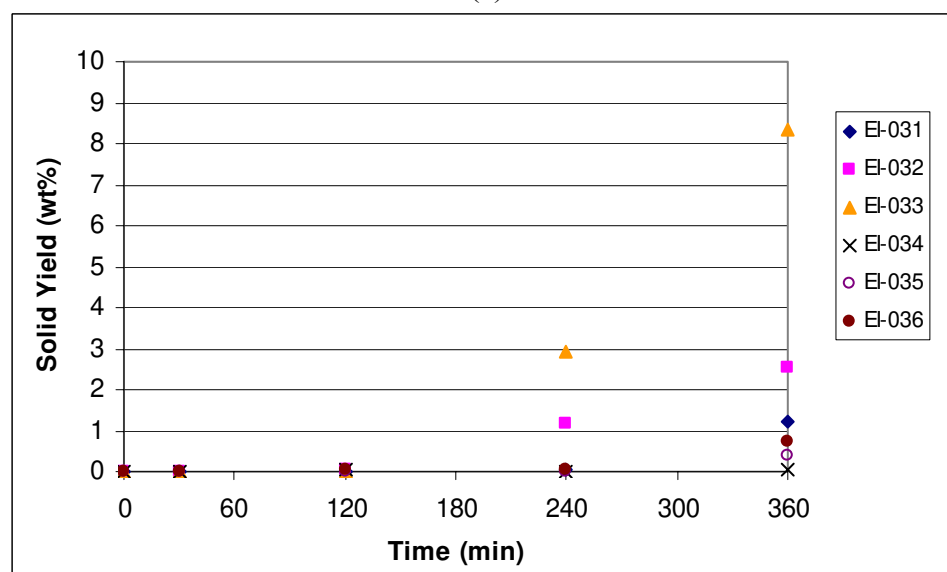
5.5 Thermal Stability Test of the Third Generation Jet Fuel Candidates in Static Conditions

The third series of candidate jet fuels was also produced from hydrotreating of the LCO/RCO 1:1 and 1:3 blends in the current JP-900 selection process (Table 3-1). To observe the boiling point effects on pyrolytic stability, the products were fractionated to produce 180-270°C, 180-300°C and 180-320°C boiling point cuts for each blend [104]. To select the prototype thermally stable jet fuels, the jet fuel boiling range is one of the important parameters to control the jet fuel's chemical composition, which is the key for thermal stability improvement.

All of the third-generation hydrotreated fuels were stressed in the 25-mL microautoclave. The results have shown that all of them are more thermally stable than JP-8 and JP-8+100, as indicated by solid yield and amount of remaining liquid (Figure 5-15 and Table C-1). To compare thermal stability between two types of blends, the hydrotreated LCO/RCO 1:3 blends showed higher stability, that is, no solid deposition, as they contain more tetralin and methyltetralin and fewer alkanes than the 1:1 blends. In the boiling range of 180-270°C for both hydrotreated blends, the presence of tetralin and methyltetralin, which is larger than the other two fuels, results in higher stability. Unlike the case of hydrotreated 1:3 blends, the 1:1 blends showed a trend of decreasing tetralin and decalin and increasing aromatics (3+ rings) with the increase in final boiling point. With the increase in aromatic content, the solid also tends to increase, as shown in Figure 5-15 and Table 4-4.



(a)



(b)

Figure 5-15: Comparison of the solid deposit with time between (a) petroleum-based jet fuel and (b) third generation of coal-based jet fuels.

Chapter 6

Properties Testing

The testing of selected physical and chemical properties of conventional and coal-based jet fuels was carried out. These results are reported and discussed in the following subsections.

6.1 Results and Discussion of H/C Ratio

Figure 6-1 shows the H/C ratio of petroleum-based and coal-based jet fuels. These results are in good agreement with the chemical composition of the fuels. Petroleum-based jet fuels, consisting of high concentrations of alkanes, have high H/C ratios while the hydrotreated jet fuels generally give lower H/C ratios. However, saturated fuels, dominated by cycloalkanes have shown high H/C ratios.

The correlation between H/C ratio and chemical composition will be discussed further in Chapter 7.

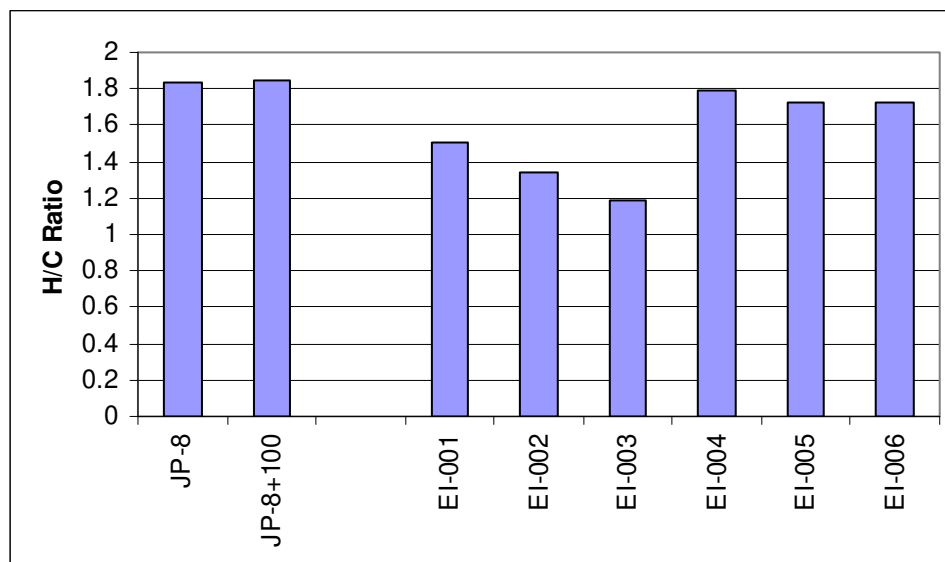
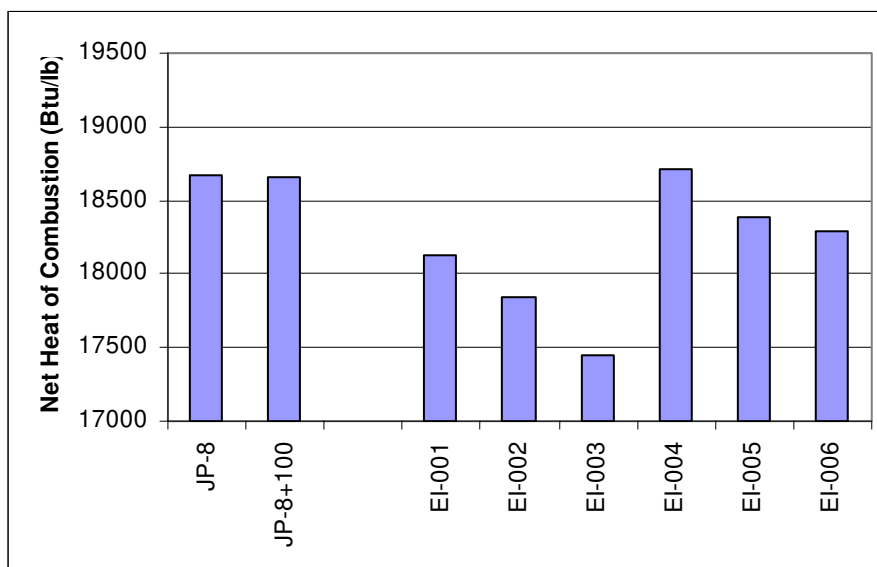


Figure 6-1: H/C ratios of petroleum-based and first generation coal-based jet fuels.

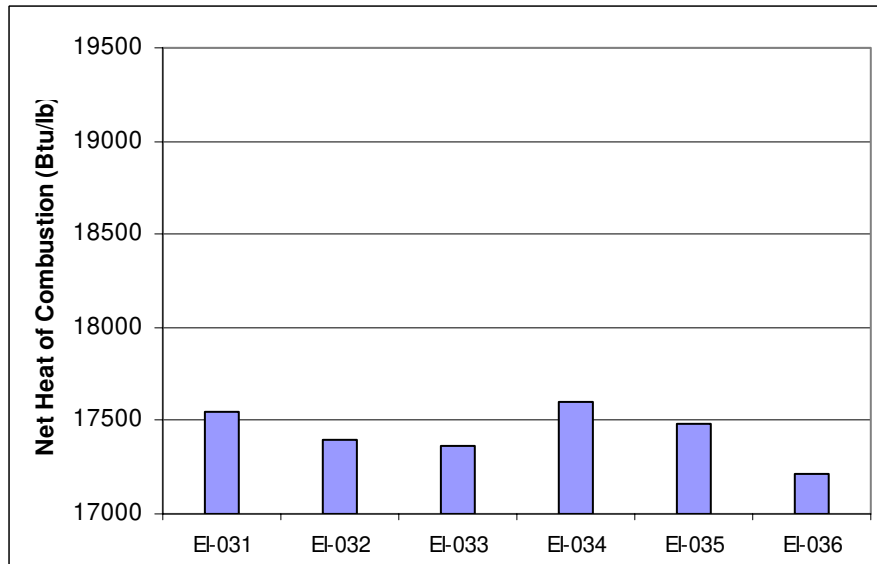
6.2 Results and Discussion of Heat of Combustion Test and Energy Density

Figure 6-2 shows the heat of combustion of the fuels. It is clearly shown that alkanes have a higher calorific value than other hydrocarbons with the same carbon number [131]. JP-8 and JP-8+100 have high heats of combustion since they are highly paraffinic mixtures. For low-alkane concentrations like coal-based jet fuels, the values of net heat of combustion are lower. Table 6-1 gives information on heat of combustion for pure compounds such as octane and C_{10} compounds. In addition, the alkanes of small carbon numbers (octane in this case) give higher heat of combustion than do those higher carbon numbers (decane) as heat of combustion varies directly with hydrogen content

[78]. For the same carbon numbers, the heat of combustion also increases with hydrogen content.



(a)



(b)

Figure 6-2: Net heats of combustion of (a) petroleum-based and first generation coal-based jet fuels and (b) third generation coal-based jet fuels.

Table 6-1: Heat of combustion of pure compounds from API Technical Data Book [131] and Perry's Chemical Engineers' Handbook [120].

Fuel	Q_g (Btu/lb) measured	Q_n (Btu/lb) calculated	Q_n (Btu/lb) at 77°F from [120, 131]	H/C
<i>n</i> -Octane	N/A	N/A	19098	2.25
<i>n</i> -Decane	20390	20376	19019	2.2
Decalin	19370 (mixture of cis and trans)	19358 (mixture of cis and trans)	18323 (cis), 18288 (trans)	1.8
Tetralin	18330	18322	17423	1.2
Naphthalene	N/A	N/A	16707	0.8

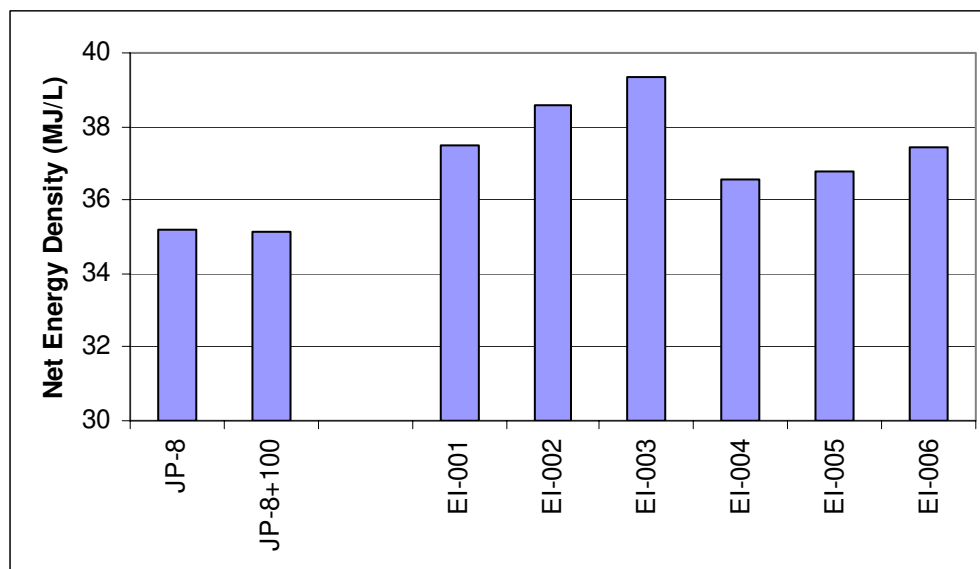
The jet fuel specification in Table 2-3 gives the minimum limit of net heat of combustion to be 18,400 Btu/lb. Net heats of combustion of only JP-8, JP-8+100, EI-004 (saturated LCO) and EI-005 (saturated LCO/RCO) exceed the specification, with the values 18,676, 18,653, 18,706 and 18,383 Btu/lb respectively. All hydrotreated fuels are lower in net heat of combustion, especially EI-003 (hydrotreated RCO) in Figure 6-2 (a). By blending the feedstock with LCO (which has a relatively high hydrogen content) and undergoing hydrotreatment, the heat of combustion values can be increased and the aromatic contents of hydrotreated and saturated products will be reduced; however, the addition of LCO also enhances the ability to produce solid deposit and gas. As a result, one can summarize that a compromise must be made between thermal stability and composition, and this information can be obtained from a correlation of the jet fuel heats of combustion and their compound classes, which will be discussed in the next chapter.

In Figure 6-2 (b), the net heats of combustion of six fuel candidates can be seen not to differ greatly from each other, as a result of their similarity in aromatic contents.

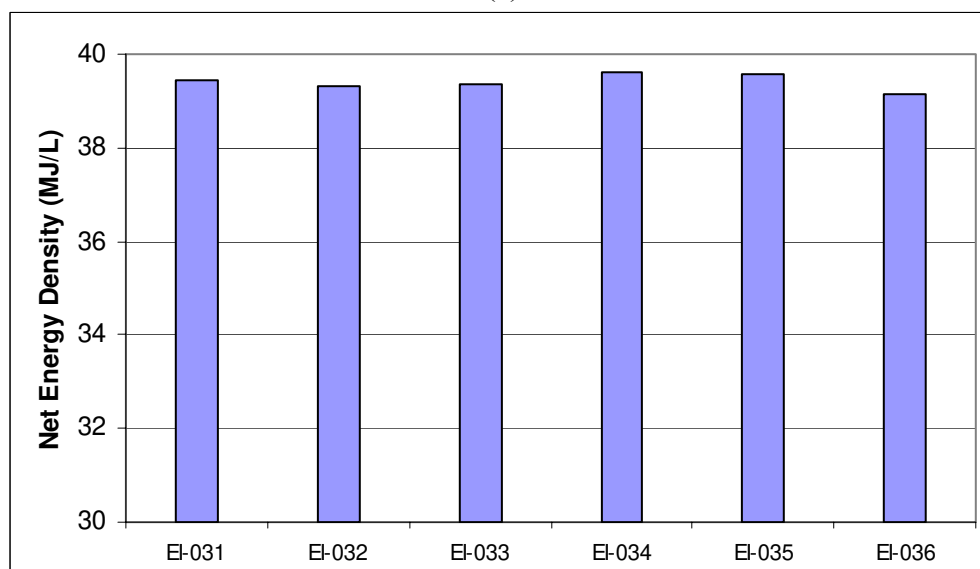
But, the high-aromatic fuels with the 180-320°C cut point give a low value of heat of combustion, in agreement with their low hydrogen content.

As discussed in Chapter 2, the energy density results shown in Figure 6-3 have been calculated from values of net heat of combustion and specific gravity. It is obvious that the energy density shown in Figure 6-3 (a) rose with fuel density, and that the hydrotreated fuels show an advantage over the rest of the fuels. But, the energy density of hydrotreated fuels in Figure 6-3 (b) tended to have the same trend as heat of combustion, in agreement with their similar densities. In this work, the energy density values of hydrotreated coal-based jet fuels are in the range of 39-40 MJ/L.

However, there is as yet no specification for JP-900's energy density. If one of hydrotreated coal-based jet fuels is selected for the future JP-900, there may need to be a trade-off with heat of combustion on a weight basis. This combustion property is very important and has to be considered along with other properties such as smoke point.



(a)



(b)

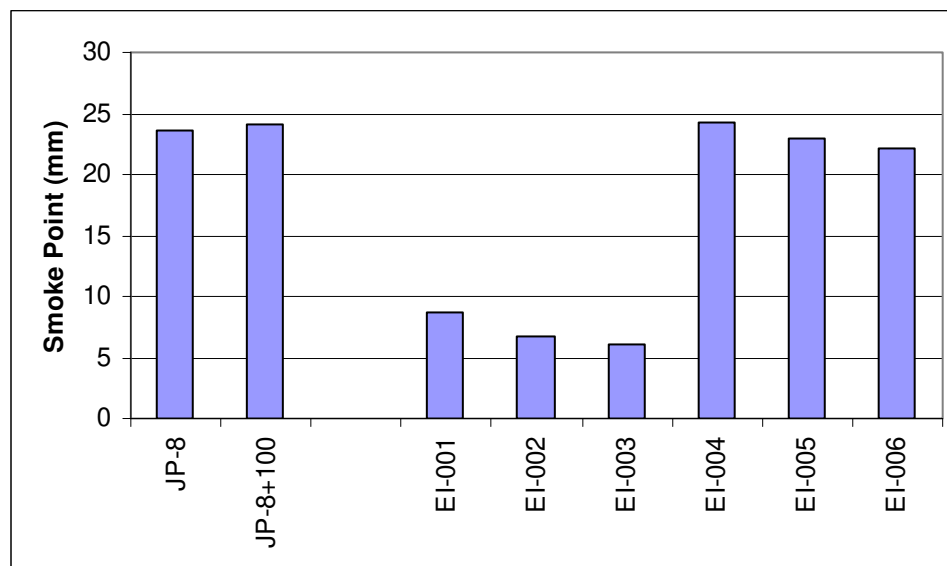
Figure 6-3: Net energy densities of (a) petroleum-based and first generation coal-based jet fuels and (b) third generation coal-based jet fuels.

6.3 Results and Discussion of Smoke Point Test

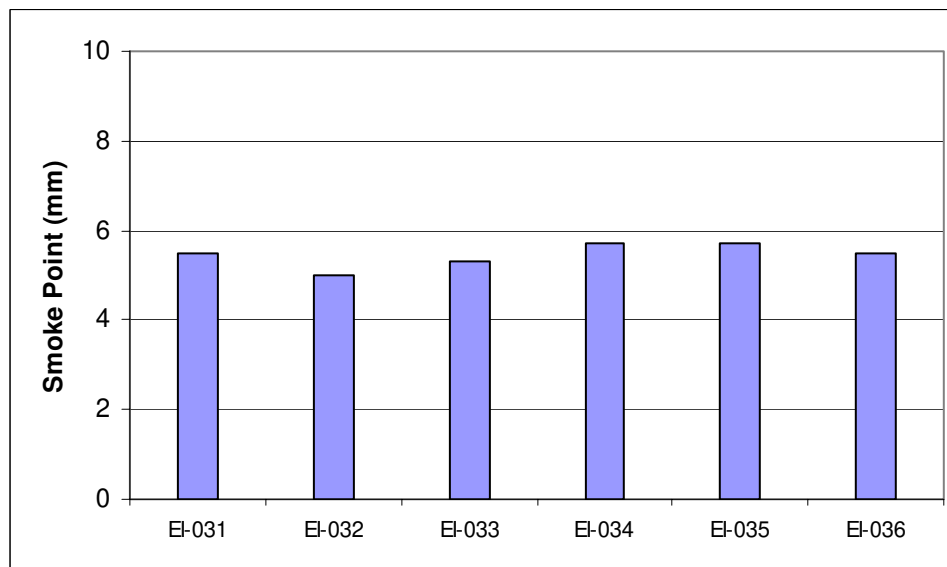
The other problem associated with high aromatic contents is low smoke point, resulting in high sooting tendencies and emissions [132], as seen from tests with the hydrotreated fuels shown in Figure 6-4 (a) and (b). The hydrotreated fuels have aromatics as a major component, and the hydrotreated fuel smoke points were all lower than 10 mm. The specification for minimum smoke point, 19 mm [13, 69], was achieved only by the saturated fuels: 24.3 mm for EI-004, 23.0 mm for EI-005 and 22.1 mm for EI-006. Compared with petroleum-based jet fuels, EI-001 also gave the highest smoke point, indicating that it is cleanest burning and would have the lowest emissions.

6.4 Results and Discussion of Flash Point Test

In Figure 6-5, all coal-based jet fuel flash points meet the ASTM D 1655 specification, which is a minimum of 100°F. All coal-based jet fuels had flash points in the range 160-180°F for hydrotreated fuels and 140-150°F for saturated fuels, while the petroleum-based jet fuel gave flash points around 120°F. There is not much variation among the third-generation coal-based jet fuels due to the similar aromatic contents. The results have shown that the fuels with high aromatics tended to give high flash points. And, these results agree with the data from API Technical Data Book [131]. For example, the flash points of decalin, tetralin and naphthalene are 136, 160 and 176°F, respectively [131]. Thus, it can be summarized that flash point varies directly with the aromatic contents.

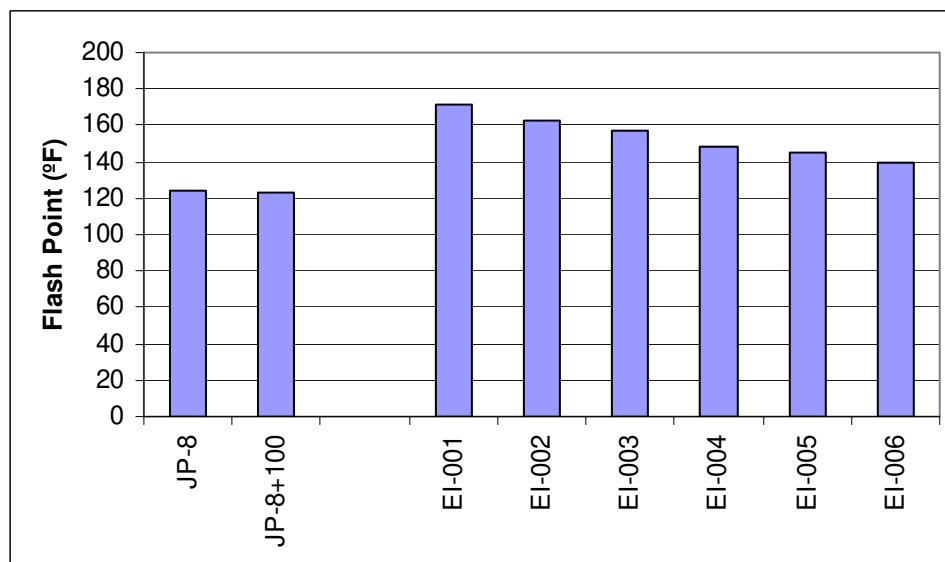


(a)

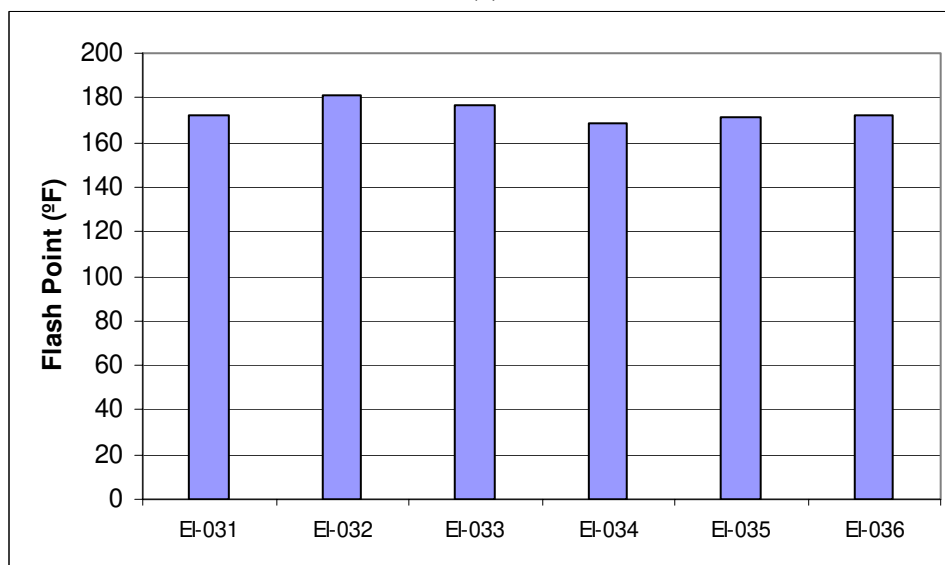


(b)

Figure 6-4: Smoke points of (a) petroleum-based and first-generation coal-based jet fuels and (b) third-generation coal-based jet fuels.



(a)



(b)

Figure 6-5: Flash points of (a) petroleum-based and first-generation coal-based jet fuels and (b) third-generation coal-based jet fuels.

6.5 Results and Discussion of Viscosity Test

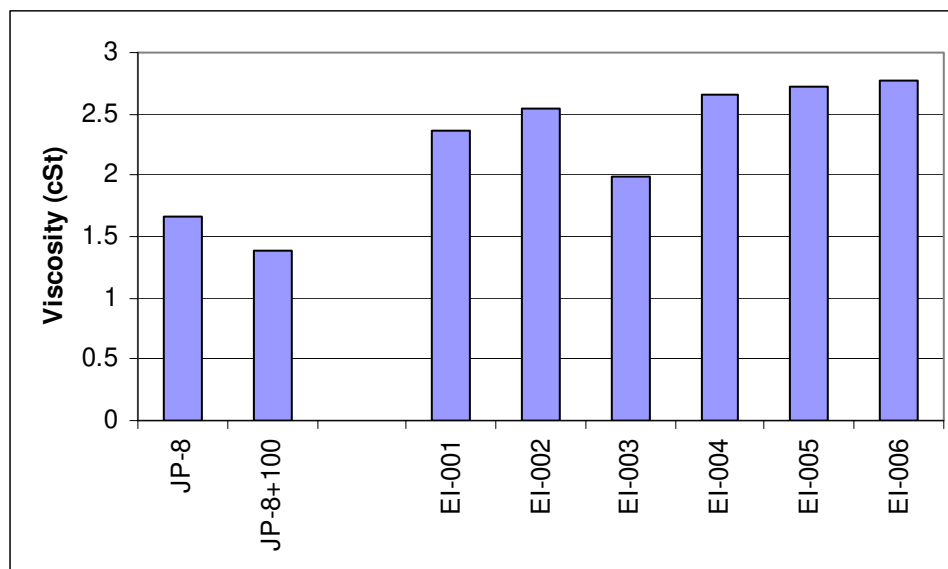
The results shown in Figure 6-6 cannot explain the effects of chemical composition or compound classes on the viscosity of each fuel, due to the variation in viscosity results. In comparison, conventional fuels like JP-8 and JP-8+100 have the lowest viscosities, indicating the highest abilities to flow at a given temperature. But, there is a trend to explain why saturated fuels have very much higher viscosities than the hydrotreated fuels, especially EI-003 (hydrotreated RCO). The presence of alkanes, cycloalkanes and aromatics did not show obvious effects on the three groups of fuels.

According to Riazi's work [85], the key factor to the determination of viscosity is molecular weight and boiling point of the fuel sample. Table 6-2 also shows that the viscosity increases with the molecular weight for the compounds of same carbon numbers, for example C₆ (cyclohexane and benzene) and C₁₀ (decane, tetralin and naphthalene). The exception of this statement is the case of decalin. Viscosities of both *cis*-decalin and *trans*-decalin are extremely high compared to pure compounds of the same carbon number or similar molecular weight. In general, the viscosities of alkanes are very low compared to cycloalkane and aromatic compounds of the same carbon number, even though they have the highest molecular weight of all. However, one can still summarize that the saturated fuels, consisting of high decalin and cycloalkane concentrations, are likely to have poor fluidity. And, hydrotreated RCO, which is composed of high percentages of tetralin and naphthalene, tended to flow better. The hydrotreated fuels of the cut point 180-320°C that have multi-ring aromatics have shown higher viscosity than the rest (Figure 6-6 (b)).

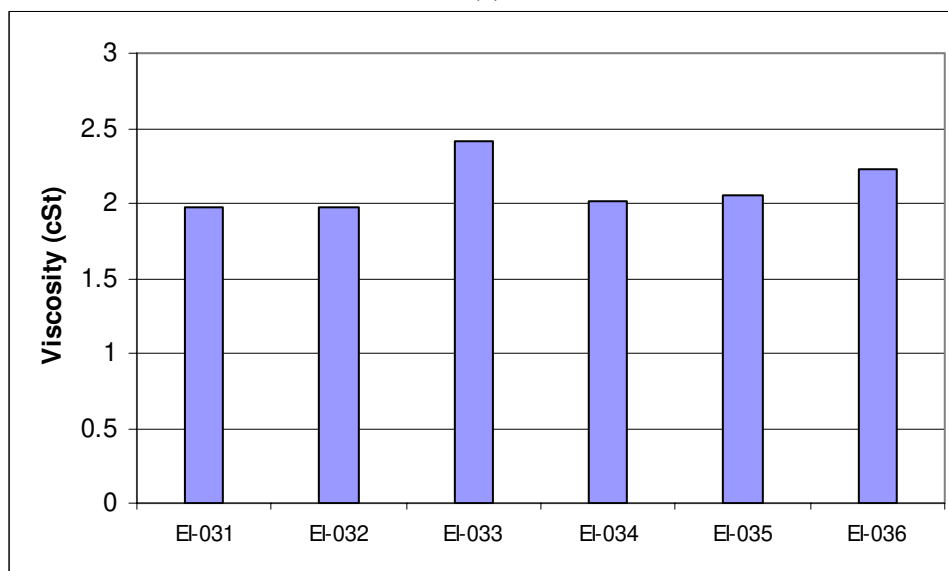
The specification of viscosity has been given as maximum 8.0 cSt at -20°C (-4°F) [13], but in the Saybolt universal viscosity test equipment that is available in The Energy Institute laboratories, the measurement was performed at a fuel temperature of 100°F. Kerosene, representing the petroleum-based JP-8 and JP-8+100, shows its kinematic viscosity at -4°F to be 5.1 cSt (obtained from a nomograph for viscosities of liquids at 1 atm in Perry's Chemical Engineers' Handbook [120]). This reference confirms that JP-8 and JP-8+100's viscosities are not over 8 cSt and pass the specification.

Table 6-2: Viscosities and freezing points of some compounds from API Technical Data Book [131].

Compounds	Molecular weight	Kinematic viscosity (v) (cSt) at 100°F (37.8°C) [131]	Kinematic viscosity (v) (cSt) at 210°F (37.8°C) [131]	Freezing points (°F)
Benzene	78.11	0.59	N/A	41.96
Cyclohexane	84.16	0.94	N/A	43.80
Octane	114.23	0.64	N/A	-70.18
Naphthalene	128.17	N/A	0.77	176.52
Tetralin	132.20	1.66	0.76	-32.35
<i>cis</i> -Decalin	138.25	2.66	1.09	-45.36
<i>trans</i> -Decalin	138.25	1.82	0.85	-22.86
Decane	142.28	1.01	0.55	-21.36
Undecane	156.31	1.26	0.64	-14.07
Dodecane	170.34	1.54	0.75	14.75
Eicosane	282.55	5.39	1.98	97.57



(a)



(b)

Figure 6-6: Viscosities of (a) petroleum-based and first generation coal-based jet fuels and (b) third generation coal-based jet fuels.

It is not practical to estimate the viscosity of the fuel sample at -4°F because most of its compounds are solid at this temperature. Naphthalene is solid at room temperature, as its freezing point is about 176°F . Thus, it has no fluidity at -4°F , which is the temperature for viscosity measurement required by specification. This situation also applies to cyclohexane (FP = 43.80°F), benzene (FP = 41.96°F), and 2-methylnaphthalene (FP = 94.24°F), but not to *cis*-decalin (FP = -45.36°F), *trans*-decalin (FP = -22.68°F), tetralin (FP = -32.35°F) and 1-methylnaphthalene (FP = -22.86°F). So, the fluidity of the fuel has yet to be worked out in terms of both fuel's viscosity and freezing point to meet the specification. And, the overall effects have to be considered rather than each individual one because the fuels are complex mixtures.

6.6 Results and Discussion of Cloud Point Test

The cloud point is selected to describe the low-temperature property of fuel samples due to the availability of equipment and a coolant. All tests have been performed by Scott Berkhouz [121]. In Figure 6-7, the EI-003 (hydrotreated RCO) has the lowest cloud point, followed with EI-006 (saturated RCO) while the cloud points of EI-001 (hydrotreated LCO) and EI-004 (saturated LCO) are over -50°F . The low cloud point of EI-003 indicates that the naphthalene and 2-methylnaphthalene, which have high freezing points (above 90°F) did not affect the overall low-temperature property of the fuel. This cloud point result, together with the viscosity result, shows the highest fluidity for hydrotreated RCO among the coal-based fuels.

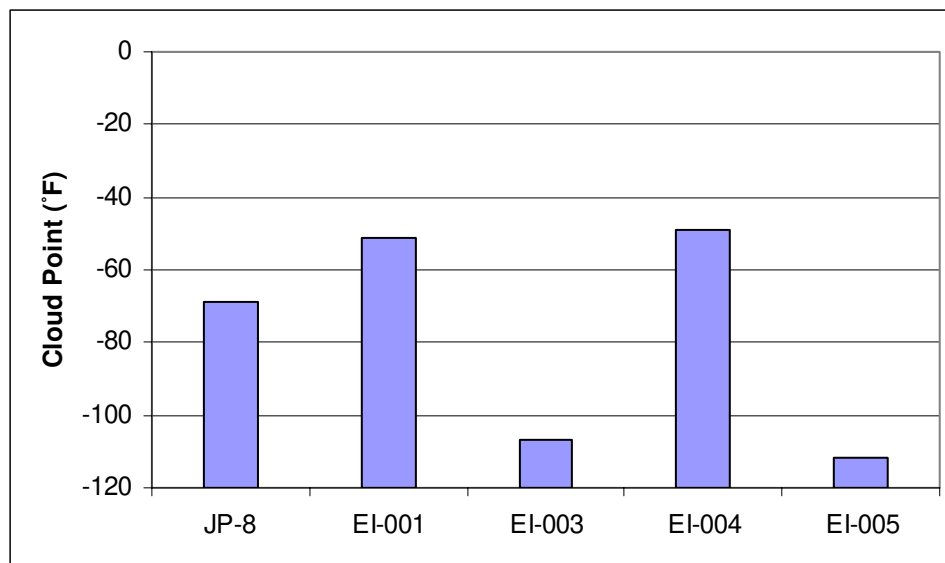


Figure 6-7: Cloud points of petroleum-based and first-generation coal-based jet fuels.

6.7 Results and Discussion of Combustion Tests

Results of combustion tests performed by Silvano Saretto are summarized in Figure C-9 and C-10. The emissions and soot volume fractions of JP-8 and third-generation jet fuels, EI-037 and EI-038, are compared. Coal-based jet fuels have shown higher NO_x emission but lower CO emission than the JP-8.

Considering soot formation, both EI-037 and EI-038 yielded much higher soot volume fractions (in ppm) than the JP-8 did at the same equivalence ratio. This agrees with the smoke point test results because soot volume fraction is a function of smoke point and H/C ratio [108].

6.8 Summary of Thermal Stability, Properties and Combustion Test

To this point, the most important factor for developing a formula of JP-900 would be aromatic content, including hydroaromatics such as tetralin, which helps improve thermal stability in pyrolytic regime but tends to give a low smoke point, resulting in high sooting tendencies and emissions [132]. The hydrotreated fuels appear to be low in net heat of combustion due to high aromatic and low paraffinic concentration. However, with the higher aromatic content, the fuels' density and energy density are significantly higher. A heavy fuel of high energy density is desirable when storage volume limits fuel capacity [78]. For fluidity properties, hydrotreated fuels are likely to flow better than saturated fuels, which contained a lot of viscous decalins. EI-003 has shown the best viscosity property among the rest.

The current aromatic content in conventional jet fuel is about 25 volume% [13, 69]. However, the specification for future jet fuel may have to increase aromatic content [77] to improve the fuel's thermal stability and energy density. The selection of chemical composition for JP-900 will be discussed in the next chapter referring to the correlation of compound classes and the properties of the fuels.

Chapter 7

Relationship of Chemical Composition and Properties:

Graphical and Numerical Analyses

This chapter discusses the relationship between chemical composition and jet fuel properties in terms of graphic plots, multiple regression analysis (MLR) and the artificial neural network (ANN) approach. The main goal is to establish meaningful and statistically significant correlations among physical and chemical aspects. To assist the development of prototype JP-900, these composition-property relationships will be key factors in designing and comparing fuel refining routes, catalyst selection, and blending options [70].

In this work, the term “chemical composition” is used to mean the compound classes which were obtained from GC/MS analysis. In most cases, a relationship between composition and physical properties can be established by multiple linear regression analysis or the use of an artificial neural network. Ternary diagrams are also produced as part of numerical analysis, to clearly display relationships among three main components and properties.

Thermal stability in static tests and properties such as net heat of combustion, smoke points, flash points and viscosity have been evaluated by graphical and numerical analyses. Some properties that have not been studied in as much detail are QCM results, thermal stability in dynamic conditions and cloud points, due to the limited quantity of

data on these properties. Also, H/C ratio was not studied for a mathematical model because this parameter is obviously known to increase with hydrogen percentage in the mixtures.

7.1 Relationship of Chemical Composition and Solid Deposition Rate (Static Condition)

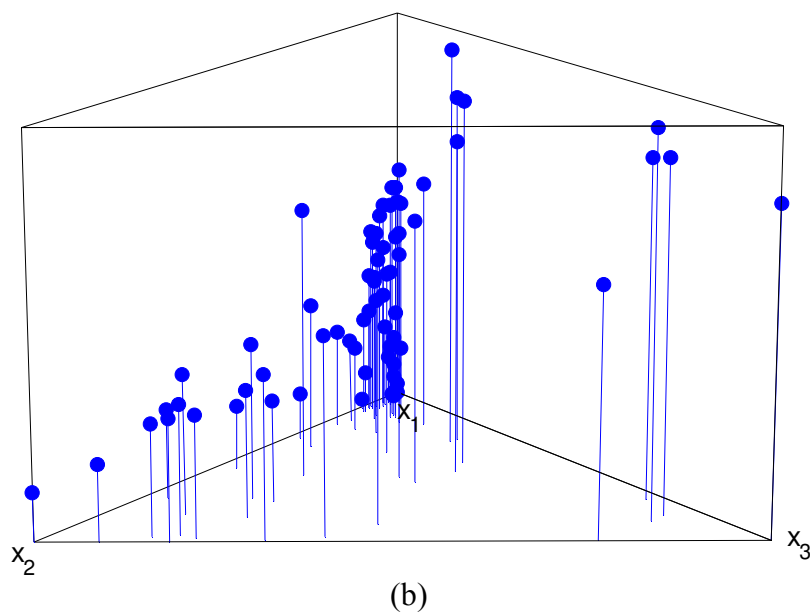
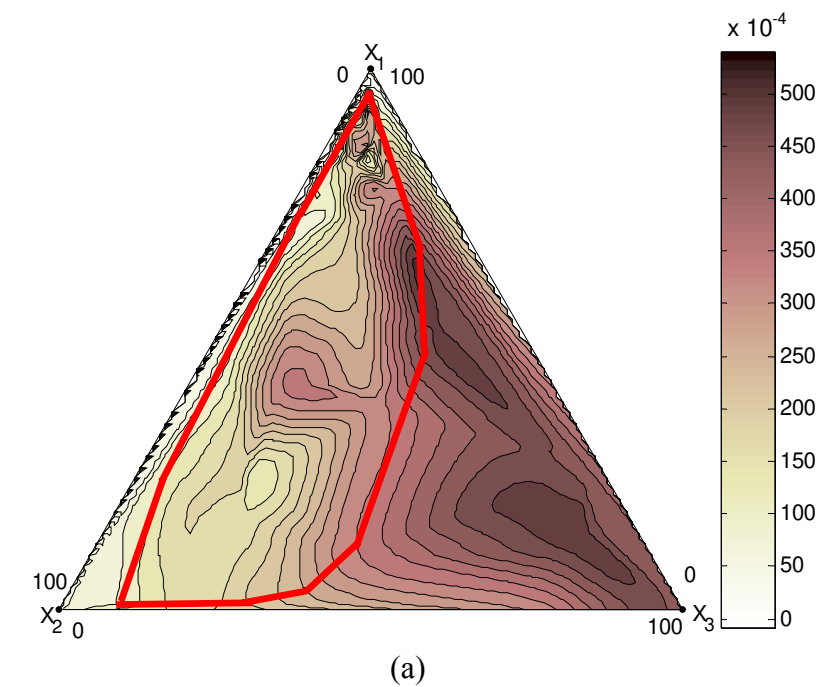
Solid deposition rates (R_s) in wt%/min of jet fuel model compounds, conventional petroleum-based jet fuels and coal-based jet fuels have been summarized in Table C-1. The solid deposition rate is the overall rate of solid yield (wt%) with an increase of stressing time (min) (See Figure 5-1 to Figure 5-3). Ternary diagrams of three chemical compositions versus solid deposition rates were plotted using total data sets in Table C-1. MATLAB source code for ternary diagram plots is described in Appendix D.1. The ternary axis has been transformed from Cartesian product axis (two-dimensional X-Y axis). Figure 7-1 displays a plot of total aromatics, total cycloalkanes and the sum of alkanes, alkenes and cycloalkenes. The color bar on the right of Figure 7-1 (a) indicates the colors which match the deposition rate (wt%/min). Light color represents slow deposition rate ($0-250 \times 10^{-4}$ wt%/min) while dark color shows fast deposition rate ($250-500 \times 10^{-4}$ wt%/min). The three-dimensional plot in Figure 7-1 (b) displays the three composition variables versus solid deposition rate, which is indicated by the stem height.

The pyrolytic deposition rates at a temperature of 480°C have shown significant variation throughout the composition mixtures. The high deposition rate or fast deposition reaction ($250-500 \times 10^{-4}$ wt%/min) has been observed when the amounts of

alkane, alkene and cycloalkene (X_3) increased. (The contour colors appeared to be darker as X_3 increased from the triangle base at the opposite side of X_3 to the X_3 corner.) From the Figure, it appears that having more aromatics and cycloalkanes seemed to help decrease the rate of solid deposition. However, the types of aromatics, hydroaromatics and cycloalkanes responsible for this have to be identified.

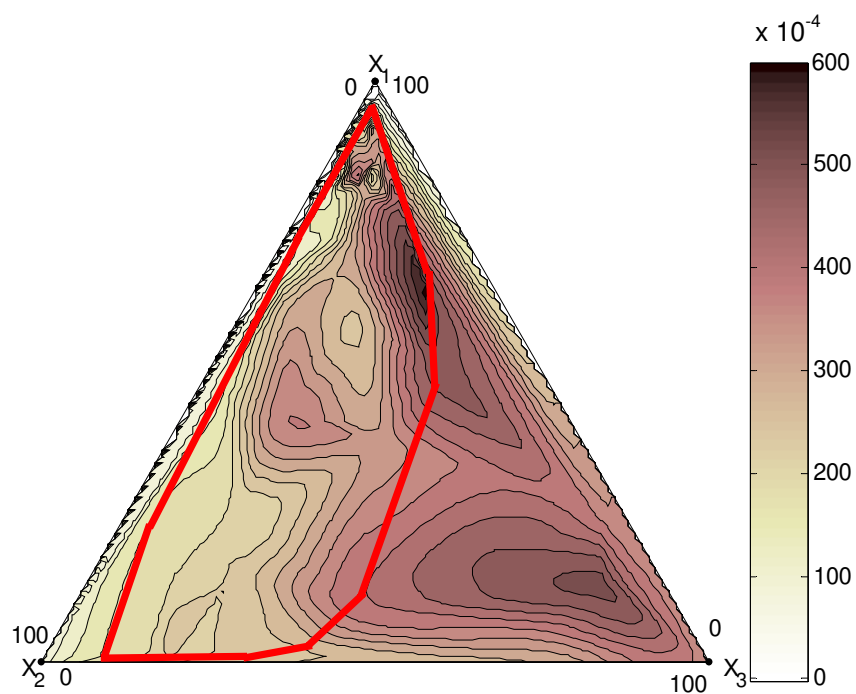
It is typical for coal-based jet fuels that most samples are dominated by hydroaromatics (which were included as aromatics) as shown. The area (red frame) in Figure 7-1 (a) represents the constrained region of sixty-six coal-based jet fuels and their blends (EI-001 to EI-038 and B-001 to B-026). The chemical composition of these coal-based jet fuel samples is governed by the degree of hydrotreatment and saturation of LCO and RCO. In this region, the lighter contour lines present at the high concentration of total aromatics and hydroaromatics (X_1) and cycloalkanes (X_2) also indicate that cycloalkanes and/or hydroaromatics might be the key for inhibiting solid deposition. From the plots, cycloalkanes seem to have a more significant effect relative to the hydroaromatics (as indicated by large area at the X_2 corner covered by light contour lines when compared to that of X_1). In the middle of the region, which had similar amounts of X_1 and X_2 , a fast rate (dark contour color) was observed.

Figure 7-2 (a) and (b) were plotted from actual data sets in Table C.1 as well. To compare with the average solid deposition rates (R_s), initial solid deposition rates after the induction period (R_s') were also plotted against three compositions. The contour and stem plots have shown to be similar to Figure 7-1 (a) and (b), thus either R_s or R_s' can be used to represent kinetic of solid deposition. In this work, average solid deposition rate (R_s) will be used as a main parameter in final selection of jet fuel chemical composition.

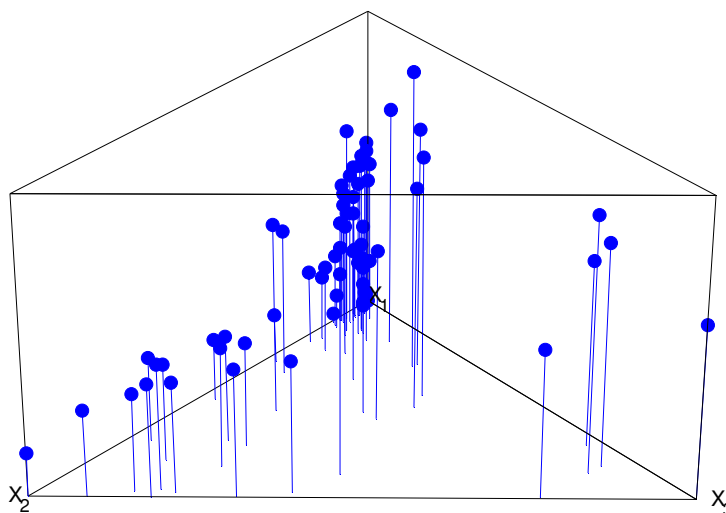


X_1 : aromatics and hydroaromatics (including tetralin)
 X_2 : cycloalkanes (including decalin)
 X_3 : alkanes and others

Figure 7-1: Ternary diagram plot between chemical composition (wt%) and solid deposition rate of jet fuel ($R_s \times 10^4$ wt%/min): (a) contour plot and (b) 3-D plot.



(a)



(b)

X_1 : aromatics and hydroaromatics (including tetralin)

X_2 : cycloalkanes (including decalin)

X_3 : alkanes and others

Figure 7-2: Ternary diagram plot between chemical composition (wt%) and solid deposition rate of jet fuel ($R_s \times 10^4$ wt%/min): (a) contour plot and (b) 3-D plot.

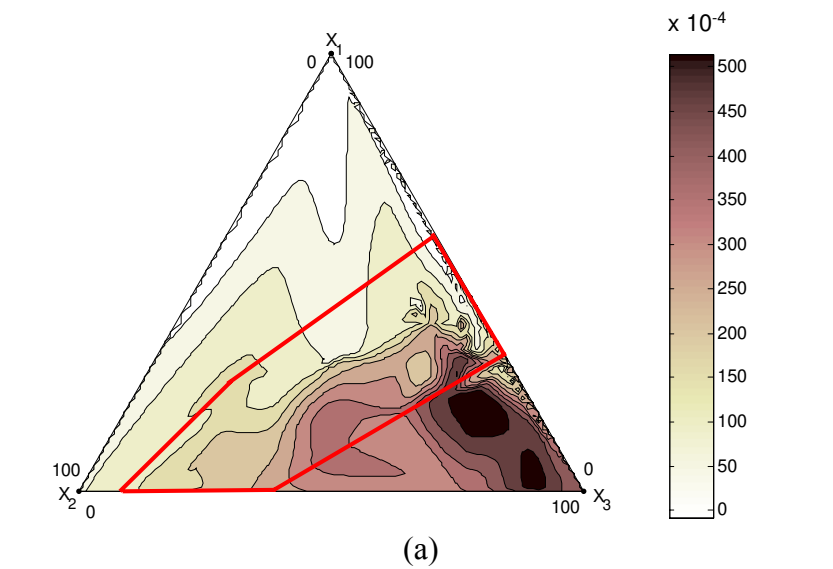
To check the effects of tetralin and decalin, solid deposition rates were plotted against tetralin (wt%) and decalin (wt%) in Figure 7-3 (a) and (b), respectively. The contour plots agree with previous analysis, in that the fast deposition rates were observed at the corner of X_3 which consisted of mainly alkanes with alkenes and cycloalkenes. By increasing tetralin and decalin amounts in Figure 7-3 (a) and (b), respectively (observe the contour line from the base of triangle X_2X_3 to the top of corner X_1), solid deposit rates decrease.

In Figure 7-3 (a), high deposition rates were observed at high concentrations of X_3 , which is alkanes, alkenes, cycloalkenes and other aromatics (excluding tetralin). This suggests that the combination of aromatics and alkanes can play a major role in the instability of jet fuels. However, the thermal stability of jet fuels can still be improved by tetralin, as shown by the slow deposition rate. In the constrained region, the concentration range of tetralin is 0-55%. From the plot, it is not quite clear that tetralin (X_1) in this region is the key to inhibit solid deposition. When tetralin increased vertically from the X_2X_3 base to X_1 corner, the contour colors varied by the amount of X_2 and X_3 . The rate of deposition seemed to increase when the amount of X_3 in the mixture increased, at the right side of the region; however, the interpolation by MATLAB has shown that the more tetralin (closer to the X_1 corner), the lower solid deposition rate.

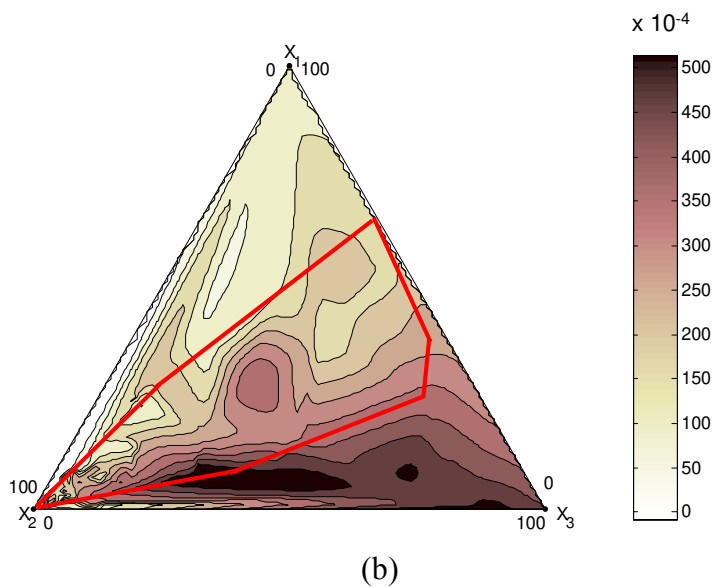
Tetralin by itself is a very stable component as its deposition rate is 0 wt%/min. Decalin is also stable with deposition rate of 64×10^{-4} wt%/min. When present in hydrocarbon mixtures, tetralin also tends to have a greater effect on improving thermal stability. By increasing decalin from 0 to 65% in Figure 7-3 (b), the improvement of

thermal stability seems to increase at the right side of the constrained region. However, some high deposition rates are still observed in the middle of the region.

One can summarize this discussion by saying that the ternary plots support the previous results that tetralin and decalin present in coal-based jet fuel can help improve thermal stability [35, 50, 58, 115]. The coal-based jet fuel composition is constrained by the limitation of hydrotreatment and saturation of original LCO and RCO. By having either tetralin or decalin at about 40-50%, the rate of solid deposition has been significantly decreased.



X_1 = tetralin, X_2 = cycloalkanes (including decalin), X_3 = others



X_1 = decalin, X_2 = total aromatics (including tetralin), X_3 = others

Figure 7-3: Ternary diagram between chemical composition (wt%) versus contour lines of ($R_s \times 10^4$ wt%/min) of jet fuels: (a) X_1 = tetralin and (b) X_2 = decalin.

7.1.1 Multiple Linear Regression (MLR) of Chemical Composition-Thermal Stability Relationship

To determine the significant effects of chemical composition on thermal stability, the weight percentage of eight compound classes in all these fuel samples has been determined and was used in statistical analysis with solid deposition rates. Multiple linear regression analysis has been performed for the correlation between three to five compound classes and the deposition rates. Statistical parameters (such as goodness of fit) and outcome of analysis such as adequacy and quality of data set and error were determined and modified based on the knowledge of solid deposition chemistry. Scatter diagrams of compound classes have also been plotted to make a clear picture of composition effects on deposition rates (Figure 7-4). Thus, a good correlation of five compound class percentages in jet fuel samples and their solid deposit rates have been found from twenty-seven samples (EI-001, EI-002, EI-004 to EI-006, B-001 to B-003, B-005 to B-009, B-011 to B-014, B-016 to B-018, B-020 to B-026). The second generation of coal-based jet fuels (EI-007 to EI-038) was not included since they contained different types of aromatic products after having undergone only one-stage hydrotreatment. The chemical composition of second-generation jet fuels also had multiring aromatic contents and did not distribute properly (Figure 7-5), resulting in difficulty to fit the model with MLR. Also, the aromatic contents in this generation are rarely present in the real jet fuel. In addition, all eight compound classes which were previously expected to be variables for the correlation have been reduced to only three to five variables. Statistically, the number of data sets of eight variables for effective fitting should be around eighty to ninety [133].

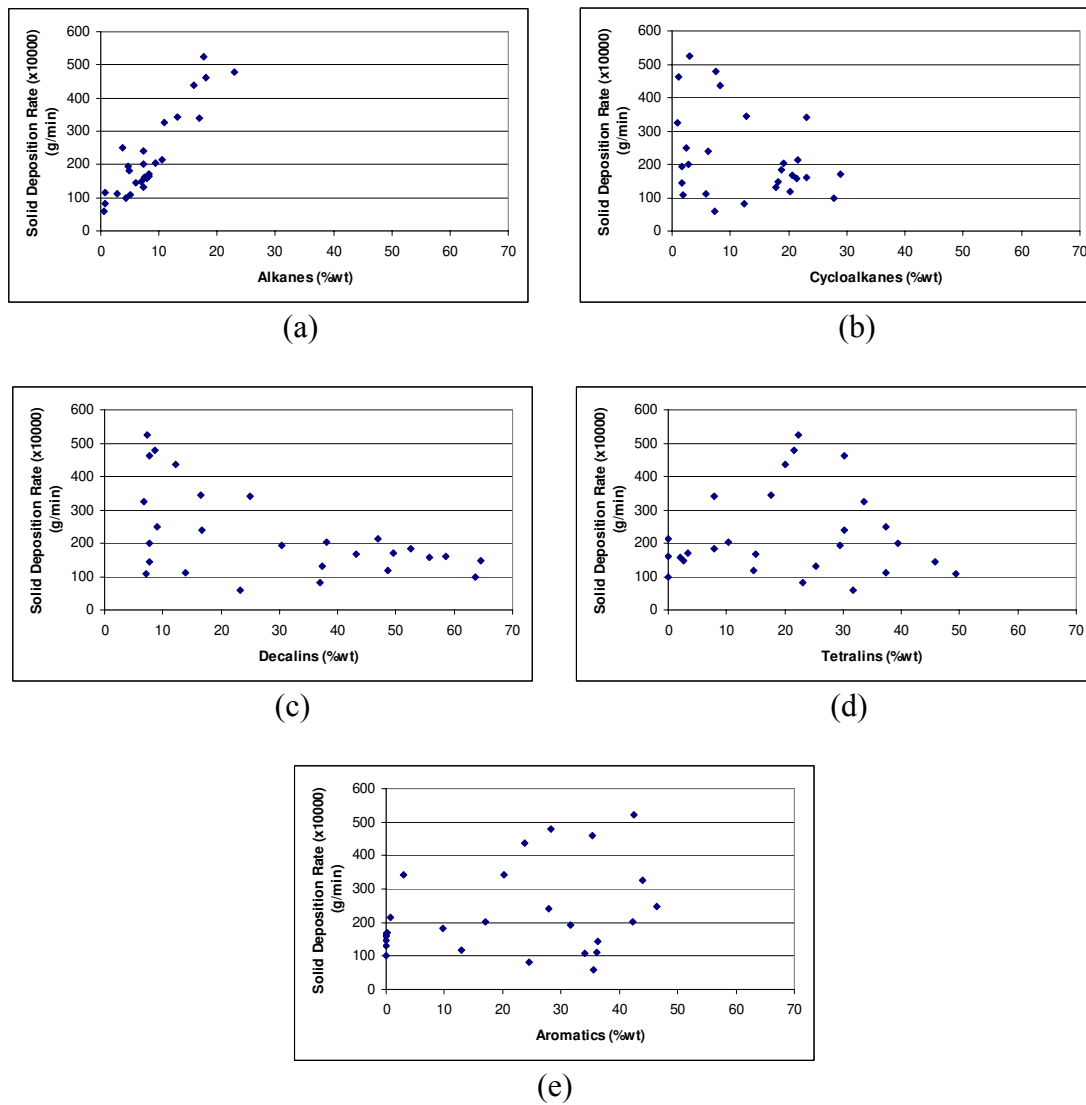


Figure 7-4: Scatter plots between solid deposition rates of twenty-seven jet fuel samples and their compositions: (a) alkanes, (b) cycloalkanes, (c) decalins, (d) tetralins and (e) aromatics.

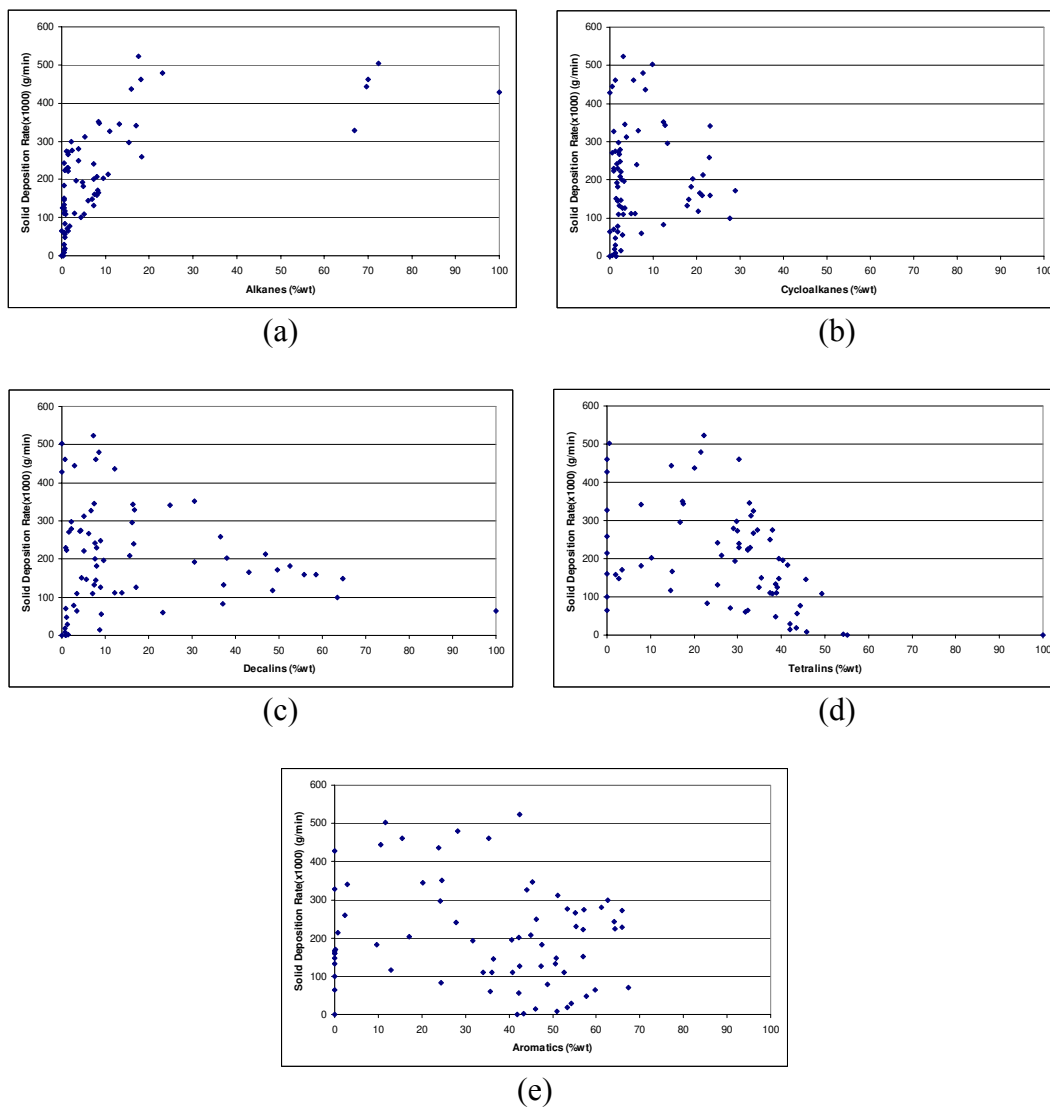


Figure 7-5: Scatter plots between solid deposition rates of sixty-eight jet fuel samples and their compositions: (a) alkanes, (b) cycloalkanes, (c) decalins, (d) tetralins and (e) aromatics.

The regression model for twenty-seven jet fuels obtained from Minitab software is shown as Equation (7-1).

$$(R_s \times 10^4) = 330 + 14.2 X_{alkane} - 4.98 X_{cycloalkane} - 2.47 X_{decalin} - 6.19 X_{tetralin} + 1.75 X_{aromatic} \quad (7-1)$$

The solid deposition rate can be displayed as a linear equation of alkanes, cycloalkanes, decalins, tetralins and aromatics in Equation (7-1). The relatively large, positive coefficient of alkanes indicated that alkanes significantly promote the development of solid deposits when compared to the other components. This is in agreement with previous work of model compound data by Lai and Song [134]. Aromatics also played a role but not as significant as alkanes. Unlike alkanes and aromatics, cycloalkanes, decalins and tetralins have shown to slow solid deposition rate. Because of the relatively large negative coefficient, tetralins seem to have the highest impact on inhibiting deposition [35, 50, 58, 115]. The presentation of Equation (7-1) also agrees with scatter plots in Figure 7-3, as the deposition rate tends to increase with alkane content and decrease with the increase in cycloalkanes, decalins, and tetralins.

Figure 7-6 shows the high R^2 (0.943) for the plot between actual and predicted solid deposit rate.

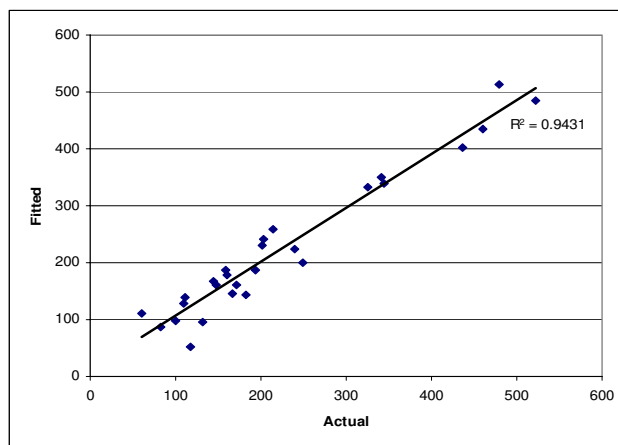


Figure 7-6: Actual vs. fitted solid deposition rate on twenty-seven jet fuel samples.

7.1.2 Artificial Neural Network (ANN) Approach of Chemical Composition - Thermal Stability Relationship

MLR is an effective method to establish a linear relationship such as the twenty-seven samples in the previous section. The variables (five compound classes) of those samples were quite consistent as they came from the blends of the first generation of jet fuels. But, to explain the variation in chemical distribution presented in Figure 7-5, some type of non-linear relationship has been taken into consideration.

The program NeuroShell 2 (Release 4.0) from Ward Systems Group, Inc. was used to correlate chemical composition with thermal stability. The back propagation method was selected to train and test the network. Again, it is not recommended to generate the network with eight variables while having an insufficient data set (only 40-70 data sets), because the network will likely overfit the data [98, 135]. Thus, five

variables (alkanes, cycloalkanes, decalins, tetralins and aromatics) were again used as input of the network.

Various numbers of data sets were fed to back propagation network architecture with different layers and neurons until high goodness of fit (R^2), low mean square error (MSE) and constant minimum average error were obtained. But, the most important thing is to check how well the network does on the production set. Forty-one data sets (EI-001 to EI-006, EI-031 to EI-033, EI-036, EI-037, B-001 to B-028, JP-8 and JP-8+100) have successfully produced the lowest MSE . Thirty-seven training sets were trained and produced a $MSE = 693.203$. Then four production sets were tested by the network, and good correlation with a low MSE of 914.851 was obtained. The network used is a three-layer back propagation network, which contains five neurons for the first layer, four neurons for the second layer, and one neuron for the third or output layer. The result is shown in Table 7-1 and actual versus network solid deposition rate is also plotted in Figure 7-7.

In addition, NeuroShell 2 also computed the relative contribution factors from the weights in the finished network. They are similar to the coefficients in MLR but do not present positive or negative values. From Table 7-1, alkanes have the most significant effects on solid deposition rate, compared with lesser effects of decalins and tetralins.

Table 7-1: ANN results for five compound classes vs. solid deposition rate ($R_s \times 10^4$ wt%/min) of forty-one jet fuel samples.

Architecture of network:	BP-3 (5,4,1)	
Total data set:	41	
	Training set	Production set
Patterns processed:	37	4
Output:		
r squared:	0.9658	0.9867
Mean squared error:	693.203	914.851
Mean absolute error:	17.899	28.618
Min. absolute error:	0	12.213
Max. absolute error:	74.085	38.119
Min. average error:	0.0001713	
Relative contribution factors:		
Alkanes	0.40939	
Decalins	0.20477	
Tetralins	0.16281	
Cycloalkanes	0.13996	
Aromatics	0.08307	

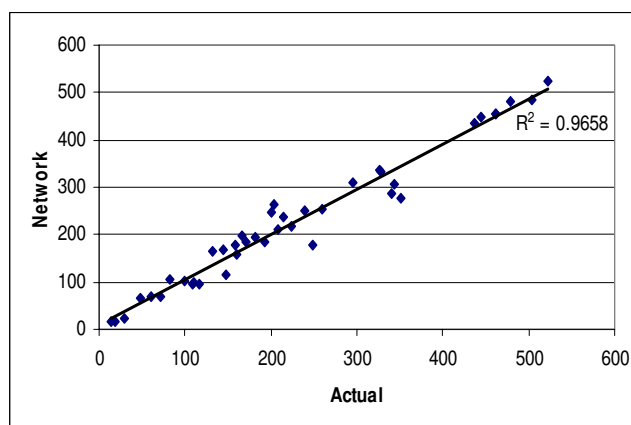


Figure 7-7: Actual vs. network solid deposition rate on forty-one jet fuel samples.

The network constructed from forty-one data sets has produced the low *MSE* and high R^2 for the prediction of solid deposition rate. Also, all sixty-eight jet fuel samples (including twenty-four data sets of the second generation) from Table 3-1 and Table C-1 have been fed to a network architecture. Sixty-two of them have been used as a training set. After training, the trained network model, consisting of weighting factors (Appendix D.3) and three layers, was tested by the six production sets. The result is shown in Table 7-2 and Figure 7-8. However, the network obtained from training all sixty-eight data sets is worse than the above network. High *MSE*, poor goodness of fit and relative contribution factors have been produced from the new network. The significant effect of chemical composition on solid deposition rate that was previously dominated by alkanes has then become an effect of tetralins.

As discussed in Section 7.1.1.1, the second generation coal-based jet fuels consist of different types of aromatics that are not likely to be found in normal jet fuels. The variety of heavy aromatics can cause a variation when training the network. It can be observed that most of the second-generation jet fuels have similar amounts of aromatics and hydroaromatics but their solid deposition rates are significantly different. It is very difficult to find a relationship from these fuels unless more experiments are conducted and the number of aromatic rings is one of the input variables. However, the network produced from the training of sixty-eight fuels has shown that tetralin had become a significant factor to solid deposition rate when training among highly aromatic jet fuels.

Table 7-2: ANN results for five compound classes vs. solid deposition rate ($R_s \times 10^4$ wt%/min) of sixty-eight jet fuel samples.

Architecture of network:	BP-3 (5,4,1)	
Total data set:	68	
	Training set	Production set
Patterns processed:	62	6
Output:		
r squared:	0.91	0.8329
Mean squared error:	1519.448	2718.786
Mean absolute error:	23.853	42.121
Min. absolute error:	0	0
Max. absolute error:	139.24	82.973
Min. average error:	0.0006794	
Relative contribution factors:		
Tetralins	0.27015	
Alkanes	0.2637	
Decalins	0.18811	
Cycloalkanes	0.14906	
Aromatics	0.12898	

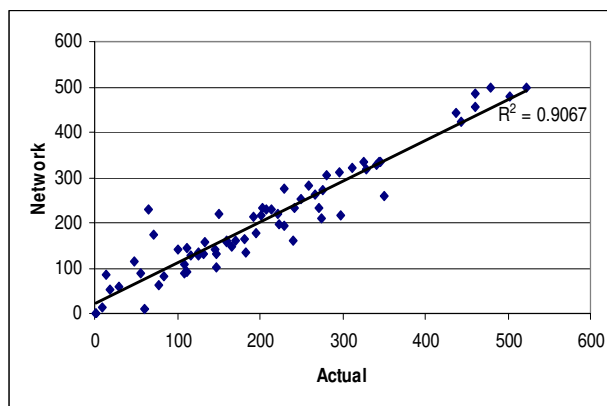


Figure 7-8: Actual vs. network solid deposition rate on sixty-eight jet fuel samples.

In summary, a chemical composition-solid deposition rate relationship can be established by MLR and by ANN. ANN is more effective for correlating non-linear relationship or very complex data sets. From the available data, the network trained from forty-one jet fuel samples has produced the best result (highest R^2 and lowest MSE) for both the training set and the production set. However, it is recommended to have more data sets to generate and test the network so that the network can predict accurate output from the available data set and another unseen data set.

Another observation from training the network of five compound classes and solid deposition rate is that the deviation of output is quite high compared with the deviation of input. Thus, a significant difference between actual deposition rate and that predicted by the network is observed. This situation can be improved when hundreds of sets of data are obtained and used to train the network, and some outliers are discarded. However, the network from data available in this work is acceptable for the time being. The network can predict deposition rate from identified compound classes. The chemical composition of future jet fuel candidates after hydrotreatment and saturation processes can be fed to the network and their solid deposition trends can be determined. The selection of the final fuel composition can be made based on the predicted output.

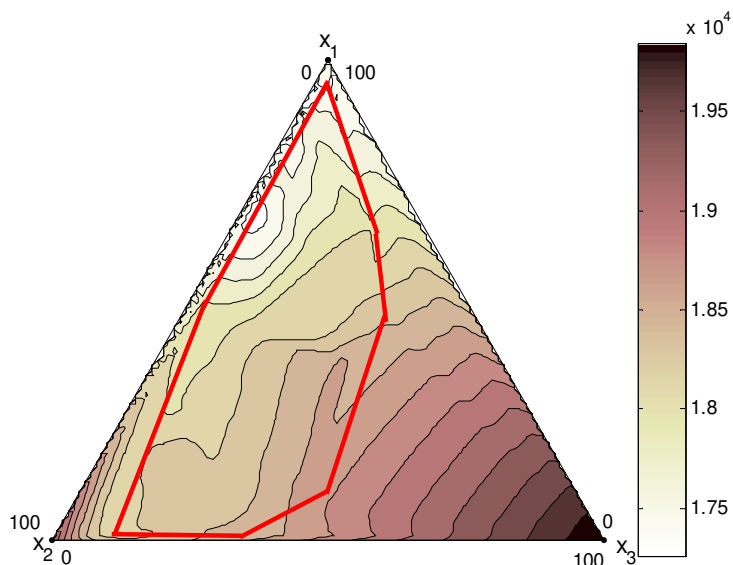
The relationship between solid deposition in dynamic test condition and jet fuel chemical composition has been briefly discussed in Chapter 5. The graphical and numerical studies of solid deposition in a flow reactor were not performed due to the limited number of data sets. The available results of chemical compositions versus solid deposition from flow reactor conditions are summarized in Table C-2 [129].

7.2 Relationship of Chemical Composition and Combustion Properties

7.2.1 Relationship of Chemical Composition and Net Heat of Combustion

(Q_n)

Figure 7-9 is a ternary contour plot among aromatics and hydroaromatics (X_1), cycloalkanes (X_2) and alkanes, alkenes and cycloalkenes (X_3) and net heat of combustion. Dark contour color indicates high heat of combustion, which is found close to the corner of 100 wt% cycloalkanes (X_2) and alkanes, alkenes and cycloalkenes (X_3). Aromatics and hydroaromatics (X_1) have comparatively low heats of combustion [131], and heats of combustion below 18500 Btu/lb have been observed when the concentration of aromatics increased in the mixtures.



X_1 : aromatics and hydroaromatics (including tetralin)
 X_2 : cycloalkanes (including decalin)
 X_3 : alkanes and others

Figure 7-9: Ternary diagram plot between chemical composition (wt%) and jet fuels' net heat of combustion: A contour plot.

The minimum net heat of combustion allowed by ASTM is 18,400 Btu/lb. The red frame in Figure 7-9, indicating the constrained region, shows that the net heat of combustion values vary between 17,200 and 18,700 Btu/lb. EI-004 (saturated LCO) and some blends meet or exceed this specification. Their composition lies at the right side of the region representing significant amounts of alkanes, alkenes and cycloalkenes.

Figure 7-10 displays scatter plots between net heat of combustion of fifty-four (EI-001 to EI-036 and B-001 to B-018) coal-based jet fuel samples and their chemical composition. Significant trends of increases in net heat of combustion with increase of alkanes, cycloalkanes, alkenes and cycloalkenes and decrease of total aromatics were observed. The MLR between two composition variables and net heat of combustion is obtained in Equation (7-2).

$$Q_n = 17712 + 17.4 (X_{alkane} + X_{cycloalkane} + X_{alkene} + X_{cycloalkene}) - 2.82 (X_{aromatic} + X_{tetralin}) \quad (7-2)$$

or $Q_n = 17712 + 17.4 X_{non-aromatic} - 2.82 X_{total\ aromatic}$

This regression model presents highest R^2 (0.887) compared to the other models with different variables. The coefficients show that alkanes+cycloalkanes+alkenes+cycloalkenes have more significant effects on the net heat of combustion than the aromatics+tetralins. A plot for goodness of fit (R^2) is shown in Figure 7-11 (a).

However, ANN was also used for the modeling of net heat of combustion with fifty-four data sets. Two different models are shown in Table 7-3 and Table 7-4. Table 7-3 is obtained from training data sets by two input variables (alkanes+cycloalkanes+alkenes+cycloalkenes) and (aromatics+tetralins) using the three-layer back propagation

method. The network shows good prediction ($R^2 = 0.9105$ and $MSE = 15292.25$) for both the training set and the production set. Similar to the MLR model, relative contribution factors show that alkanes+cycloalkanes+alkenes+cycloalkenes have greater effect on the net heat of combustion than the aromatics+ tetralins.

A network model from training three input variables, aromatics+tetralins, cycloalkanes and alkanes+alkenes+cycloalkenes, is shown Table 7-4. This model has produced a result better than above model, with R^2 (0.9164) and MSE (13915.2). The goodness of fit of both models is shown in Figure 7-11 (b) and (c).

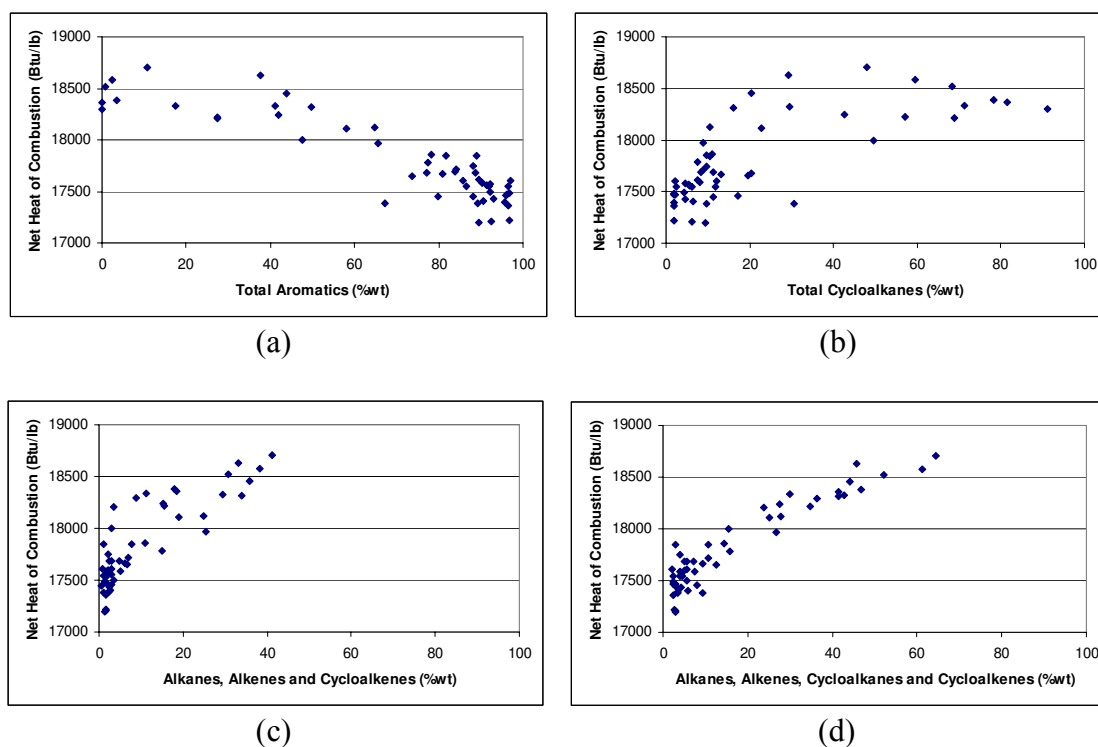


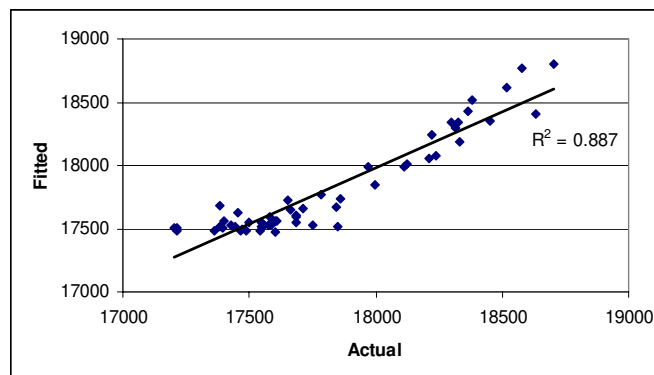
Figure 7-10: Scatter plots between net heat of combustion of fifty-four jet fuel samples and their compositions: (a) total aromatics, (b) total cycloalkanes, (c) alkanes, alkenes and cycloalkenes, (d) alkanes, alkenes, cycloalkanes and cycloalkenes.

Table 7-3: ANN results for two compound classes vs. net heat of combustion of fifty-four jet fuel samples.

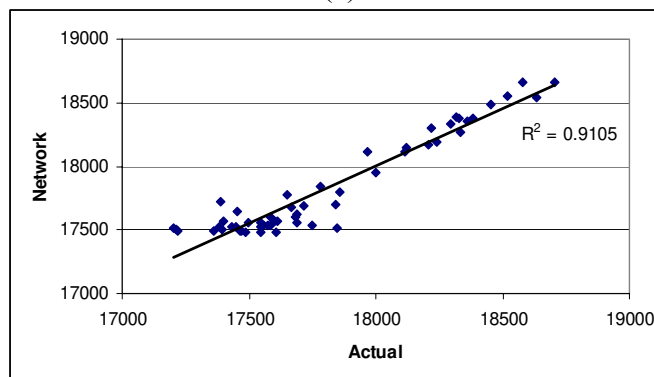
Architecture of network:	BP-3 (2,2,1)	
Total data set:	54	
	Training set	Production set
Patterns processed:	50	4
Output:		
r squared:	0.9105	0.9287
Mean squared error:	15292.25	7493.855
Mean absolute error:	88.795	58.462
Min. absolute error:	0.32	7.525
Max. absolute error:	336.293	164.297
Min. average error:	0.0009705	
Relative contribution factors:		
Alkanes+cycloalkanes+alkenes+cycloalkenes	0.80112	
Aromatics+tetralins	0.19888	

Table 7-4: ANN results for three compound classes vs. net heat of combustion of fifty-four jet fuel samples.

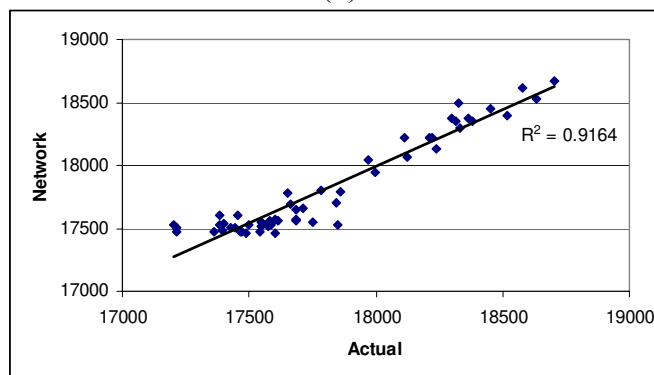
Architecture of network:	BP-3 (3,2,1)	
Total data set:	54	
	Training set	Production set
Patterns processed:	50	4
Output:		
r squared:	0.9164	0.9833
Mean squared error:	13915.2	8190.32
Mean absolute error:	87.529	75.322
Min. absolute error:	2.553	4.031
Max. absolute error:	325.303	124.404
Min. average error:	0.0010732	
Relative contribution factors:		
Aromatics+tetralins	0.45437	
Cycloalkanes	0.38279	
Alkanes+alkenes+cycloalkenes	0.16284	



(a)



(b)



(c)

Figure 7-11: Actual vs. predicted net heats of combustion on fifty-four jet fuel samples: (a) MLR, (b) ANN and two variables, and (c) ANN and three variables.

7.2.2 Relationship of Chemical Composition and Net Energy Density

A ternary contour plot among aromatics and hydroaromatics (X_1), cycloalkanes (X_2) and alkanes and others (X_3) and net energy density is shown in Figure 7-12. Dark contour color represents high energy density, which is found close to the apexes of aromatics and hydroaromatics (X_1) and cycloalkanes (X_2). Energy density appears to be relatively low due to high concentration of low-density alkanes. (The contour colors are opposite from those of Figure 7-9.) However, there is no specification for energy density at the present time. Therefore, the energy density will not be the main consideration for the optimum composition.

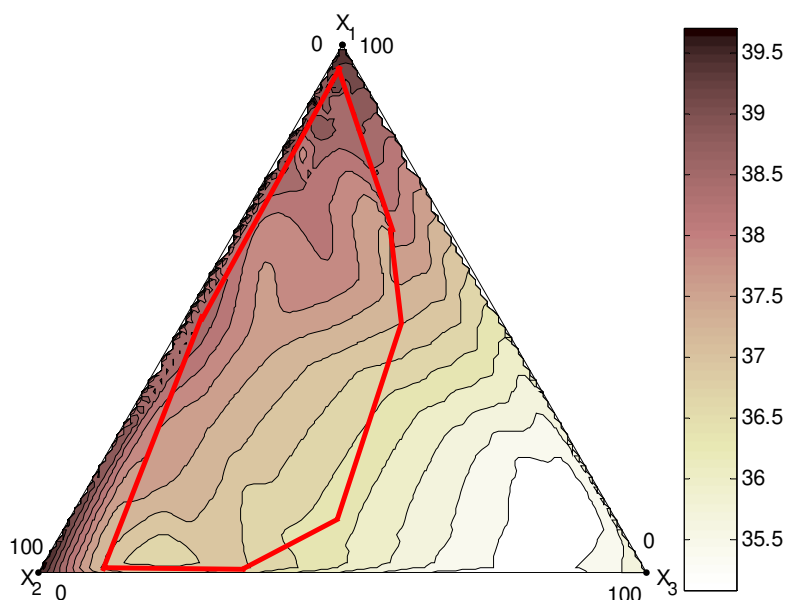


Figure 7-12: Ternary diagram plot between chemical composition (wt%) and jet fuels' net energy density: A contour plot.

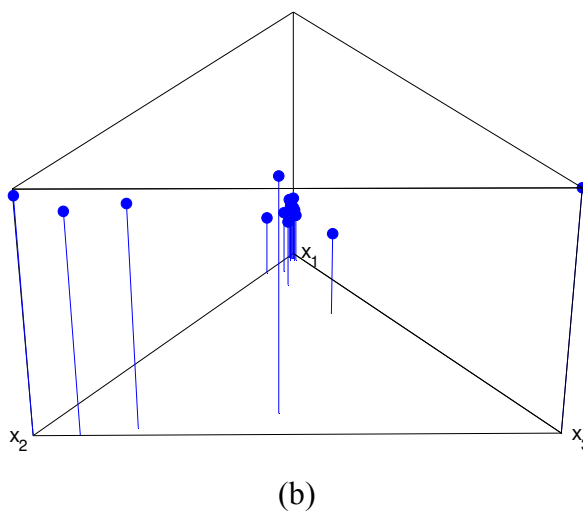
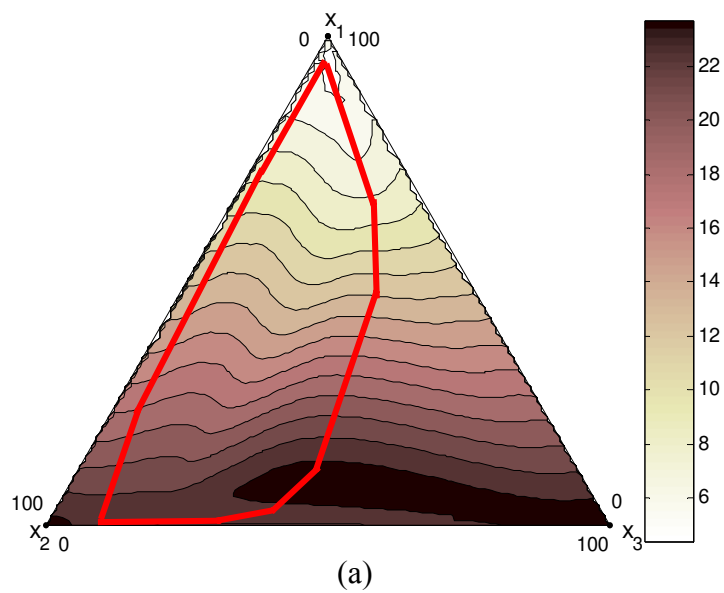
7.2.3 Relationship of Chemical Composition and Smoke Point (S)

The chemical composition-smoke point relationship can be understood from graphic display in Figure 7-13. Both ternary plots show that highly aromatic mixtures produce smoke at short flame height. And, the flame height or smoke point increased as aromatics content decreased.

The number of smoke point tests is quite small and the smoke points are separated into two different groups (below 10 mm and higher than 20 mm). (The ASTM specification is that the smoke point be at least 19 mm.) One can try establishing a chemical composition-smoke point relationship from the available data set (EI-001 to EI-006, EI-031 to EI-041 in Table C-6). The MLR model can be written as follows:

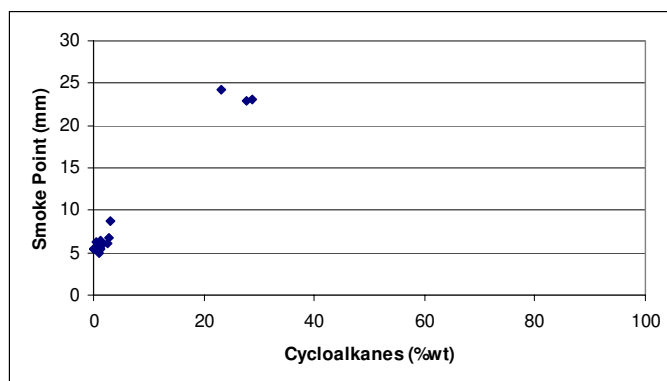
$$S = 15.0 - 0.101 (X_{aromatic} + X_{tetralin}) + 0.327 X_{cycloalkane} \quad (7-3)$$

Equation (7-3) has been obtained from the relationship of the coal-based jet fuel data set, which was composed mainly of aromatics and cycloalkanes. The amount of alkanes does not play a significant role in the correlation, due to the small alkane content in the mixture (Figure 7-14(c)); therefore, the smoke point of coal-based jet fuels rather depends on aromatics and cycloalkanes. The ANN model is also presented in terms of total aromatics and cycloalkanes in Table 7-5. ANN's relative contribution factors show that the total aromatics term from the ANN model has more significant effect than the cycloalkanes whereas the MLR's coefficients present the opposite results. However, the ANN model seemed to give more accurate results (MLR: $R^2 = 0.981$ and ANN: $R^2 = 0.9922$, $MSE = 0.352$). Both goodness of fit (R^2) between actual and prediction by MLR and ANN are shown in Figure 7-15.

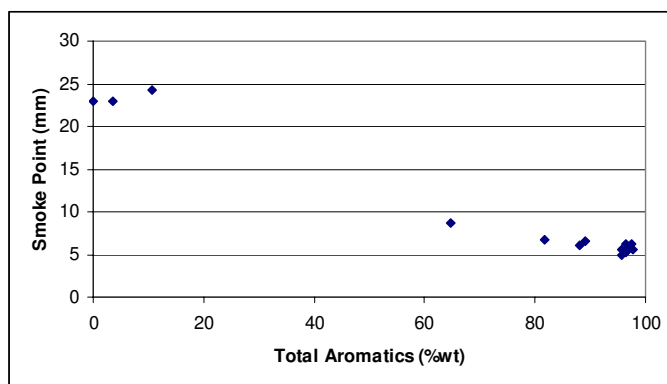


X_1 : aromatics and hydroaromatics (including tetralin)
 X_2 : cycloalkanes (including decalin)
 X_3 : alkanes and others

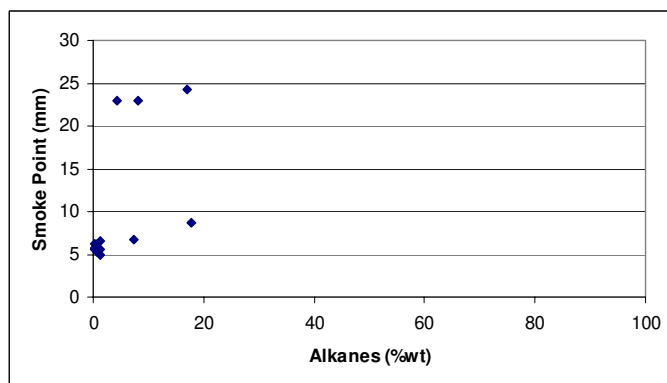
Figure 7-13: Ternary diagram plot between chemical composition (wt%) and jet fuels' flash points (°F): (a) contour plot and (b) 3-D plot.



(a)



(b)

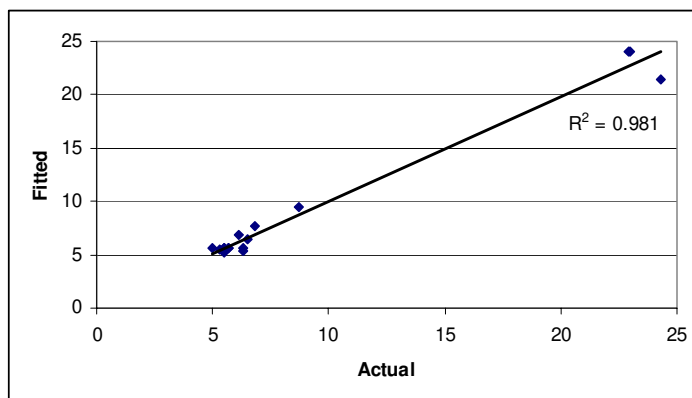


(c)

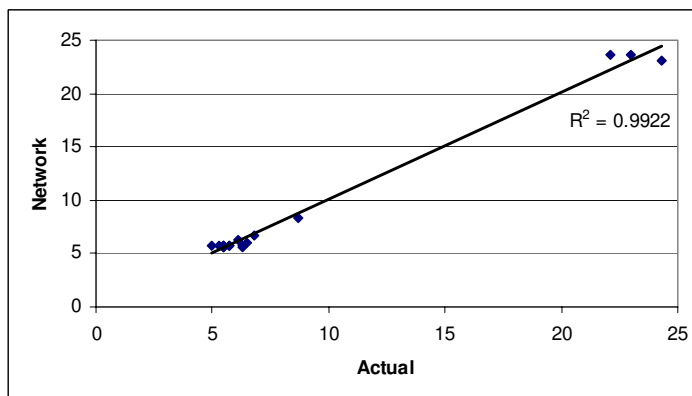
Figure 7-14: Scatter plots between smoke points of seventeen jet fuel samples and their compositions: (a) cycloalkanes and (b) total aromatics.

Table 7-5: ANN results for three compound classes vs. smoke point of seventeen jet fuel samples.

Architecture of network:	BP-3 (2,2,1)	
Total data set:	17	
	Training set	Production set
Patterns processed:	15	2
Output:		
r squared:	0.9922	1
Mean squared error:	0.352	0.121
Mean absolute error:	0.432	0.248
Min. absolute error:	0.014	0.026
Max. absolute error:	1.49	0.588
Min. average error:	0.0000854	
Relative contribution factors:		
Total aromatics	0.53268	
Cycloalkanes	0.46732	



(a)



(b)

Figure 7-15: Actual vs. predicted smoke point on seventeen jet fuel samples: (a) MLR and (b) ANN.

7.3 Relationship of Chemical Composition and Flash Point (T_f)

Flash points of thirty data sets (EI-001 to EI-006, EI-031 to EI-036, B-001 to B-018) have been plotted versus three components of jet fuels in Figure 7-16. Contour lines are only presented for the region constrained by chemical composition of the thirty coal-based jet fuels. The flash points of 100% aromatics, hydroaromatics, cycloalkanes, alkanes, alkenes and cycloalkenes have not been shown in the plot.

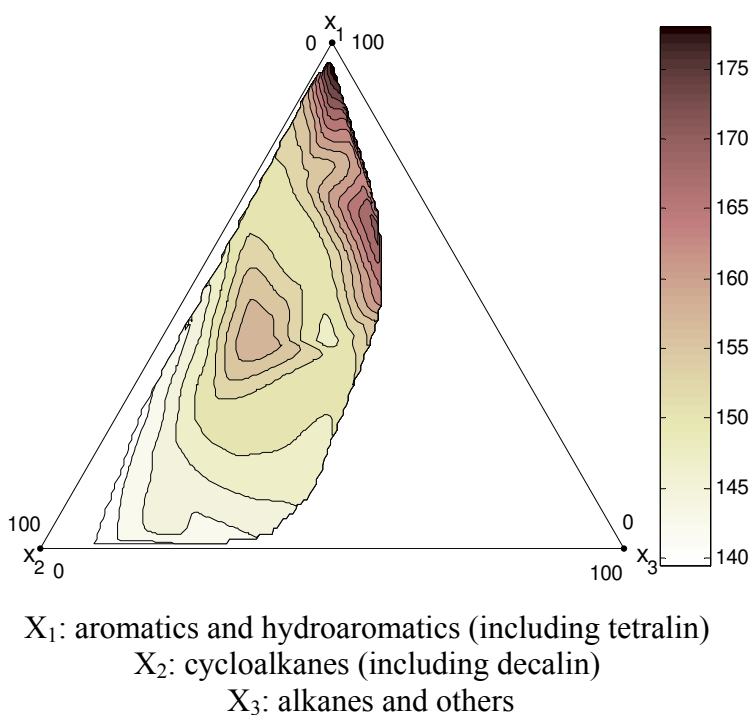


Figure 7-16: Ternary diagram between chemical composition (wt%) versus contour lines of flash point ($^{\circ}\text{F}$) of jet fuels.

The increase in aromatics and hydroaromatics potentially increases flash points. In the opposite direction, alkanes and cycloalkanes are likely to have low flash points.

Scatter plots in Figure 7-17 also support the ternary plot. MLR has been used to create a model for all data sets. Input variables have been added or discounted to perform the regression analysis. The best statistical model ($R^2=0.834$) was selected as the following equation.

$$T_f = 151 + 0.354 X_{aromatic} - 0.145 (X_{cycloalkane} + X_{decalin}) \quad (7-4)$$

From Table 7-6, ANN results from two input variables show better results ($R^2=0.9264$ and $MSE=10.701$) than Equation (7-4). The plots between actual flash point and prediction by Equation (7-4) are compared in Figure 7-18 (a) and (b). The goodness of fit by ANN is significantly shown.

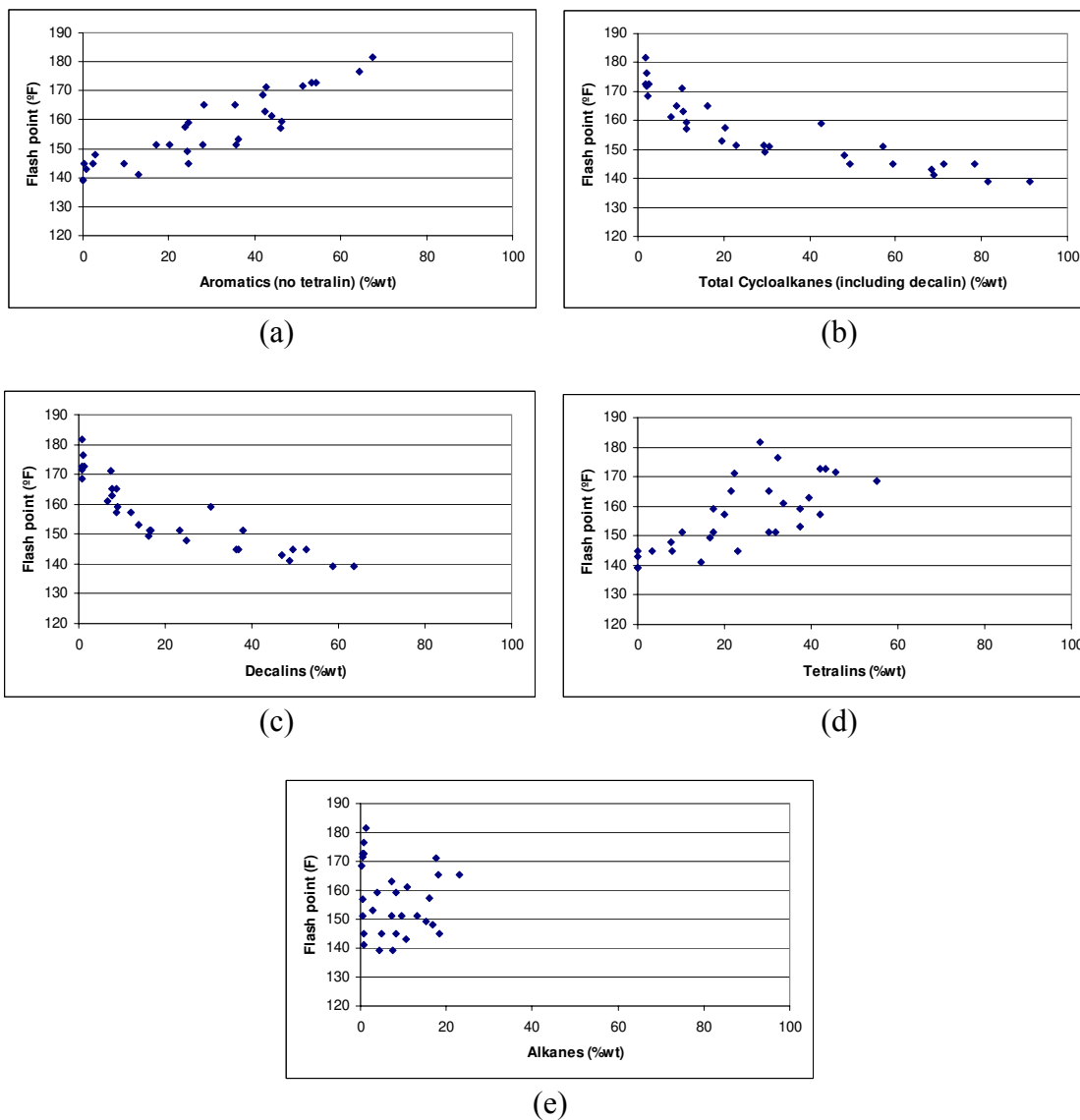
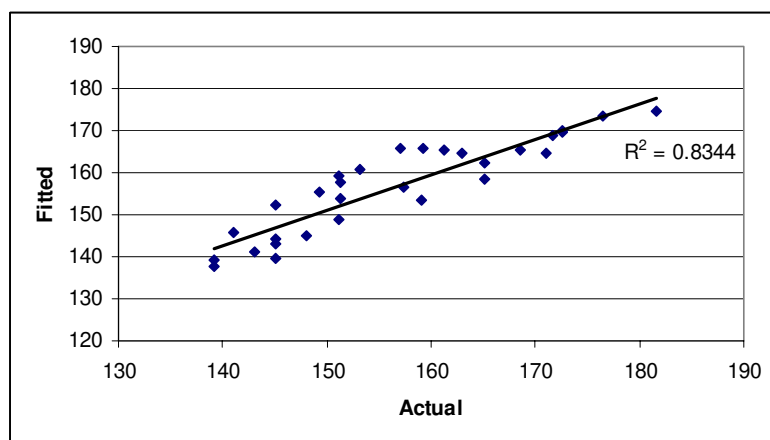


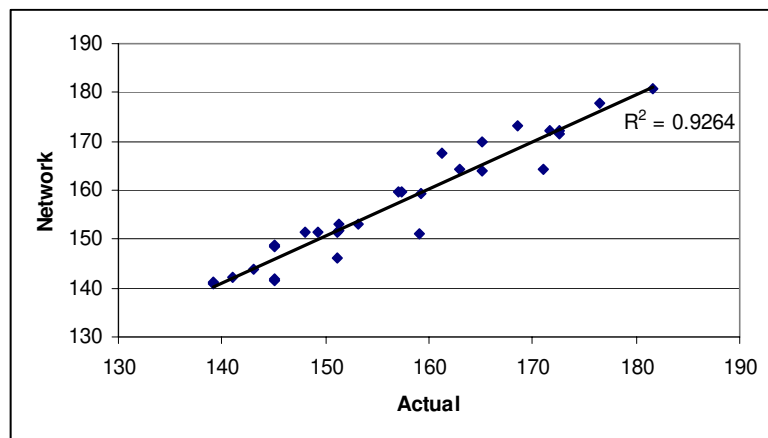
Figure 7-17: Scatter plots between flash points of thirty jet fuel samples and their compositions: (a) total aromatics (excluding tetralins), (b) total cycloalkanes (including decalins), (c) decalins, (d) tetralins and (e) alkanes.

Table 7-6: ANN results for three compound classes vs. flash point of thirty jet fuel samples.

Architecture of network:	BP-5 (2,2,2,2,1)	
Total data set:	30	
	Training set	Production set
Patterns processed:	26	4
Output:		
r squared:	0.9264	0.9965
Mean squared error:	10.701	13.812
Mean absolute error:	2.5	3.523
Min. absolute error:	0.109	2.298
Max. absolute error:	8.094	4.849
Min. average error:	0.004815	
Relative contribution factors:		
Cycloalkanes	0.62091	
Aromatics	0.37909	



(a)



(b)

Figure 7-18: Actual vs. predicted flash point on thirty jet fuel samples: (a) MLR and (b) ANN.

7.4 Relationship of Chemical Composition and Viscosity

Viscosity tests of only twelve coal-based jet fuel samples (EI-001 to EI-006 and EI-031 to EI-036) have been performed due to limitation of sample quantity. However, scatter plots in Figure 7-19 show some relationships between aromatics and cycloalkanes (especially tetralins and decalins) and viscosity. The viscosity of coal-based jet fuels varied between 1.97 and 2.77 cSt.

As discussed earlier in Chapter 6, the viscosity of a complex mixture depends on the molecular weight of compounds present in the mixture. The viscosity increases with the molecular weight for compounds of the same carbon numbers. In this study, the molecular weights of jet fuel samples have not been determined; however, the trend of low molecular weight aromatics and tetralins likely decreases the viscosity. Cycloalkanes and decalin, other major components that have higher molecular weights than aromatics, tend to increase the viscosity value.

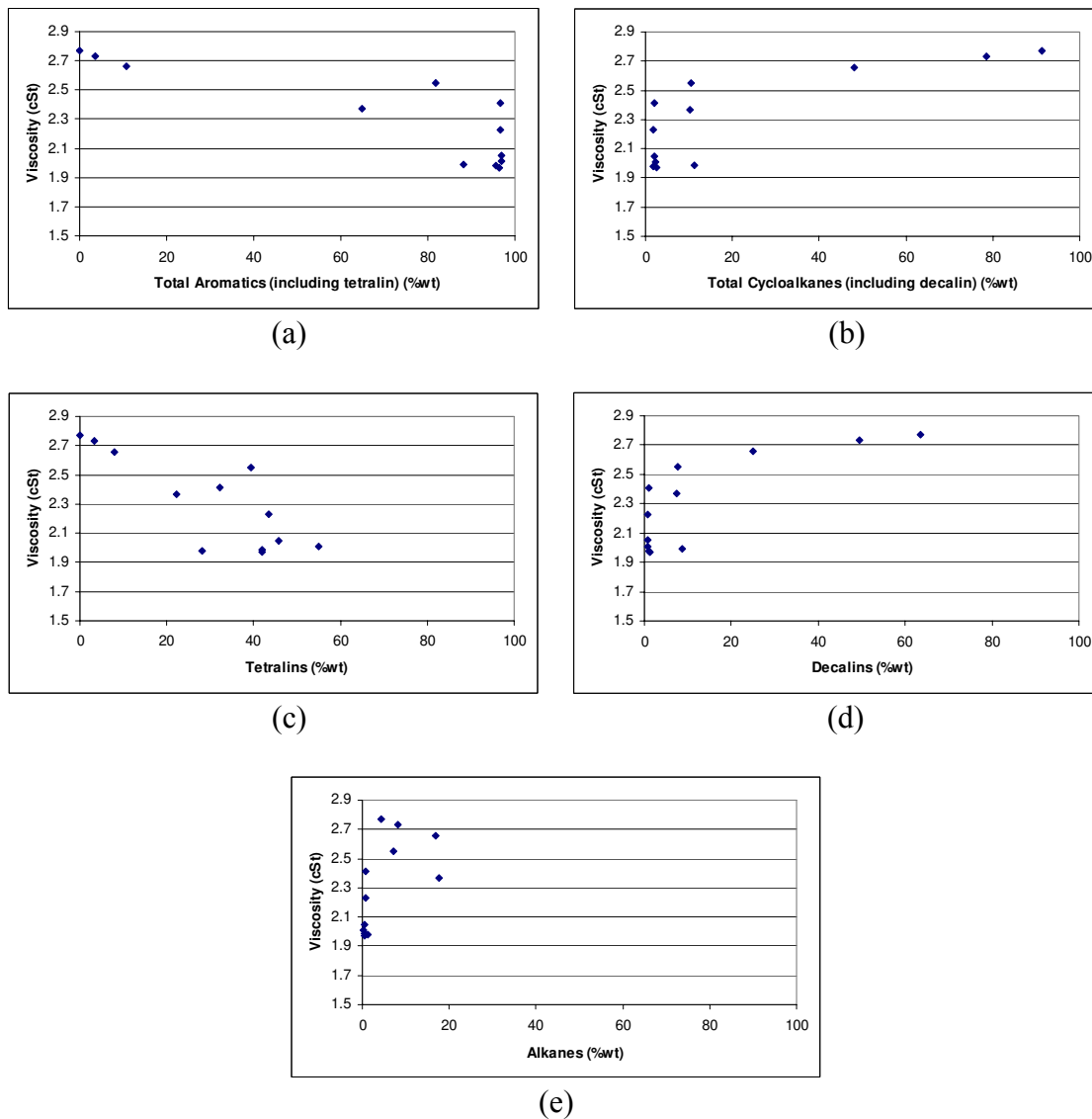


Figure 7-19: Scatter plots between viscosity of twelve jet fuel samples and their compositions: (a) total aromatics (including tetralins), (b) total cycloalkanes (including decalins), (c) tetralins, (d) decalins and (e) alkanes.

7.5 Summary and Application of Graphic, MLR and ANN Models

The major application of the numerical studies in this Chapter is to be able to obtain and/or predict the final output by feeding known concentration of chemical compositions input into the models.

For visualization purposes, ternary plots of three chemical compositions versus contour lines and/or three-dimensional stem plots were presented for solid deposition rate, net heat of combustion, smoke point and flash point. The constrained regions indicate the range of chemical composition of coal-based jet fuel limited by degree of hydrotreatment and aromatics saturation processes. Once the chemical compositions of a new fuel product are determined, the properties discussed above can be estimated from the color of contour lines.

The MLR models of all properties have been created from the first and third generation of coal-based jet fuels and their blends. Every model was formulated to satisfy statistical analyses based on fundamental knowledge of the fuel chemistry. Output properties of future products can be predicted by substituting known chemical composition inputs to the equation. However, there is a limitation of MLR models to predict data from very complex systems because the models were made by estimating a linear relationship between multiple input variables and output. They can predict accurate results for only linear systems.

For non-linear or very complex systems, ANN models have been shown to be more powerful than MLR. ANN can predict the output with high goodness of fit and small errors between actual and network. Unlike MLR models, the equations of ANN

cannot be displayed but they actually exist between each layer inside the network. Weight distributions of each neuron in each layer are similar to coefficients in MLR models. (Weight distributions of all network models are shown in Appendix D.4.) The final relative distribution factors of input variables calculated from the finished network can also indicate the significant effect of the particular variable to the output.

Properties and chemical composition networks have been correlated by training sets, and the networks have been tested by production sets to obtain the highest R^2 and lowest MSE . To predict the properties output, known chemical compositions can be fed to the ANN structures, consisting of multiple layers and neurons. For the chemical composition-solid deposit rate relationship, data sets from different chemical compositions from alkane-rich, decalin-rich and tetralin-rich jet fuels have been trained and tested, but for properties such as heat of combustion, smoke point, flash point and viscosity, the models were established from coal-based jet fuels only.

For all properties output, the input variables and their significant effects are similar for both MLR and ANN models. ANN is more effective than MLR as it can establish non-linear relationships of complex systems and it can also accurately predict unseen data set. However, the limitation of MLR and ANN is that both models are not able to predict data which are out of the ranges of the trained data sets.

7.5.1 Optimization of Chemical Composition

Another aspect of this study is to optimize the chemical composition to meet ASTM specifications. Each chemical composition-property relationship has to be considered before the final selection of chemical composition. In the current study, ternary diagram plots were used to design the most desirable chemical composition.

For coal-based jet fuels, the chemical compositions that can provide high thermal stability (indicating by a slow solid deposition rate), high net heat of combustion and high smoke point will be selected based on the presentation of ternary plots. Flash point has not been involved in this discussion because all coal-based jet fuels have passed specification. Viscosity and cloud point were also discounted because of the limited data set.

Figure 7-20 was plotted from chemical composition-solid deposition rate data which is the same as Figure 7-1. The area in the yellow contour line indicates slow deposition rate ($0-250 \times 10^{-4}$ wt%/min), whereas the blue line indicates the limits of aromatics to meet smoke point specification at 19 mm. The mixtures that contain less than 35% aromatics (including tetralin) have been estimated from Figure 7-13 to produce smoke at the flame height about 19 mm. The green lines present in several areas indicate the mixtures for which their net heat of combustion values pass specification. The areas were estimated from Figure 7-9.

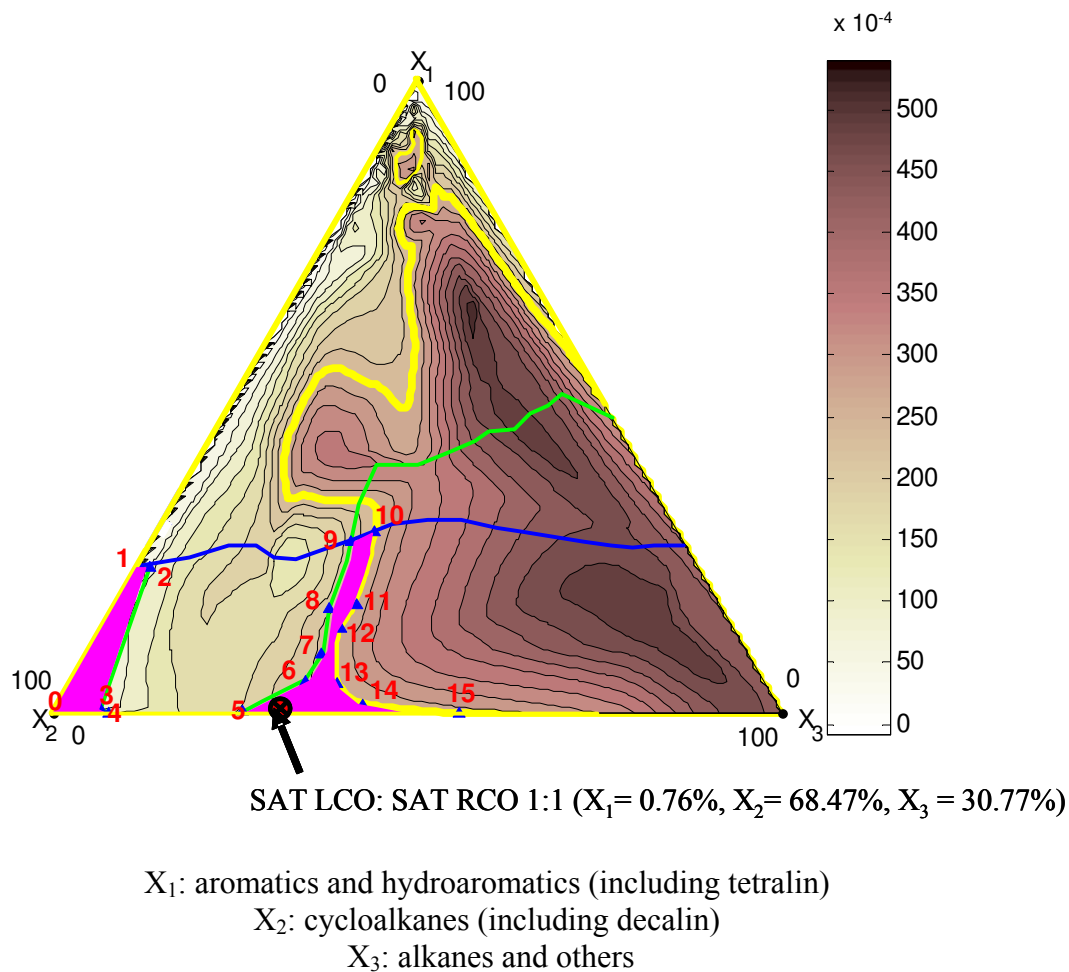


Figure 7-20: Ternary diagram plot between chemical composition and solid deposition rate ($R_s \times 10^4$ wt%/min). Area in the yellow lines indicates slow solid deposition rate ($0-250 \times 10^4$ wt%/min). Green lines point out area of net heat of combustion under ASTM limit. Blue line indicates smoke point limitation. Pink area displays the optimum area.

From the ternary diagram analysis, the optimum chemical compositions can be determined as the two areas underneath the pink shading that meet requirements of slow solid deposition rate, net heat of combustion above 18400 Btu/lb and smoke point at 19 mm. The coordinates of this region can be estimated as shown in Table 7-7. For the

existing data, the B-005 (marked by a black dot in Figure 7-20) is the only sample having a chemical composition that can meet all requirements. B-005, the 1:1 blend of saturated LCO and saturated RCO, is composed of 0.76% aromatics and hydroaromatics, 68.47% cycloalkanes and 30.77% alkanes and the others. It can also be reported as 47% decalin, 0.76% aromatics and 0% tetralin. However, there might be more existing candidates that also have good quality and high thermal stability to be acceptable JP-900 prototypes. But, that depends on how the criteria of optimization or specification were set. Coal-based jet fuels that are composed largely of aromatics, so tetralins or decalins can still be desirable in JP-900 if the limitations of aromatics, net heat of combustion and smoke points are flexible.

Table 7-7: Coordinates (X_1, X_2, X_3) correspond with the optimized areas shaded in pink color.

Position	X_1	X_2	X_3
0	0	0	0
1	19.97	66.25	13.78
2	19.97	65.09	14.95
3	0.55	80.64	18.82
4	0.01	79.97	20.02
5	0.18	64.04	35.78
6	4.31	54.39	41.31
7	8.09	50.71	41.20
8	14.27	46.58	39.15
9	28.87	35.56	35.57
10	23.55	39.41	37.04
11	24.92	35.90	39.18
12	11.52	46.76	41.71
13	4.14	50.76	45.11
14	1.21	49.24	49.55
15	0.00	38.39	61.61

The optimization methods by ternary plots can only be made for three input variables. To consider the importance of more than three compositions, MLR and ANN models can be used to correlate more input variables with properties, but they cannot display graphic relationship of more than three variables. However, the advantage of these two methods is that the optimum compositions from complex systems can be computed from the equations or the models. More data sets are necessary to establish the relationship of more multiple input variables. In addition, the contour ternary diagram was constructed from the interpolation of each data set. There might be some statistical errors associated in the boundaries of each property but they are not possible to be found from the graphic solution. Further work on optimization using MLR and ANN models will give more detail about this uncertainty.

7.5.2 Proposed Route for Production of Prototype JP-900

The optimum chemical composition can be made under the two pink shading areas in Figure 7-20. For the existing data, B-005 (and maybe B-004) is found to have compositions which are thermally stable while remaining good combustion properties. B-005 can be produced by blending saturated LCO and saturated RCO at a 1:1 ratio. To produce saturated LCO, the feedstock LCO from fluid catalytic cracking unit has to be hydrotreated (using a NiMo catalyst) at 710 psig and 685°F. After that, the saturation of aromatic rings will be performed using a Pt-Pd catalyst and operated at higher pressure at 2100 psig and lower temperature at 400-600°F. Saturated RCO can be produced in the same step as the saturated LCO.

Chapter 8

Relationship of Pyrolytic Stability and Hydrogen Types from ¹H NMR Spectroscopy: Quantitative Analyses

The discussion in Chapter 7 focused on finding meaningful correlations between chemical composition and properties by graphical plots, multiple regression analysis (MLR) and artificial neural network (ANN) approaches. This information is important for the final selection of the chemical composition of jet fuel. Similarly, this Chapter aims to find the relationship between quantified structures of jet fuels and their thermal stability. The significant effects of these particular structures on the solid deposition rate will be investigated by numerical analyses and compared with the chemical composition studied in previous Chapters.

It is well known that hydrogen abstraction from a hydrogen donor to stabilize a free radical at an elementary stage of pyrolysis is a key reaction for the improvement of jet fuel thermal stability [45, 62, 115]. As a result, the hydrogen donor structures in coal-based jet fuels are the main focus for this particular study. The identification and quantification of hydrogen types has been determined by ¹H NMR spectroscopy. These input variables and the solid deposition rate output will be investigated to determine if a correlation exists. As a consequence, reaction mechanisms of hydrocarbon decomposition in jet fuels can be made from this information, along with that previously discussed in Chapter 5.

8.1 Relationship of Hydrogen Types and Solid Deposition Rate

Types of hydrogen in bonding forty-four jet fuel samples have been identified and quantified, as shown in Table 4-6. Based on the literature [73, 108, 109], the hydrogen bonding types (in percents) have been classified into: H_A : chemical shift at 0.7–1.1 ppm; H_B : chemical shift at 1.1–1.4 ppm; H_C : chemical shift at 1.4–1.6 ppm; H_D : chemical shift at 1.7–2.0 ppm; H_E : chemical shift at 2.0–5.0 ppm; H_F : chemical shift at 6.5–7.05 ppm; and H_G : chemical shift at 7.05–9.0 ppm.

After performing ^1H NMR spectroscopy on forty-four jet fuel samples, the chemical shifts from all samples were compared and identified based on literature cited in Chapter 3. However, there is one single peak at around 2.6–2.7 ppm (in region E) that is always present in hydrotreated fuels but has never been identified in any literature. To identify this peak, four different pure compounds (decalin, tetralin, naphthalene and indane) were analyzed by ^1H NMR spectroscopy, as shown in Figure 8-1 and Figure 8-2 and Table 8-1. Positions of the ^1H NMR chemical shifts were approximated using the ^1H chemical shift simulation program in ChemDraw software and were compared with reference from Sadtler Research Laboratories [136].

Based on ChemDraw simulation and reference of NMR chemical shift index [136], the decalin molecule has three different chemical shifts. But the experimental result has shown four different peaks in region A, B, C and D, similar to those of saturated jet fuel samples. (See Figure 8-1 (a) and Table 8-1.) Since decalin does not have $-\text{CH}_3$ (represented by region A), it can be postulated that the absorption of each hydrogen (at position a, b and c) splits into multiple peaks (spin-spin splitting). These multiple

absorptions are caused by the interaction (or coupling) of the nuclear spins of nearby atoms. In other words, the tiny magnetic field of one nucleus affects magnetic field felt by neighboring nuclei [109]. As a result, it is not possible to identify each single hydrogen type from the multiplets as they are an accumulation of $-\text{CH}_2-$ (position a), $-\text{CH}_2-$ (position b) and $-\overset{|}{\underset{|}{\text{C}}}\text{H}-$ (position c). However, it is understood that the peak on the left side represents hydrogen in $-\overset{|}{\underset{|}{\text{C}}}\text{H}-$ (partially or totally) as it is the least electron-shielded nucleus.

In Figure 8-1 (b), tetralin has three main chemical shifts in region D, E and F. The peak in regions D and E represents $-\text{CH}_2-$ at positions a and b in the tetralin molecule, respectively. The chemical shifts of position c and d overlap with each other and represent monoaromatic ring of tetralin. The outstanding peak of position b at particular chemical shifts of 2.6-2.7 ppm is considered the highest potential for hydrogen abstraction due to its weak C-H bond [58, 137], and this peak always present in hydrotreated fuels. To study effects of hydrogen type on the deposition of solids, it is important to include this significant peak of region E in a mathematical model as E_1 . As a result, the chemical shift area of region E_1 was integrated and the number of hydrogen (H_{E1}) in percentage is obtained. This new chemical shift identification is shown in Figure 8-3.

Hydrogens at position a and b of the indane molecule in Figure 8-2 (b) have shown the same chemical shifts as those of positions a and b of tetralin molecule. By having both indane and tetralin, the concentration of hydrogen donors in the jet fuel mixture system is increased. However, the amount of indane that is present in jet fuel is

very small compared to amount of tetralin. Thus, the main hydrogen donor source is still tetralin.

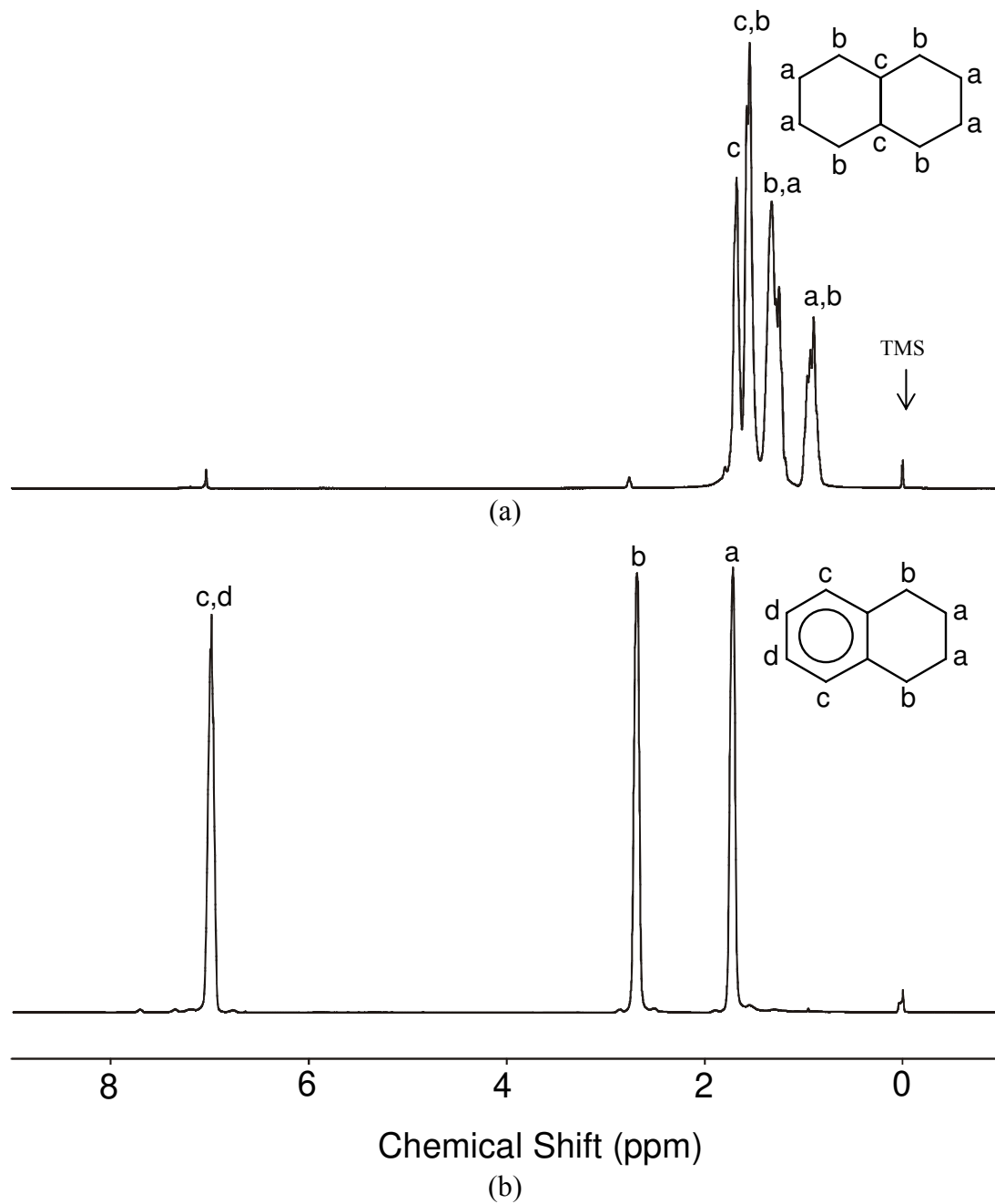


Figure 8-1: ¹H NMR spectra of (a) decalin and (b) tetralin.

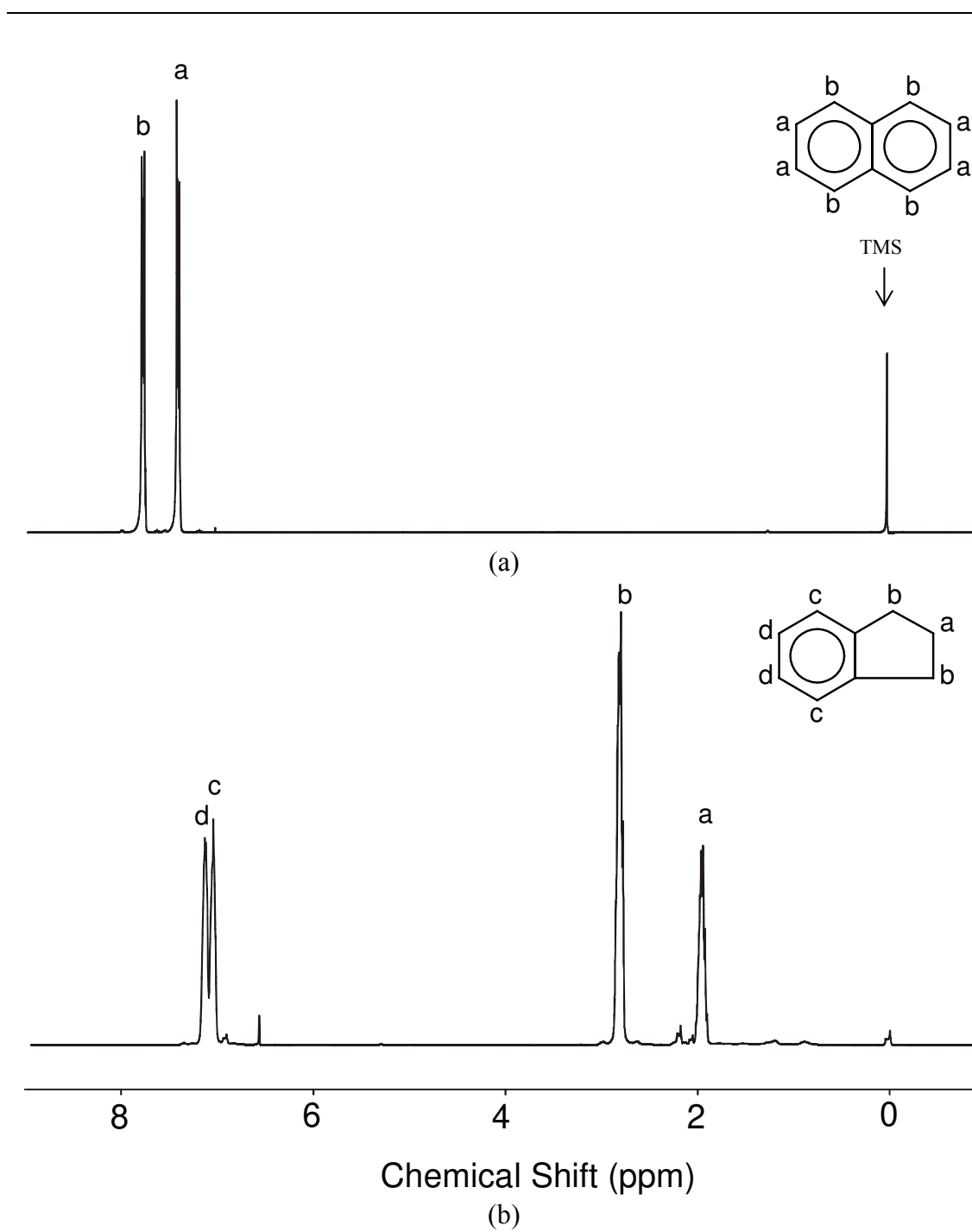
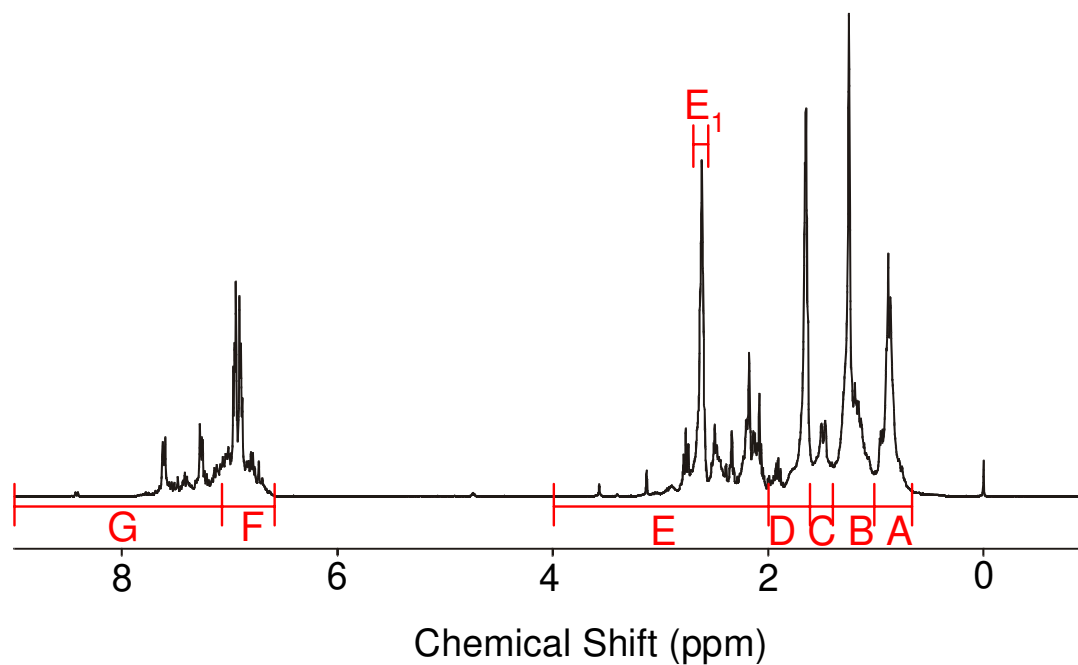


Figure 8-2: ¹H NMR spectra of (a) naphthalene and (b) indane.

Table 8-1: ^1H NMR chemical shifts in seven regions (%) of pure compounds.

Compounds	Region A	Region B	Region C	Region D	Region E	Region F	Region G
Decalin	15.47	33.40	32.87	18.26	0	0	0
Tetralin	0	0	0	33.41	33.34	31.67	1.58
Naphthalene	0	0	0	0	0	0	100
Indane	0	0	0	19.53	42.72	16.77	20.99

Figure 8-3: Chemical shifts of ^1H NMR spectra in seven regions.

Naphthalene has two chemical shifts in the diaromatic ring region (region G). The result is the same as those reported in the literature [136] and simulated by ChemDraw program.

Figure 8-4 shows the scatter plots between different hydrogen types of all regions (in percents) and solid deposition rates (R_s). From Figure 8-4 (a) and (b), solid deposition rates increased with the increase in number of hydrogens in regions A and B, which represent saturated primary and saturated secondary ($-\text{CH}_3$ and $-\text{CH}_2-$) groups. With saturated fuels, overlapping between $-\text{CH}_3$ and $-\text{CH}_2-$ can occur in region A. The saturated tertiary ($-\overset{|}{\text{C}}\text{H}-$) group represented by region C and aromatic hydrogens of regions F and G seemed to have an effect of inhibiting solid deposition rate. From Figure 8-4 (b), the overlapping of chemical shifts between the saturated tertiary ($-\overset{|}{\text{C}}\text{H}-$) group of decalin and the saturated secondary ($-\text{CH}_2-$) group of tetralin represented by region D has shown the most significant trend of inhibiting solid deposition. The hydrogen in region E_1 (or the $-\text{CH}_2-$ group of position b in tetralin molecule) has some effects on solid deposition while that of region E did not show any significant trend because there is some overlapping between many hydrogen structures.

In order to find a quantitative relationship between these hydrogen types and their significant effects on the solid deposition rates, numerical analyses by MRL and ANN were once again used for establishing linear and non-linear relationships. Assuming a linear relationship, the best correlation of solid deposition rate in terms of five hydrogen types can be found as follows:

$$(R_s \times 10^4) = 442 + 2.34 (H_A + H_B) - 11.3 (H_C + H_D + H_{E1}) \quad (8-1)$$

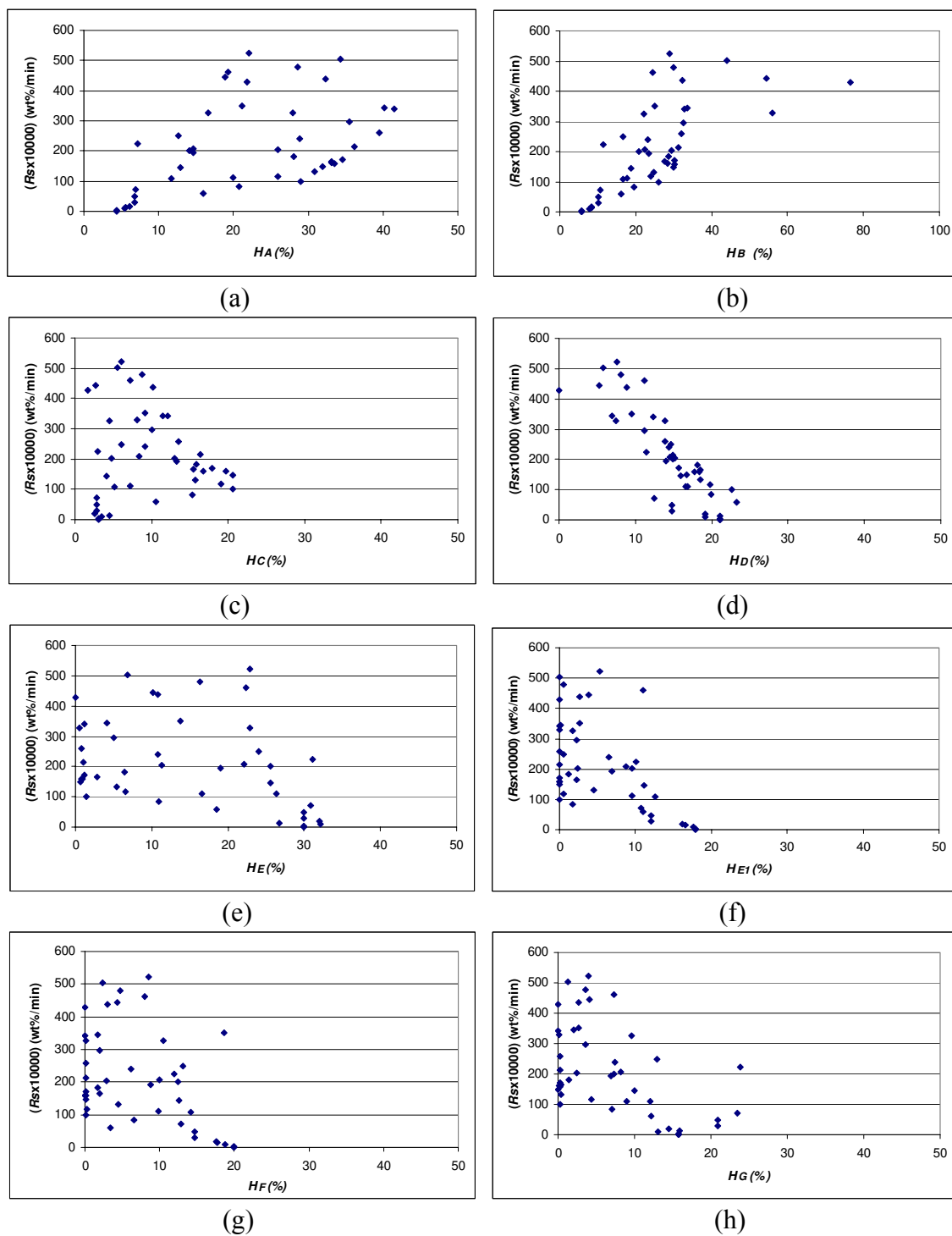


Figure 8-4: Scatter plots between solid deposition rates of forty-four jet fuel samples and their hydrogen structures in percentages: (a) region A, (b) region B, (c) region C, (d) region D, (e) region (E), (f) region E1, (g) region F and (h) region G.

Equation (8-1) represents a linear function between hydrogen types and solid deposition rates with $R^2 = 0.787$. As expected, the summation of H_C , H_D and H_E (saturated tertiary hydrogen atom of decalin and saturated secondary hydrogen atoms at position a and b of tetralin) seemed to have the highest significant effect of inhibiting solid deposition, while the saturated primary and secondary hydrogen atoms are likely to promote deposition. The H_F and H_G are not involved in the equation due to the limitation of the linear regression on insignificant parameters.

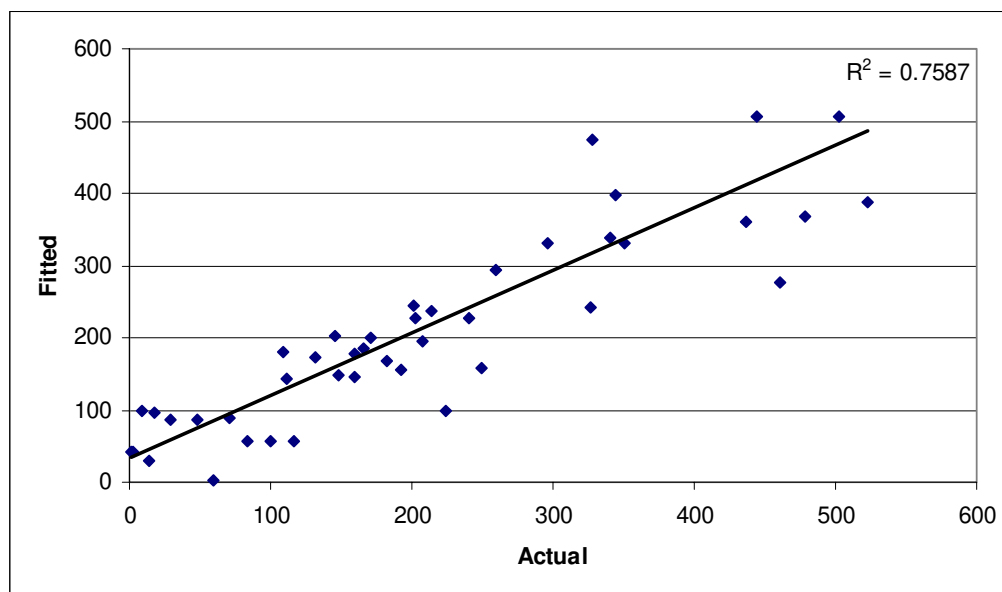
However, the R^2 obtained from this model is very low and MSE is quite high when compared to the previous relationship (Equation 7-1) of five chemical compositions and solid deposition rate ($R_s \times 10^4$). The Minitab program also had some limitations (such as meaningful determination of positive or negative coefficients) when including all seven regions as parameters for a linear relationship, so the use of ANN for analysis of a non-linear relationship is more practical. Discounting the insignificant hydrogen types of region E, NeuroShell 2 computed the network using three-layer back propagation architecture. The result of the best ANN model is shown in Table 8-2.

Once again, thirty-nine data sets were used for training and five production sets were simulated in network model to check accuracy of prediction. The final ANN model gives $R^2 = 0.9879$ and $MSE = 264.17$ and shows better correlation than the above MLR model and the other solid deposition rate models in Chapter 7. The relative contribution factors have determined that H_D (including saturated tertiary hydrogen atoms of decalin and saturated secondary hydrogen atoms at position a of tetralin and indane) in the range of 10-23% has the most significant effect on solid deposition rates. Aliphatic hydrogen atoms (H_A and H_B) indicative of alkane compounds also have high contributions to solid

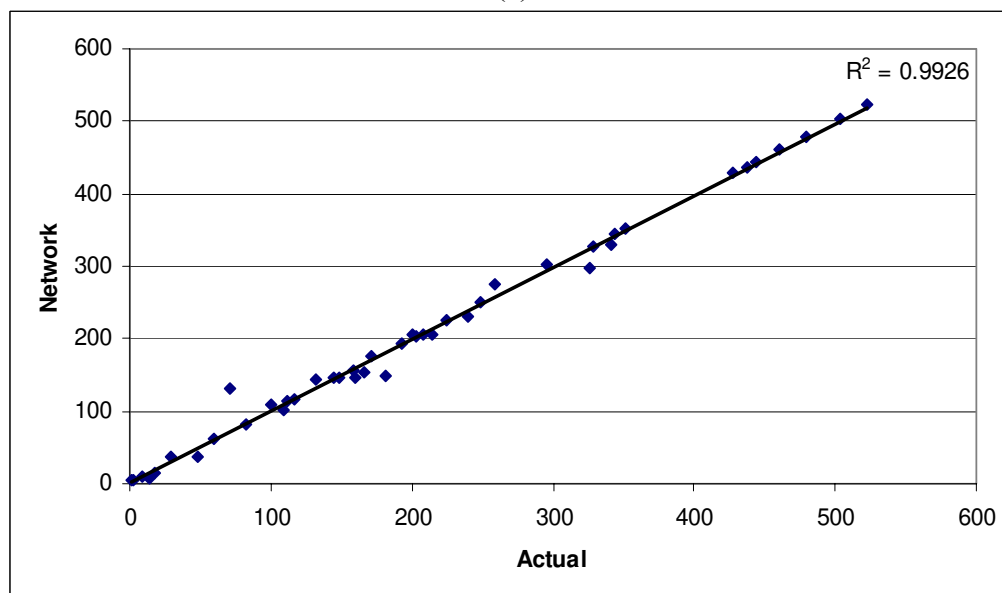
deposition rates, followed by saturated tertiary hydrogen atoms (H_C), aromatic hydrogen atoms (H_F and H_G) and saturated secondary hydrogen atoms of tetralin at position b (H_{E1}). These effects from the ANN model have shown more accurate prediction than the MLR model. See Figure 8-5. For the future use, the ANN model would be more effective for the prediction of solid deposition rate from the hydrogen structures characterized by ^1H NMR.

Table 8-2: ANN results for six hydrogen types vs. ($R_s \times 10^4$) (wt%/min) of forty-hour jet fuel samples.

Architecture of network:	BP-3 (5,8,1)	
Total data set:	44	
	Training set	Production set
Patterns processed:	39	5
Output:		
r squared:	0.9879	0.992
Mean squared error:	264.165	76.267
Mean absolute error:	7.435	5.887
Min. absolute error:	0	0.63
Max. absolute error:	63.356	18.188
Min. average error:	0.0000097	
Relative contribution factors:		
H_D	0.38171	
H_A+H_B	0.21713	
H_C	0.14785	
H_F+H_G	0.14425	
H_{E1}	0.10906	



(a)



(b)

Figure 8-5: Actual vs. predicted solid deposition rate on forty-four jet fuel samples: (a) MLR and (b) ANN.

From the MLR and ANN models, H_D has clearly shown the most significant effect to inhibit solid deposition, while H_A and H_B are the two key components that promote the rate. H_C , H_F+H_G and H_{EI} also show some small effects on suppressing solid deposition. In the fuel mixture, H_C , H_D , H_{EI} are expected to have the highest potential of donating protons to stabilize free radicals. Conversely, H_A and H_B are hydrogen atoms of aliphatic compounds that are likely to form primary and secondary alkyl radicals as a result of C-C bond breaking. To investigate the overall effect, the ratio of $(H_C+H_D+H_{EI})/(H_A+H_B)$ has been plotted against the solid deposition rate in Figure 8-6. A nice exponential model has been obtained with $R^2 = 0.9335$. $H_C+H_D+H_{EI}$ has shown to vary inversely with the amount of H_A+H_B while retaining the same relationship with solid deposition. Consequently, one can conclude that the solid deposition rates from the three models depends substantially on $H_C+H_D+H_{EI}$ (expected hydrogen donor structures) and the summation of H_A and H_B (or saturated primary and secondary hydrogen types). And, for both hydrotreated and saturated coal-based jet fuels, H_D is found to be high when the amount of RCO was increased in feedstock ratio (Table 4-6).

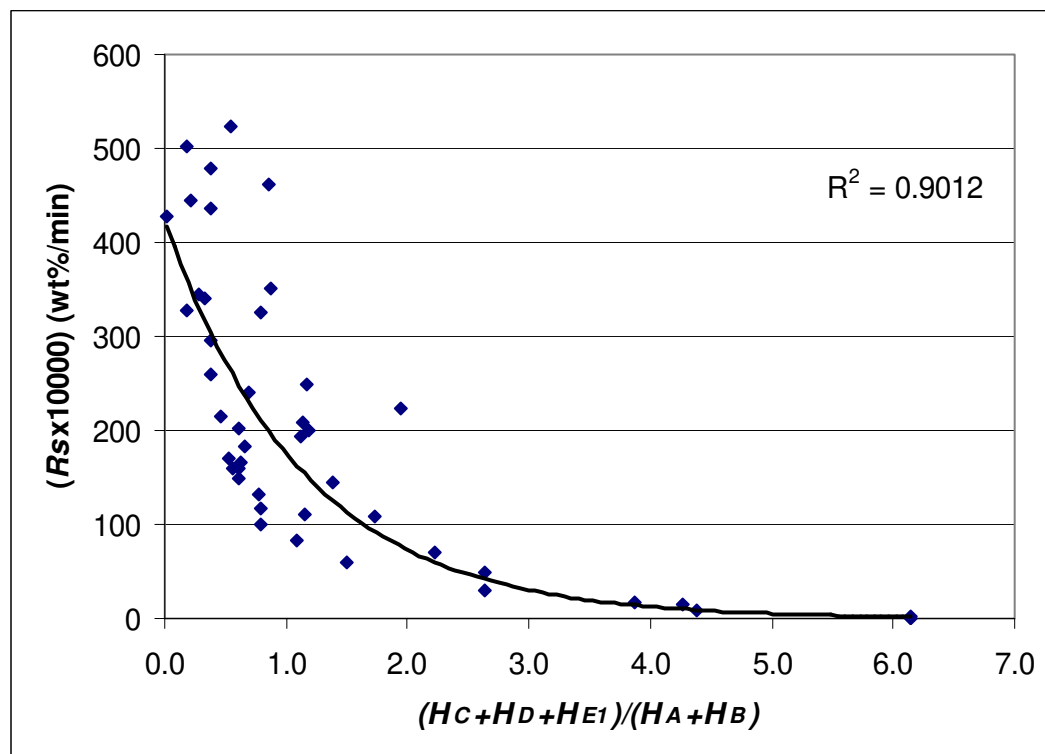


Figure 8-6: Correlation between solid deposition rate ($R_s \times 10^4$) (wt%/min) and $(H_C + H_D + H_{E1}) / (H_A + H_B)$ ratio.

To ensure that the hydrogen structures ($H_A + H_B$, H_C , H_D , $H_F + H_G$) from ^1H NMR analysis correspond with chemical composition from GC/MS analysis, each structure has been plotted against the respective suspected compound in Figure 8-7. It can be observed that the weight percentage of tetralin as well as indene directly correspond with $H_C + H_D + H_{E1}$ while the combination of alkane and alkene agree with percentages of aliphatic hydrogens ($H_A + H_B$). Figure 8-7 (c) shows an agreement with the previous discussion, in that hydrogen structures of tertiary carbon atoms in region C and D ($H_C + H_D$) are from decalin composition. Also, hydrogen structures of region G (H_G)

significantly correspond with the naphthalene component as shown in Figure 8-7 (d). Because corresponding results between ^1H NMR and GC/MS analyses are shown, the accuracy of characterization by both analyses can be confirmed.

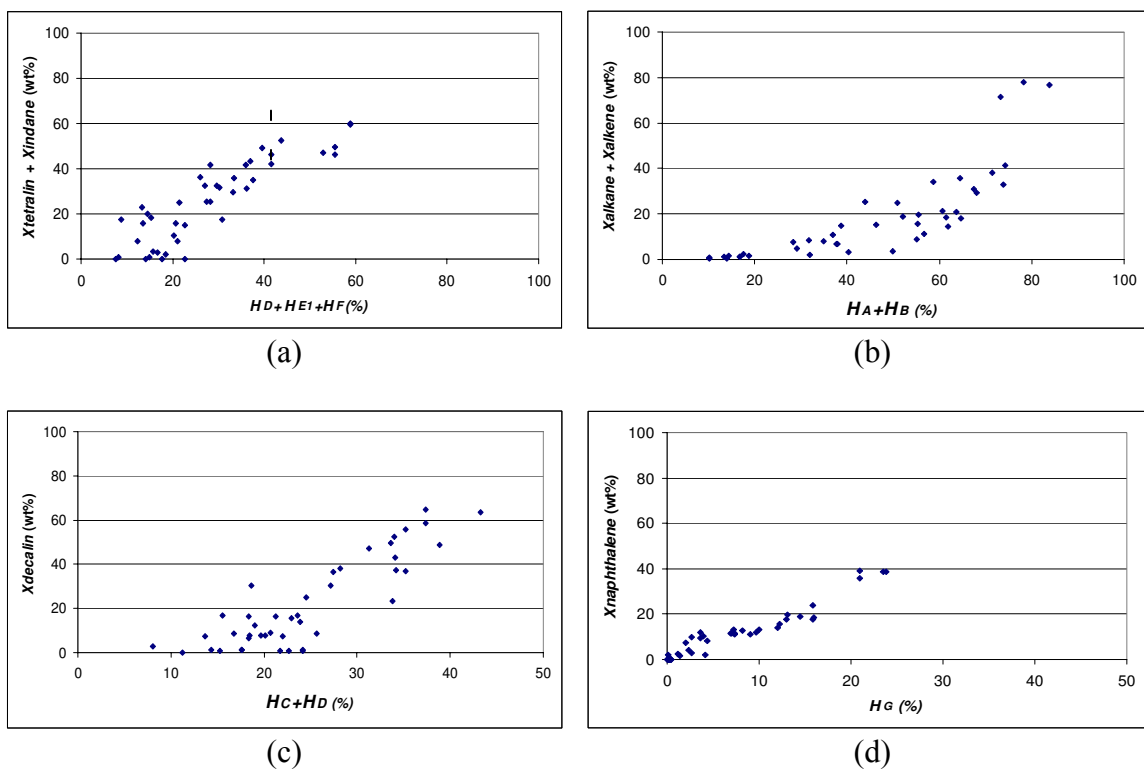


Figure 8-7: Scatter plots showing the correspondence between hydrogen structures (%) from ^1H NMR analysis and chemical composition (wt%) from GC/MS analysis.

From the three models discussed above, the hydrogen atoms in region D seem to help in suppressing solid deposition. The hydrogen structures in this region are dominated by the $-\text{CH}-$ group of decalin and $-\text{CH}_2-$ group of tetralin (at position a). Decalin is a stable compound and can act as a hydrogen donor. Its hydrogen in $-\text{C}-\text{H}-$ bonds has the highest potential for hydrogen transfer to stabilize the free radical because

it is likely to form a more stable tertiary alkyl radical instead of a secondary alkyl radical [137]. Tetralin is a better hydrogen donor because the effectiveness of H-transfer is substantially higher with tetralin than with decalin [59]. Considering its deposition rate, tetralin also appears to be the most stable compound among jet fuel model compounds [35, 40, 61].

The major type of hydrogen in the tetralin molecule that is likely to be donated to any free radicals is the secondary hydrogen atom ($-\text{CH}_2-$) which is adjacent to the benzene ring (position b in Figure 8-1 (b)). Tetralin has four hydrogen atoms adjacent to the benzene ring that are particularly amenable to abstraction by a radical. From Table 2-2, E_a of hydrogen abstraction to Ph-C• radical for tetralin is 13.2 kcal/mol. This is one of the lowest E_a among hydrogen donors (no. 27-34), compared to a common hydrogen acceptor, the Ph-C• radical. The great stability of the aromatic ring by electron delocalization results in an abstraction of hydrogen from weaker $-\text{CH}_2-$ bonds. However, this hydrogen, represented by H_{EI} in the three models, has shown a smaller effect in suppressing solid deposition when compared to H_D , which represents tertiary hydrogen atoms in decalin and another secondary hydrogen atom (position a) in tetralin. However, the combination of H_C , H_D and H_{EI} is the key factor representing all structures that has highest potential to donate hydrogen to stabilize free radicals. This investigation also supports the study of Song *et al.* [58].

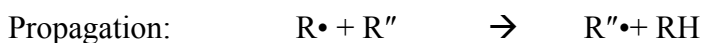
From the above discussion, H_A and H_B are the main factors that promote solid deposition rates. It is obvious that regions A and B represent saturated primary, secondary and possibly tertiary hydrogen atoms in long-chain alkanes. However, the effect of H_A and H_B on the solid deposition rates in the model does not directly involve

those hydrogen structures but is mainly due to the C-C bond associated with such hydrogen structures. These C-C bonds are relatively weak and likely to break when experiencing high temperatures. Tertiary alkyl radicals are more likely to occur than primary and secondary alkyl radicals because of their relatively low heats of formation, but they are rarely found in coal-based jet fuels.

8.2 Mechanisms for Coal-Based Jet Fuel Stressing in Pyrolytic Regime in Static Condition

Discussion of the major reactions in stressing of coal-based jet fuels is provided here. When jet fuel is stressed in the pyrolytic regime at a temperature of 480°C, the initial reaction of the hydrocarbons is pyrolysis of alkanes. As previously discussed, chain scission during alkane pyrolysis is due to thermolysis of their relatively weak C-C bonds, resulting in formation of alkyl free radicals. For coal-based jet fuels which have small amounts of alkanes, alkyl radicals can still be produced following this radical mechanism, and they can react with other molecules to abstract hydrogen, resulting in a stable species and a new alkyl radical. A characteristic of such a mechanism is that hydrogen atoms have to participate in the reaction routes as far as initiation and propagation of the radical reactions are concerned [138].

Chain scission of alkanes:



The free radicals above will then be stabilized by hydrogen-transferring reactions from hydrogen donors. Cycloalkanes, hydroaromatics and aromatics are abundant compounds in coal-based jet fuels and tend to be stable components. From the earlier discussion, decalin and tetralin have been proposed to be good hydrogen donors in coal-based jet fuels, while aromatics have been observed as precursors to the growth of polyaromatics, resulting in solid deposition. Their reactions under pyrolytic regime are as follows:

Dehydrogenation of decalin:

In Figure 8-8 (a), dehydrogenation of decalin is the reaction involved with hydrogen abstraction. The donated hydrogen will result in stabilization of free radicals and decalin will be converted to tetralin and finally to naphthalene. From the three models above, the tertiary hydrogen in the decalin molecule is expected to contribute to this process. This reaction is the major reaction pathway for saturated fuels which contain decalin as a major component. As presented in Figure 5-8, the longer the stressing time, the more hydrogen of tetralin (region E1) is present. Thus, the main reaction is the conversion of decalin to tetralin and then naphthalene in remaining liquid.

However, decalin in the pyrolytic regime can also undergo cracking processes, as some alkylbenzenes and alkenes have been observed after 30-minute reaction time in all experiments with saturated fuels. Figure 8-8 (b) also shows the significant cracking of the C-C bond after a tertiary hydrogen is donated.

Cracking of decalin:

Figure 8-8 (c) displays the major initiation process in the decomposition of pure decalin, which is the cleavage of the C-C bond that is shared with both rings, with the formation of a biradical [55, 138]. Alkenes are the main products from this reaction.

The other two reactions are not likely to be main reaction pathways of coal-based jet fuel pyrolysis because the cracking products (such as toluene and alkenes) from reaction (b) and (c) are observed but with small amounts when compared to tetralin and naphthalene.

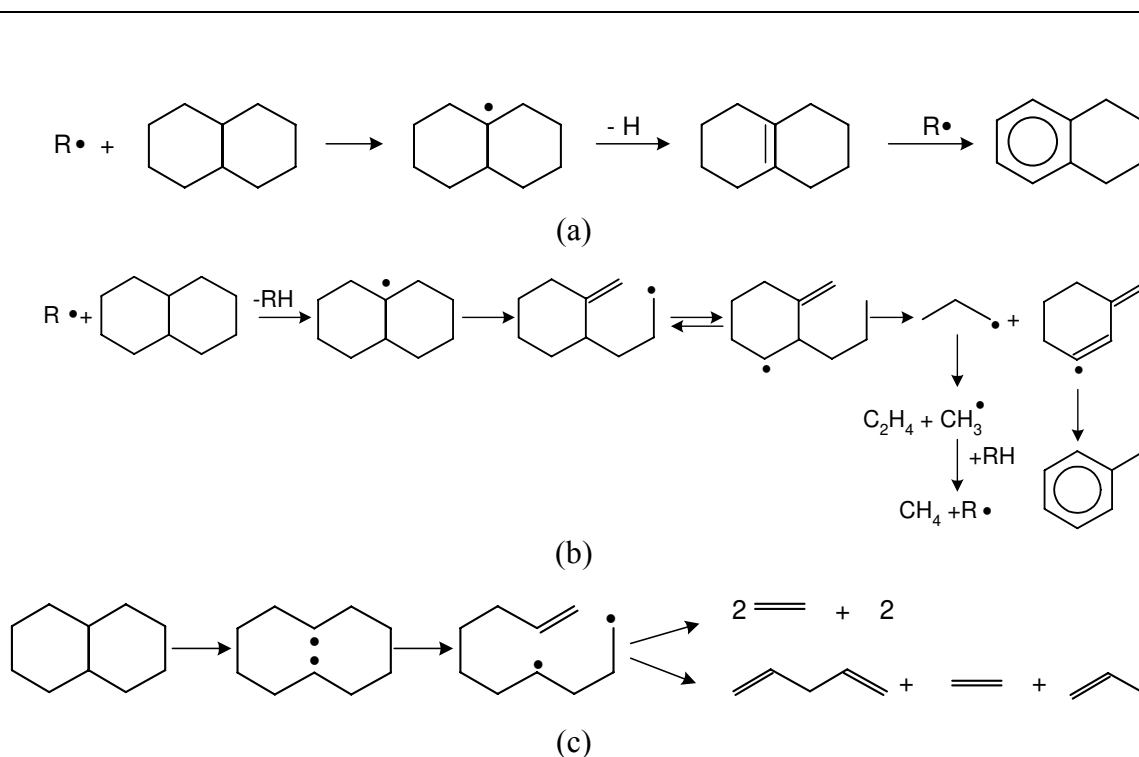


Figure 8-8: Major reactions of decalin in coal-based jet fuels: (a) dehydrogenation of decalin [58], (b) dehydrogenation of decalin followed with cracking [55], and (c) formation of biradical [55, 138].

Reactions of tetralin:

As mentioned in Chapter 2, there are three major routes of tetralin degradation. Results from GC/MS analyses of stressed products (Appendix C) have confirmed the conversion of tetralin (a major component in coal-based jet fuels) into various compounds. Major products, such as toluene, ethylbenzene, naphthalene, indane and indene, increase as the reaction time increased. For particular coal-based jet fuel reactions, it is possible to classify the mechanisms of tetralin pyrolysis into dehydrogenation, isomerization and cracking.

Dehydrogenation of tetralin:

Figure 8-9 (a) is the direct dehydrogenation of tetralin into naphthalene. Tetralin has four hydrogen atoms adjacent to the benzene ring that are particularly amenable to abstraction by an alkyl radical. At the high temperature of the pyrolysis regime ($>400^{\circ}\text{C}$), hydrogen attached to C atoms at the α position is abstracted to stabilize a free radical. Then, the abstraction of a second hydrogen atom by a radical is more facile. The allylic hydrogen atoms adjacent to the double bond are now also activated, which leads to sequential abstraction of a further two hydrogen atoms and finally the relatively stable end product naphthalene [45]. This is how tetralin stabilizes the free radicals that form during the pyrolytic degradation of the fuel and results in enhancement of thermal stability.

This reaction is assumed to be a major reaction pathway of tetralin pyrolysis for most hydrotreated fuels, especially hydrotreated RCO, the stressed products of which always contain significant of naphthalene residue. The reduction of hydrogen attached to

C atoms at the α position in hydrotreated LCO/RCO with an increase in stressing time (presented in ^1H NMR spectra in Figure 5-7) also supports this discussion.

Isomerization of tetralin:

Tetralin can undergo isomerization by opening the saturated ring to form 1-methylindane [51, 138]. This reaction can be observed by results from GC/MS analysis that show the increase of 1-methylindane with increasing stressing time.

Cracking of tetralin:

This is a degradation of tetralin by rupture of the saturated ring. The reaction leads to products such as ethylbenzene, benzene, ethylene and toluene [53, 138].

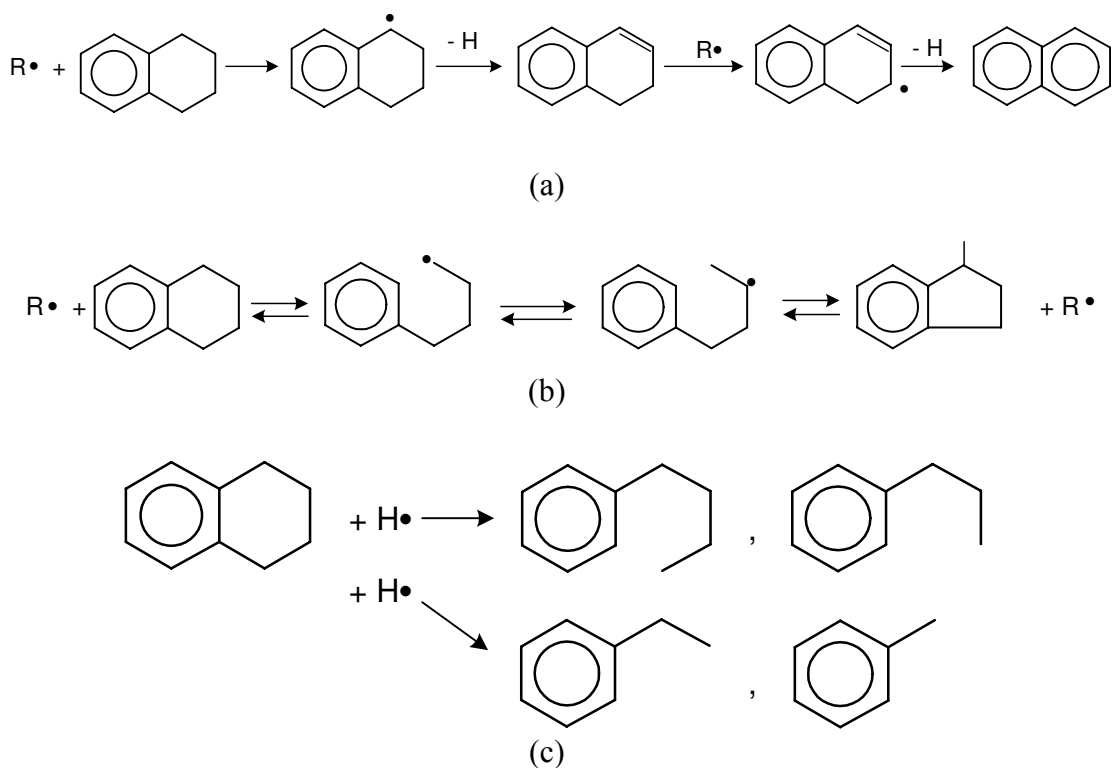


Figure 8-9: Major reactions of tetralin in coal-based jet fuels: (a) dehydrogenation [32, 53, 138], (b) isomerization [51, 53, 138], and (c) cracking [53, 138].

Condensation of aromatics:

Aromatics also undergo pyrolysis reactions. However, the aromatic ring is not ruptured but converted into polynuclear aromatics by condensation, with hydrogen being released and the molecular weight being increased [23]. From GC/MS results, biphenyl and binaphthyl have been found when stressing time increased as shown in Figure 8-10 (a) and (b). Condensation of aromatic compounds such as benzene and naphthalene in coal-based jet fuels lead to polynuclear aromatics of high molecular weight. These polyaromatics further react to form coke or solid deposit. The GC/MS results of stressed product from Appendix C can be relatively compared to proposed mechanism by Renjun (1993) [23] and Song *et al.* (1992) [32].

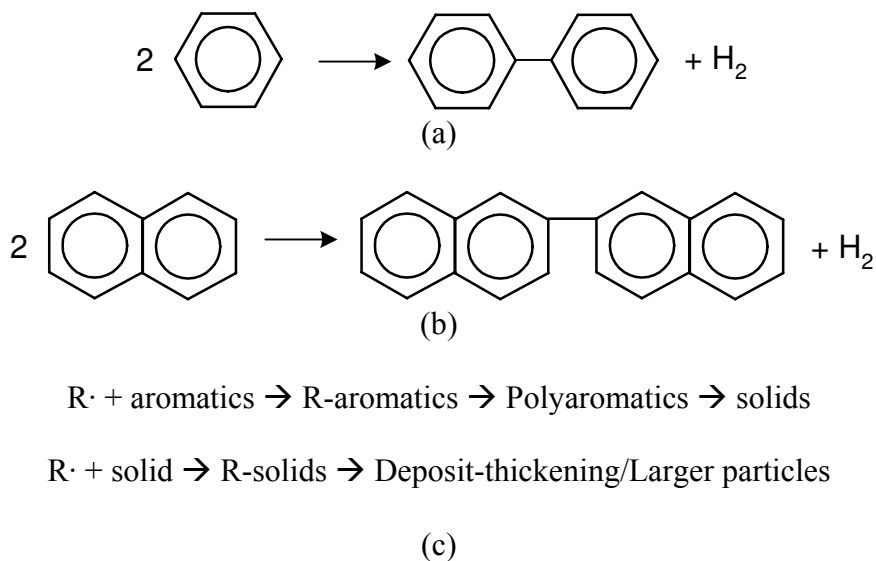


Figure 8-10: Condensation of aromatics to (a) biphenyl and (b) binaphthyl [23] and (c) solid formation from polyaromatics [32].

In summary, tetralin and decalin can donate hydrogen atoms to stabilize free radicals in the complex mixture of coal-based jet fuels. Their structural features that affect solid deposition can be identified and quantified by GC/MS and ^1H NMR spectroscopy. The results have shown that composition and structure have significant effects on the inhibition of solid deposition rates as shown by various mathematical models.

Chapter 9

Conclusions and Suggestions for Future Work

9.1 Conclusions

The pilot-scale production of thermally stable coal-based jet fuel, the so-called JP-900, has been performed on coal-derived liquids and a blend of coal-derived liquids with petroleum refinery streams. Three generations of hydrotreated and saturated coal-based jet fuels have been produced and their thermal stability properties have been tested in static and dynamic conditions in the autoxidative and pyrolytic regimes. Other properties, such as combustion characteristics, net heat of combustion, smoke point, flash point, viscosity and cloud point were also determined.

9.1.1 General Conclusions

To produce a future thermally stable jet fuel that can be utilized in advanced jet engines, the fuel quality has to meet ASTM specification requirements. It is important to obtain information on chemical composition, thermal stability and physical properties as the following:

- 1) GC/MS analysis was conducted on the fresh petroleum-derived jet fuels (JP-8 and JP-8+100) and coal-based jet fuel (JP-900) candidates from PARC. The compositions of all jet fuels were reported quantitatively based on eight basic compound classes. The distinction between petroleum-derived and coal-based jet fuels is mainly the

amount of alkanes, cycloalkanes and aromatics. The conventional JP-8 and JP-8+100 fuels are composed of alkanes as a major component while cyclic structures are abundant in JP-900 candidates.

2) The pyrolysis stability of the coal-based jet fuels has been extensively studied by stressing the fuels in a batch reactor. This is an important study because the condition represents the period after landing of high-Mach flight advanced jet aircraft, where some fuel is confined in very hot fuel lines for a certain period of time [6]. It is clear that most coal-based jet fuels produced lower solid and gas yields with increasing time than JP-8 and JP-8+100 did. With increasing concentration of RCO feed (or coal tar distillate components) to produce the hydrotreated and/or saturated fuel candidates, less solid deposition and gas formation were observed. This may be due to the increase of thermally stable components such as decalin and tetralin and the reduction of unstable alkanes.

In addition, thermal stability test results from the same samples in different systems such as batch and flow reactors or different metal surface have been varied from sample to sample. To make a final selection, a compromise between different systems is very important and leads to the investigation of optimum point.

3) The distribution of chemical compositions throughout the test in static conditions has been observed. For coal-based jet fuels, most of the aromatics in the stressed products are mainly naphthalene, followed by alkylbenzenes and multi-ring aromatics. The precipitation of solid naphthalene after the completion of reaction, observed from stressing hydrotreated RCO, is not a desirable effect.

4) Results from the quartz crystal microbalance (QCM) have shown that some hydrotreated coal-based jet fuels of the second generation which contain high tetralin concentrations can yield acceptable oxidative solid deposition rates.

5) The stressing of third generation jet fuels in static conditions has shown that the jet fuel boiling range is one of the important parameters to control the chemical composition of jet fuel, which is the key for thermal stability improvement.

6) The hydrotreated fuels appear to be low in net heat of combustion due to their high aromatic and low alkane concentrations. However, with the presence of high aromatic content, the fuel density and energy density are also significantly higher. This high energy density is desirable when storage volume limits fuel capacity.

The other problem associated with high aromatic contents is low smoke point, resulting in high sooting tendencies and emissions. However, there are signs of a trend toward lower fuel quality even at the present time. Specification requirements for maximum aromatic content and minimum smoke point have been relaxed in recent years and there has been some movement toward an allowable increase in naphthalene content [77].

7) In many cases, the relationship of composition and physical properties can be established by multiple linear regression (MLR) and artificial neural network (ANN) analysis. For the output of all properties, the input variables and their significant effects are similar for both MLR and ANN models. ANN is more effective than MLR as it can establish non-linear relationships of complex systems and it can also accurately predict unseen data sets. However, the limitation of MLR and ANN is that neither model is able to predict data that are out of the ranges of trained data set.

8) Tetralin and decalin can donate their hydrogen atoms to stabilize free radicals in a complex mixture of coal-based jet fuels. The structural features of these H-containing groups that affect solid deposition can be identified and quantified by GC/MS and ^1H NMR spectroscopy. The results from the two analyses have been found to be in good agreement. In addition, compositions and structures of jet fuels were found to have significant effects on the inhibition of solid deposition rate, as shown by various mathematical models.

9.1.2 Conclusions from Ternary Diagram

For visualization purposes, ternary diagrams have been used to display relationships of three main components with properties. The optimization methods using ternary plots have been performed to obtain chemical compositions that meet slow solid deposition rate, net heats of combustion above 18400 Btu/lb, and a smoke point at 19 mm. The 1:1 blend of saturated LCO and saturated RCO (B-005), composed of 0.76% aromatics and hydroaromatics, 68.47% cycloalkanes (47% decalin) and 30.77% alkanes and the others, is the only one sample that meet all requirements. However, there might be more existing candidates that also have good quality and high thermal stability to be acceptable JP-900 prototypes. But, that depends on how the criteria of optimization or specification were set.

9.2 Suggestions for Future Work

1) For static conditions, more data sets are necessary to establish relationships among more multiple input variables. Variation of more complex mixtures would help to create more desirable models for properties prediction. However, it is also interesting to make a test blend in the optimized area and check whether it meets the specification.

2) The autoxidative region can be studied in batch reactors at 250°C. The solid should be measured after this run and the reaction continued at 480°C. A connection between experiments in a microreactor and those in a QCM study would provide information of autoxidation effects on pyrolysis.

3) Further experimental data on solid deposition from different jet fuel mixtures during dynamic conditions should be performed and correlated with their chemical composition.

4) It might be interesting to observe the kinetics of the pyrolysis of coal-based jet fuels. Reaction kinetics in these complex fuel mixtures can be examined using site-specific ^{13}C -labeling [139, 140], but the high cost associated with ^{13}C -labeled compounds at specific sites in the molecule could be a problem.

5) Future study and inclusion of jet fuel lubricity to the ternary diagram will help in selection of the most desirable chemical composition of jet fuel.

6) The thermal stability tests reported in this work were performed on 316 stainless steel surface. The variation of metal surface should be performed to observe the effects of the surface on solid deposition rate.

Bibliography

1. Hazlett, R.N., *Thermal Oxidation Stability of Aviation Turbine Fuels (Monograph: 1)*. ASTM. 1991, Philadelphia, PA.
2. Kazakova, E., *Structure-Thermal Stability Relationship during Pyrolysis of Pure Hydrocarbon*. M.S. Thesis 1998, The Pennsylvania State University.
3. Andrésen, J.M., Strohm, J.J., Boyer, M.L., Song, C., Schobert, H.H. and Butnark, S., *Thermal Stability of Hydrotreated Refined Chemical Oil Derived Jet Fuels in the Pyrolytic Regime*. Preprints of Papers, American Chemical Society Division of Fuel Chemistry, 2001. **46**(1): p. 208-210.
4. Gregory, R., *Report for The Pennsylvania State University on the Production of a Cycloparaffinic-Rich Fuel for Assessment as Future Jet Fuel*. July 1997, Report from BP Oil International Ltd. (Sunbury, U.K.) to The Pennsylvania State University.
5. Wilson, G.R., *Project Report on AFOSR-Subcontract for Advanced Thermally Stable Coal-Based Jet Fuels for The Pennsylvania State University*. 2000, PARC Technical Services Inc. (Pittsburgh, PA) to The Pennsylvania State University.
6. Song, C., Lai, W. and Schobert, H.H., *Condensed-Phase Pyrolysis of n-Tetradecane at Elevated Pressures for Long Duration. Product Distribution and Reaction Mechanisms*. Industrial Engineering Chemistry Research, 1994. **33**: p. 534-547.
7. Badger, M.W., Zabarnick, S. and Wilson, G.R., *Selection of Prototype Thermally Stable Jet Fuels. 2. Quartz Crystal Microbalance Tests for Thermal-Oxidative Stability*. Preprints of Papers, American Chemical Society Division of Petroleum Chemistry, 2002. **47**(3): p. 198-200.
8. Statistical Abstract of the United States. U.S. Census Bureau, Department of Commerce. <http://www.census.gov/prod/www/statistical-abstract-us.html>, 1999.
9. Corporan, E., Roquemore, W. M., Harrison, W. E., Jacobson, A. and Phelps, D. K. *Air Force Programs to Reduce Particulate Matter Emissions from Aircraft*. in *38th AIAA/ASME/SAE/ASEE Joint Propulsion Conference & Exhibit*. 2002. Indianapolis, Indiana.

10. Edwards, T., Harrison, W.E. and Maurice, L.Q. *Properties and Usage of Air Force Fuel: JP-8; AIAA 2001-0498*. in *39th AIAA Aerospace Sciences Meeting and Exhibit*. 2001. Reno, NV.
11. Song, C., Hsu, S. and Mochida, I., *Chemistry of Diesel Fuels*. 2000: Taylor&Francis, New York.
12. Edwards, T., *System Drivers for High Heat Sink Fuels*. Preprints of Papers, American Chemical Society Division of Petroleum Chemistry, 2000. **45**(3): p. 436-439.
13. ASTM, *Annual Book of ASTM Standards*. 2000, Philadelphia, PA.
14. Edwards, T., *Recent Research Results in Advanced Fuels*. Preprints of Papers, American Chemical Society, Division of Petroleum Chemistry, 1996. **41**(2): p. 481-487.
15. Aeronautical Systems Center, *Turbine Fuels, Aviation, Kerosene Types, NATO F-34(JP-8), NATO F-35, and JP-8 + 100*.
http://assist2.daps.dla.mil/eAccess/index.cfm?ident_number=33505,1999.
16. The Energy Institute, *Advanced Thermally Stable Jet Fuel*. Pennsylvania State University. <http://www.energy.psu.edu/factsheets/Jet%20Fuels.pdf>, 2003.
17. Hazlett, R.N., *Free Radical Reactions Related to Fuel Research*, In *Frontiers of Free Radical Chemistry*. 1980: Pryor, W.A. Ed., Academic Press, New York. p. 195-223.
18. Zarbanick, S., *Chemical Kinetic Modeling of Jet Fuel Autoxidation and Antioxidant Chemistry*. Industrial Engineering and Chemistry Research, 1993. **115**: p. 1012-1017.
19. Heneghan, S.P. and Harrison III, W.E., *Antioxidants in Jet Fuels: A New Look*. Preprints of Papers, American Chemical Society, Division of Petroleum Chemistry, 1992. **37**(2): p. 404-411.
20. Morris, R.E., Hazlett, R.N. and McIlvaine III, C.L., *The Effects of Stabilizer Additives on the Thermal Stability of Jet Fuel*. Industrial & Engineering Chemistry Research, 1988. **27**(8): p. 1524-1528.
21. Beaver, B.D., Gao, L., Fedak, M.G., Coleman, M.M. and Sobkowiak, M., *Model Studies Examining the Use of Dicyclohexylphenylphosphine to Enhance the Oxidative and Thermal Stability of Future Jet Fuels*. Energy & Fuels, 2002. **16**(5): p. 1134-1140.

22. Edwards, T. *USAF Supercritical Hydrocarbon Fuels Interests*, AIAA 93-0807. in *31st Aerospace Sciences Meeting and Exhibit*. 1993. Reno, NV.
23. Renjun, Z., *Fundamentals of Pyrolysis in Petrochemistry and Technology*. 1993, Boca Raton, FL: CRC Press, Inc.
24. Nohara, D. and Sakai, T., *Kinetic-Study of Model Reactions in the Gas-Phase at the Early Stage of Coke Formation*. Industrial Engineering Chemistry Research, 1992. **31**(1): p. 14-19.
25. Dagaut, P., Cathonnet, M., and Boettner, J.C., *Kinetic Modeling of Propane Oxidation and Pyrolysis*. International Journal of Chemical Kinetics, 1992. **24**(9): p. 813-837.
26. Dagaut, P., Boettner, J.C. and Cathonnet, M., *Ethylene Pyrolysis and Oxidation - A Kinetic Modeling Study*. International Journal of Chemical Kinetics, 1990. **22**(6): p. 641-664.
27. Zhang, H.Y. and McKinnon, J.T., *Elementary Reaction Modeling of High-Temperature Benzene Combustion*. Combustion Science and Technology, 1994. **107**(4-6): p. 261-300.
28. Bittner, J.D. and Howard, J.B. *Composition Profiles and Reaction Mechanisms in A Near-Sooting Premixed Benzene/Oxygen/Argon Flame*. in *Eighteenth Symposium (International) on Combustion*, The Combustion Institute, Pittsburgh. 1981.
29. Kossiakoff, A. and Rice, F.O., *Thermal Decomposition of Hydrocarbons, Resonance Stabilization and Isomerization of Free Radicals*. Journal of American Chemical Society, 1943. **65**: p. 590-595.
30. Voge, H.H. and Good, G.M. *Thermal Cracking of Higher Paraffins*. Journal of American Chemical Society, 1949. **71**: p. 593-597.
31. Frenklach, M., Clary, D.W., Gardiner, W.C. and Stein, S.E., *Twentieth Symposium (International) on Combustion*, The Combustion Institute, Pittsburgh, 1984: p. 1067-1076.
32. Song, C., Peng, Y., Jiang, H. and Schobert, H.H., *On the Mechanisms of PAH and Solid Formation during Thermal Degradation of Jet Fuels*. Preprints of Papers, American Chemical Society Division of Petroleum Chemistry, 1992. **37**: p. 484-492.

33. Fabuss, B.M., Kafesjian, R., Smith, J.O. and Satterfield, C.N., *Thermal Decomposition Rates of Saturated Cyclic Hydrocarbons*. Industrial & Engineering Chemistry Process Design and Development, 1964. **3**: p. 248-254.
34. Lai, W. and Song, C., *Pyrolysis of Alkylcyclohexanes in or near the Supercritical Phase. Product Distribution and Reaction Pathways*. Fuel Processing Technology, 1996. **48**: p. 1-27.
35. Yu, J. and Eser, S., *Thermal Decomposition of Jet Fuel Model Compounds under Near-Critical and Supercritical Conditions. 2. Decalin and Tetralin*. Industrial Engineering Chemistry Research, 1998. **37**(12): p. 4601-4608.
36. Badger, G.M., and Spotswood, T.M., *Formation of Aromatic Hydrocarbons at High Temperatures. IX. Pyrolysis of Toluene, Ethylbenzene, Propylbenzene, and Butylbenzene*. Journal of Chemical Society, Abstracts, 1960: p. 4420-4427.
37. Szwarc, M., *The C-H Bond Energy in Toluene and Xylene*. Journal of Chemical Physics, 1948. **16**: p. 128-136.
38. Billaud, F., Chaverot, P., Berthelin, M. and Freund, E., *Thermal Decomposition of Cyclohexane at Approximately 810°C*. Industrial & Engineering Chemistry Research, 1988. **27**(5): p. 759-764.
39. Savage, P.E. and Klein, M.T., *Asphaltene Reaction Pathways. 2. Pyrolysis of n-Pentadecylbenzene*. Industrial & Engineering Chemistry Research, 1987. **26**: p. 488-494.
40. Yu, J. and Eser, S. *Thermal Decomposition of Jet Fuel Model Compounds under Near-Critical and Supercritical Conditions. 1. n-Butylbenzene and n-Butylcyclohexane*. Industrial Engineering Chemistry Research, 1998. **37**(12): p. 4591-4600.
41. Peng, Y., Ma, X., and Schobert, H.H., *Thermopyrolysis Mechanism of n-Alkylbenzene: Experiment and Molecular Simulation*. Preprints of Papers, American Chemical Society Division of Petroleum Chemistry, 1998. **43**(3): p. 368-372.
42. Peng, Y., *A Study on the Pyrolysis of Alkylbenzenes in Relation to the Thermal Stability of Jet fuels*. Ph.D. Thesis 1995, The Pennsylvania State University: University Park.
43. Edwards, T. and Liberio, P., *The Relationship between Oxidation and Pyrolysis in Fuels Heated to ~590°C (1100°F)*. Preprints of Papers, American Chemical Society, Division of Petroleum Chemistry, 1994. **39**(1): p. 92-96.

44. Yoon, E.M., *Exploratory Screening and Development of Potential Jet Fuel Thermal Stabilizers Over 400°C*. Ph.D. Thesis 1996, The Pennsylvania State University.
45. Coleman, M.M., Sobkowiak, M., Fearnley, S.P. and Song, C., *Hydrogen Donors as High Temperature (>400°C) Stabilizers for Jet Fuels – A Dilemma*. Preprints of Papers, American Chemical Society Division of Petroleum Chemistry, 1998. **43**(3): p. 353-356.
46. Simões, J.A.M., Greenberg, A. and Liebman, J.F., *Energetics of Organic Free Radicals*. 1st ed. Structure Energetics and Reactivity in Chemistry Series (SEARCH series); v 4. 1996, London; New York: Blackie Academic & Professional.
47. Tsang, W., *Heat of Formation of Organic Free Radicals by Kinetic Models, in Energetics of Organic Free Radicals*. 1996, Blackie Academic and Professional: London.
48. Ma, X. and Schobert, H.H., *Estimating Heats of Formation of Hydrocarbon Radicals by a Combination of Semiempirical Calculation and Family Correlation with Experimental Values*. Journal of Physical Chemistry, 2000. **104**: p. 1064-1074.
49. Camaioni, D.M., Autrey, S. T., Salinas, T. B., and Franz, J. A., *Calculation of the Effects of Branching and Conjugation on Intrinsic Barriers for H Atom Transfer Reactions Involving Hydrocarbons*. Journal of the American Chemical Society, 1996. **118**: p. 2013-2022.
50. Butnark, S., *Hydrogenation of Coal Tar Fractions and Refinery Streams*. M.S. Thesis 1999, The Pennsylvania State University.
51. Grigorieva, E.N., Panchenko, S.S., Fedorova, V.Y., Kagan, D.N., and Kaletchitz, I.V., *Tetralin Pyrolysis under H₂ Pressure, between 350 and 510°C*. Fuel Processing Technology, 1994. **38**: p. 85-97.
52. Hooper, R.J., Battaerd, H.A., and Evans, D.G., *Thermal Dissociation of Tetralin between 300 and 450°C*. Fuel, 1979. **58**: p. 132-138.
53. Bredael, P. and Vinh, T.H., *Pyrolysis of Hydronaphthalenes: Pyrolysis of Tetralin, 1,2-Dihydronaphthalene and 2-Methylindene*. Fuel, 1979. **58**: p. 211-214.
54. Brodski, D.M., Djega-Mariadassou, G., Li, C. and Kandiyoti, R., *Comparison of Product Distributions from the Thermal Reactions of Tetralin in a Stirred Autoclave and a Flowing-Solvent Reactor*. Fuel, 1994. **73**: p. 789-794.

55. Billaud, F., Chaverot, P. and Freund, E., *Cracking of Decalin and Tetralin in the Presence of Mixtures of n-Decane and Steam at about 810°C*. Journal of Analytical and Applied Pyrolysis, 1987. **11**: p. 39-53.
56. Penninger, J.M., *New Aspects of the Thermal Hydrocracking of Indan and Tetralin*. International Journal of Chemical Kinetics, 1982. **14**: p. 761-780.
57. Bredael, P. and Rietvelde, D., *Pyrolysis of Hydronaphthalenes 2. Pyrolysis of Cis-Decalin*. Fuel, 1979. **58**: p. 215-218.
58. Song, C., Eser, S., Schobert, H.H. and Hatcher, P.G., *Pyrolytic Degradation Studies of a Coal-Derived and a Petroleum-Derived Aviation Jet Fuel*. Energy & Fuels, 1993. **7**: p. 234-243.
59. Song, C., Lai, W. and Schobert, H.H., *Hydrogen-Transferring Pyrolysis of Cyclic and Straight-Chain Hydrocarbons*. Preprints of Papers, American Chemical Society Division of Fuel Chemistry, 1992. **37**(4): p. 1655-1663.
60. Donath, E.E. and Hess, M., *Thermally Stable Hydrocarbon Fuels*. Chemical Engineering Progress, 1960. **56**: p. 68-71.
61. Yu, J. and Eser, S., *Kinetics of Supercritical-Phase Thermal Decomposition of C10-C14 Normal Alkanes and Their Mixtures*. Industrial Engineering Chemistry Research, 1997. **36**(3): p. 574-584.
62. Ma, X. and Schobert, H.H., *Estimating the Activation Energy of Hydrogen-Abstraction Reactions Involving Hydrocarbons by Thermochemical Properties*. Industrial & Engineering Chemistry Research, 2003. **42**(6): p. 1151-1161.
63. Bell, R.P., *The Theory of Reactions Involving Proton Transfers*. Proceedings of the Royal Society of London, 1936. **A154**: p. 414-429.
64. Evans, M.G. and Polanyi, M., *Further Considerations on the Thermodynamic of Chemical Equilibria and Reaction Rates*. Transactions of the Faraday Society., 1936. **32**: p. 1333-1360.
65. Evans, M.G. and Polanyi, M., *Inertia and Driving Force of Chemical Reactions*. Transactions of the Faraday Society., 1938. **34**: p. 11-29.
66. Willems, P.A. and Froment, G.F., *Kinetic Modeling of the Thermal Cracking of Hydrocarbons. 2. Calculation of Activation Energies*. Industrial & Engineering Chemistry Research, 1988. **27**: p. 1966-1971.

67. Mukherjee, J., Sarofim, A.F., and Longwell, J.P., *Polycyclic Aromatic Hydrocarbons from the High-Temperature Pyrolysis of Pyrene*. Combustion and Flames, 1994. **96**(3): p. 191-200.
68. Dyroff, G.V., *Manual on Significance of Tests for Petroleum Products*. Fifth Edition ed. 1989, Philadelphia, PA: American Society for Testing and Materials.
69. Coordinating Research Council, *Handbook of Aviation Fuel Properties, Society of Automotive Engineers, CRC Report No. 530*. 1983.
70. Cookson, D.J. and Smith, B.E., *Observed and Predicted Properties of Jet and Diesel Fuels Formulated from Coal Liquefaction and Fischer-Tropsch Feedstocks*. Energy & Fuels, 1992. **6**: p. 581-585.
71. Cookson, D.J. and Smith, B.E., *Calculation of Jet and Diesel Fuel Properties Using ¹³C NMR Spectroscopy*. Energy & Fuels, 1990. **4**: p. 152-156.
72. Cookson, D.J., Iliopoulos, P. and Smith, B.E., *Composition-Property Relations for Jet and Diesel Fuels of Variable Boiling Range*. Fuel, 1994. **74**(1): p. 70-78.
73. Cookson, D.J., Latten, J.L., Shaw, I.M. and Smith, B.E., *Property-Composition Relationships for Diesel and Kerosene Fuels*. Fuel, 1985. **64**: p. 509-519.
74. Garrigues, S., Andrade, J.M., de la Guardia, M. and Prada, D., *Multivariate Calibrations in Fourier Transform Infrared Spectrometry for Prediction of Kerosene Properties*. Analytica Chimica Acta, 1995. **317**: p. 95-105.
75. Strauss, K.H., *Thermal Stability Testing of Aviation Turbine Fuel - A History, Aviation Fuel: Thermal Stability Requirement*. American Society for Testing and Materials. 1992, Philadelphia, PA.
76. Clark, R.H. and Bishop, G.J., "Measures of Fuel Thermal Stability - Which answer is Correct?", *Aviation Fuel: Thermal Stability Requirement*, ed. ASTM. 1992, Philadelphia, PA.
77. Kirklin, P.W. and David, P. *Aviation Fuel : Thermal Stability Requirements*. 1992, Philadelphia, PA: ASTM.
78. Goodger, E. and Vere, R., *Aviation Fuels Technology*. 1985, Hong Kong: MacMillan Publishers Ltd.
79. Parr Instrument Company, *Analytical Methods for Oxygen Bombs*, in *Operating Manual for the 1241 Oxygen Bomb Calorimeter*. 1994: Moline, IL.

80. Naegeli D.W. and Moses, C.A., *Effect of Fuel Molecular Structure on Soot Formation in Gas Turbine Engines*. ASME Paper No. 80-GT-62, 1980.
81. Olson, D.B., Pickens, J.C. and Gill, R.J., *The Effects of Molecular Structure on Soot Formation, II Diffusion Flames*". Combustion and Flame, 1985. **62**: p. 43-60.
82. Katritzky, A.R., Petrukhin, R., Jain, R. and Karelson, M., *QSPR Analysis of Flash Points*. Journal of Chemical Information and Computer Sciences, 2001. **41**: p. 1521-1530.
83. Katritzky, A.R., Lobanov, V.S. and Karelson, M., *CODESSA Reference Manual Version 2.0; University of Florida, Gainesville, FL*. 1996.
84. Satyanarayana, K. and Rao, P.G. *Improved Equation to Estimate Flash Points of Organic Compounds*. Journal of Hazard Matter, 1992. **32**: p. 81-85.
85. Riazi, M., *Prediction of Thermophysical Properties of Petroleum Fractions*, in *Chemical Engineering*. 1979, The Pennsylvania State University.
86. Hu, J. and Burns, A.M., *New Method Predicts Cloud, Pour, Flash Points of Distillate Blends*. Hydrocarbon Processing and Petroleum Refiner, 1970. **49**: p. 213-216.
87. Saiban, S. and Brown, T.C., *Kinetic Model for Cloud-Point Blending of Diesel Fuels*. Fuel, 1997. **76**(14/15): p. 1417-1423.
88. Cookson, D.J., Iliopoulos, P. and Smith, B.E., *Compositon-Property Relations for Jet and Diesel Fuels of Variable Boiling Range*. Fuel, 1995. **74**(1): p. 70-78.
89. Neter, J., Wasserman, W. and Kutner, M.H., *Applied Linear Statistical Models: Regression, Analysis of Variance, and Experimental Designs*. Third Edition ed. 1990: Richard D. Irwin, Inc.
90. Garson, D., *Multiple Regression*. North Carolina State University. <http://www2.chass.ncsu.edu/garson/pa765/regress.htm>, July 2003.
91. Montgomery, D.C., Peck, E.A. and Vining, G.G. *Introduction to Linear Regression Analysis*. 3rd ed. 2001, New York: J. Wiley.
92. MEDCALC Statistical Software, *Multiple Regression*. <http://www.medcalc.be/manual/mpage06-04c.html>, July 2003.

93. Cravener, T.L. and Roush, W.B., *Prediction of Amino Acid Profiles in Feed Ingredients: Genetic Algorithm Calibration of Artificial Neural Networks*. Animal Feed Science and Technology, 2001. **90**: p. 131-141.
94. Zupan, J. and Gasteiger, J. *Neural Networks in Chemistry and Drug Design*. Second Edition ed. 1999: WILEY-VCH Verlag GmbH, D-69469 Weinheim (Federal Republic of Germany).
95. Zupan, J. and Gasteiger, J. *Neural Networks for Chemists: An Introduction*. 1993, Weinheim ; New York.
96. Ward Systems Group, Inc., *NeuroShell 2 Online Tutorial*. 1993-1998: MD.
97. Demuth, H. and Beale, M., *Neural Network Toolbox: For Use with MATLAB*. 1998: The MathWorks, Inc. Natick, MA.
98. Rudnick, L.R., *Personal Communication*. February 2003: University Park, PA.
99. Gregory, R., *Report for The Pennsylvania State University on the Production of a Cycloparaffinic-Rich Fuel for Assessment as Future Jet Fuel*. 1997, Report from BP Oil International Ltd. (Sunbury, U.K.) to The Pennsylvania State University.
100. Badger, M.W., *The Identification of Recalcitrant Nitrogen Containing Compounds During the Production of Coal-Based Jet Fuel*. Preprints of Papers, American Chemical Society Division of Petroleum Chemistry, 2000. **45**(3): p. 531-533.
101. Wilson, G.R., *Project Report on AFOSR-Subcontract for Advanced Thermally Stable Coal-Based Jet Fuels for The Pennsylvania State University*. 2001, PARC Technical Services Inc. (Pittsburgh, PA) to The Pennsylvania State University.
102. Wilson, G.R., *Project Report on AFOSR-Subcontract for Advanced Thermally Stable Coal-Based Jet Fuels for the Pennsylvania State University*. 2002a, PARC Technical Services Inc. (Pittsburgh, PA) to Pennsylvania State University.
103. Wilson, G.R., *Project Report on AFOSR-Subcontract for Advanced Thermally Stable Coal-Based Jet Fuels for the Pennsylvania State University*. 2002b, PARC Technical Services Inc. (Pittsburgh, PA) to Pennsylvania State University.
104. Butnark, S., Badger, M., and Schobert, H.H., *Selection of Prototype Thermally Stable Jet Fuels. 3. Jet Fuel Boiling Range and Its Affect on Pyrolytic Stability*. Preprints of Papers, American Chemical Society Division of Petroleum Chemistry, 2002. **47**(3): p. 201-203.

105. Clifford, D.J., *GC Quantitation*, in *Class Note: EGEE 597D*. 2002, The Pennsylvania State University.
106. King, S.B., Wake Forest University, *Typical Chemical Shifts in Carbon NMR Spectra*. <http://www.wfu.edu/~ylwong/chem/nmr/c13/c13chemshift.html>, 2003.
107. King, S.B., Wake Forest University, *Typical Chemical Shifts in Proton NMR Spectra*. <http://www.wfu.edu/~ylwong/chem/nmr/h1/chemshiftlist.html>, 2003.
108. Gülder, Ö.L., Glavincevski, B., and Das, S., *Effect of Molecular Structure on Soot Formation Characteristics of Aviation Turbine Fuels*. *Journal of Engineering for Gas Turbines and Power*, 1989. **111**: p. 77-83.
109. McMurry, J., *Organic Chemistry*. 4th ed. 1996, Pacific Grove: Brooks/Cole Pub. Co.
110. Song, C. and Nomura, M., *Catalytic Effects of MoCl₃- and NiCl₂-Containing Molten Salts for Hydroliquefaction of Morwell Brown and Taiheiyo Subbituminous Coals*. *Bulletin of the Chemical Society of Japan*, 1986. **59**: p. 3643-3648.
111. Strohm, J.J., Andrésen, J.M., and Song, C., *Characterization and Pyrolytic Performance of Hydrotreated Derivatives from a Light Cycle Oil for Advanced Jet Fuel Applications*. Preprints of Papers, American Chemical Society Division of Petroleum Chemistry, 1999. **44**(3): p. 386-390.
112. Zabarnick, S. and Grinstead, R.R., *Studies of Jet Fuel Additives Using the Quartz Crystal Microbalance and Pressure Monitoring at 140°C*. *Industrial Engineering Chemistry Research*, 1994. **33**: p. 2771-2777.
113. Roan, M.A., *Flow Reactor Studies of Petroleum-Derived Jet Fuels*. M.S. Thesis 1999, The Pennsylvania State University.
114. Roan, M.A. and Boehman, A.L., *Thermal Stability as a Function of Fuel Composition*. Preprints of Papers, American Chemical Society Division of Petroleum Chemistry, 2002.
115. Strohm, J.J., *Novel Hydrogen Donors for the Improved Thermal Stability of Advanced Aviation Jet Fuels*, in *Department of Energy and Geo-Environmental Engineering*. M.S. Thesis 2002, The Pennsylvania State University.
116. Altin, O., Bock, G. and Eser, S., *Thermal Stressing of Petroleum and Coal-Derived Jet Fuels on Inconel 718*. Preprints of Papers, American Chemical Society Division of Petroleum Chemistry, 2002. **47**(3): p. 208-211.

117. LECO Corporation, *CHN-600 Determinator Instruction Manual*. 1983.
118. Grabner Instruments, *Technical Description: MINIFLASH: Fully Automatic Flash Point Tester (CCCFP-Method)*. 2003: Vienna, Austria.
119. ASTM, *Annual Book of ASTM Standards*. 1956, Philadelphia, PA.
120. Perry, R.H., Green, D.W. and Maloney, J.O., *Perry's Chemical Engineers' Handbook*. 7th / ed. 1997, New York: McGraw-Hill.
121. Berkous, S.K., Schobert, H.H., Burgess, C.E. and Clifford, D.J., *Effects of Low Temperature Oxidation of Jet Fuel on Cloud Point*. Preprints of Papers, American Chemical Society Division of Fuel Chemistry, 2002. **47**(3): p. 187-188.
122. Imschweiler, D., Lee, S.-Y., Saretto, S., McKeand, M., Linevsky, M., Litzinger, T.A., and Santoro, R.J., *Fuel Additive Studies for Soot Reduction in a High-Pressure Model Gas Turbine Combustor*. Propulsion Engineering Research Center, 14th annual symposium, The Pennsylvania State University, 2002.
123. Butnark, S., Badger, M., and Schobert, H.H., *Evaluation of Coal Tar Pitch Fractions as Feedstocks for Thermally Stable Jet Fuel*. Preprints of Papers, American Chemical Society Division of Fuel Chemistry, 1999. **44**(3): p. 662-666.
124. Yoon, E.M., Selvaraj, L., Eser, S., and Coleman, M.M., *High-Temperature Stabilizers for Jet Fuels and Similar Hydrocarbon Mixtures. 2. Kinetic Studies*. Energy & Fuels, 1996. **10**: p. 812-815.
125. Veytsman, B. and Coleman, M.M., *High Temperature Limit of Jet Fuel Stability - A Simple Kinetic Model*. Preprints of Papers, American Chemical Society Division of Petroleum Chemistry, 1998. **43**(3): p. 387-389.
126. Zabarnick, S., *Pseudo-Detailed Chemical Kinetic Modeling of Antioxidant Chemistry for Jet Fuel Applications*. Energy & Fuels, 1998. **12**: p. 547-553.
127. Pajak, J., Krebs, V., Mareche, J.F. and Furdin, G., *Hydrogen Transfer from Tetralin and Decalin to High-temperature Coal Tars. Relation with Carbon Deposit Formation*. Fuel Processing Technology, 1996. **48**: p. 73-81.
128. Paushkin, Y.M., *The Chemical Composition and Properties of Fuels for Jet Propulsion*. 1962, New York: Pergamon Press.
129. Roan, M.A., *The Effect of Dissolved Oxygen on the Pyrolytic Degradation of Jet Fuels*. 2003, The Pennsylvania State University.
130. Schobert, H.H., *Personal Communication*. August 2001: University Park, PA.

131. Department of Refining, A.P.I., *Technical Data Book, Petroleum Refining*. Metric ed. 1987, Washington, D.C.: American Petroleum Institute.
132. Pande, G.S. and Hardy, D.R., *An In-Depth Evaluation of combustion Performance Predictors of Aviation Fuels Sooting Tendencies*. Energy & Fuels, 1995. **9**: p. 448-457.
133. Roush, W.B., *Personal Communication*. March-April 2002: University Park, PA.
134. Lai, W. and Song, C., *Reactive Structure Index for Correlation of High Temperature Thermal Stability of Saturated Hydrocarbons*. Preprints of Papers, American Chemical Society Division of Petroleum Chemistry, 1996. **41**(2): p. 524-528.
135. Technical Support; Ward Systems Group, Inc., *Personal Communication*. May 2002 - May 2003, Frederick, MD.
136. Sadtler Research Laboratories, *NMR Chemical Shift Index*. 1994, Philadelphia, PA.
137. Ma, X., *Personal Communication*. June 2003: University Park, PA.
138. Hillebrand, W., Hodek, W. and Kölling, G., *Steam Cracking of Coal-Derived Oils and Model Compounds I. Cracking of Tetralin and t-Decalin*. Fuel, 1984. **63**: p. 756-761.
139. McKinney, D.E., Bortiatynski, J.M. and Hatcher, P.G., *Use of Site Specific ¹³C-Labeling to Examine the Thermal Stressing of 1-Phenylhexane: A Case Study for the Determination of Reaction Kinetics in Complex Fuel Mixtures Versus Model Compound Studies*. Preprints of Papers, American Chemical Society Division of Petroleum Chemistry, 1996. **41**(2): p. 457-463.
140. McKinney, D.E., *Use of ¹³C-labeled Compounds to Trace Their Reactivity in Fossil Fuel Systems*. Ph.D. Thesis 1998, The Pennsylvania State University.

Appendix A

Nomenclature

Abbreviation

ANN	=	Artificial neural network
ASTM	=	American Society for Testing and Materials
BP	=	Back propagation
FP	=	Freezing point
GC/MS	=	Gas chromatography/Mass spectrometry
HDN	=	Hydrodenitrogenation
HDS	=	Hydrodesulfurization
LCO	=	Light cycle oil
MLR	=	Multiple linear regression
MSE	=	Mean square error
<i>MW</i>	=	Molecular weight
NMR	=	Nuclear magnetic resonance
RCO	=	Refined chemical oil
<i>RF</i>	=	Response factor

Roman

<i>A_{known}</i>	=	Known peak area of the target
<i>A_{istd}</i>	=	Peak area of the internal standard

$C_{unknown}$	=	Unknown concentration of the target
C_{istd}	=	Concentration of internal standard
E_a	=	Activation energy (kcal/mol)
f	=	Transfer function
H	=	Hydrogen in weight percent
H_A	=	Percent of hydrogens having chemical shift at 0.7–1.1 ppm
H_B	=	Percent of hydrogens having chemical shift at 1.1–1.4 ppm
H_C	=	Percent of hydrogens having chemical shift at 1.4–1.6 ppm
H_D	=	Percent of hydrogens having chemical shift at 1.7–2.0 ppm
H_E	=	Percent of hydrogens having chemical shift at 2.0–4.0 ppm
H_{EI}	=	Percent of hydrogens having chemical shift at 2.6–2.7 ppm
H_F	=	Percent of hydrogens having chemical shift at 6.5–7.05 ppm
H_G	=	Percent of hydrogens having chemical shift at 7.05–9.0 ppm
m	=	Mass (g)
n	=	Mole
P	=	Pressure (psi)
Q_g	=	Gross heat of combustion (Btu/lb)
Q_n	=	Net heat of combustion (Btu/lb)
R	=	Gas constant (0.082 atm.L/g mol.K)
R^2	=	Coefficient of determination
R_s	=	Solid deposition rate (wt%/min)
S	=	Smoke point (mm)
T	=	Temperature (K)

T_f	=	Flash point (°F)
V	=	Volume (L)
X_{alkane}	=	Alkane composition (%)
$X_{aromatic}$	=	Aromatic composition (%)
$X_{cycloalkane}$	=	Cycloalkane composition (%)
$X_{decalin}$	=	Decalin composition (%)
$X_{naphthalene}$	=	Naphthalene composition (%)
$X_{non-aromatic}$	=	Non-aromatics composition (%)
$X_{tetralin}$	=	Tetralin composition (%)
$X_{total\ aromatic}$	=	Total aromatics composition (%)

Greek

ν	=	Kinematic viscosity (cSt)
-------	---	---------------------------

Appendix B

GC/MS Analysis of Chemical Composition of Jet Fuels

B.1 Response Factor of Compound Classes and Determination of Eight Compound Classes' Concentration

Table B-1: Response factor (RF) of hydrocarbon compounds to THF internal standard.

Compound	Time (min)	RF	Compound	Time (min)	RF
Alkanes			Hydroaromatics		
Octane	3.3	1.3	Indane	6.8	1.3
Decane	6.1	1.1	Indene	6.9	1.3
Undecane	7.7	1.1	Tetralin	8.8	1.2
Dodecane	9.1	1.1	Naphthalene, methyl naphthalene		
Tridecane	10.5	1.0	Naphthalene	9.1	1.3
Tetradecane	11.9	1.0	Naphthalene 1-methyl	10.9	1.2
Eicosane	18.5	2.9	Other Aromatics		
Alkenes			Biphenyl	11.8	1.7
1-decene	6.0	1.3	Acenaphthylene	12.7	2.4
Cycloalkanes			Acenaphthene	13.2	1.5
Cyclohexane methyl	2.6	1.1	Dibenzofuran	13.6	2.3
Decalin trans	7.2	1.1	Anthracene 9,10 dihydro	15.5	2.7
Decalin cis	7.8	1.2	Anthracene	16.6	2.2
Bicyclohexyl	10.8	0.9	Phenanthrene	16.7	2.0
Benzenes, alkylbenzenes			Fluoranthene	19.4	2.1
Benzene	2.2	0.7	Pyrene	19.9	2.0
Toluene	3.0	0.9	Binaphthalene	22	2.1
Ethylbenzene	4.2	1.1	Note: RFs of other minor alkane, alkene, cycloalkane compounds are assumed to be equal to one, while aromatics are assumed to be equal to two.		
Benzene trimethyl	6.6	1.4			
Benzene butyl	7.1	0.8			
Benzene cyclohexyl	11.0	1.2			

B.2 MATLAB Source Code for Peak Identification

The source code function for the determination of eight compound classes' percentages is created by MATLAB program in the file name "FindPercent.m".

```
function [CompSum, Percent] = FindPercent(conc,rep);

% FUNCTION [CompSum, Percent] = FindPercent(conc,rep);
% PURPOSE:
% Find percentage of each compound class.
% SYNTAX:
% [CompSum, Percent] = FindPercent(A); where A = [conc rep];
% [CompSum, Percent] = FindPercent(conc,rep);
% INPUTS:
% conc = Column vector of each compound's concentration from calculation of peak
area identified by GC/MS analysis.
% rep = Column vector containing compound class numbers (1-8).
% OUTPUTS:
% CompSum = Column vector of total concentration for each compound class.
% Percent = Column vector of percentage for each compound class.
%
% @date: 13-May-2003 22:19:06

% If there is only one input, it will be separated into two variables.
% "Nargin" stands for number of function input arguments.
if nargin < 2
    rep = conc(:,2);
    conc = conc(:,1);
end

% Response factor of eight compound classes.
factor = [1 1 1 1.2 1.3 2 1.1 1.2];

% Separate all compounds into eight classes and multiply by the response factor of each
class.
% The accumulation of concentration of each compound class' is represented as "comp".
% The final value of "total" is the final concentration of all compounds.
total = 0;
for k=1:8
    index = find(rep==k);
```

```
    comp{k} = factor(k)*conc(index);  
    total = total + sum(comp{k});  
end
```

% Calculate sum of each compound class' concentration and its associated percentage.

```
CompSum = zeros(8,1);  
Percent = zeros(8,1);  
for k=1:8  
    CompSum(k) = sum(comp{k});  
    Percent(k) = CompSum(k)/total*100;  
end
```

% Two-column display of summation of each compound class' concentration and its percentage.

```
[CompSum Percent]
```

B.3 Chromatogram of Petroleum and Coal-Based Jet Fuels from GC/MS Analysis

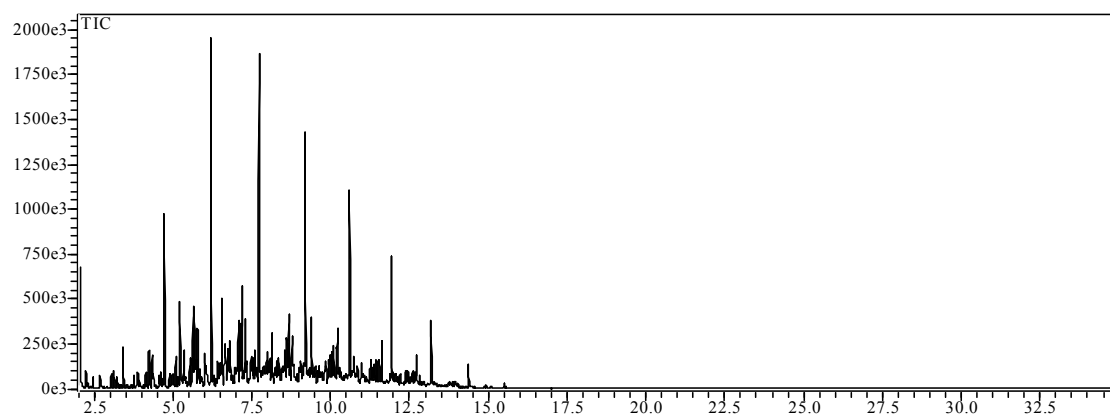


Figure B-1: Chromatogram of JP-8 from GC/MS analysis.

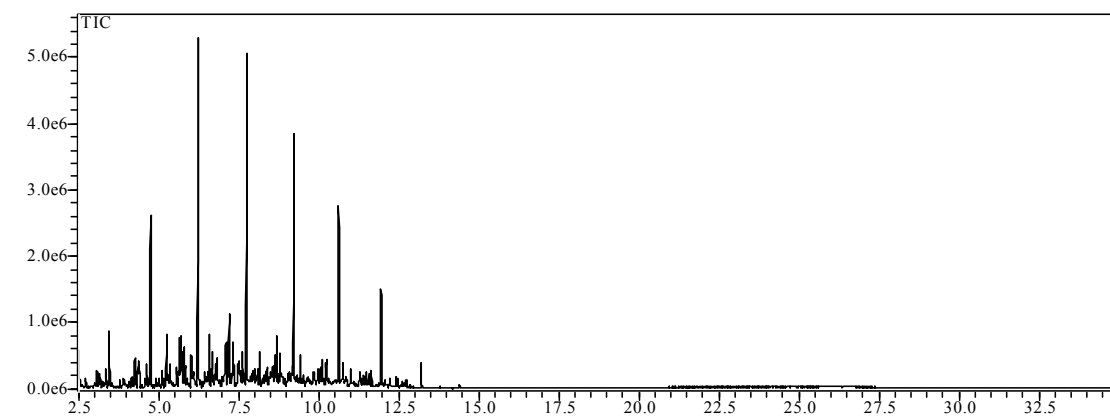


Figure B-2: Chromatogram of JP-8 +100 from GC/MS analysis.

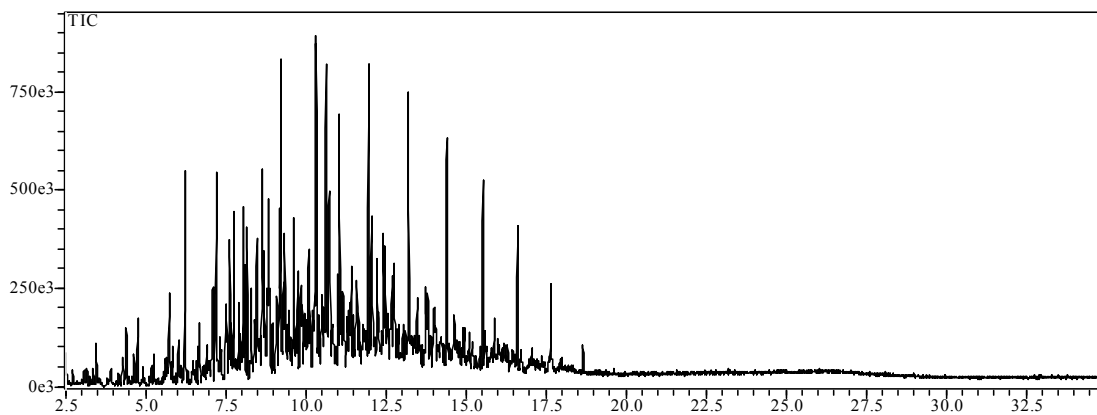


Figure B-3: Chromatogram of EI-001 (hydrotreated LCO) from GC/MS analysis.

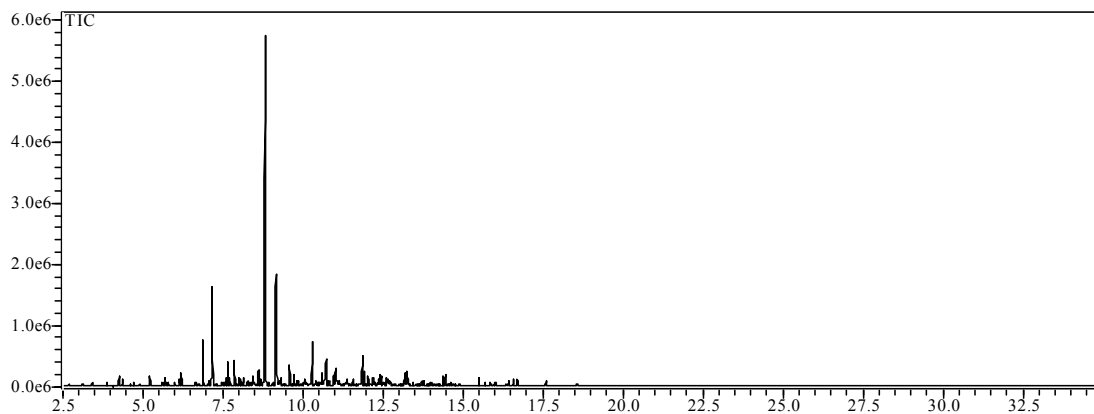


Figure B-4: Chromatogram of EI-002 (hydrotreated LCO/RCO) from GC/MS analysis.

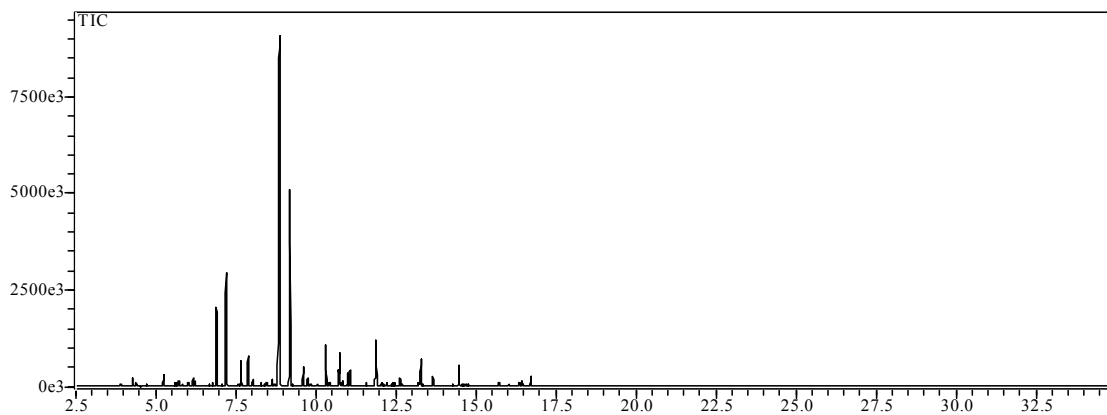


Figure B-5: Chromatogram of EI-003 (hydrotreated RCO) from GC/MS analysis.

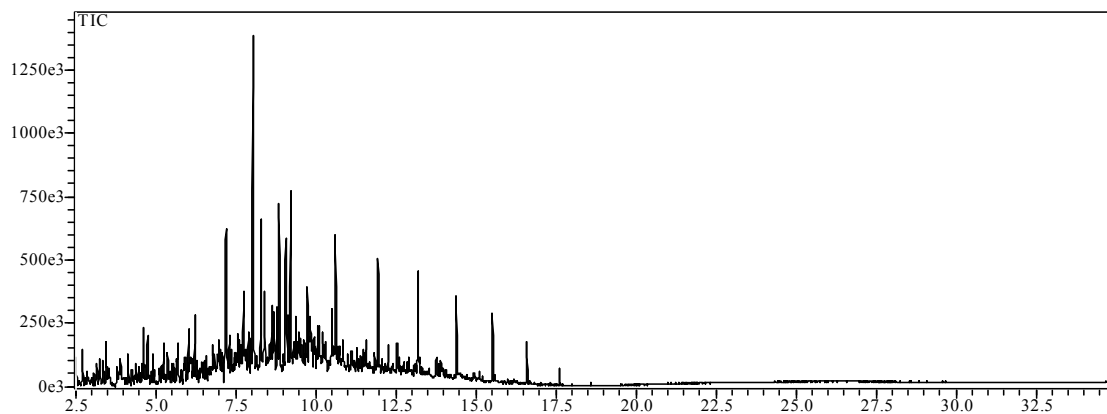


Figure B-6: Chromatogram of EI-004 (saturated LCO) from GC/MS analysis.

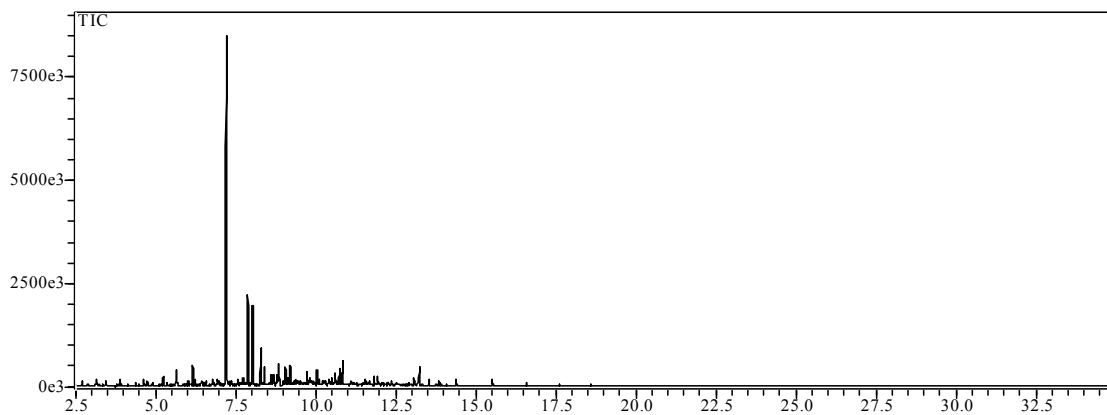


Figure B-7: Chromatogram of EI-005 (saturated LCO/RCO) from GC/MS analysis.

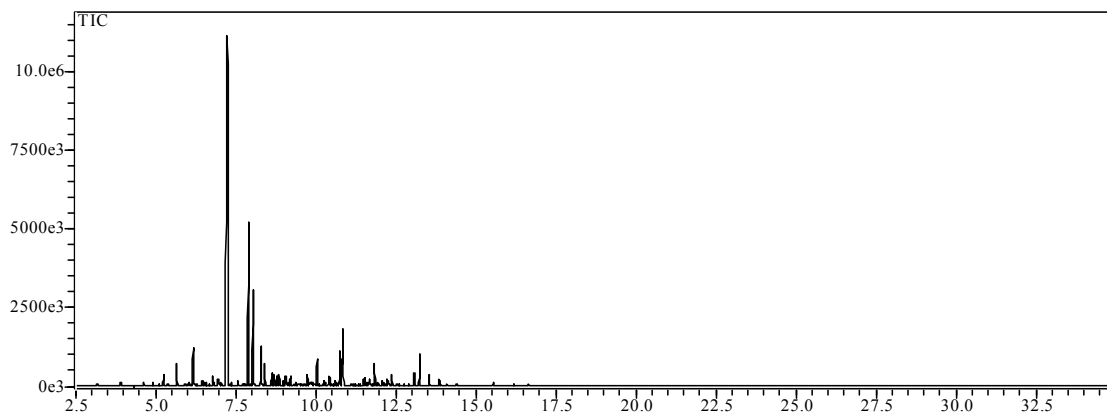


Figure B-8: Chromatogram of EI-006 (saturated RCO) from GC/MS analysis.

Appendix C

Thermal Stability and Properties Test Results

C.1 Weight of Gases in Static Thermal Stability Test

C.1.1 Calculation of N₂ Weight before Stressing

The 25-mL microautoclave was pressurized with N₂ about 100-150 psig in each test.

From
$$PV = nRT = \frac{m RT}{MW}$$

Then,
$$m = MW \cdot \frac{PV}{RT}$$

where $m = \text{weight of gas}$

$MW = \text{average gas molecular weight.}$

Thus,
$$m = \frac{28 \text{ g/gmol} \times 100 \text{ psig} \times 25 \times 10^{-3} \text{ L} \times 1 \text{ atm}}{0.082 \frac{\text{atm} \cdot \text{L}}{\text{gmol} \cdot \text{K}} \times 296 \text{ K} \times 14.7 \text{ psi}}$$

and $m = 0.22 \text{ g.}$

If $P = 150 \text{ psig,}$ $m = 0.32 \text{ g.}$

The scale in the laboratory measured N₂ in the 25-mL reactor (from the difference of reactor weight before and after N₂ pressurization) for all tests to be around 0.20 – 0.32 g. The number is close to the calculated value from ideal gas equation above. Thus the gas measurement method by weight different can be considered a reliable one.

C.1.2 Calculation of Gas Weight after Stressing

The gas products after stressing consisted of hydrocarbon gas mixtures and initial N₂. In this test, the gas weight was obtained from difference of total reactor weight before and after the release of gas, subtracting the weight of N₂. To check the hydrocarbon gas produced from stressing, the pressure increase after quenching and cooling down to room temperature was recorded. Similar to calculation in C.1.1, the number was plugged into ideal gas equation. And, the average molecular weight of hydrocarbon gas products has to be estimated from the gases' molecular weights and their percentages (obtained from peak area from GC headspace analysis). One example of their calculation is shown below:

Example of gas products from stressing hydrotreated LCO/RCO (EI-002) for 2 hours is shown below. The pressure of gas mixtures after reaction at room temperature was 250 psig. From Figure C-1, the GC peaks represent 41 wt% CH₄ (*MW*=16), 30 wt% C₂H₄ (*MW*=28), 20 wt% C₃H₈ (*MW*= 44), 3 wt% C₄H₁₀ (*MW*= 58) and 5 wt% C₄H₈ (*MW*=56). However, N₂ (*MW* =28) gas which had been added to the initial system still existed but the peak was unable to be detected by FID method.

Estimation of gas molecular weight is therefore,

$$MW_{avg} = (0.41 \times 16) + (0.30 \times 28) + (0.20 \times 44) + (0.03 \times 58) + (0.05 \times 56) \\ \cong 29$$

From
$$m = MW \frac{PV}{RT}$$

Thus,
$$m = \frac{29 \text{ g/gmol} \times 250 \text{ psig} \times 25 \times 10^{-3} \text{ L} \times 1 \text{ atm}}{0.082 \frac{\text{atm. L}}{\text{gmol.K}} \times 296 \text{ K} \times 14.7 \text{ psi}}$$

$$m = 0.52 \text{ g.}$$

The scale in the laboratory also measured total hydrocarbon gas produced to be 0.52 g. This can represent the accuracy of scale measurement which can be proved by the above calculation.

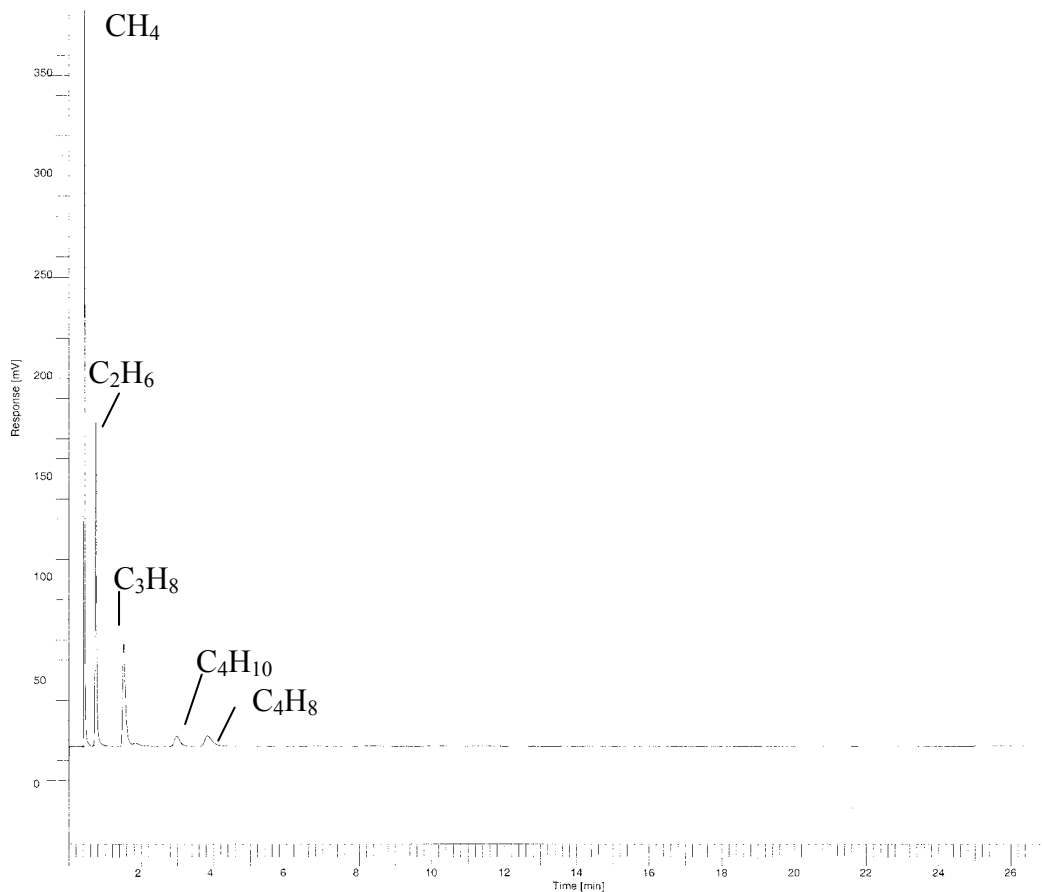
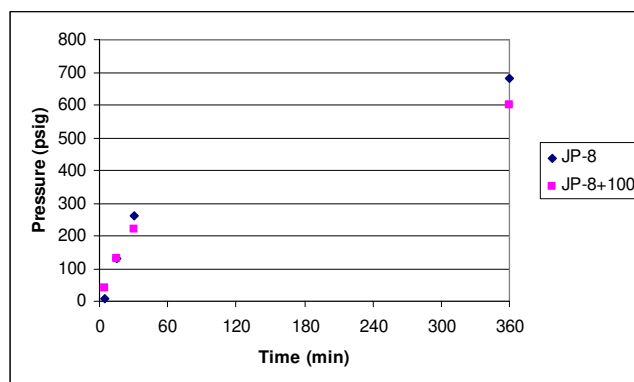
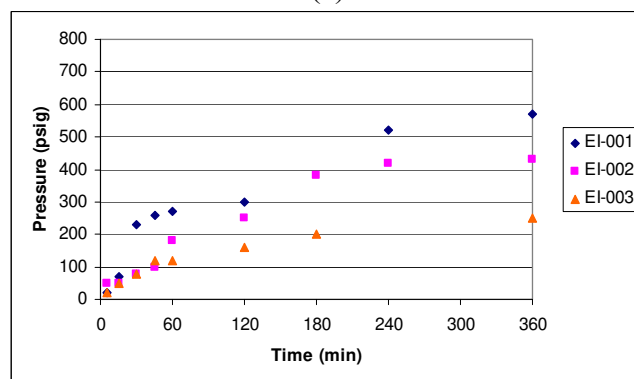


Figure C-1: GC trace of gas formation from stressing of hydrotreated LCO/RCO at 480°C (100 psig N₂) for 2 hours.

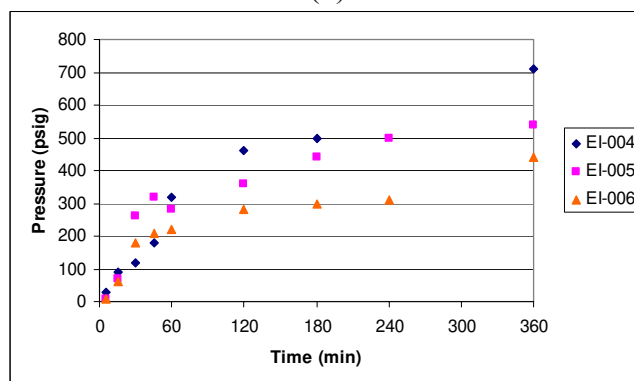
The pressures of hydrocarbon gases produced from conventional fuels and six coal-based jet fuel candidates are presented in Figure C-2. The trends below are similar to those gas formations in Figure 4-3 to 4-5.



(a)



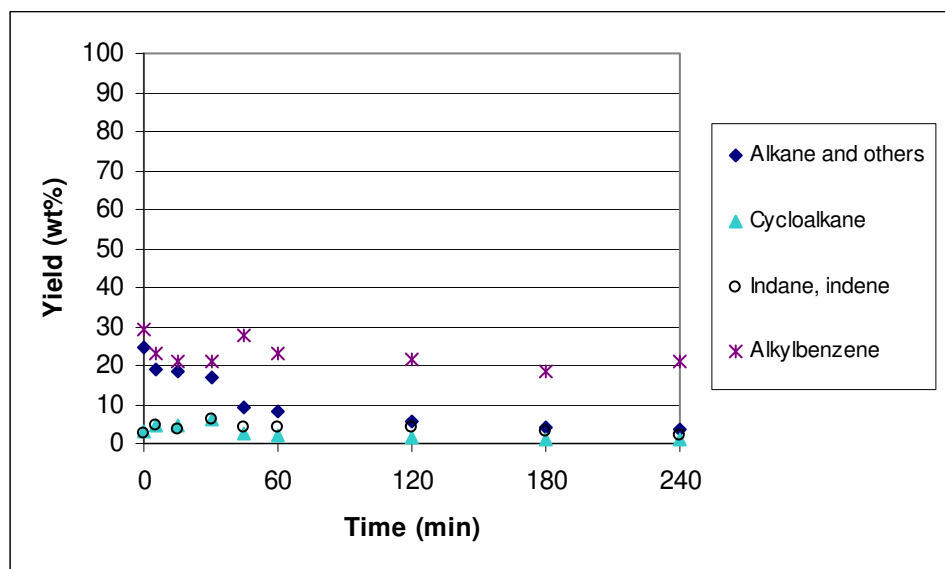
(b)



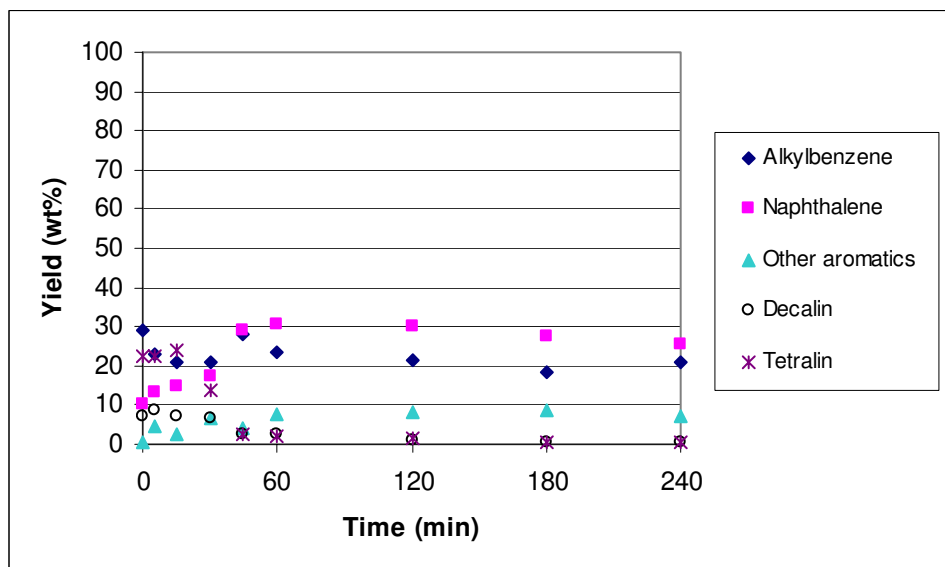
(c)

Figure C-2: Pressure record of hydrocarbon gases produced from stressing (a) petroleum-based jet fuels, (b) hydrotreated fuels and (c) saturated fuels at 480°C under N₂ 100 psig.

C.2 Chemical Distribution of Stressed Jet Fuels with the Increasing Time

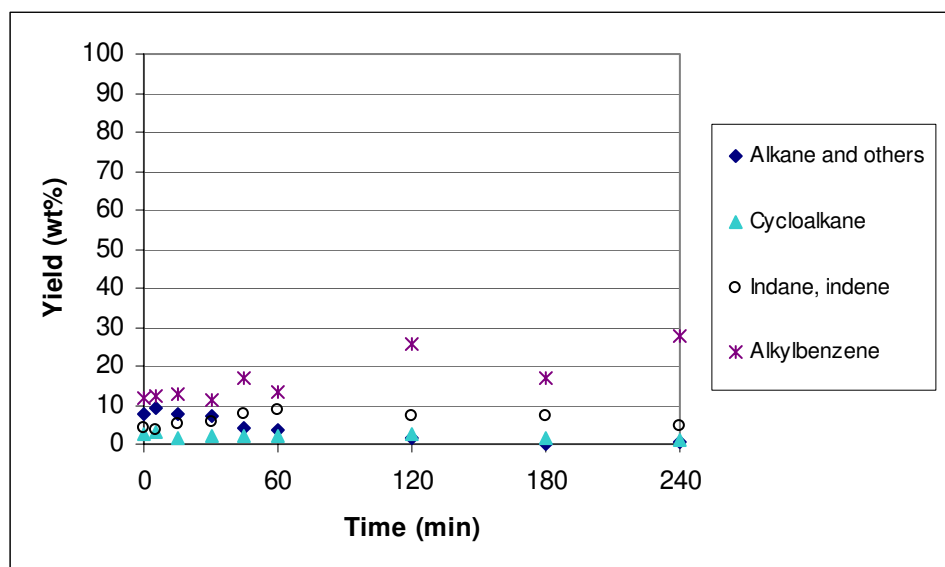


(a)

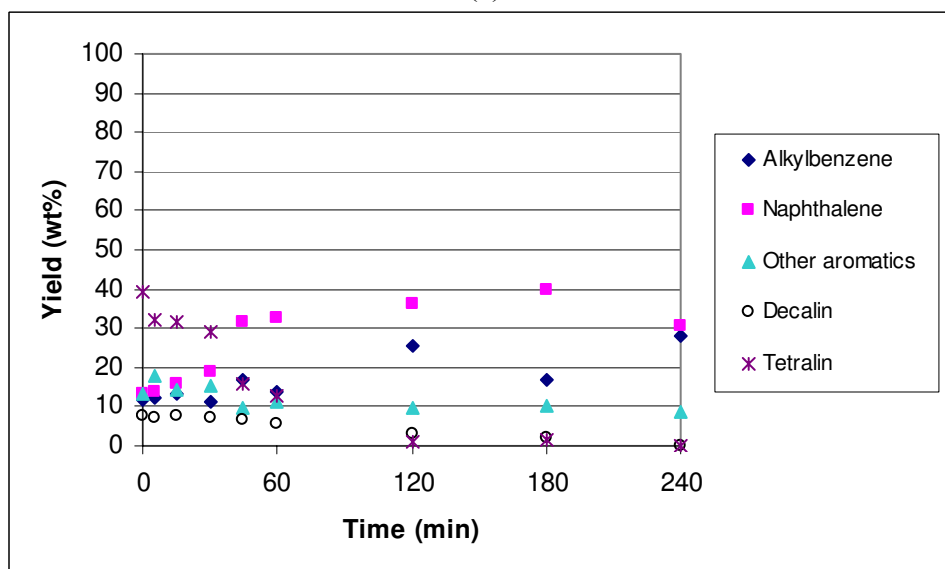


(b)

Figure C-3: Chemical distribution of stressed EI-001 (hydrotreated LCO) with the increasing time: (a) class 1-5 and (b) class 5-9.

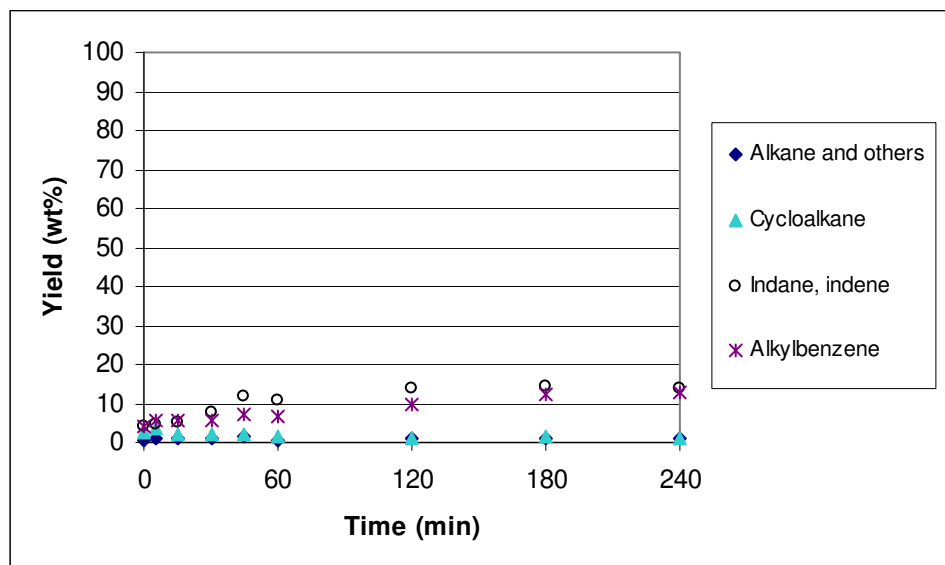


(a)

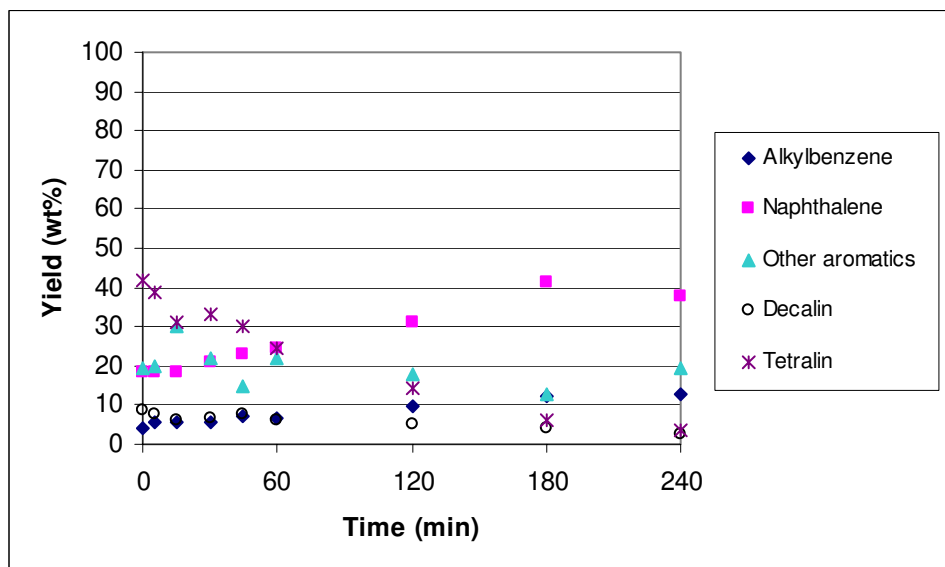


(b)

Figure C-4: Chemical distribution of stressed EI-002 (hydrotreated LCO/RCO) with the increasing time: (a) class 1-5 and (b) class 5-9.

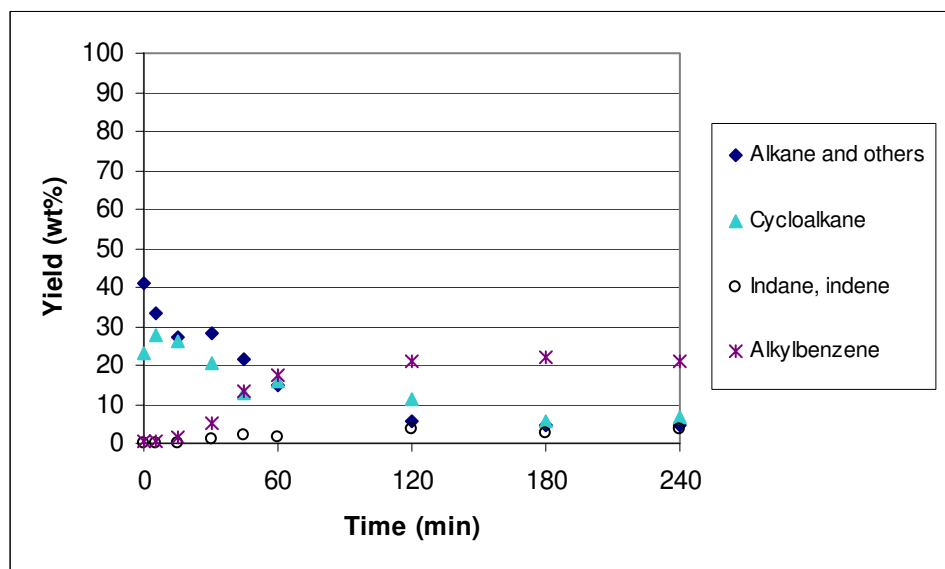


(a)

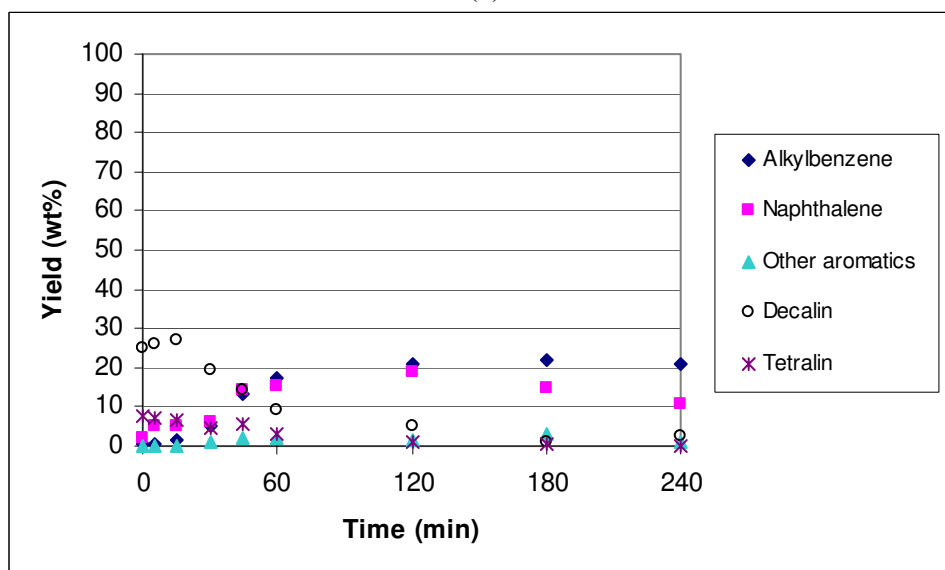


(b)

Figure C-5: Chemical distribution of stressed EI-003 (hydrotreated RCO) with the increasing time: (a) class 1-5 and (b) class 5-9.

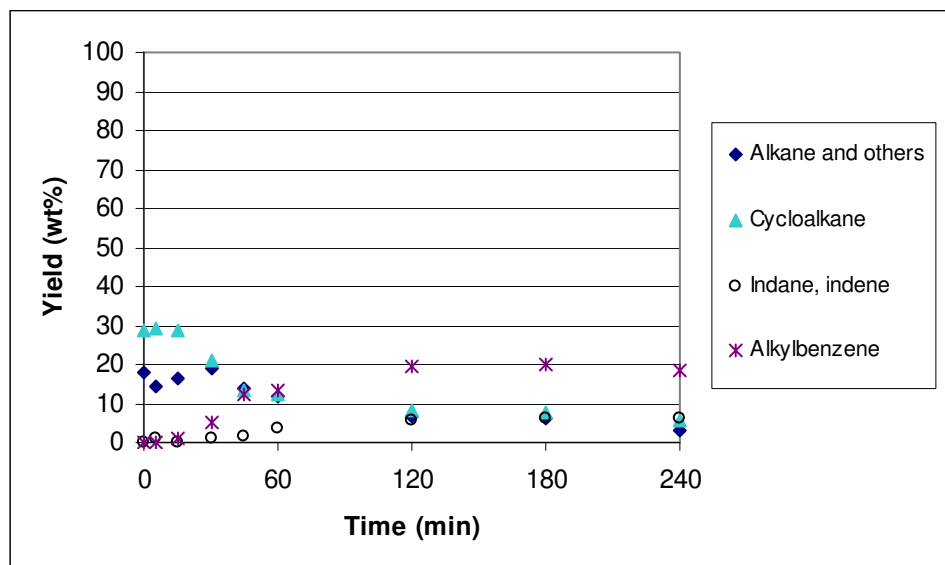


(a)

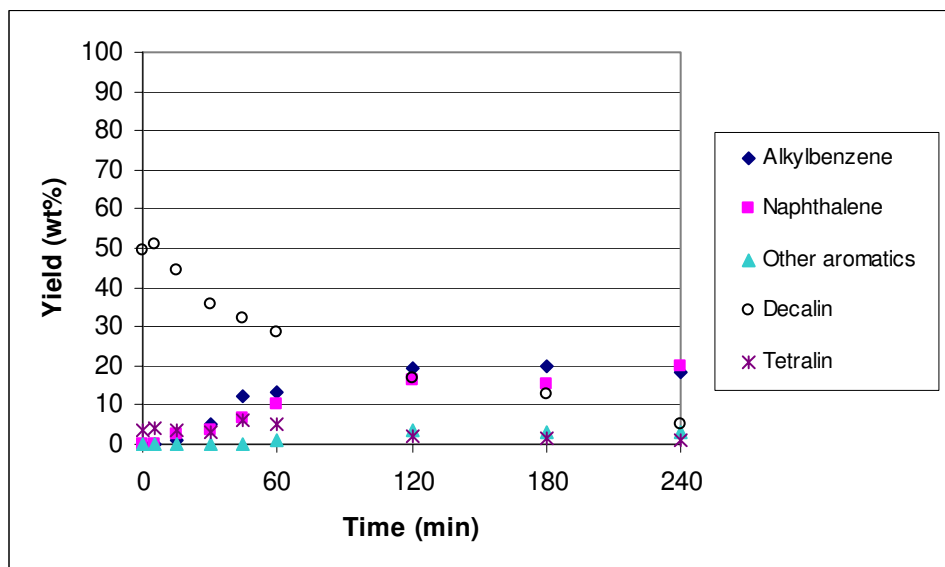


(b)

Figure C-6: Chemical distribution of stressed EI-004 (saturated LCO) with the increasing time: (a) class 1-5 and (b) class 5-9.

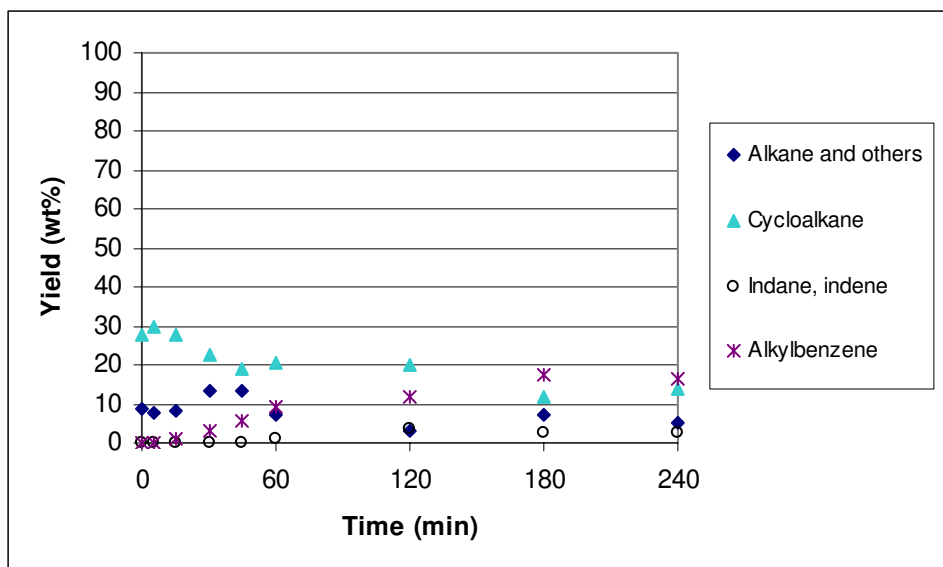


(a)

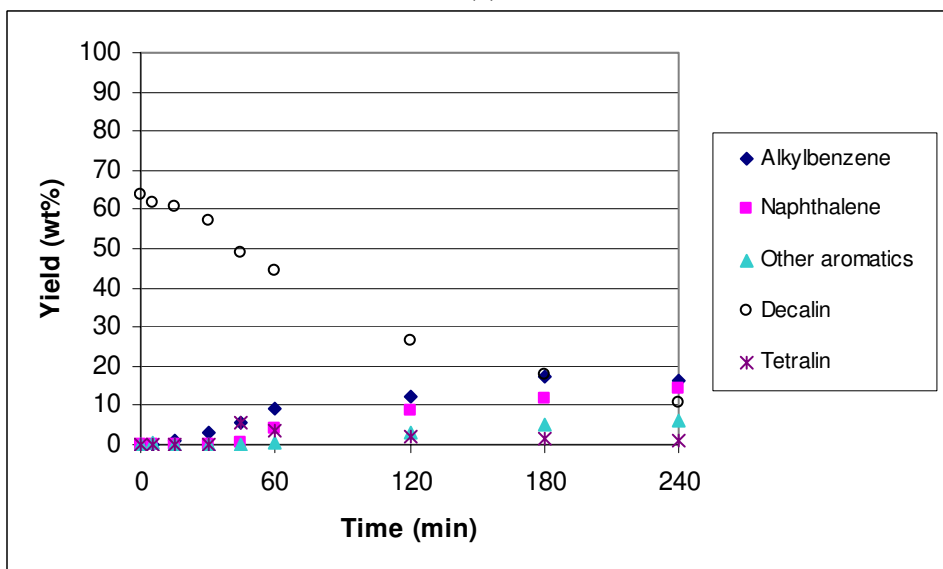


(b)

Figure C-7: Chemical distribution of stressed EI-005 (saturated LCO/RCO) with the increasing time: (a) class 1-5 and (b) class 5-9.



(a)



(b)

Figure C-8: Chemical distribution of stressed EI-006 (saturated RCO) with the increasing time: (a) class 1-5 and (b) class 5-9.

C.3 Summary of Thermal Stability and Properties Testing Results

Table C-1: Solid deposition rate of model compounds, petroleum-based and coal-based jet fuels (static condition).

Sample number	Sample name	($R_s \times 10000$) (wt%/min)	($R_s' \times 10000$) (wt%/min)
N/A	Decalin	64	90
N/A	Tetralin	0	0
N/A	Norpar-13	428	354
N/A	JP-8	503	518
N/A	JP-8+100	461	452
EI-001	HDT LCO	523	604
EI-002	HDT (LCO/RCO)	201	319
EI-003	HDT RCO	14	19
EI-004	SAT LCO	341	410
EI-005	SAT (LCO/RCO)	171	256
EI-006	SAT RCO	100	179
EI-007	HDT (LCO/ RCO 1:3), 110-126-3	65	111
EI-008	HDT (LCO/ RCO 1:3), 110-126-6	78	119
EI-009	HDT (LCO/ RCO 1:3), 110-126-7	109	145
EI-010	HDT (LCO/ RCO 1:3), 111-126-3	133	156
EI-011	HDT (LCO/ RCO 1:3), 111-126-6	147	225
EI-012	HDT (LCO/ RCO 1:3), 111-126-7	151	216
EI-013	HDT (LCO/ RCO 1:3), 112-126-3	242	287
EI-014	HDT (LCO/ RCO 1:3), 112-126-6	183	208
EI-015	HDT (LCO/ RCO 1:3), 112-126-7	126	150
EI-016	HDT (LCO/ RCO 1:3), 113-126-3	126	150
EI-017	HDT (LCO/ RCO 1:3), 113-126-6	56	66
EI-018	HDT (LCO/ RCO 1:3), 113-126-7	111	130
EI-019	HDT (LCO/ RCO 1:1), 110-126-1	280	330
EI-020	HDT (LCO/ RCO 1:1), 110-126-2	229	272
EI-021	HDT (LCO/ RCO 1:1), 110-126-4	272	310
EI-022	HDT (LCO/ RCO 1:1), 111-126-1	312	366
EI-023	HDT (LCO/ RCO 1:1), 111-126-2	276	320
EI-024	HDT (LCO/ RCO 1:1), 111-126-4	298	325
EI-025	HDT (LCO/ RCO 1:1), 112-126-1	346	399
EI-026	HDT (LCO/ RCO 1:1), 112-126-2	266	309
EI-027	HDT (LCO/ RCO 1:1), 112-126-4	274	317
EI-028	HDT (LCO/ RCO 1:1), 113-126-1	196	234
EI-029	HDT (LCO/ RCO 1:1), 113-126-2	230	274
EI-030	HDT (LCO/ RCO 1:1), 113-126-4	222	264

Table C-1 (continued)

Sample number	Sample name	($R_s \times 10000$) (wt%/min)	($R_s' \times 10000$) (wt%/min)
EI-031	HDT (LCO/ RCO 1:1) cut 180-270°C	29	50
EI-032	HDT (LCO/ RCO 1:1) cut 180-300°C	71	104
EI-033	HDT (LCO/ RCO 1:1) cut 180-320°C	224	348
EI-034	HDT (LCO/ RCO 1:3) cut 180-270°C	1	1
EI-035	HDT (LCO/ RCO 1:3) cut 180-300°C	9	29
EI-036	HDT (LCO/ RCO 1:3) cut 180-320°C	18	30
EI-037	HDT (LCO/ RCO 1:1) cut 180-270°C	48	84
EI-038	HDT (LCO/ RCO 1:3) cut 180-270°C	2	4
B-001	HDT LCO: HDT RCO 3:1	461	489
B-002	HDT LCO: HDT RCO 1:1	326	484
B-003	HDT LCO: HDT RCO 1:3	249	419
B-004	SAT LCO: SAT RCO 3:1	259	270
B-005	SAT LCO: SAT RCO 1:1	214	258
B-006	SAT LCO: SAT RCO 1:3	160	231
B-007	HDT LCO: SAT LCO 3:1	479	490
B-008	HDT LCO: SAT LCO 1:1	437	451
B-009	HDT LCO: SAT LCO 1:3	344	349
B-010	HDT LCO: SAT RCO 3:1	351	385
B-011	HDT LCO: SAT RCO 1:1	203	217
B-012	HDT LCO: SAT RCO 1:3	182	200
B-013	HDT RCO: SAT LCO 3:1	111	175
B-014	HDT RCO: SAT LCO 1:1	240	269
B-015	HDT RCO: SAT LCO 1:3	296	320
B-016	HDT RCO: SAT RCO 3:1	60	97
B-017	HDT RCO: SAT RCO 1:1	83	128
B-018	HDT RCO: SAT RCO 1:3	117	172
B-019	HDT (LCO/RCO) + 10% Decalin	208	314
B-020	HDT (LCO/RCO) + 10% Tetralin	145	227
B-021	HDT (LCO/RCO) + 20% Decalin	193	298
B-022	HDT (LCO/RCO) + 20% Tetralin	109	187
B-023	SAT (LCO/RCO) + 10% Decalin	159	228
B-024	SAT (LCO/RCO) + 10% Tetralin	166	243
B-025	SAT (LCO/RCO) + 20% Decalin	148	202
B-026	SAT (LCO/RCO) + 20% Tetralin	132	212
B-027	HDT (LCO/RCO) + Norpar-13	444	378
B-028	SAT (LCO/RCO) + Norpar-13	328	303

Table C-2: Chemical composition versus solid deposit in flow condition (stainless steel surface) [129].

No sparge- Average

No.	Class 1	Class 2	Class 3	Class 4	Class 5	Class 6	Class 7	Class 8	Autoxidative Carbon	Total Carbon
EI-001	24.84	3.03	2.66	29.30	10.13	0.44	7.31	22.29	551 ± 295 µg carbon	791 ± 304 µg carbon
EI-002	7.86	2.77	4.00	11.95	13.13	13.21	7.70	39.38	1129 ± 163 µg C/cm ²	1293 ± 178 µg C/cm ²
EI-003	0.55	2.52	4.02	4.13	18.56	19.38	8.79	42.05	995±280 µg carbon	1341±221 µg carbon
EI-004	41.27	23.08	0.00	0.67	2.25	0.00	24.93	7.80	150 ± 18 µg carbon	331 ± 21 µg carbon
EI-005	18.00	28.84	0.00	0.20	0.00	0.00	49.57	3.39	168 ± 81 µg carbon	342 ± 177 µg carbon
EI-006	8.71	27.71	0.00	0.05	0.00	0.00	63.54	0.00	88 ± 42 µg carbon	179 ± 83 µg carbon

2 hour N₂- Average

No.	Class 1	Class 2	Class 3	Class 4	Class 5	Class 6	Class 7	Class 8	Autoxidative Carbon	Total Carbon
EI-001	24.84	3.03	2.66	29.30	10.13	0.44	7.31	22.29	136 ± 75 µg carbon	244 ± 76 µg carbon
EI-002	7.86	2.77	4.00	11.95	13.13	13.21	7.70	39.38	1495 ± 6 µg C/cm ²	1815 ± 223 µg C/cm ²
EI-003	0.55	2.52	4.02	4.13	18.56	19.38	8.79	42.05	605±120 µg carbon	694±200 µg carbon
EI-004	41.27	23.08	0.00	0.67	2.25	0.00	24.93	7.80	128 ± 37 µg carbon	212 ± 76 µg carbon
EI-005	18.00	28.84	0.00	0.20	0.00	0.00	49.57	3.39	100 ± 34 µg carbon	228 ± 104 µg carbon
EI-006	8.71	27.71	0.00	0.05	0.00	0.00	63.54	0.00	94 ± 17 µg carbon	204 ± 6 µg carbon

Continuous N₂- Average

No.	Class 1	Class 2	Class 3	Class 4	Class 5	Class 6	Class 7	Class 8	Autoxidative Carbon	Total Carbon
EI-001	24.84	3.03	2.66	29.30	10.13	0.44	7.31	22.29	118 ± 96 µg carbon	228 ± 144 µg carbon
EI-002	7.86	2.77	4.00	11.95	13.13	13.21	7.70	39.38	1383 ± 900 µg C/cm ²	1286 ± 854 µg C/cm ²
EI-003	0.55	2.52	4.02	4.13	18.56	19.38	8.79	42.05	703±39 µg carbon	784±93 µg carbon
EI-004	41.27	23.08	0.00	0.67	2.25	0.00	24.93	7.80	63 ± 25 µg carbon	111 ± 68 µg carbon
EI-005	18.00	28.84	0.00	0.20	0.00	0.00	49.57	3.39	81 ± 11 µg carbon	174 ± 4 µg carbon
EI-006	8.71	27.71	0.00	0.05	0.00	0.00	63.54	0.00	49 ± 11 µg carbon	105 ± 22 µg carbon

Table C-3: Chemical composition versus solid deposit in flow condition (Inconel 718 surface) [116].

No.	Class 1	Class 2	Class 3	Class 4	Class 5	Class 6	Class 7	Class 8	Carbon Deposit ($\mu\text{g C}/\text{cm}^2$ alloy surface)
EI-001	24.84	3.03	2.66	29.30	10.13	0.44	7.31	22.29	2.0
EI-002	7.86	2.77	4.00	11.95	13.13	13.21	7.70	39.38	9.8
EI-003	0.55	2.52	4.02	4.13	18.56	19.38	8.79	42.05	24.4
EI-004	41.27	23.08	0.00	0.67	2.25	0.00	24.93	7.80	12.6
EI-005	18.00	28.84	0.00	0.20	0.00	0.00	49.57	3.39	11.9
EI-006	8.71	27.71	0.00	0.05	0.00	0.00	63.54	0.00	16.7

Table C-4: QCM deposition results for the petroleum-based jet fuels and the second generation of coal-based jet fuels.

Sample number	Sample name	QCM deposit ($\mu\text{g}/\text{cm}^2$)	Description
N/A	JP-8+100	0.5	slow oxidation and low deposition
N/A	JP-8	4.6	slow-moderate oxidation, moderate-high deposition
EI-007	HDT (LCO/ RCO 1:3), 110-126-3	1.4	fast oxidation, low deposition
EI-008	HDT (LCO/ RCO 1:3), 110-126-6	2.5	very fast oxidation, low-moderate deposition
EI-009	HDT (LCO/ RCO 1:3), 110-126-7	0.6	very fast oxidation, low deposition
EI-010	HDT (LCO/ RCO 1:3), 111-126-3	2.9	moderate-fast oxidation, moderate deposition
EI-011	HDT (LCO/ RCO 1:3), 111-126-6	4.9	fast oxidation, moderate-high deposition
EI-012	HDT (LCO/ RCO 1:3), 111-126-7	4.9	fast oxidation, moderate-high deposition
EI-013	HDT (LCO/ RCO 1:3), 112-126-3	N/A	N/A
EI-014	HDT (LCO/ RCO 1:3), 112-126-6	N/A	N/A
EI-015	HDT (LCO/ RCO 1:3), 112-126-7	N/A	N/A
EI-016	HDT (LCO/ RCO 1:3), 113-126-3	7.4	moderate oxidation, high deposition
EI-017	HDT (LCO/ RCO 1:3), 113-126-6	2.7	fast oxidation, low-moderate deposition
EI-018	HDT (LCO/ RCO 1:3), 113-126-7	2.9	fast oxidation, moderate deposition
EI-019	HDT (LCO/ RCO 1:1), 110-126-1	-0.7	fast oxidation, very low deposition
EI-020	HDT (LCO/ RCO 1:1), 110-126-2	0.7	fast oxidation, low deposition
EI-021	HDT (LCO/ RCO 1:1), 110-126-4	3.7	moderate oxidation, moderate deposition
EI-022	HDT (LCO/ RCO 1:1), 111-126-1	3.5	fast oxidation, moderate deposition
EI-023	HDT (LCO/ RCO 1:1), 111-126-2	0.9	fast oxidation, low deposition
EI-024	HDT (LCO/ RCO 1:1), 111-126-4	1.7	fast oxidation, low-moderate deposition
EI-025	HDT (LCO/ RCO 1:1), 112-126-1	17.1	fast oxidation, very high deposition
EI-026	HDT (LCO/ RCO 1:1), 112-126-2	N/A	N/A
EI-027	HDT (LCO/ RCO 1:1), 112-126-4	2.6	fast oxidation, low-moderate deposition
EI-028	HDT (LCO/ RCO 1:1), 113-126-1	3.8	moderate-fast oxidation, moderate deposition
EI-029	HDT (LCO/ RCO 1:1), 113-126-2	3.7	moderate-fast oxidation, moderate deposition
EI-030	HDT (LCO/ RCO 1:1), 113-126-4	2	fast oxidation, low-moderate deposition

Table C-5: H/C ratios of petroleum-based and coal-based jet fuels.

Sample number	Sample name	H/C
N/A	JP-8	1.84
N/A	JP-8+100	1.85
EI-001	HDT LCO	1.51
EI-002	HDT (LCO/RCO)	1.34
EI-003	HDT RCO	1.19
EI-004	SAT LCO	1.79
EI-005	SAT (LCO/RCO)	1.73
EI-006	SAT RCO	1.73
EI-007	HDT (LCO/ RCO 1:3), 110-126-3	1.19
EI-008	HDT (LCO/ RCO 1:3), 110-126-6	1.22
EI-009	HDT (LCO/ RCO 1:3), 110-126-7	1.24
EI-010	HDT (LCO/ RCO 1:3), 111-126-3	1.20
EI-011	HDT (LCO/ RCO 1:3), 111-126-6	1.18
EI-012	HDT (LCO/ RCO 1:3), 111-126-7	1.21
EI-013	HDT (LCO/ RCO 1:3), 112-126-3	1.09
EI-014	HDT (LCO/ RCO 1:3), 112-126-6	1.29
EI-015	HDT (LCO/ RCO 1:3), 112-126-7	1.24
EI-016	HDT (LCO/ RCO 1:3), 113-126-3	1.31
EI-017	HDT (LCO/ RCO 1:3), 113-126-6	1.26
EI-018	HDT (LCO/ RCO 1:3), 113-126-7	1.32
EI-019	HDT (LCO/ RCO 1:1), 110-126-1	1.22
EI-020	HDT (LCO/ RCO 1:1), 110-126-2	1.19
EI-021	HDT (LCO/ RCO 1:1), 110-126-4	1.11
EI-022	HDT (LCO/ RCO 1:1), 111-126-1	1.31
EI-023	HDT (LCO/ RCO 1:1), 111-126-2	1.16
EI-024	HDT (LCO/ RCO 1:1), 111-126-4	1.15
EI-025	HDT (LCO/ RCO 1:1), 112-126-1	1.37
EI-026	HDT (LCO/ RCO 1:1), 112-126-2	1.19
EI-027	HDT (LCO/ RCO 1:1), 112-126-4	1.20
EI-028	HDT (LCO/ RCO 1:1), 113-126-1	1.39
EI-029	HDT (LCO/ RCO 1:1), 113-126-2	1.28
EI-030	HDT (LCO/ RCO 1:1), 113-126-4	1.28
EI-031	HDT (LCO/ RCO 1:1) cut 180-270°C	1.14
EI-032	HDT (LCO/ RCO 1:1) cut 180-300°C	1.14
EI-033	HDT (LCO/ RCO 1:1) cut 180-320°C	1.11
EI-034	HDT (LCO/ RCO 1:3) cut 180-270°C	1.15
EI-035	HDT (LCO/ RCO 1:3) cut 180-300°C	1.14
EI-036	HDT (LCO/ RCO 1:3) cut 180-320°C	1.16
EI-037	HDT (LCO/ RCO 1:1) cut 180-270°C	1.17
EI-038	HDT (LCO/ RCO 1:3) cut 180-270°C	1.13

Table C-5 (continued)

Sample number	Sample name	H/C
B-001	HDT LCO: HDT RCO 3:1	1.44
B-002	HDT LCO: HDT RCO 1:1	1.35
B-003	HDT LCO: HDT RCO 1:3	1.27
B-004	SAT LCO: SAT RCO 3:1	1.81
B-005	SAT LCO: SAT RCO 1:1	1.81
B-006	SAT LCO: SAT RCO 1:3	1.77
B-007	HDT LCO: SAT LCO 3:1	1.60
B-008	HDT LCO: SAT LCO 1:1	1.70
B-009	HDT LCO: SAT LCO 1:3	1.70
B-010	HDT LCO: SAT RCO 3:1	1.62
B-011	HDT LCO: SAT RCO 1:1	1.73
B-012	HDT LCO: SAT RCO 1:3	1.74
B-013	HDT RCO: SAT LCO 3:1	1.31
B-014	HDT RCO: SAT LCO 1:1	1.48
B-015	HDT RCO: SAT LCO 1:3	1.67
B-016	HDT RCO: SAT RCO 3:1	1.36
B-017	HDT RCO: SAT RCO 1:1	1.49
B-018	HDT RCO: SAT RCO 1:3	1.61
B-019	HDT (LCO/RCO) + 10% Decalin	1.37
B-020	HDT (LCO/RCO) + 10% Tetralin	1.43
B-021	HDT (LCO/RCO) + 20% Decalin	1.35
B-022	HDT (LCO/RCO) + 20% Tetralin	1.34
B-023	SAT (LCO/RCO) + 10% Decalin	1.79
B-024	SAT (LCO/RCO) + 10% Tetralin	1.82
B-025	SAT (LCO/RCO) + 20% Decalin	1.76
B-026	SAT (LCO/RCO) + 20% Tetralin	1.64

Table C-6: Heat of combustion and energy density of model compounds, petroleum-based and coal-based jet fuels.

Sample number	Sample name	Q_g (Btu/lb)	Hydrogen (wt%)	Q_n (Btu/lb)	Specific gravity, 60°F	Energy density (MJ/L)
N/A	Decane	20390	15.5	20376	0.73	34.60
N/A	Decalin	19370	13.0	19358	0.90	40.34
N/A	Tetralin	18330	9.1	18322	0.97	41.47
N/A	Norpar-13	20410	N/A	N/A	N/A	N/A
N/A	JP-8	19880	13.2	18676	0.81	35.19
N/A	JP-8+100	19833	12.9	18653	0.81	35.14
EI-001	HDT LCO	19140	11.2	18121	0.89	37.51
EI-002	HDT (LCO/RCO)	18750	9.9	17843	0.93	38.60
EI-003	HDT RCO	18260	8.9	17446	0.97	39.36
EI-004	SAT LCO	19886	12.9	18706	0.84	36.55
EI-005	SAT (LCO/RCO)	19500	12.2	18383	0.86	36.77
EI-006	SAT RCO	19440	12.5	18297	0.88	37.45
EI-007	HDT (LCO/ RCO 1:3), 110-126-3	18389	9.0	17573	0.96	39.43
EI-008	HDT (LCO/ RCO 1:3), 110-126-6	18257	9.1	17430	0.97	39.29
EI-009	HDT (LCO/ RCO 1:3), 110-126-7	18253	9.3	17401	0.96	38.78
EI-010	HDT (LCO/ RCO 1:3), 111-126-3	18215	9.1	17384	0.96	38.89
EI-011	HDT (LCO/ RCO 1:3), 111-126-6	18388	8.8	17587	0.96	39.27
EI-012	HDT (LCO/ RCO 1:3), 111-126-7	18043	9.1	17211	0.96	38.51
EI-013	HDT (LCO/ RCO 1:3), 112-126-3	17954	8.3	17201	0.96	38.43
EI-014	HDT (LCO/ RCO 1:3), 112-126-6	18727	9.6	17849	0.96	39.72
EI-015	HDT (LCO/ RCO 1:3), 112-126-7	18397	9.3	17547	0.95	38.79
EI-016	HDT (LCO/ RCO 1:3), 113-126-3	18571	9.7	17683	0.94	38.85
EI-017	HDT (LCO/ RCO 1:3), 113-126-6	18464	9.5	17601	0.95	38.88
EI-018	HDT (LCO/ RCO 1:3), 113-126-7	18343	9.8	17454	0.94	38.09
EI-019	HDT (LCO/ RCO 1:1), 110-126-1	18342	8.3	17582	0.94	38.58
EI-020	HDT (LCO/ RCO 1:1), 110-126-2	18286	8.9	17472	0.97	39.28
EI-021	HDT (LCO/ RCO 1:1), 110-126-4	18233	8.4	17466	0.97	39.27
EI-022	HDT (LCO/ RCO 1:1), 111-126-1	18607	9.8	17714	0.94	38.76
EI-023	HDT (LCO/ RCO 1:1), 111-126-2	18356	8.8	17556	0.97	39.47
EI-024	HDT (LCO/ RCO 1:1), 111-126-4	18293	8.7	17497	0.97	39.31
EI-025	HDT (LCO/ RCO 1:1), 112-126-1	18778	10.1	17859	0.92	38.29
EI-026	HDT (LCO/ RCO 1:1), 112-126-2	18491	8.8	17686	0.95	39.09
EI-027	HDT (LCO/ RCO 1:1), 112-126-4	18375	9.1	17548	0.96	39.10
EI-028	HDT (LCO/ RCO 1:1), 113-126-1	18612	10.4	17665	0.94	38.63
EI-029	HDT (LCO/ RCO 1:1), 113-126-2	18626	9.6	17748	0.94	38.66
EI-030	HDT (LCO/ RCO 1:1), 113-126-4	18486	9.6	17611	0.94	38.62

Table C-6 (continued)

Sample number	Sample name	Q_g (Btu/lb)	Hydrogen (wt%)	Q_n (Btu/lb)	Specific gravity, 60°F	Energy density (MJ/L)
EI-031	HDT (LCO/ RCO 1:1) cut 180-270°C	18336	8.7	17544	0.97	39.44
EI-032	HDT (LCO/ RCO 1:1) cut 180-300°C	18113	7.9	17394	0.97	39.31
EI-033	HDT (LCO/ RCO 1:1) cut 180-320°C	18068	7.7	17362	0.98	39.38
EI-034	HDT (LCO/ RCO 1:3) cut 180-270°C	18403	8.8	17605	0.97	39.64
EI-035	HDT (LCO/ RCO 1:3) cut 180-300°C	18270	8.6	17486	0.97	39.59
EI-036	HDT (LCO/ RCO 1:3) cut 180-320°C	17983	8.4	17216	0.98	39.14
B-001	HDT LCO: HDT RCO 3:1	18931	10.5	17969	0.91	38.04
B-002	HDT LCO: HDT RCO 1:1	18699	10.0	17784	0.93	38.47
B-003	HDT LCO: HDT RCO 1:3	18545	9.4	17687	0.95	39.08
B-004	SAT LCO: SAT RCO 3:1	19741	12.7	18580	0.85	36.73
B-005	SAT LCO: SAT RCO 1:1	19712	13.1	18517	0.86	37.04
B-006	SAT LCO: SAT RCO 1:3	19531	12.8	18362	0.87	37.16
B-007	HDT LCO: SAT LCO 3:1	19381	11.7	18316	0.88	37.38
B-008	HDT LCO: SAT LCO 1:1	19578	12.3	18453	0.87	37.13
B-009	HDT LCO: SAT LCO 1:3	19764	12.4	18632	0.85	36.95
B-010	HDT LCO: SAT RCO 3:1	19323	11.9	18241	0.89	37.66
B-011	HDT LCO: SAT RCO 1:1	19373	12.6	18221	0.89	37.51
B-012	HDT LCO: SAT RCO 1:3	19490	12.7	18334	0.88	37.63
B-013	HDT RCO: SAT LCO 3:1	18643	10.9	17653	0.94	38.49
B-014	HDT RCO: SAT LCO 1:1	19109	10.9	18114	0.91	38.13
B-015	HDT RCO: SAT LCO 1:3	19331	11.0	18326	0.87	37.19
B-016	HDT RCO: SAT RCO 3:1	18310	10.1	17386	0.95	38.32
B-017	HDT RCO: SAT RCO 1:1	19001	11.0	17999	0.93	38.72
B-018	HDT RCO: SAT RCO 1:3	19284	11.8	18209	0.90	38.22

Table C-7: Smoke points of model compounds, petroleum-based and coal-based jet fuels.

Sample number	Sample name	Smoke point (mm)
N/A	Decalin	24.4
N/A	Tetralin	6.5
N/A	Ethylbenzene	7.0
N/A	JP-8	23.6
N/A	JP-8+100	24.1
EI-001	HDT LCO	8.7
EI-002	HDT (LCO/RCO)	6.8
EI-003	HDT RCO	6.1
EI-004	SAT LCO	24.3
EI-005	SAT (LCO/RCO)	23.0
EI-006	SAT RCO	22.1
EI-031	HDT (LCO/ RCO 1:1) cut 180-270°C	5.5
EI-032	HDT (LCO/ RCO 1:1) cut 180-300°C	5.0
EI-033	HDT (LCO/ RCO 1:1) cut 180-320°C	5.3
EI-034	HDT (LCO/ RCO 1:3) cut 180-270°C	5.7
EI-035	HDT (LCO/ RCO 1:3) cut 180-300°C	5.7
EI-036	HDT (LCO/ RCO 1:3) cut 180-320°C	5.5
EI-037	HDT (LCO/ RCO 1:1) cut 180-270°C	6.3
EI-038	HDT (LCO/ RCO 1:3) cut 180-270°C	6.3
EI-039	x621 cut 2	5.4
EI-040	x622 cut 2	5.2
EI-041	x651 cut 2	6.4

Table C-8: Flash points of petroleum-based and coal-based jet fuels.

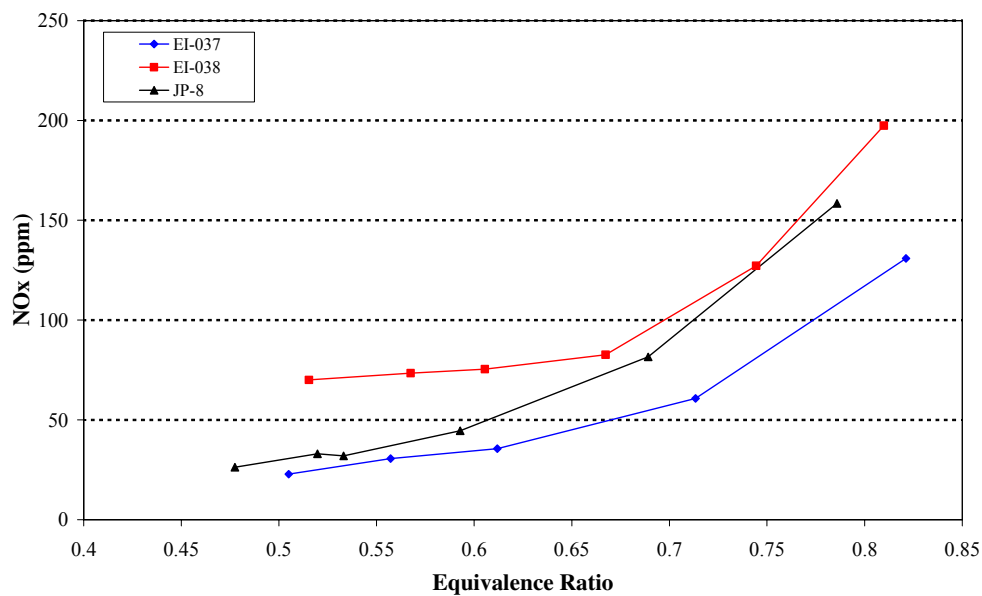
Sample number	Sample name	Flash point (°F)
N/A	JP-8	124.1
N/A	JP-8+100	123.1
EI-001	HDT LCO	171.1
EI-002	HDT (LCO/RCO)	163.0
EI-003	HDT RCO	157.1
EI-004	SAT LCO	148.0
EI-005	SAT (LCO/RCO)	145.0
EI-006	SAT RCO	139.1
EI-031	HDT (LCO/ RCO 1:1) cut 180-270°C	172.6
EI-032	HDT (LCO/ RCO 1:1) cut 180-300°C	181.6
EI-033	HDT (LCO/ RCO 1:1) cut 180-320°C	176.5
EI-034	HDT (LCO/ RCO 1:3) cut 180-270°C	168.6
EI-035	HDT (LCO/ RCO 1:3) cut 180-300°C	171.7
EI-036	HDT (LCO/ RCO 1:3) cut 180-320°C	172.6
B-001	HDT LCO: HDT RCO 3:1	165.2
B-002	HDT LCO: HDT RCO 1:1	161.2
B-003	HDT LCO: HDT RCO 1:3	159.3
B-004	SAT LCO: SAT RCO 3:1	145.0
B-005	SAT LCO: SAT RCO 1:1	143.1
B-006	SAT LCO: SAT RCO 1:3	139.1
B-007	HDT LCO: SAT LCO 3:1	165.2
B-008	HDT LCO: SAT LCO 1:1	157.3
B-009	HDT LCO: SAT LCO 1:3	151.3
B-010	HDT LCO: SAT RCO 3:1	159.1
B-011	HDT LCO: SAT RCO 1:1	151.2
B-012	HDT LCO: SAT RCO 1:3	145.0
B-013	HDT RCO: SAT LCO 3:1	153.1
B-014	HDT RCO: SAT LCO 1:1	151.3
B-015	HDT RCO: SAT LCO 1:3	149.2
B-016	HDT RCO: SAT RCO 3:1	151.2
B-017	HDT RCO: SAT RCO 1:1	145.0
B-018	HDT RCO: SAT RCO 1:3	141.1

Table C-9: Viscosity of petroleum-based and coal-based jet fuels.

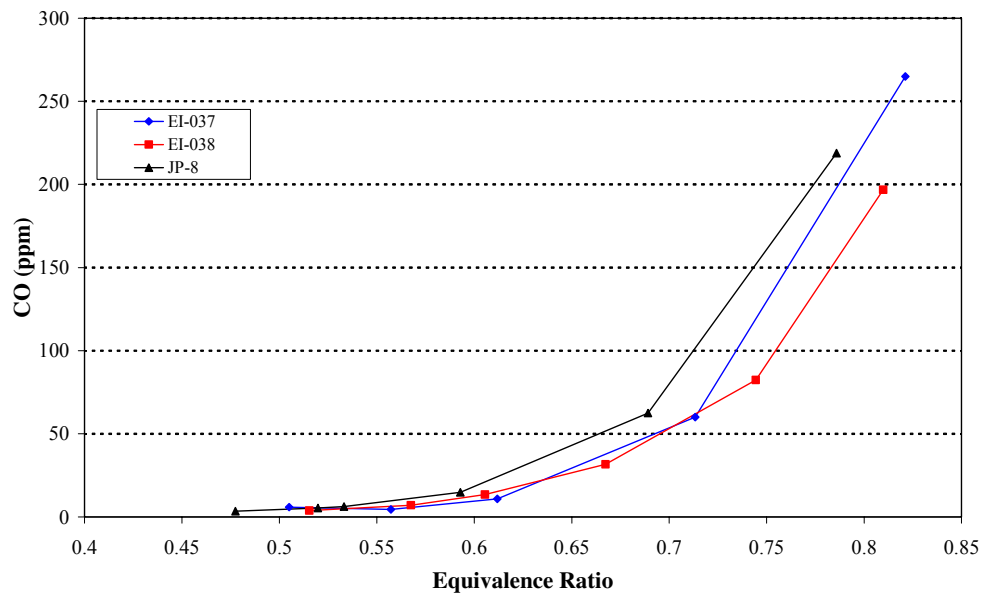
Sample number	Sample name	Viscosity (cSt)
N/A	JP-8	1.66
N/A	JP-8+100	1.39
EI-001	HDT LCO	2.37
EI-002	HDT (LCO/RCO)	2.55
EI-003	HDT RCO	1.99
EI-004	SAT LCO	2.66
EI-005	SAT (LCO/RCO)	2.73
EI-006	SAT RCO	2.77
EI-031	HDT (LCO/ RCO 1:1) cut 180-270°C	1.97
EI-032	HDT (LCO/ RCO 1:1) cut 180-300°C	1.98
EI-033	HDT (LCO/ RCO 1:1) cut 180-320°C	2.41
EI-034	HDT (LCO/ RCO 1:3) cut 180-270°C	2.01
EI-035	HDT (LCO/ RCO 1:3) cut 180-300°C	2.05
EI-036	HDT (LCO/ RCO 1:3) cut 180-320°C	2.23

Table C-10: Cloud points of petroleum-based and coal-based jet fuels.

Sample number	Sample name	Cloud point (°F)
N/A	JP-8	-69
N/A	JP-8+100	N/A
EI-001	HDT LCO	-51
EI-002	HDT (LCO/RCO)	N/A
EI-003	HDT RCO	-107
EI-004	SAT LCO	-49
EI-005	SAT (LCO/RCO)	N/A
EI-006	SAT RCO	-112



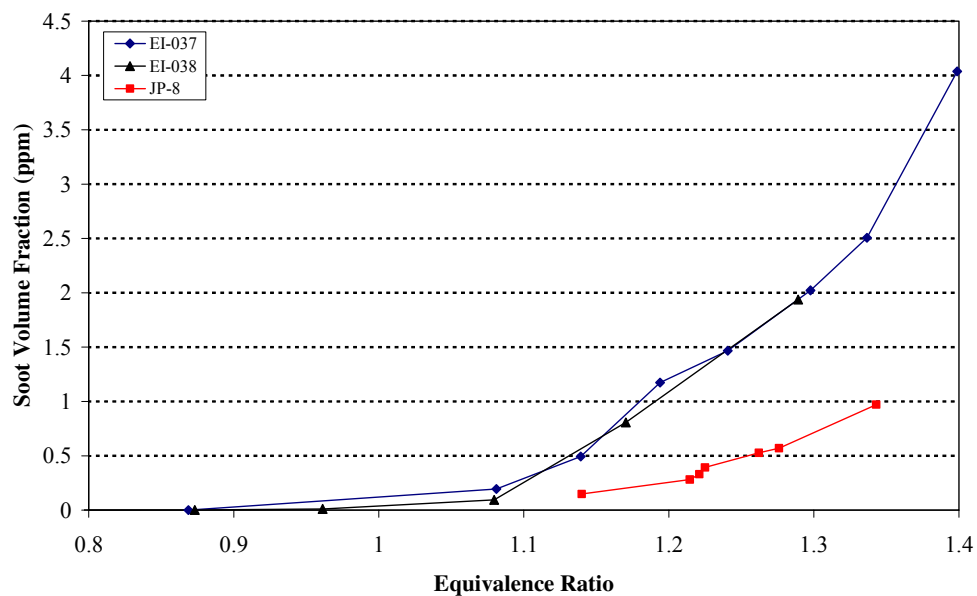
(a)



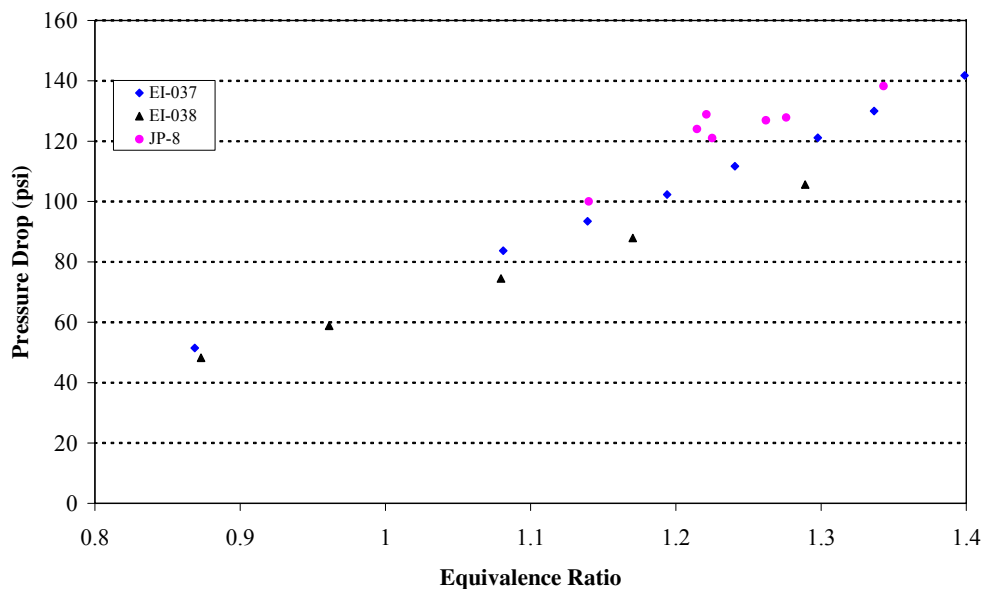
(b)

Figure C-9: Comparison of (a) NOx emissions and (b) CO emissions corrected to 15% oxygen. (Chamber pressure = 0.56 MPa (5atm): $T_{up} = 700^{\circ}\text{K}$ (800°F))

Note: Experiments performed by Dr. Silvano Saretto.



(a)



(b)

Figure C-10: JP-8 vs. coal based jet fuel (a) soot sweep comparison and (b) pressure drop across peanut injector. (Chamber pressure = 0.56 MPa (5atm); T_{up} = 660°K (530°F))
Note: Experiments performed by Dr. Silvano Saretto.

Appendix D

Numerical Analyses

D.1 MATLAB Source Code for Ternary Diagram Plots

function TernaryPlot(x1,x2,z,flag)

```

% FUNCTION TernaryPlot(x1,x2,z,flag)
% PURPOSE:
% To display ternary plots of three major composition. Ternary plots are
% shown as contour plot, regular plot and three dimensional stem plot.
% SYNTAX:
% TernaryPlot(x1,x2,z,flag);
% TernaryPlot(A,flag); where A = [x1 x2 z];
% TernaryPlot(A); where A = [x1 x2 z] and flag will be set to 1.
% INPUTS:
% x1 = Column vector containing composition x1.
% x2 = Column vector containing composition x2.
% z = Column vector containing property at the composition (x1,x2,x3)
% where  $x1+x2+x3 = 1$ .
% flag = Plot type (scalar).
% OUTPUTS:
% If flag == 1, two dimensional contour plot in ternary axis is displayed.
% If flag == 2, two dimensional regular plot in ternary axis is displayed.
% If flag == 3, three dimensional stem plot in ternary axis is displayed.
% EXAMPLE:
% Suppose we have three column vectors x1, x2, and z. Then if we would
% like to get two dimensional stem plot in ternary axis, the following
% commands are equivalent:
% TernaryPlot(x1,x2,z,3);
% TernaryPlot([x1 x2 z],3);
% SEE ALSO:
% TernaryTrans.m
% @date: 13-May-2003 23:23:10

if nargin == 2 % If number of function input argument equal 2
    z = x1(:,3);
    x2 = x1(:,2);
    x1 = x1(:,1);

```

```

    flag = x2;
elseif nargin == 1
    z = x1(:,3);
    x2 = x1(:,2);
    x1 = x1(:,1);
    flag = 1;
end

```

`[x1,x2] = TernaryTrans(x1,x2);` % Call function TernaryTrans.m for transforming cartesian product axis into ternary axis.

% Two dimensional interpolation

```

xx = linspace(min(x1),max(x1),100);
yy = linspace(min(x2),max(x2),100);
[xx,yy] = meshgrid(xx,yy);
zz = griddata(x1,x2,z,xx,yy,'cubic');

```

if flag==1 % Ternary contour plot

```

    figure;
    [c,h] = contourf(xx,yy,zz,25);
    hold on;
    xcorner = [50 0 100 50];
    ycorner = [50*sqrt(3) 0 0 50*sqrt(3)];
    plot(xcorner,ycorner,'k.-');
    axis([0 100 0 50*sqrt(3)]);
    text(50,50*sqrt(3),'x_1');
    text(-3,-2,'x_2');
    text(102,-2,'x_3');
    colorbar;
    axis equal off;
    colormap pink;
    CM = flipud(colormap);
    colormap(CM);

```

elseif flag == 2 % Ternary regular plot

```

    figure;
    h = plot(x1,x2,'b. ');
    set(h,'MarkerSize',15);
    hold on;
    xcorner = [50 0 100 50];
    ycorner = [50*sqrt(3) 0 0 50*sqrt(3)];
    plot(xcorner,ycorner,'k.-');
    axis([0 100 0 50*sqrt(3)]);
    text(50,50*sqrt(3),'x_1');
    text(-3,-2,'x_2');

```

```

text(102,-2,'x_3');
axis equal off;

elseif flag == 3 % Three dimensional stem plot
figure;
stem3(x1,x2,z,'b','fill');
box;
hold on;
V = [0 0 0;
     100 0 0;
     50 50*sqrt(3) 0;
     0 0 max(z);
     100 0 max(z);
     50 50*sqrt(3) max(z)];
idx = [1 2 3 1 4 5 6 3 2 5 4 6];
plot3(V(idx,1),V(idx,2),V(idx,3),'k');
axis off;
text(50,50*sqrt(3),0,'x_1');
text(-3,-2,0,'x_2');
text(102,-2,0,'x_3');
camproj('perspective');
end

```

function [xx,yy] = TernaryTrans(x,y)

```

% FUNCTION TernaryTrans(x,y)
% PURPOSE:
% To transform cartesian product axis into ternary axis.
% INPUTS:
% x = Column vector containing composition x1.
% y = Column vector containing composition x2.
% OUTPUTS:
% xx = Column vector containing composition x1 in ternary axis.
% yy = Column vector containing composition x2 in ternary axis.
% SEE ALSO:
% TernaryPlot.m
% @date: 13-May-2003 23:34:15

yy = sqrt(3)/2*x;
xx = sqrt(3)/2*(200-(2*y+x))/sqrt(3);

```

D.2 Multiple Linear Regression Analysis

MLR of chemical composition and solid deposition rate from Minitab Release 13.3

The regression equation is:

$$(R_s \times 10000 \text{ wt\%/min}) = 330 + 14.2 \text{ alkane} - 6.19 \text{ tetralin} + 1.75 \text{ aromatics} - 4.98 \text{ cycloalkanes} - 2.47 \text{ decalins}$$

Predictor	Coef	SE Coef	T	P
Constant	329.7	177.1	1.86	0.077
alkane	14.219	3.355	4.24	0.000
tetralin	-6.187	2.190	-2.83	0.010
aromatics	1.746	1.697	1.03	0.315
cycloalkanes	-4.976	3.129	-1.59	0.127
decalin	-2.467	1.763	-1.40	0.176

S = 34.28 R-Sq = 94.3% R-Sq(adj) = 93.0%

Analysis of Variance

Source	DF	SS	MS	F	P
Regression	5	409019	81804	69.60	0.000
Residual Error	21	24684	1175		
Total	26	433703			

MLR of chemical composition and net heat of combustion from Minitab Release 13.3

The regression equation is:

$$Q_n = 17712 + 17.4 (\text{alkane+cycloalkane+alkene+cycloalkene}) - 2.82 (\text{aromatics+tetralin})$$

Predictor	Coef	SE Coef	T	P
Constant	17711.9	154.0	115.04	0.000
alkane+cycloalkane +alkene+cycloalkene	17.422	2.829	6.16	0.000
aromatics+tetralin	-2.820	1.580	-1.78	0.080

S = 140.5 R-Sq = 88.7% R-Sq(adj) = 88.2%

Analysis of Variance

Source	DF	SS	MS	F	P
Regression	2	7899063	3949532	200.02	0.000
Residual Error	51	1007053	19746		
Total	53	8906116			

Source	DF	Seq SS
alkane+cycloalkane + alkene+cycloalkene	1	7836159
all_aro+	1	62904

MLR of chemical composition and smoke point from Minitab Release 13.3

The regression equation is:

$$S = 15.0 - 0.101 \text{ total aromatics} + 0.327 \text{ cycloalkanes}$$

Predictor	Coef	SE Coef	T	P
Constant	14.975	3.721	4.02	0.001
total aromatics	-0.10122	0.03833	-2.64	0.019
cycloalkanes	0.3267	0.1355	2.41	0.030

$$S = 1.014 \quad R\text{-Sq} = 98.1\% \quad R\text{-Sq}(\text{adj}) = 97.8\%$$

Analysis of Variance

Source	DF	SS	MS	F	P
Regression	2	743.40	371.70	361.68	0.000
Residual Error	14	14.39	1.03		
Total	16	757.79			

Source	DF	Seq SS
all_aro+	1	737.43
cycloalk	1	5.97

MLR of chemical composition and flash point from Minitab Release 13.3

The regression equation is:

$$Tf = 151 + 0.354 \text{ aromatics} - 0.145 \text{ total cycloalkanes}$$

Predictor	Coef	SE Coef	T	P
Constant	150.903	5.870	25.71	0.000
aromatics	0.3540	0.1144	3.09	0.005
total_cycloalkanes	-0.14508	0.08049	-1.80	0.083

$$S = 5.056 \quad R\text{-Sq} = 83.4\% \quad R\text{-Sq}(\text{adj}) = 82.2\%$$

Analysis of Variance

Source	DF	SS	MS	F	P
Regression	2	3478.1	1739.0	68.04	0.000
Residual Error	27	690.1	25.6		
Total	29	4168.2			

Source	DF	Seq SS
aromatics	1	3395.1
total_cycloalkanes	1	83.0

MLR of hydrogen types and solid deposition rate from Minitab Release 13.3

The regression equation is:

$$(R_s \times 10000 \text{ wt\%/min}) = 442 + 2.34 A+B - 11.3 C+D+E1$$

Predictor	Coef	SE Coef	T	P
Constant	441.50	59.46	7.42	0.000
A+B	2.3406	0.5673	4.13	0.000
C+D+E1	-11.328	1.379	-8.22	0.000

S = 69.38 R-Sq = 78.7% R-Sq(adj) = 77.6%

Analysis of Variance

Source	DF	SS	MS	F	P
Regression	2	711311	355655	73.89	0.000
Residual Error	40	192532	4813		
Total	42	903843			

Source	DF	Seq SS
A+B	1	386334
C+D+E1	1	324977

Unusual Observations

Obs	A+B	solid de	Fit	SE Fit	Residual	St Resid
1	50.9	523.0	345.0	17.8	178.0	2.66R
7	43.9	461.0	211.5	10.8	249.5	3.64R
42	83.8	328.0	461.2	24.1	-133.2	-2.05R

R denotes an observation with a large standardized residual

D.3 Artificial Neural Network Analysis

ANN of chemical composition and solid deposition rate from NeuroShell 2 Release

4.0

Structure 1: Three-layer back propagation [5 (linear), 4 (logistic), 1(logistic)]

Weights between layer 1 and 2:

	bias	1	2	3	4	5
1	20.85	0.94	11.73	16.76	15.89	3.25
2	-1.47	2.89	0.52	2.46	1.01	-0.18
3	-12.27	0.48	-13.41	5.72	-9.85	6.47
4	12.48	10.45	-0.40	1.00	-1.03	1.07

Weights between layer 2 and 3:

	bias	1	2	3	4
1	-8.87	-2.50	-10.82	-7.59	11.73

Structure 2: Three-layer back propagation [5 (linear), 4 (logistic), 1(logistic)]

Weights between layer 1 and 2:

	bias	1	2	3	4	5
1	-4.51	-10.21	10.18	-9.31	10.17	6.19
2	4.83	2.81	0.15	3.08	3.09	-0.64
3	-3.96	-7.10	-0.94	3.39	-11.53	0.79
4	6.26	6.55	-8.27	1.58	-4.36	-6.24

Weights between layer 2 and 3:

	bias	1	2	3	4
1	1.46	-2.25	-5.83	-1.91	5.27

ANN of chemical composition and net heat of combustion from NeuroShell 2**Release 4.0**

Structure 1: Three-layer back propagation [3 (linear), 2 (logistic), 1(logistic)]

Weights between layer 1 and 2:

	bias	1	2	3
1	0.14	2.55	-5.51	5.44
2	-1.22	1.25	-0.89	-0.23

Weights between layer 2 and 3:

	bias	1	2
1	1.14	1.29	-4.63

Structure 2: Three-layer back propagation [2 (linear), 2 (logistic), 1(logistic)]

Weights between layer 1 and 2:

	bias	1	2
1	1.84	-0.52	2.18
2	9.33	-8.16	-28.55

Weights between layer 2 and 3:

	bias	1	2
1	-1.10	3.11	-0.93

ANN of chemical composition and smoke point from NeuroShell 2 Release 4.0

Structure: Three-layer back propagation [2 (linear), 2 (logistic), 1(logistic)]

Weights between layer 1 and 2:

	bias	1	2
1	-0.68	-1.48	1.71
2	0.39	0.94	-1.05

Weights between layer 2 and 3:

	bias	1	2
1	0.33	-2.81	1.80

ANN of chemical composition and flash point from NeuroShell 2 Release 4.0

Structure 1: Five-layer back propagation [2 (linear), 2 (logistic), 2 (logistic), 2 (logistic), 1(logistic)]

Weights between layer 1 and 2:

	bias	1	2
1	1.83	1.85	5.92
2	-9.61	6.46	-2.24

Weights between layer 2 and 3:

	bias	1	2
1	-2.58	11.03	-6.27
2	4.67	-5.54	1.27

Weights between layer 3 and 4:

	bias	1	2
1	-0.76	2.02	-9.11
2	-1.24	-12.29	1.45

Weights between layer 4 and 5:

	bias	1	2
1	-0.69	-6.35	6.18

Structure 2: Four-layer back propagation [3 (linear), 4 (logistic), 4 (logistic), 1 (logistic)]

Weights between layer 1 and 2:

	bias	1	2	3
1	-5.22	-3.39	4.58	3.15
2	-1.37	1.38	0.25	-1.60
3	-0.11	0.38	0.99	-2.92
4	-0.11	-1.70	4.56	-3.53

Weights between layer 2 and 3:

	bias	1	2	3	4
1	-1.67	2.85	-6.43	5.95	1.13
2	-1.15	0.33	-0.83	1.79	0.21
3	-2.46	1.24	0.70	-1.42	5.18
4	-0.84	-8.39	0.01	2.79	1.98

Weights between layer 3 and 4:

	bias	1	2	3	4
1	-0.68	7.05	-2.81	-3.96	-1.72

ANN of hydrogen types and solid deposition rate from NeuroShell 2 Release 4.0

Four-layer back propagation [5 (linear), 8 (logistic), 1 (logistic)]

Weights between layer 1 and 2:

	bias	1	2	3	4	5
1	-2.82	-0.47	-3.93	4.79	1.56	0.67
2	1.13	3.19	-4.19	5.61	1.06	-2.81
3	-0.56	-0.92	-1.52	2.77	0.33	2.69
4	1.17	0.91	-0.45	-0.41	0.81	0.89
5	-0.38	-1.48	2.26	-8.23	-0.42	0.72
6	-1.44	-1.27	2.22	-1.86	3.04	-0.45
7	-0.22	-0.06	-0.02	0.57	0.02	0.16
8	2.61	2.65	2.78	6.88	-0.69	1.79

Weights between layer 2 and 3:

	bias	1	2	3	4	5	6	7	8
1	0.35	-3.30	5.15	3.35	-2.35	3.70	-3.01	-0.30	-4.88

Vita

Suchada Butnark was born in Chonburi, Thailand on December, 21, 1974. She received the B.Eng. degree in Chemical Engineering from Chulalongkorn University, Bangkok, Thailand in April 1996. From May to June 1996, she participated in the Exchange Student for Technical Experience Program (IAESTE) at the Department of Petroleum Engineering and Applied Geophysics, Norwegian University of Science and Technology, Trondheim, Norway. After that, she was selected by National Science and Technology Development Agency of Thailand (NSTDA) and Canadian Women in Engineering and Science Program (WES) to be a visiting researcher at National Fire Laboratory, National Research Council, Ottawa, Canada. She conducted a one-year research on fire tests and established a fire growth for apartment buildings. She entered The Pennsylvania State University in August 1997 and has been a graduate research assistant under supervision of Professor Harold H. Schobert at The Energy Institute since January 1998. She received the M.S. degree in Fuel Science in December 1999. In March 2000, she was awarded the third place winner from the Fifteenth Annual Graduate Exhibition, The Pennsylvania State University. Currently, she is a member of American Chemical Society. She is also the principal author of several preprints of papers on the production and properties' study of thermally stable coal-based jet fuels for American Chemical Society conferences.